GROWTH AND PROPERTIES OF BULK CZTSSe AND Sb_2Se_3 FOR SOLAR CELLS

Theodore Douglas Christopher Hobson

Thesis submitted in accordance with the requirements of the

UNIVERSITY OF LIVERPOOL

For the degree of

DOCTOR IN PHILOSOPHY

Stephenson Institute for Renewable Energy

Department of Physics

May 2020

For Holly

Abstract

This thesis presents investigations into growth techniques to produce bulk polycrystalline and single crystals of the materials $Cu_2ZnSnS_{4x}Se_{4(1-x)}$ (CZTSSe) and Sb_2Se_3, in order to better understand bulk properties of relevance for photovoltaics. For CZTSSe, a technique to grow ~100 μm monograins from a molten NaCl/KCl mix proved successful for compositions $0 \leq x \leq 1$ in increments of $\Delta x = 0.1$, with a more ordered kesterite phase demonstrated compared to directly synthesised feedstock. From this series, Vegard relations were measured as: a (Å) = -0.268(3)x + 5.6949(17) and c (Å) = -0.516(6)x + 11.345(3) while Raman modes were observed to follow two-mode behaviour as: ω_{CZTSe} (cm^{-1}) = (44.6 ± 1.6)x + (194.6 ± 0.8) and ω_{CZTS} (cm^{-1}) = (7.1 ± 1.3)x + (329.0 ± 0.8). These relationships are intended to be used as reference data to aid the measurement of sulphur-selenium ratios in CZTSSe thin films. Samples consistent with single crystals of Sb_2Se_3 with 4 mm diameter and 1 cm length were grown via vertical Bridgman, with the {100} crystal planes evidenced through optical means and XRD. These crystals exhibited low-angle boundary defects consistent with ripplocations. They also demonstrated anisotropies in the polarised Raman spectra, with sample rotation able to resolve the overlapping 187 and 190 cm^{-1} peaks. The 253 cm^{-1} peak in the Raman spectra was consistent with reports of Sb_2O_3. Se-poor and stoichiometric Sb_2Se_3 single crystals were non-conductive, while Se-rich were p-type, and Sn and Cl were found to induce p-type and n-type doping respectively, with a maximum hole density from Sn-doping of 10^{15} cm^{-3} and electron density from Cl of 10^{17} cm^{-3}. Barrier heights of 0.37 eV for p-Sb_2Se_3 / In interfaces and 0.56 eV for n-Sb_2Se_3 / Au interfaces were estimated. Deep level electron traps at 400, 700 and 850 meV were detected in n-type single crystals, thought to result from V_{Se} and V_{Se} defects, while photoluminescence peaks at 0.9, 1.1 and 1.2 eV were assigned to donor-acceptor pair transitions resulting from Sn and Cl impurities. Thermally evaporated thin film Sb_2Se_3 / CdS solar cells were prepared from n-type, intrinsic and p-type doped source material, all reaching ~1 % efficiency. Of these, the p-type devices decreased in efficiency after ageing in air, while the intrinsic and n-type increased slightly, possibly due to Sb_2O_3 formation from oxidisation.

Declarations

All of the measurements presented in this thesis were carried out by the author apart from the following, separated by institution:

Stephenson Institute for Renewable Energy, University of Liverpool:

1. Oliver S Hutter:
    a. Collaborated with the author on the synthesis of CZTSSe feedstock and growth of crystallised solid solutions series (Sections 4.2.1, 4.2.3, 5.2.1, 5.2.2 and 5.2.3)
    b. Carried out differential scanning calorimetry of NaCl/KCl mix (fig. 4.1) and CZTSSe feedstock series (fig. 5.2)
    c. Prepared Sb_2Se_3 thin films by CSS (Section 4.3.5) and air-annealed them (Section 6.6.5.1)
    d. Carried out SEM for several samples (figs. 5.1, 6.4 and 7.19)
2. Jonathan D Major:
    a. Sputtered CdS layer and deposited thermally evaporated Sb_2Se_3 layers for thin film devices (Sections 4.3.7 and 7.7)
    b. Carried out deep-level transient spectroscopy measurements (fig. 7.12)
3. Nicole Fleck carried out Raman measurements of the crystallised CZTSSe solid solution series ($0 \leq x \leq 1$) (figs. 5.11 and 5.12a)

Other departments at the University of Liverpool:

1. EBSD by Elisabetta Mariani in the Dept. of Earth, Ocean and Ecological Sciences (figs. 6.16a-c)
2. ICP-OES by Stephen Moss in analytical services at the Dept. of Chemistry (Table 5.2, figs. 5.3 and 5.4, Table 6.5)

Other institutions:

1. ICP-MS by Chris Ottley and Emily Unsworth in the Department of Earth Sciences at the University of Durham (Table 6.6)
2. Quadrupole SIMS by Guillaume Zoppi in the Dept. of Mathematics, Physics and Electrical Engineering at the University of Northumbria (fig. 6.19)
3. Hall effect by Bhaskar Das in the Chemical Engineering and Materials Science Department at the University of Minnesota (fig. 7.3, Table 7.3)
4. Photoluminescence by Maarja Grossberg, Tavi Raadik and Juri Krustok at the Department of Materials Science at the Tallinn University of Technology (figs. 7.14a and 7.15)

Acknowledgements

I have had the privilege of working with colleagues who are both great scientists and great friends. I have learnt so much from the people around me that I can't possibly relate all the ways in which they have made this work possible. I'll simply start by saying it has been a pleasure to collaborate with Oliver Hutter, Nicole Fleck, Huw Shiel, Laurie Philips, Leanne Jones, Tom Featherstone, Matt Smiles, Jack Swallow, Sylvia Mariotti, Isabel Vazquez-Fernandez, Luke Daniels and Holly Edwards to produce work I feel we should all be very proud of. The same goes for my many other collaborators both inside and outside the University of Liverpool. You have all been a joy to work with.

However, the work that makes up this thesis would also not have been possible without the invaluable help and assistance of Phil Murgatroyd, Tom Shalvey, Jessica Stoner, Tom Baines, Max Birkett, Annette Pressman, Joe Horne, Peter Yates, Manuel Apollo and Luke Thomas. There's no way I've repaid even half of the help you've given me over the years.

It's not just direct collaboration that makes a PhD, and all of my colleagues have been brilliant people to spend time with both inside and outside the lab, making the Stephenson Institute an exciting and friendly place to work. I want to offer additional thanks to Leanne and Nicole for being wonderful desk-mates and making our end of the office the 'cool corner', at least in my mind. Having Tom F around to chat was another thing that made be glad to be where I was, and along with Jack Beane, provided a welcome excuse for me to wander around the office. Thanks to Olivia Voyce for always encouraging us to be better people and to Daniel Bromley and Alex Wright for standing up for the rights of students. Thanks to Joe for injecting humour into our lunchtimes and being an unbeatable fountain of trivia, and thanks to Phil for always being there to help me out, whatever the issue. Thanks to Holly for being a great CZTS bestie and to Hatem Amli for brightening up the office.

Thanks to Oliver for teaching me a little of what he knows and most of what I know, even if not all the facts were what I'd consider 'fun'. Thanks to Laurie for being an essential beacon of competence while the rest of us are bumbling around. Thanks to Tom B for introducing me to some

great music, and to Matt for picking up the dad-joke baton after Tom went over to the dark side. Thanks also to Luke for leading the SIRE football team to victory (the first time) and to Jacob for organising games under lockdown that helped keep me sane. Thanks to Huw for reminding us that there's more to life than work, Jack S for always having a great sense of humour and Tom S for putting up with all of us. Thanks to Pete, Sylvia and Annette for making me feel welcome when I first started. I also want to thank Bruna Baggio, Angeline Kasina, Kieran Routledge, Mark Forster, Gaia Neri, Stefano Mensa, Charlotte Smith, Liam Banerji, Daniel Cheung and Khezar Saeed for all helping to make the Institute the fun and social place it is.

It goes without saying that I need to thank my supervisors Ken Durose and Jon Major for their support and encouragement as much as for their sympathy and patience with me. Thanks are always due to Vince Vasey for keeping the whole lab ticking over and I owe a great thanks to Tim Veal, Dmitry Schkukin, Jon Alaria, Frank Jaeckel, Vin Dhanak and Laurence Hardwick for all their help and for trusting me with their equipment. I want to thank my examiners Liam O'Brien and David Lane for their helpful discussions and feedback.

Thanks also need to go to my parents Kate Hobson and Hugh Pearman, my brother Ben, sisters Harriet and Lydia and all my friends in other places. To my oldest friends Joe Drane, Ayla Richardson, Roman Sheppard-Dawson and Sophie Wolfson, I owe a great thanks. I want to thank Holly Gilson for being my wonderful and constant partner in all things.

This work was finished during a difficult time for many people, and all I can do is say thank you to all my friends and family, and to wish you all the very best. This work, like me, is better for me having known all of you.

Contents

1. Introduction

1.1 Context for Photovoltaics

The conversion of solar radiation into electricity serves many purposes, but perhaps the most crucial is to reduce global greenhouse gas emissions and prevent catastrophic climate change[1]. If a meaningful reduction in the emissions of greenhouse gases is to occur, the vast majority of the energy utilised by human society must shift from CO_2-emitting fossil fuels to low-carbon sources. Renewable energy sources are expected to form a significant, if not dominant, part of this low-carbon energy infrastructure. In order to effectively reduce emissions, there are two broad conditions: a) the amount of time taken for a renewable energy installation to generate energy equivalent to the amount used to manufacture it, known as the energy payback time, must be a small fraction of its total lifetime[2] and b) the monetary cost of the installation should similarly be a small fraction of the value generated from energy output over its lifetime, with the 'monetary payback time' quantifying the time taken for an installation to generate the value of its installation. Furthermore, the monetary payback time must be such that the cost of the power generated from the installation on a day-to-day basis is competitive with, or lower than, power from fossil fuels, due to the latter's market dominance[1,2]. Wind and photovoltaic (PV) solar power have, at present, similar installed capacity worldwide, at 591 and 505 GW respectively[3] with both predicted to grow rapidly in the near future[4]. However, of the two, solar capacity is projected to expand by 700 GW by 2024, compared to 350 GW for wind[4], as shown in fig. 1.1. This may not be surprising, as 100 GW of new solar capacity was installed in 2018 alone[3]. Projections for both wind and solar are significantly larger than the predicted growth for hydropower, the renewable technology with the greatest capacity at present, at 1132 GW[3]. Indeed, this market growth would bring solar power almost level with the (projected) capacity for hydropower, at ~1250 GW by 2024[4]. The immense growth potential of solar power relates to the sheer quantity of solar radiation available, which at its peak provides an irradiance of 1000 Wm^{-2} at the Earth's surface. Even averaged over the year and the day/night cycle, a surface irradiance of 100-300 Wm^{-2} is provided[5], varying with latitude and climate. It should be noted that an acceleration in

the growth of solar power beyond these projections is possible if the cost of solar power could be reduced. This motivates research into the production of cheaper solar modules.

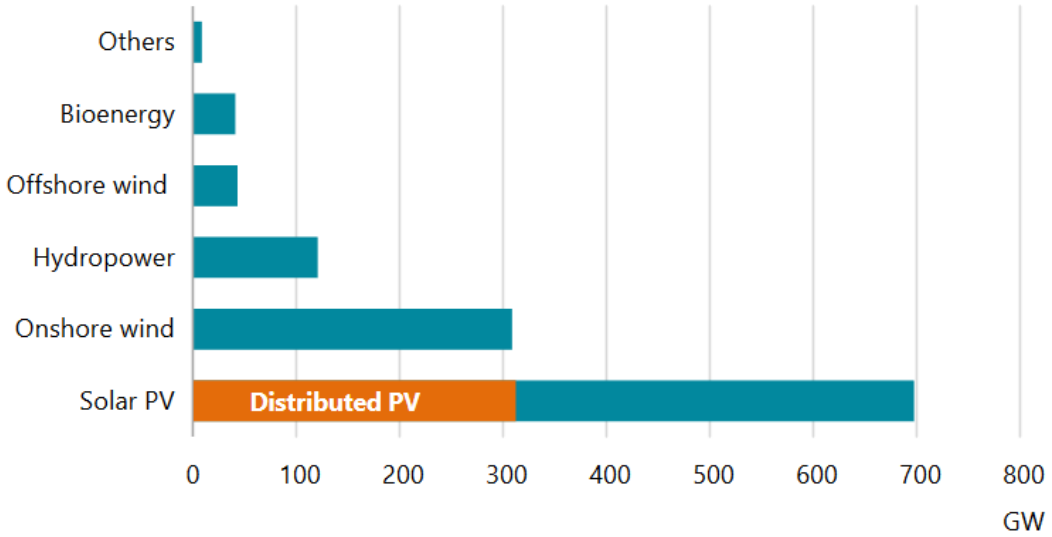

Fig. 1.1 Projected increase in renewables capacity from 2019 to 2024, without accounting for possible acceleration from cost reductions. Image reproduced from [4].

Low costs and short energy payback times usually go hand-in-hand, with a common specific cost target for solar PV being 0.50 \$/W_p (W_p being watts at peak power, i.e. when irradiance is 1000 Wm^{-2})[9]. However, mass production has now pushed production costs for CdTe-based modules below 0.53 \$/W_p, making research targets more demanding[10,11]. The worldwide solar PV market was worth around \$30.8 billion in 2016, projected to reach \$57.3 billion by 2022[12], with monocrystalline and polycrystalline silicon-based (c-Si) modules making up around a 95% market share[2]. Indeed, an explosion of Si-based installations in China accounted for around 45% of market growth in 2018, with the United States, Japan, Germany and India following in terms of annual installed capacity[3]. The non-c-Si share of the solar PV market is largely made up of 'thin film' PV modules, which are the ultimate focus of this work. The reasons for studying thin film technologies, and their merits compared to the dominant silicon-based technologies, are discussed in the next section.

1.2 Motivation for Researching CZTSSe and Sb_2Se_3

In order for solar PV to provide a cut to global greenhouse emissions at the scale required, power generation on the level of terawatts (TW) is necessary[13], meaning that in addition to low financial costs and short energy payback times, abundant raw material is required. Silicon-based modules have an energy payback time of 1-2.5 years (depending on latitude/climate) and a roughly 20 yr lifespan[2] but further reductions in energy payback time are limited by energy-intensive manufacturing processes, such as the extraction of Si from its highly stable naturally-occurring form of SiO_2 through a carbothermic reduction reaction at >1600°C[6], and its purification through the Siemens process at ~1100°C[7]. The highest-performing monocrystalline wafer cells[2] also require melting (Si melts at 1414°C[8]) for single crystal (Czochralski) growth. The area of these cells is limited by the size of the crystal that is grown and material is then lost when crystals are sectioned into wafers (kerf losses), with further losses when wafers are cut into a square form. These necessities of cell production raise energy requirements and monetary costs further[14]. Relatively large quantities of processed Si are also required to produce a single PV module, as silicon is an indirect-gap semiconductor with a low absorption coefficient, necessitating thick wafers[14].

In forming Si-based modules for PV installations, soldered ribbon connections are used to connect cells in series, as shown in fig. 1.2a, but these introduce another production step, with the ribbons potentially acting as points of failure for the module during its lifetime. These ribbon connections also contribute to shading on the top surface of the cell, reducing the active area[15].

Thin film PV addresses some of the limitations of silicon-based technologies, as direct-gap materials having high absorption coefficients mean that much thinner, polycrystalline layers may be used. High purity is also not required as the thin layers do not require long carrier lifetimes[14] and materials are often self-doping[16]. These features serve to reduce the materials and processing cost of thin film PV modules relative to silicon, even if the base material is more expensive by volume[17]. Thin film modules can also be fabricated in the form of monolithic cells on a single large substrate with integral contacts as shown in fig, 1.2b, formed through deposition[18]. This approach avoids the complications of soldering connections between cells as in a Si-based array, reducing costs

further[5]. The addition of a transparent conductive oxide layer (TCO) on the top surface of a thin film cell also allows module interconnections without the issue of shading cell underneath.

Currently, the best commercially performing thin film technologies are based on cadmium telluride (CdTe) and copper-indium-gallium sulphide/selenide (CIGS), but they bring their own limitations, namely, the high toxicity of Cd[19,20], the low abundance of Te in the Earth's crust[19] and the high material costs of In and Ga[20]. All of these serve to reduce the viability of these technologies for TW-scale power generation, meaning that there is a strong incentive to investigate alternative thin film technologies.

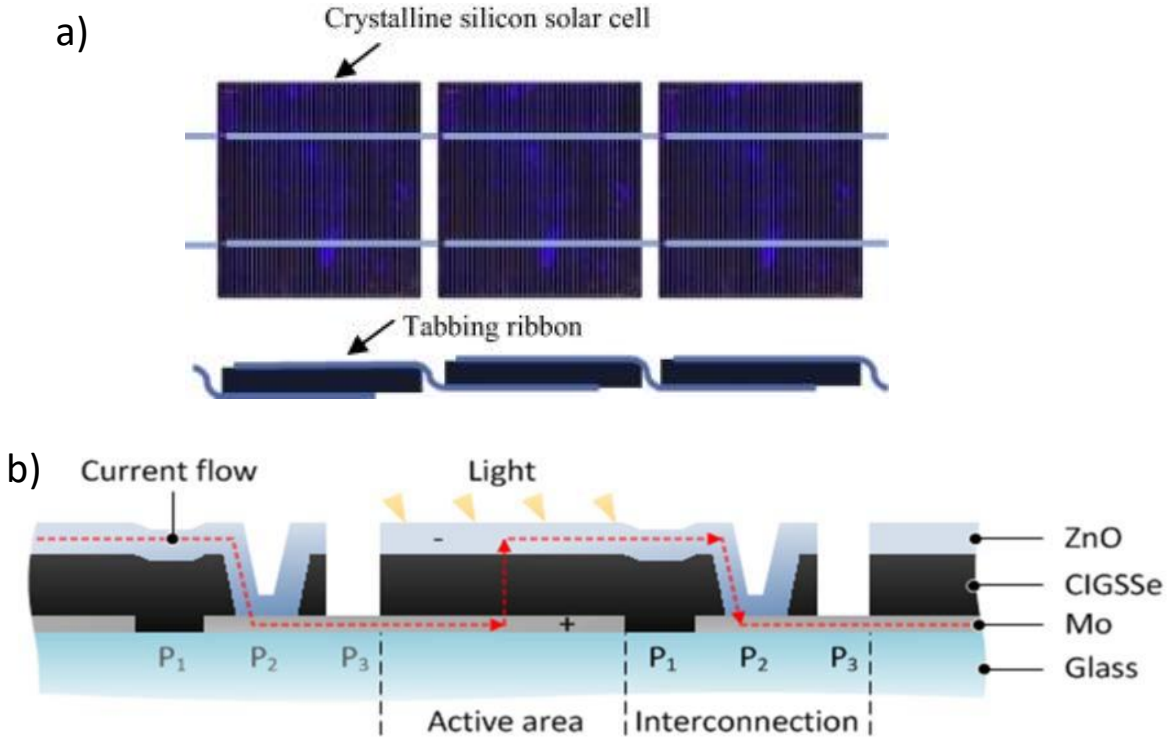

Fig. 1.2 a) Illustration of series ribbon interconnections for Si solar cells, reproduced from [15]. b) Illustration of monolithic connections in CIGSSe solar module, where light enters through transparent conductive ZnO layer, reproduced from [18].

This work concerns two emerging thin film technologies, Copper-zinc tin sulpho/selenide, ($Cu_2ZnSn(S,Se)_4$, often abbreviated to CZTSSe) and antimony selenide (Sb_2Se_3). These materials were selected due to their similar properties, both being crystalline chalcogenide semiconductors with bandgaps in a similar range. They both have the advantage of being chemically and thermally stable in air and sunlight, but must be processed under an inert atmosphere in order to prevent oxidisation. They were also selected because both are constituted from relatively abundant and low-toxicity elements. CZTSSe replaces the expensive In and Ga in CIGS with more readily available Zn and Sn, and does not contain any highly toxic elements, and although Sb_2Se_3 is more toxic, this is still mild compared to Cd[20]. As well as having great abundance, the elemental constituents of CZTSSe and Sb_2Se_3 may be found at sites widely distributed around the world, as is demonstrated in Table 1.1, with the data taken from the US Geological Survey[21]. As such, the market for these materials may be less susceptible to the uncertainties of global trade and diplomacy. The reader should note that many factors influence prices besides scarcity, so the values in Table 1.1 should not be taken to directly correlate with prices. Scarcity of a given source element can also be addressed by developing multiple PV-technologies in parallel because, as a group, they are less vulnerable to geopolitical issues centred around a single key resource. Coupled with the multitude of factors at play in developing different low-cost PV technologies, it is clear that a pluralistic approach is valuable. Despite their differing chemistry, the similarities of CZTSSe and Sb_2Se_3 mentioned above mean there are significant overlaps in the preparation and analysis procedures for bulk samples of both materials, making it feasible to study both in parallel. Studying both materials is also expected to allow comparisons between them, and a judgement to be made on which looks more promising for the PV field.

Element	Estimated world production 2019 / ktonnes	Estimated world reserves / ktonnes	Estimated world resources (not yet extracted) / ktonnes	Main sites of production (> 100 ktonne in 2019)
Cd	25,000	Data not available	Widely recovered from zinc ores	U.S., Canada, China, Japan, Kazakhstan, South Korea, Mexico, Netherlands, Peru, Russia
Te	470	31,000	Data not available	U.S. Bulgaria, Canada, China, Japan, Russia, South Africa, Sweden
Cu	24,400	870,000	2.1 million	U.S. Australia, Chile, China, DMRC, Indonesia, Kazakhstan, Mexico, Peru, Russia, Zambia
In	760	Data not available	1-100 ppm in zinc deposits	China, South Korea
Ga	320,000	Data not available	50 ppm in bauxite	China, Russia, Ukraine, Japan, South Korea
Se	2810	99,000	1 ppm in copper deposits	China, Japan, Germany, Belgium, Russia, Finland
Sb	160,000	1.5 million	Data not available	China, Russia, Tajikistan, Turkey, Bolivia, Burma, Australia, Iran, Kyrgyzstan, Kazakhstan, Laos, Mexico, Vietnam
Zn	13,000	250,000	1.9 million	China, Peru, Australia, India, U.S., Mexico, Bolivia, Canada, Russia, Kazakhstan, Sweden
Sn	310,000	4.7 million	Current extraction rates sustainable	China, Indonesia, Burma, Peru, Bolivia, Brazil, Nigeria, Australia, Vietman, Malaysia, Rwanda, Russia, Laos,
S	79,000	Large reserves	5-600 million	China, U.S. Russia, Saudi Arabia, Canada, Kazakhstan, India, Japan, UAE, South Korea, Iran, Qatar, Chile, Poland, Finland, Australia, Kuwait, Germany, Venezuala, Italy, Netherlands, Brazil,

Table 1.1 Estimated extraction rates, reserves and world resources of key elements for thin film PV technologies, and main locations of production (descending order of amount processed). Data from the US Geological Survey[21]

Apart from its non-toxicity and abundant elemental constituents, being a quinary semiconductor compound, CZTSSe also has significant flexibility in its composition, allowing optimal properties for PV to be selected[13]. Despite its advantages, however, the power conversion efficiencies of CZTSSe-based solar cells are still significantly lower than those of CdTe or CIGS, meaning longer energy (and monetary) payback times which make the material unattractive for commercial scale-up. Significant improvements in efficiency are therefore necessary before CZTSSe can contribute to reducing greenhouse gas emissions[22]. This performance gap compared to the established technologies can be attributed in large part to the low open-circuit voltage in CZTSSe (V_{OC}, see Section 2.3.2) as a function of bandgap. Whereas V_{OC}-values in the best CdTe and CIGS devices are ~60% of E_g/q (where E_g is the bandgap), the proportion for CZTSSe is only 40%. For comparison, the highest possible value of V_{OC} as a proportion of bandgap is ~80%, which has been achieved in epitaxial GaAs solar cells[23]. This means that if the cause of this V_{OC}-deficit can be identified, there are promising opportunities to address the performance gap for CZTSSe.

The V_{OC}-deficit may come as a result of the chemical flexibility which, while it benefits CZTSSe in other ways, allows for unintended local variations in composition. These variations may translate to potential fluctuations at the band-edge, i.e. band-tailing, reducing the effective bandgap, increasing rates of recombination and so reducing V_{OC}[24]. Similarly, local changes in bandgap as a result of disorder and the formation of competing secondary phases (see Section 2.3.1) may contribute to band-tailing[23]. These problems are non-existent for a single-element material like crystalline silicon, and far less pronounced in binary materials such as CdTe, where only very small deviations from stoichiometry are tolerated[25]. Ternary compounds generally have fewer secondary phases simply by virtue of fewer possible combinations of elements in the system.

Antimony selenide (Sb_2Se_3) offers similar advantages to CZTSSe due to its cheap and abundant elemental constituents.. There are also no secondary phases that are likely to form alongside Sb_2Se_3 during processing[20], which is an issue for CZTSSe. Solar cells based on this material have yet to reach the efficiencies offered by CZTSSe[26,27], however, and are still a long way below those

of CdTe and CIGS[28], meaning that the efficiency of cells must be increased significantly to make Sb_2Se_3 commercially viable.

Part of the motivation of this work was the fact that the number of publications looking into the bulk properties of PV semiconductors is generally dwarfed by the literature reporting variations in thin film device design and processing. In this thesis the approach taken has been to prepare bulk samples of CZTSSe and Sb_2Se_3, and where possible, single crystals. The aim was to produce data of use in the development of thin film solar cells. For example, for both materials, the relationship between lattice parameters, bandgap and S-Se content, the Vegard relation, was intended to be studied to a greater precision than previous work. Single crystals were expected to enable this due to superior compositional homogeneity and formation under close-to-equilibrium conditions. Similarly, the position and assignment of Raman bands, dependent on S-Se content and atomic ordering, were intended to be measured to higher precision, with single crystals offering similar advantages.

For Sb_2Se_3, an additional aim was to examine the origin of conductivity, so that this could be incorporated into solar cell production in future, while another key question was how its orthorhombic structure influenced Raman spectra, an understanding of which could make Raman measurements of thin films more informative. The higher purities achievable with single crystals (as opposed to thin films) was hoped to allow the effects of controlled impurity levels upon conductivity to be studied, while the ability to isolate specific crystal planes was expected to allow for orientation-dependent Raman measurements.

For both materials, it was intended that information on point defects in the bulk material, both shallow and deep-level, be gained, as defects often play a crucial role in the limits to the efficiency of solar cells (see Section 2.2.6). Additionally, single crystals ought to allow point defects to be studied with much less interference from the interfaces, grain boundaries and impurities that complicate solar cell based studies. Processing conditions close to equilibrium (which occurs during crystal growth) are also expected to reduce the prevalence of other bulk defects such as slip plane dislocations. Once again, applying the same analysis techniques (e.g. photoluminescence and deep-level transient

spectroscopy, see Chapter 3) to both materials was expected to allow point defects in each to be studied in parallel.

At the outset of this project, the optimum bulk crystal growth methods had not been developed for either CZTSSe or Sb_2Se_3 at the University of Liverpool laboratories. Indeed, crystal growth is a field where, even when literature reports of a process do exist, they are often difficult to replicate in a new setting, where different equipment and experience on the part of researchers may make a crucial difference. Therefore, one of the objectives of this work was to establish reliable crystal growth protocols, and these form part of the conclusions of the work (Chapter 7).

1.3 Structure of this Thesis

The thesis is arranged as follows:

a) Chapter 2. Literature review

Chapter 2 provides an in-depth explanation of the challenges facing solar cells based on CZTSSe and Sb_2Se_3 and compares them to other technologies in a review of the literature. It also covers the basic principles of thin film solar cell operation.

b) Chapter 3. Experimental methods

Chapter 3 covers the experimental methods used in this work, and includes the mathematical equations brought up later in the work. It also covers the specific experimental details for all the investigations reported in this work, including the equipment and choice of parameters for both sample fabrication and characterisation.

c) Chapter 4. Vegard relation and Raman mode evolution in CZTSSe

Chapter 4 describes a study into the structure of bulk CZTSSe polycrystals prepared by several means. Fabrication routes for bulk CZTSSe were successfully applied, and high-quality reference data on the crystal lattice parameters and trends in Raman spectra, intended to inform the production of thin film solar cells, was gathered.

d) Chapter 5. Growth and physical characterisation of doped and undoped crystalline Sb_2Se_3 and $Sb_2(S,Se)_3$

Chapter 5 compares the success of growing Sb_2Se_3 single crystals through multiple different methods, with crystal orientation, mechanical properties and chemical analysis carried out on the crystals. The synthesis of the sulpho/selenide variant $Sb_2(S,Se)_3$ is also investigated.

e) Chapter 6. Sb_2Se_3: Electrical Characterisation and Photovoltaic Devices

Chapter 6 primarily concerns the fundamental electrical properties of bulk Sb_2Se_3 as inferred from a series of measurements on the samples grown in Chapter 5 and assumed to be single crystals. Doping, metal-semiconductor junctions and crystal point defects were all investigated for these single crystals. Additionally, Chapter 6 describes a study into PV test devices based on Sb_2Se_3 (Section 6.7) that attempts to apply some of the insights gained from the single crystal work to solar cells, e.g. the formation of devices using intentionally-doped source material.

f) Chapter 7. Conclusions

Chapter 7 provides conclusions for the whole thesis, with sections divided by results chapter and a subsection on suggested further work based on these conclusions. The extent to which the aims of this project were met through the course of experimental work is discussed, as well as the relative success of the CZTSSe-based work, compared to Sb_2Se_3. A list of the publications that the work reported in this thesis contributed to is provided after Chapter 7.

1.4 References

[1] T. Bruckner *et al.*, "Energy Systems," in *Climate Change 2014: Mitigation of Climate Change. Contribution of Working Group III to the Fifth Assessment Report of the Intergovernmental Panel on Climate Change*, O. Edenhofer *et al.*, Ed. Cambridge, United Kingdom and New York, NY, USA: Cambridge University Press, 2014, pp. 511–597.

[2] Fraunhofer ISE, "Photovoltaics Report," 2019. [Online]. Available: https://www.ise.fraunhofer.de/content/dam/ise/de/documents/publications/studies/Photovoltaics-Report.pdf. [Accessed: 14-Apr-2020].

[3] REN21, "Renewables 2019 global status report," 2019. [Online]. Available: https://www.ren21.net/wp-content/uploads/2019/05/gsr_2019_full_report_en.pdf. [Accessed:

06-Jul-2020].

[4] IEA, “Renewables 2019, analysis and forecast to 2024,” 2019. [Online]. Available: https://www.iea.org/reports/renewables-2019. [Accessed: 06-Jul-2020].

[5] J. Nelson, *The Physics of Solar Cells*, 1st ed. London: Imperial College Press, 2003.

[6] D. H. Filsinger and D. B. Bourrie, “Silica to Silicon: Key Carbothermic Reactions and Kinetics,” *J. Am. Ceram. Soc.*, vol. 73, no. 6, pp. 1726–1732, 1990.

[7] W. C. O’Mara, R. B. Herring, and L. P. Hunt, *Handbook Of Semiconductor Silicon Technology*. Park Ridge, NJ: Noyes Publications, 1990.

[8] W. M. Haynes, *CRC Handbook of Chemistry and Physics*, 95th ed. London, New York: CRC Press, Taylor & Francis Group, 2014.

[9] I. L. Repins *et al.*, “Kesterite successes , ongoing work , and challenges : a perspective from vacuum deposition,” *IEEE J. Photovoltaics*, vol. 3, no. 1, pp. 1–7, 2012.

[10] M. Mcgehee, “Emerging High-Efficiency Low-Cost Solar Cell Technologies,” 2014. [Online]. Available: https://web.stanford.edu/group/mcgehee/presentations/McGehee’s 2014 Energy Seminar.pdf. [Accessed: 14-Apr-2020].

[11] J. D. Major, R. E. Treharne, L. J. Phillips, and K. Durose, “A low-cost non-toxic post-growth activation step for CdTe solar cells,” *Nature*, vol. 511, no. 7509, pp. 334–337, 2014.

[12] Zion Market Research, “Solar Panel Market (Mono-crystalline, Poly-crystalline, and Thin-film Solar Panel) for Residential, Commercial and Utility Applications: Global Industry Perspective, Comprehensive Analysis, and Forecast, 2016 - 2022,” New York, United States, 2018.

[13] K. Ito, *Copper Zinc Tin Sulfide-Based Thin-Film Solar Cells*, 1st ed. Nagano: John Wiley and Sons, 2015.

[14] J. Nelson, *The Physics of Solar Cells*, 1st ed. London: Imperial College Press, 2003.

[15] M. T. Zarmai, N. N. Ekere, C. F. Oduoza, and E. H. Amalu, “A review of interconnection technologies for improved crystalline silicon solar cell photovoltaic module assembly,” *Appl. Energy*, vol. 154, pp. 173–182, 2015.

[16] M. Kumar, A. Dubey, N. Adhikari, S. Venkatesan, and Q. Qiao, “Strategic review of secondary phases, defects and defect-complexes in kesterite CZTS-Se solar cells,” *Energy Environ. Sci.*, no. 8, pp. 3134–3159, 2015.

[17] A. B. Pressman, “Electrical properties of cadmium telluride thin film solar cells activated with magnesium chloride,” PhD Thesis, Dept. of Physics, University of Liverpool, 2017.

[18] R. Moser, D. Seiler, H. P. Huber, and G. Marowsky, “Observation of a spot diameter dependency in confined laser ablation of zinc oxide on copper-indium-diselenide,” *Phys. Procedia*, vol. 56, no. C, pp. 1034–1040, 2014.

[19] R. Schlatmann, “Technological trends in thin film Si and CIGS photovoltaic technology,” in *Society of Vacuum Coaters 54th Annual Technical Conference Proceedings*, 2011, pp. 497–501.

[20] K. Zeng, D.-J. Xue, and J. Tang, “Antimony selenide thin-film solar cells,” *Semicond. Sci. Technol.*, vol. 31, pp. 1–13, 2016.

[21] U.S. Geological Survey, “Mineral commodity summaries 2020: U.S. Geological Survey,” 2020.

[22] H. Azimi, Y. Hou, and C. J. Brabec, “Towards low-cost, environmentally friendly printed

chalcopyrite and kesterite solar cells," *Energy Environ. Sci.*, vol. 7, no. 6, pp. 1829–1849, 2014.

[23] S. Bourdais *et al.*, "Is the Cu/Zn disorder the main culprit for the voltage deficit in kesterite solar cells?," *Adv. Energy Mater.*, vol. 6, no. 12, p. 1502276, 2016.

[24] M. Kumar, A. Dubey, N. Adhikari, S. Venkatesan, and Q. Qiao, "Strategic review of secondary phases, defects and defect-complexes in kesterite CZTS-Se solar cells," *Energy Environ. Sci.*, no. 8, pp. 3134–3159, 2015.

[25] J. H. Greenberg, "P-T-X phase equilibrium and vapor pressure scanning of non-stoichiometry in CdTe," *J. Cryst. Growth*, vol. 161, no. 1–4, pp. 1–11, 1996.

[26] Z. Li *et al.*, "9.2%-efficient core-shell structured antimony selenide nanorod array solar cells," *Nat. Commun.*, vol. 10, no. 1, pp. 1–10, 2019.

[27] W. Wang *et al.*, "Device characteristics of CZTSSe thin-film solar cells with 12.6% efficiency," *Adv. Energy Mater.*, vol. 4, no. 7, 2014.

[28] M. A. Green, E. D. Dunlop, J. Hohl-Ebinger, M. Yoshita, N. Kopidakis, and A. W. Y. Ho-Baillie, "Solar cell efficiency tables (Version 55)," *Prog. Photovoltaics Res. Appl.*, vol. 28, no. 1, pp. 3–15, 2020.

2. Literature Review of CZTSSe and Sb_2Se_3 in Photovoltaics

2.1 Introduction and the Scope of this Chapter

This chapter reviews literature that informs the experimental work of this thesis. Section 2.2 covers the basic principles of thin film inorganic solar cells, although it is assumed that the reader has knowledge of background topics in semiconductor physics such as doping and p-n junctions, as may be found in many book-length reviews, for example: 'Materials Science and Engineering' by William D. Callister and David G. Rethwisch[1]; and 'The Physics of Solar Cells' by Jenny Nelson[2]. Sections 2.3 and 2.4 then cover the PV absorber materials CZTSSe and Sb_2Se_3 respectively, beginning with an overview of these materials within the PV field, progressing through the fundamental properties that limit solar cell efficiency, with the final subsection in each case (2.3.6 for CZTSSe and 2.4.7 for Sb_2Se_3) then identifying opportunities for new studies.

2.2 Principles of Thin Film Solar Cells

2.2.1 The Structure of a Heterojunction Solar Cell

Inorganic thin film solar cell devices typically consist of several polycrystalline layers of microscale thickness. In the 'superstrate' configuration used for CdTe, layers are deposited sequentially onto a transparent substrate as shown in fig. 2.1. In this architecture, light enters the device through the glass and a transparent conductive oxide (TCO) layer, a material of high transparency and conductivity which acts as an electrode, before being absorbed. The alternative 'substrate' configuration, as used for CIGS production[3] uses an opaque substrate and light enters through an upper TCO layer. Briefly, the functional parts of a solar cell consist of the absorber layer, the photoactive junction and the collection electrodes[2], as described in the following sections.

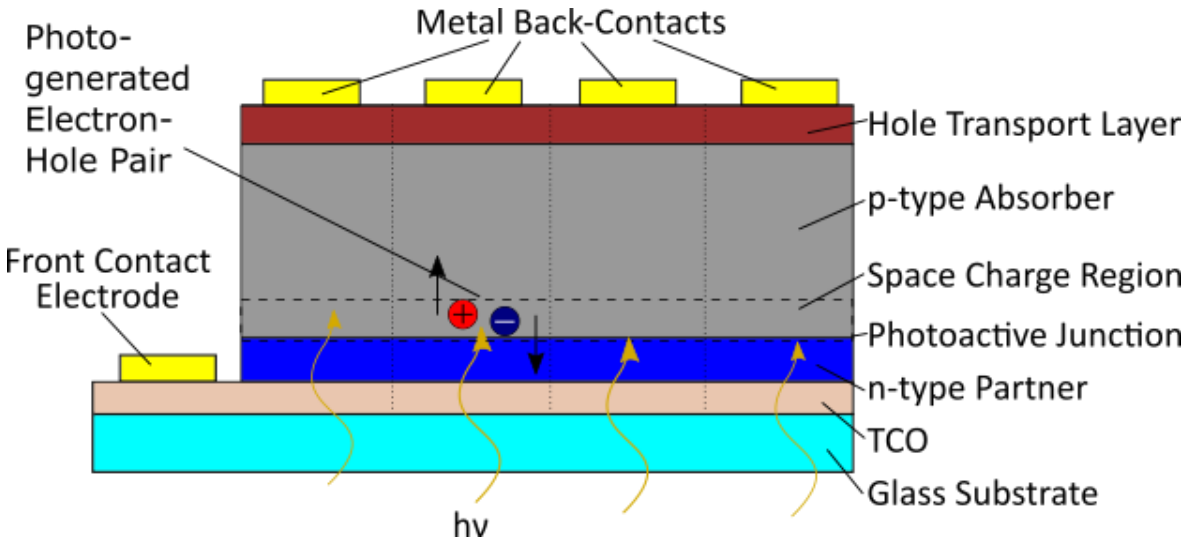

Fig. 2.1 Conventional structure for an inorganic thin film PV device (not to scale) fabricated in the superstrate configuration.

2.2.2 The Absorber Layer

Central to the device is the (usually p-type) photoactive absorber layer which, as a direct gap semiconductor, has a high absorption coefficient (usually > 10^4 cm^{-1}) meaning that effectively all incident light of energy greater than its bandgap is absorbed within a depth of ~ 1 μm. This therefore allows thin layers to be utilised, and small quantities of the bulk compound used. The absorption of a photon produces an electron in the valence band and a hole in the conduction band (see fig. 2.2) which may recombine non-radiatively (through interactions with mid-gap states) if they are not separated[2]. Other transitions are possible, but not significant at room temperature, for example the band to band radiative carrier recombination process is also shown in fig. 2.2, but transitions through intermediate levels are more probable, and overall, photoluminescent processes are weak at room temperature.

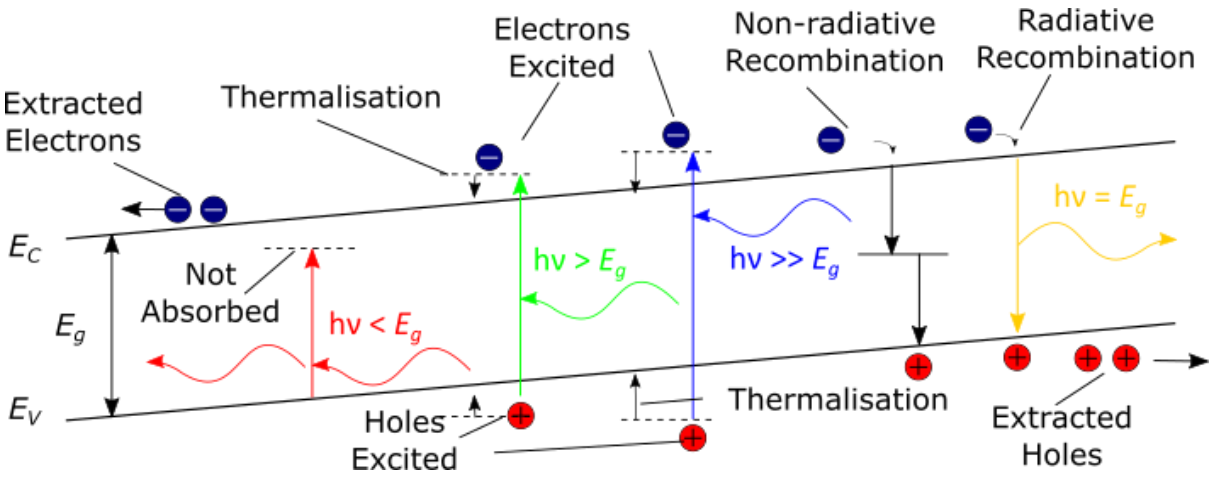

Fig. 2.2 Illustration of the radiative and non-radiative interactions within a photovoltaic absorber layer, where $E_{C,V}$ are the conduction and valence bands, E_g is the bandgap and hν is incident photon energy. Gradients in E_C and E_V represent the situation within the space charge region of a photoactive junction, where a built-in electric field drives the separation and extraction of excited charge carriers. Rates of radiative recombination are not significant at room temperature.

2.2.3 The Photoactive Junction

The photoactive junction is conventionally a p-n junction formed from pairing the (usually p-type) absorber layer with a (usually n-type) partner layer and serves to separate electron-hole pairs excited in the absorber layer. Thin film PV devices are usually heterojunctions, with an example of a p-n band structure being shown in fig. 2.3a. The junction acts as a diode due to the built-in voltage (V_{bi}) in the space charge region at the interface which is necessary to prevent carrier recombination and generate useful current. This means that only electron-hole pairs excited within, or close to, the space charge region may contribute to the device current. Appropriate partner layers to p-type absorbers are highly n-type doped to maximise V_{bi} and have bandgaps significantly larger than the absorber layer, so as not to absorb significant amounts of visible light and shade the absorber layer. The semiconductors CdS[4] and TiO_2[5] are two partner layers frequently employed in thin film PV, with thin layers (<100 nm) employed to reduce parasitic absorption. A consequence of highly-doped partner layers is that the space-charge region lies almost entirely within the absorber layer[2].

While p-n heterojunction solar cells are commonplace, it is also possible to produce a diode through pairing two layers of the same conductivity type, for instance an n-type absorber with a more

highly n-type doped (n+) layer, forming an 'isotype' heterojunction[6], with an example shown in fig. 2.3b.

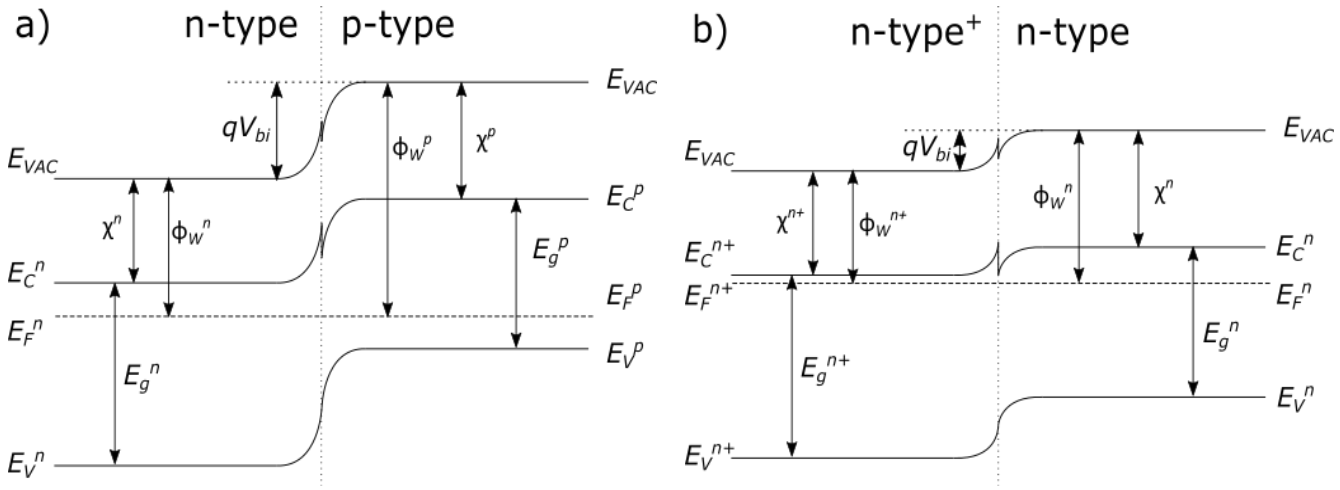

Fig. 2.3 Band diagrams for a) p-n and b) n-n+ isotype heterojunctions where E_{VAC} is the local vacuum level, q is electron charge, V_{bi} is the built-in potential, $\chi^{n,p}$ is the electron affinity, ϕ_W is the work function, E_C is the conduction band energy, E_F is the Fermi level energy, E_g is the bandgap and E_V is the valence band energy.

A recent example of a photoactive isotype junction device was formed from monolayer CuInSe2/InSe[7], but such devices are not common, especially within photovoltaics. Several possible material pairings for heterojunction solar cells were modelled in [8], using conventional PV absorber layers such as Si, CdTe and GaAs, doped either n- or p-type, and paired with highly n-type doped metal oxide materials such as In_2O_3, SnO_2 and ZnO. This work identified barely any n-n+ pairings that were viable for solar cells, while many p-n pairings were viable. As can be seen from fig. 2.3b, the disadvantage of an n-n+ junction is a reduced V_{bi} compared to p-n, reducing the effectiveness of charge separation. This is a key reason for the rarity of isotype junction devices, particularly within the field of solar cells. However, they are mentioned here because there is strong evidence for the formation of n-n+ isotype heterojunctions with Sb_2Se_3 and CdS in this work, as detailed in Chapter 6.

2.2.4 Carrier Collection at Electrodes

Separated charge carriers must be collected by electrodes if they are to contribute to the device current and generate power, with electrons usually collected at the front of the device and holes collected at the rear. For thin films, ~ 1 μm-sized grains may be present, meaning the carriers are unlikely to encounter a large number of grain boundaries between generation and collection, although this is still an important factor. For the front-contact, TCOs are used, so as to collect electrons without shading the absorber layer (see fig. 2.1)[2]. Typical examples of TCOs used for solar cells are fluorine-doped tin-oxide (FTO)[9] and tin-doped indium oxide (ITO)[10]. For the back-contact, metal contacts may be used, but the metal must have an appropriate work function in order to prevent the formation of resistive barriers. Organic materials such as Poly(3,4-ethylenedioxythiophene) (PEDOT) may also be employed as hole transport layers[11] which aid the transport of holes to the back contact due to favourable band alignments.

Fig. 2.4 shows examples of the band structure at some metal-semiconductor interfaces. If the work function of the metal ($\Phi_W{}^m$) is larger than the work function of the semiconductor ($\Phi_W{}^{n,p}$) (fig. 2.4a), an n-type semiconductor will form a (rectifying) Schottky barrier with a barrier height (Φ_B) equal to the difference in work functions. A p-type semiconductor, on the other hand, will form an Ohmic contact with the metal. Conversely, if the work function of the metal is smaller than that of the semiconductor (fig. 2.4b), an n-type semiconductor forms an Ohmic contact, while a p-type semiconductor forms a Schottky barrier[2,12].

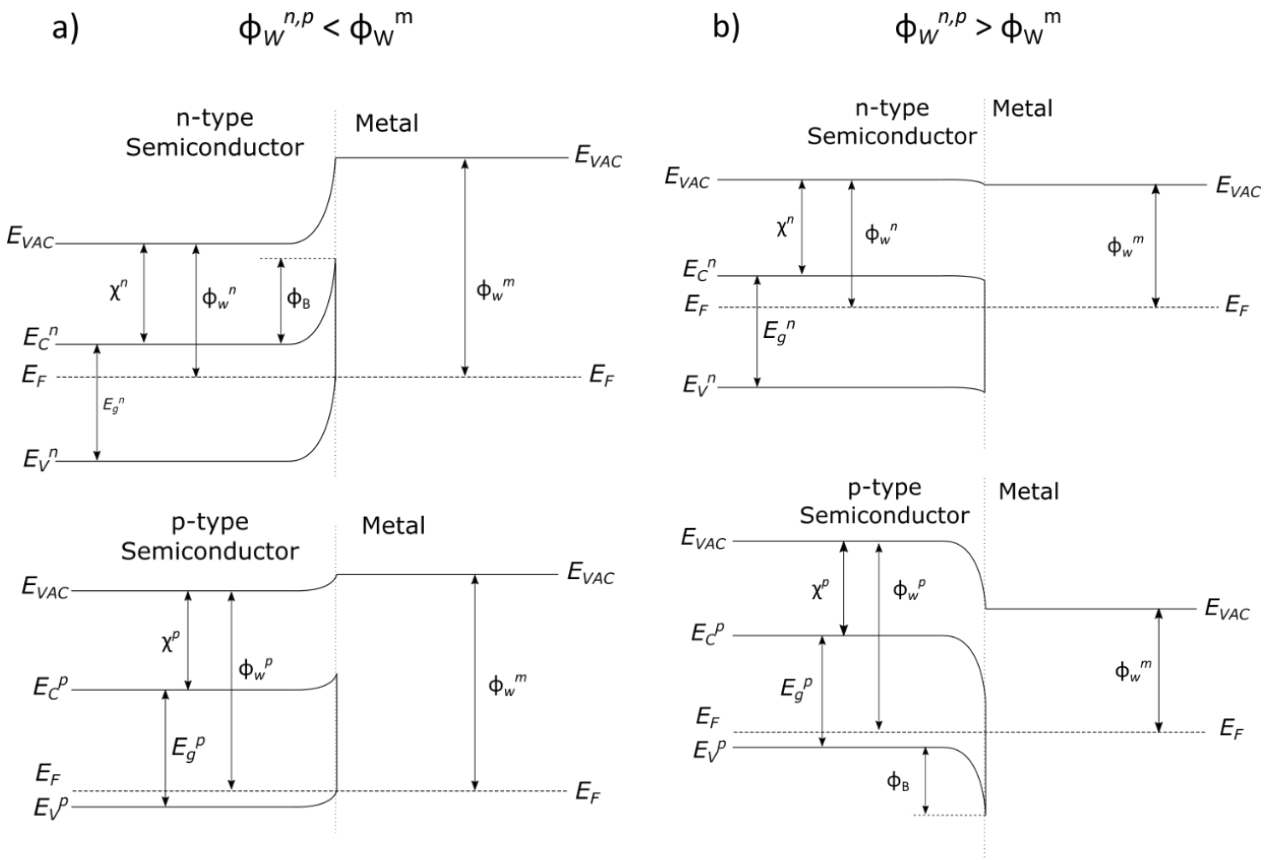

Fig. 2.4 Band diagrams for metal-semiconductor interfaces where Φ_B is the barrier height (other parameters the same as in fig. 2.3), with work functions as: a) $\Phi_W^m > \Phi_W^{n,p}$ and b) $\Phi_W^m < \Phi_W^{n,p}$.

2.2.5 Solar Cell Working Parameters and Measurement

The key parameter for any solar cell is the power-conversion efficiency, or PCE (η) which represents the total percentage of incident solar illumination converted to useful power. Device efficiencies will vary depending on the illumination spectrum, but devices are generally optimised for a solar spectrum modified to account for atmospheric absorption at mid-latitudes, referred to as AM1.5[13], and an illumination intensity of 1000 W m^{-2}. The value of η is directly proportional to the device's PV working parameters: open-circuit voltage (V_{OC}), short-circuit current (J_{SC}) and fill factor (*FF*), which may be derived from a current density (*J*) – voltage (*V*) scan of a solar cell when under illumination as shown in fig. 2.5. When the device is in the dark, all of these parameters are zero and no current flows at zero bias, as can be seen from the dark curve in fig. 2.5, while a voltage dependent current, the 'dark current' $J_{Dark}(V)$ flows under non-zero bias with the same polarity at the bias. Under illumination, the V_{OC} is the voltage when the device is not connected to electrodes (i.e. $J = 0$) while

J_{SC} is the current density when the device is shorted (i.e. $V = 0$). For all solar cells, there will be a point at which the product of J and V produces the maximum possible power, defined as the 'maximum power point' where the voltage is denoted V_{max} and the current density J_{max}. The device efficiency is based on the power generated at the maximum power point. FF is the ratio of the maximum power ($V_{max} \cdot J_{max}$) with the product of V_{OC} and J_{SC}, i.e. the ratio of the areas of the dark blue and light blue squares shown in fig, 2.5 (A_1/A_2) and so relates to the position of the maximum power point.

All of these working parameters are related to different aspects of the cell structure[2]. For instance, the V_{OC} is limited by the non-radiative recombination of charge carriers, while J_{SC} depends on the amount of light reaching the photoactive junction and FF is related to the series resistance (R_S) and shunt resistance (R_{Sh}) of the junction.

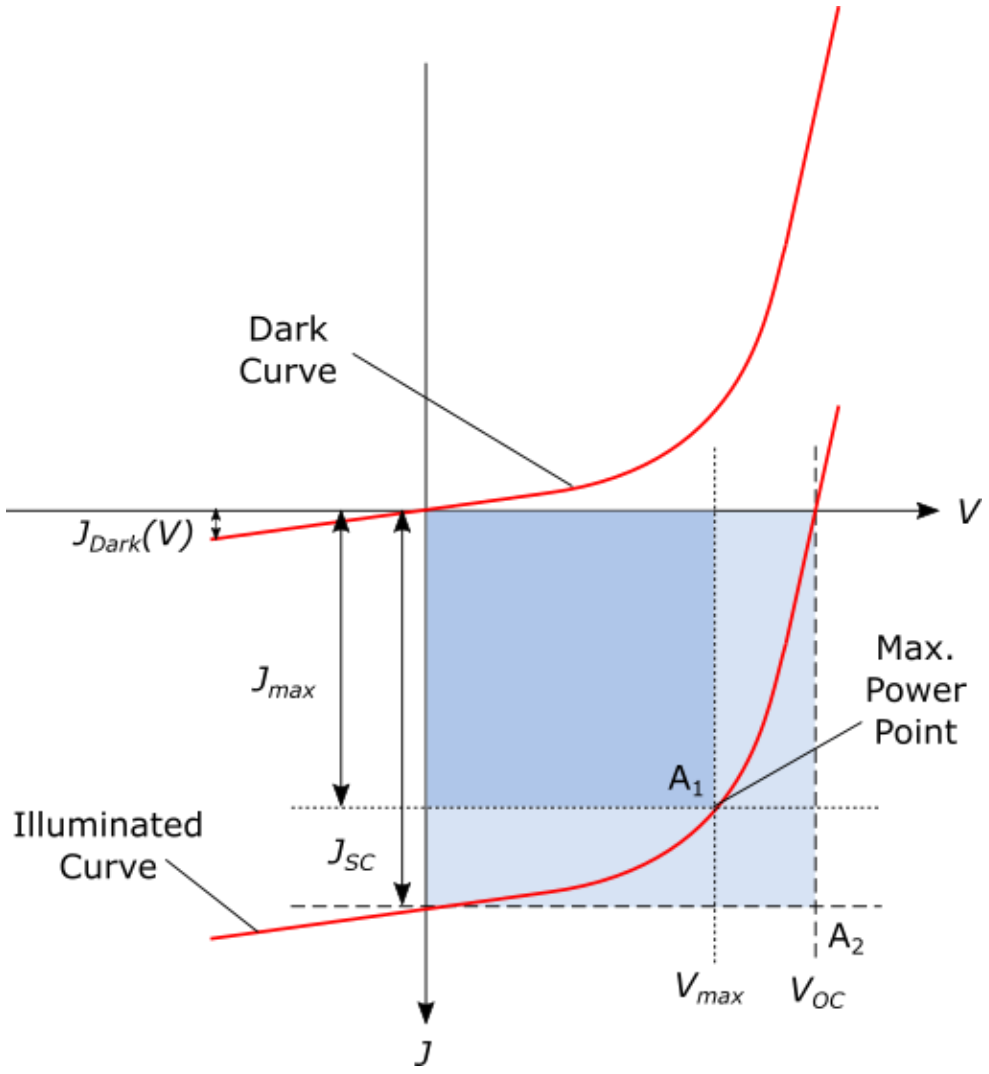

Fig. 2.5 Diagram of a *J-V* curve for a PV solar cell, both in the dark and under illumination with the working parameters for a cell under illumination, V_{OC} and J_{SC}, shown. *FF* is defined by the area of the dark blue square divided by the area of the light blue square (A_1/A_2) and R_s and R_{sh} are defined by the slope of the curve at $J = 0$ and $V = 0$ respectively.

2.2.6 Limits to Efficiency

At the most basic level, the efficiency of a solar cell is limited by the fact that a photoactive device under solar illumination must emit radiation in order to maintain 'detailed balance' with the Sun[2]. The Shockley-Queisser limit[14] defines the maximum possible efficiency of a solar cell and is an unavoidable consequence of detailed balance, but additional limits exist.

The upper limit to solar cell efficiency for a single junction solar cell may be expressed in more physical terms: Because semiconductors cannot absorb photons of energy below the bandgap, but carriers excited by high-energy photons also lose energy due to thermalisation (see fig. 2.2), it is impossible to utilise all of the energy available in the solar spectrum. As a consequence, there is an optimal bandgap range for single junction absorbers where a large proportion of the solar spectrum may be absorbed, while energy losses due to thermalisation are minimised. Theoretical calculations indicate that this range lies between 1.0 and 1.5 eV[14].

Working devices rarely approach the Shockley-Queisser limit, as technological limitations including cell design, parasitic absorption, control of junction position, recombination losses and contact barriers further reduce efficiency. For example, unfavourable optical design and parasitic absorption will reduce the amount of light reaching the junction, reducing J_{SC}; while defects in the absorber layer will increase non-radiative carrier recombination and reduce V_{OC}; diode leakage and back-contact barriers meanwhile reduce R_{sh} and increase R_s respectively, reducing FF[2].

2.3 Photovoltaic Applications of $Cu_2ZnSn(S,Se)_4$

2.3.1 Overview of CZTSSe in PV

CZTSSe is a member of the same generic class of thin film inorganic PV materials that is dominated by cadmium telluride (CdTe)[15] which has demonstrated high efficiencies of 21.0%[16]. Inorganics offer advantages over the emerging perovskites through their superior chemical stability[17], but conversely have progressed to higher efficiencies less rapidly than perovskites, as shown in the efficiency chart in fig. 2.6[18].

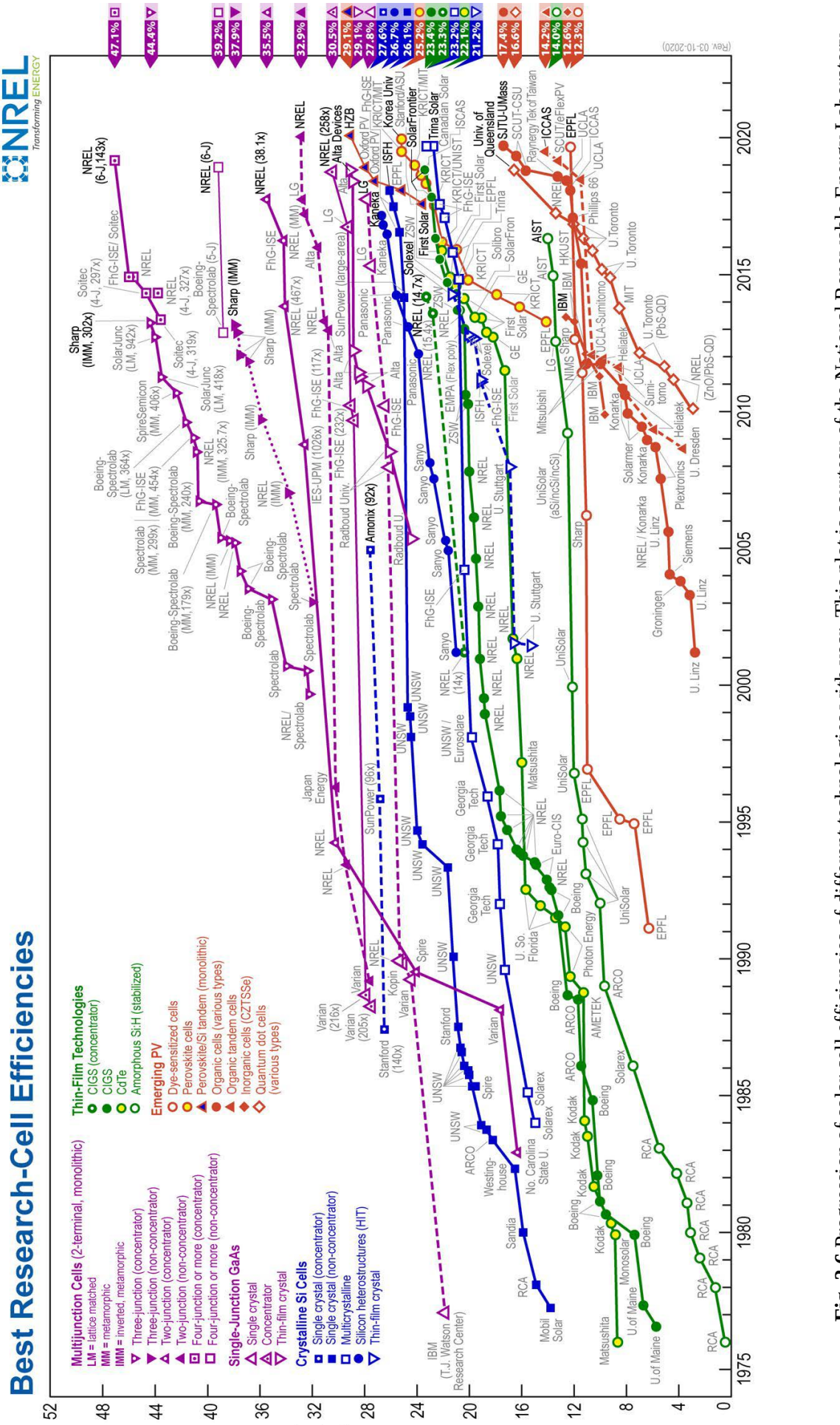

Fig. 2.6 Progression of solar cell efficiencies of different technologies with year. This plot is courtesy of the National Renewable Energy Laboratory, Golden, CO. [16]

As discussed in Chapter 1, CZTSSe is not disadvantaged by the high-toxicity of Cd and the rarity of Te, which are barriers to worldwide scale-up of CdTe[14]. As a result CZTSSe is the subject of extensive research published in the form of hundreds of papers, several reviews [19–24] and at least one book[14]. As well as its cheap, non-toxic constituent elements[24], CZTSSe has the potential for scalable solution-based processing[25], which promises low production costs and short energy payback times.

CZTSSe is also well suited as a PV absorber layer due to its high absorption coefficient of ~10^4 cm^{-1} [26], tuneable bandgap (through the substitution of S for Se) from 1.0 to 1.5 eV, in the optimal range for PV[19] (see Section 2.2.6), p-type self-doping[26] and chemical and thermal stability[24]. However, to date the highest efficiency for $Cu_2ZnSnS_{4x}Se_{4(1-x)}$ based cells, achieved with a composition of $x = 0.25$, is 12.6%, significantly lower than CdTe - 21.0% at the time of writing[16] - with a minimum efficiency of 19% estimated as necessary for commercial viability[23].

CZTSSe crystallises in the tetragonal kesterite structure (space group *I*-4) as shown in fig. 2.7 (middle) with the unit cell consisting of alternating layers of cations (metals) and anions (S or Se)[27]. The lattice parameter *c*, the long axis of the unit cell, is very close to double the value of *a*, the short axis, i.e. $c/2a \approx 1$, so the tetragonal unit cell is almost equivalent to two cubic cells. The value of $c/2a$ may be greater or less than 1, depending on the precise composition and ordering of atoms[28]. The other two crystal structures shown in fig. 2.7 are discussed in Section 2.3.3.

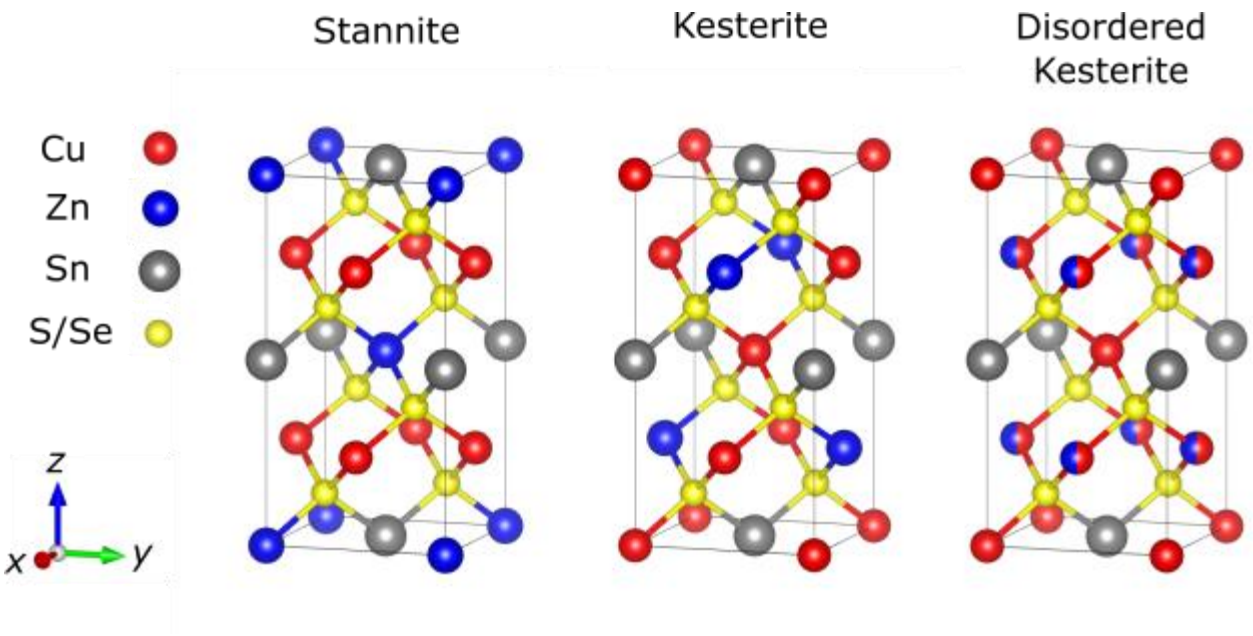

Fig. 2.7 CZTSSe crystal structures stannite, kesterite and disordered kesterite, with constituent atoms and bonds shown. Multicoloured atoms indicate equal probability of occupying the site. Image created with Vesta[41].

2.3.2 PV Devices Using CZTSSe

The present efficiency records for the series end members, the pure-selenide CZTSe and pure-sulphide CZTS are 11.4%[29] and 11.0%[16] respectively. The higher efficiency of the intermediate compound, 12.6% where $x = 0.25$ (x = S/(S+Se)), demonstrates the utility of tuning the bandgap. Among the barriers to CZTSSe cell efficiency, its limited phase stability is key, as CZTSSe exists in competition with several secondary phases such as: Zn(S,Se), Cu_x(S,Se), Sn(S,Se), Sn_2(S,Se) and $Cu_2Sn(S,Se)_3$[26,30] which compromise the homogeneity of CZTSSe thin films. The V_{OC}-deficit, the difference between V_{OC} and the potential difference across the bandgap (its fundamental maximum) is also large in CZTSSe compared to materials of similar bandgap[24,30].

2.3.3 Fundamental Properties of CZTSSe that Limit Efficiency

There are several plausible mechanisms behind the large V_{OC}-deficit in CZTSSe, such as carrier recombination at grain boundaries[19] and point defect sites in the bulk crystals[23], and band (Urbach) tailing trapping carriers in local minima, encouraging recombination[21,30,31]. Grain boundaries are a likely site for carrier recombination due to dangling atomic bonds[21], with chemical methods to passivate grain boundaries necessary in the case of CdTe[15]. However, some authors have suggested that grain boundaries may provide hole-repulsive potentials and so be beneficial to CZTSSe device performance[23]. To further complicate matters, the precipitation of the ZnS and Cu_2SnS_3 secondary phases may also passivate grain boundaries, with their formation highly dependent on stoichiometry and processing conditions[32]. One route to assess the effect of grain boundaries more clearly is to grow single crystals of CZTSSe to remove the influence of grain boundaries altogether (see Section 2.3.4) and so examine bulk recombination paths only.

Phase control of CZTSSe is difficult as it occupies a small window of chemical potential ($\Delta\mu$) surrounded by secondary phases, as demonstrated for CZTS in fig. 2.8[21], where a small deviation from stoichiometry (causing a change in $\Delta\mu$) may result in a mixture of CZTS with secondary phases. In the case of Cu-poor CZTS (fig. 2.8b), secondary phases are practically unavoidable, with the situation for CZTSe similar. Complicating matters further is the fact that CZTSSe solidifies from the melt through a peritectic reaction, where Zn(S,Se) is the first compound to solidify, and slow liquid-solid diffusion from the surrounding Cu and Sn-rich liquid is required to form CZTSSe[14]. This means that to avoid the very long processing times required for the liquid-solid diffusion, solidification from solution at temperatures below the peritectic point[33,34] is favoured. Alternatively, rapid vapour-based vacuum synthesis methods, where thin, stacked layers of metallic

precursors are sulphurised or selenised (or both) through the vapour phase [35], allow the peritectic transition to be sidestepped.

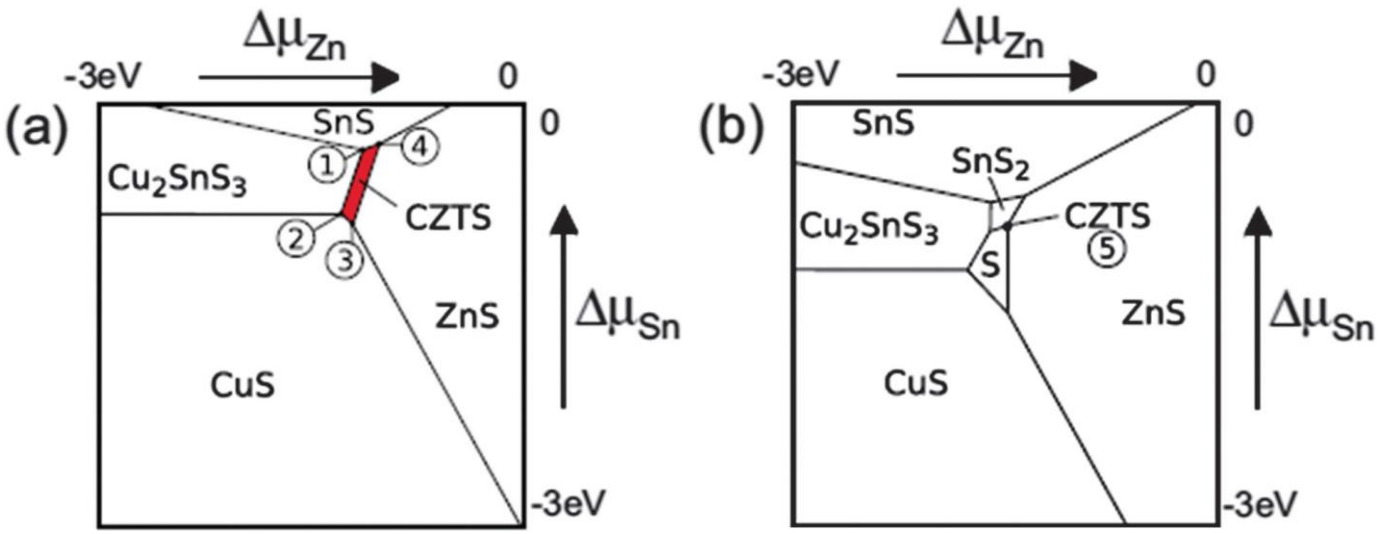

Fig. 2.8 Phase space diagrams for CZTS under a) copper-rich and b) copper-poor conditions, for varying Zn and Sn chemical potential, $\Delta\mu_{Zn,Sn}$ (correlated with concentration). Reproduced from [21].

However, for such vacuum-based methods , the issue arises that knowing the precise S-Se ratio in the CZTSSe thin film is difficult, [24], as these elements are usually incorporated through sulphurisation/selenisation, so their concentration cannot be inferred from the quantity of source material used. This is in contrast to the metals, which may be deposited as stacked layers of defined thicknesses, allowing their concentrations to be known before sulphurisation/selenisation. Chemical analysis methods such as EDX are therefore necessary to know the chalcogen ratio, but will have a lower precision than weighed quantities of precursors, and systematic errors may be introduced due to surface texture. Additionally, distinguishing CZTSSe from its secondary phases post-growth can be difficult, because as Schorr explains in [14], the tetragonal unit cell of kesterite CZTS has very similar dimensions to two stacked ZnS sphalerite cubic unit cells, as they have very similar values of lattice parameter *a*, and for kesterite, $c \approx 2a$. Additionally, the Cu and Zn atoms have very similar atomic form factors, ultimately meaning that conventional x-ray diffraction (XRD), cannot distinguish CZTS

from ZnS, a problem that also applies to their isostructural compounds $Cu_2ZnSn(S,Se)_4$ and Zn(S,Se). This situation is a rarity for XRD which is usually able to provide unambiguous phase assignments.

Even when compositionally-pure CZTSSe is formed, there is the complication that the material may be expected to adopt different structural phases. The atomic occupations of Wykcoff sites for the tetragonal stannite, kesterite and disordered kesterite structures are shown explicitly in Table 2.1, with diagrams shown in fig. 2.7. The predicted formation energies for the stannite (*I*-42*m* symmetry)[36] and kesterite (*I*-4 symmetry)[37] phases (see fig. 2.7) are very close, but it has been established that the stannite phase does not form under normal processing conditions, with the kesterite phase being more favourable[27]. Moreover, CZTSSe may adopt the ordered kesterite form, where Zn atoms occupy 2d Wyckoff sites only, or disordered kesterite, where Cu and Zn atoms are randomly distributed across the 2c and 2d Wyckoff sites[31].

Space Group	Wyckoff Site	*x* Position	*y* Position	*z* Position	Atom	
					Kesterite	Disordered Kesterite
I-4	2a	0	0	0	Cu	Cu
	2c	0	½	¼	Cu	Cu, Zn
	2d	0	½	¾	Zn	Cu, Zn
	2b	0	0	½	Sn	Sn
	8g	*x*	*y*	*z*	S, Se	S, Se
					Stannite	
I-42*m*	2a	0	0	0	Zn	
	4d	0	½	¼ and ¾	Cu	
	2b	0	0	½	Sn	
	8i	*x*	*x*	*z*	S, Se	

Table 2.1 Wyckoff positions for atoms in the kesterite, disordered kesterite and stannite phases of CZTSSe. Positions of *x*, *y* and *z* correspond to unconstrained positions. Ref. 37 is the source for *I*-4 Wyckoff positions and ref. 36 for *I*-42*m*.

Annealing studies for the series end members CZTSe and CZTS report that a transition from ordered to disordered phase occurs at 200°C for CZTSe [38] and at 260°C for CZTS[39], meaning that long anneals at temperatures below these points promote ordering. The kesterite and disordered kesterite phases have slightly different bandgaps[38,40], meaning that a varying level of disorder may contribute to band-tailing in CZTSSe[22]. Schorr reports in [14] that distinguishing between these phases is also not possible with conventional XRD, due to the similar x-ray scattering factors of Cu and Zn. Raman spectroscopy does, however, offer a means to discriminate between them, as well as being able to identify secondary chemical phases[27].

2.3.4 Growth Methods for Bulk CZTSSe Samples

Single crystals of CZTSSe at a size of ~1 cm on a side have been successfully grown from solution in Sn using the travelling heater[42] and directional gradient freeze [43] methods. Meanwhile, CZTSSe monograins several 100 μm in size have been grown from the melt by Nagaoka *et al.*[44] and from solution in molten KI by Mellikov in [14] and Grossberg *et al.*[31], while Ionkin *et al.*[45] produced grains ~ 10 μm in size from solution in a NaCl/KCl mix heated to 750°C. All of these growth routes offer the opportunity to probe bulk properties in greater detail, promising superior phase homogeneity over CZTSSe thin films.

2.3.5 Vegard Relation and Raman Mode Characterisation

The Vegard relation, the dependence of crystal lattice parameters upon composition, has been measured for the case of varying the x - value (x = S/(S+Se)) in $Cu_2ZnSnS_{4x}Se_{4(1-x)}$ and shown to be linear by He *et al.*[46] as: a (Å) = -0.28x + 5.68 and c (Å) = -0.55x + 11.38 and by Nagaoka *et al.*[44] as: a (Å) = -0.26x + 5.71 and c (Å) = -0.53x + 11.45.

The Vegard relation of CZTSSe has been applied to back-correlate the S-Se ratio in a thin film, using lattice parameters[47], providing an indirect means to accurately determine film composition. The existing Vegard datasets were generated by measuring samples at intervals of $\Delta x = 0.2$, but a trend with more data points would allow more accurate back-correlation.

The work He *et al.*[46] also showed Raman spectra for CZTSSe to contain separate CZTSe-like (ω_{CZTSe}) and CZTS-like (ω_{CZTS}) vibrational mode peaks, i.e. 'two-mode' behaviour, which was also reported in the work Grossberg *et al.*[31], but with lattice parameters reported in the latter for the series end members only. Both datasets were averaged by Adachi in [14] where linear trends of: ω_{CZTSe} (cm^{-1}) = 46.8x + 194.9 and ω_{CZTS} (cm^{-1}) = 12.2x + 324.5 were reported. Again, these trends were measured in increments of $\Delta x = 0.2$, so greater precision is desired for back-correlation to be used with these series.

2.3.6 Opportunities for Further Work

Opportunities remain to grow large CZTSSe single crystals and monograins from solution, with the use of the NaCl/KCl mix as a solvent advantageous due to its non-toxicity. If ordering can also be promoted through processing this is an additional advantage. Furthermore, while the Vegard relation and trends in Raman modes have been measured previously for CZTSSe, as compiled by Adachi in [14], these were measured to a precision of $\Delta x = 0.2$ only, so a combined study involving lattice parameters and Raman modes across the whole series, for the same sample set, with a greater number of data points, is in order. Further measurements of this kind have the potential to provide high-quality reference data to inform the production of CZTSSe thin films.

2.4 Photovoltaic Applications of Sb_2Se_3 and Mixed Alloys

2.4.1 Overview of Sb_2Se_3 in PV

The thin film inorganic material antimony selenide (Sb_2Se_3) emerged as a PV absorber more recently than CZTSSe and much more recently than CdTe, and so research is at an early stage. Sb_2Se_3 was not mentioned in the most recent (2019) solar cell efficiency tables[16], while few papers have been published and only one major review each for Sb_2Se_3[48] and its sulpho-selenide variant $Sb_2(S,Se)_3$[49].

Despite limited attention, the advantages of cheap raw materials and relatively low toxicity in Sb_2Se_3 are combined with the potential for cheap, low-temperature processing through techniques such as thermal evaporation[50] and close-space sublimation[5]. Low-temperature, vapour-based methods are feasible due to the high vapour pressure of Sb_2Se_3[50], potentially allowing low processing costs and energy payback times. Sb_2Se_3 also boasts a high absorption coefficient of $> 10^5$ cm^{-1} in the ultraviolet and visible spectrum and a direct bandgap at 1.17 eV, in the optimal range for PV[51] (see Section 2.2.6), and a lack of competing secondary phases[52] in contrast to CZTSSe.

Sb_2Se_3 crystallises in the form of covalently-bonded 1D nanoribbons held together with van der Waals interactions[53], with a full definition of the crystal structure being provided in Section 2.4.3. Despite its 1D nature, Sb_2Se_3 crystals form from nanoribbons coaxially stacked with long-range order, rather than crystals forming from lamellae, as is observed in (similarly 1-dimensional) polymer materials. Meanwhile, the van der Waals interactions are stronger in one axis than the other[54], meaning that solid Sb_2Se_3 resembles 2D materials like MoS_2 far more closely than it does polymer crystals.

The absence of dangling bonds at the van der Waals boundaries means that benign, electrically neutral grain boundaries are a strong possibility for some crystal orientations[48,55], improving the utility of Sb_2Se_3 as a polycrystalline thin film. Temperature-dependent absorption methods by Zeng *et al.*[48] have established that in addition to its direct bandgap at 1.17 eV, Sb_2Se_3 also has an indirect gap at 1.03 eV, with the conduction band minima closely-spaced in k-space. While the indirect gap does not limit absorption, it may affect device performance if electrons are able to thermalize into the indirect, as opposed to the direct, minimum, thereby reducing the effective bandgap of the device. This possibility has not been directly observed by experiment, but may explain the low photoluminescence yield of Sb_2Se_3 even at low temperatures[56], as the likelihood of indirect radiative recombination is much lower than direct recombination. If this is the case, the maximum V_{OC} value achievable in Sb_2Se_3 would be reduced, as the effective bandgap would be smaller, so the possibility of electrons thermalizing into an indirect minimum must be considered during device design, and it should ultimately be assessed whether the advantages of Sb_2Se_3 outweigh this possible issue.

The power conversion efficiencies of Sb_2Se_3-based devices have progressed rapidly since the first device was reported in 2009[57] with an efficiency of 0.66%. This increased to 2.1% by 2014[50] and 6.5% by 2017[4], with the current world record (2019) being 9.2%[58]. All of these results were achieved with sublimation based methods and employed the n-type partner-layer CdS commonly used for CdTe.

However, some evidence suggests CdS is not an ideal partner layer for Sb_2Se_3 due to Cd-diffusion, which was reported as being behind an additional 'buried' homojunction within the absorber layer[59]. Indeed, the current world-record device was fabricated in a substrate configuration on Mo foil, which allowed the post-growth annealing of the Sb_2Se_3 to occur before the CdS deposition and so limit diffusion[58]. In an attempt to find alternative partner layers, recent work has successfully utilised TiO_2 with Sb_2Se_3 deposited by close-space sublimation (CSS), which has consistently achieved efficiencies around 6%, while utilising the superstrate configuration employed in CdTe device design (see fig 2.1)[60,61]. Schottky barriers at the back contact are a recurring issue for CdTe[15] and were shown to also affect Sb_2Se_3 in Shiel *et al.*[62] where etching treatments to remove native oxides reduced series resistance, but did not increase device efficiency.

In addition to the pure selenide Sb_2Se_3, sulpho-selenide variants $Sb_2(S,Se)_3$ have also been employed to fabricate thin-film solar cells via thermal evaporation[63], which have succeeded in reaching ~ 6% efficiencies.

Despite its rapid technological progress, the small number of publications on Sb_2Se_3 mean that numerous fundamental properties of the material have yet to be fully understood[11], including its native defects, doping behaviour, Raman band assignments and extended defects.

2.4.2 Conductivity Type in Sb_2Se_3

Despite conductivity being an important property for PV applications, it has not been clearly established what the most common origin of free carriers within Sb_2Se_3 is. Inorganic semiconducting compounds may exhibit native conductivity, where point defects contribute electrons or holes to the material, an example being p-type self-doping in CZTSSe, which results from copper vacancies (V_{Cu}) and copper-zinc antisites (Cu_{Zn})[21]. Otherwise they may rely on extrinsic impurities to provide carriers, as is the case for silicon[2]. Whatever defects are present in the material must be ionised in order to contribute to doping, requiring that they be 'shallow', i.e. at an energy level not more than ~ k*T* from the conduction (for electrons) or valence bands (for holes). As mentioned in the review paper

by Zeng *et al.* [48], Sb_2Se_3 is frequently reported as being p-type, with no major works reporting bulk n-type conductivity. However, DFT calculations from Savory *et al.*[64] suggest that the pure material ought to be non-conductive, due to compensation of donors and acceptors by other native defects. This would mean that the conductivity type in Sb_2Se_3 may be very sensitive to trace impurities, but this has not often been measured directly in the case of Sb_2Se_3 thin films. Resistive behaviour was reported by Bacewicz *et al.*[65] for material synthesised directly from the elements, whereas commercial source material exhibited p-type conductivity. That work also demonstrated that Sb_2Se_3 could be extrinsically doped, finding partial success with Sn, In, Ge and Pb. The possibility of extrinsically doped Sb_2Se_3 is also supported by the theoretical work of Stoliaroff *et al.*[66] which suggests Sn and Cu for p-type and Cl, Br and I for n-type doping. Clearly if pure Sb_2Se_3 is intrinsic, but may be extrinsically doped by several routes, then the conductivity type may be very dependent on the impurities in the source material, from processing and from diffusion of the PV partner layers.

2.4.3 Crystal Structure, Anisotropy, Native Oxide and Extended Defects

a) – *The crystal structure of Sb_2Se_3*

The crystal orientation of Sb_2Se_3 grains forming the absorber layer is of great importance as the material is anisotropic, making significant variations in conductivity, absorption and band positions with crystal axes likely[67]. The controlled orientation of Sb_2Se_3 grains has already proven crucial to achieving high efficiencies through minimising carrier recombination with benign grain boundaries[9,55].

The crystal structure of Sb_2Se_3 is defined by an orthorhombic space-group, and as explained by Tideswell *et al.*[53] the atoms in Sb_2Se_3 all occupy 4c Wyckoff sites with a set of 4c positions for each of the two Sb and three Se atoms. Each set has unique positions in *x* and *z*, with the *y* position being restricted to ¼ or ¾. The possible positions of atoms on the 4c Wyckoff sites are shown in Table 2.2, as well as the experimentally measured atomic positions for the five unique atoms (i.e. the

values of *x* and *z*) as reported by Caracas *et al.*[68] The unit cell of Sb_2Se_3 is shown in fig. 2.9, showing each unique atom with a multiplicity of 4.

Atom	Wyckoff Site	*x* Position	*y* Position	*z* Position
		Theoretical		
Sb_1 Sb_2 Se_1 Se_2 Se_3	4c	x, (-x + ½), -x, (x + ½)	¼ , ¾ , ¾ , ¼	z, (z + ½), -z, (-z + ½)
		Experimental[68]		
Sb_1		0.53040	¼	0.17210
Sb_2		0.64750	¾	0.46040
Se_1	4c	0.62890	¾	0.05530
Se_2		0.71410	¼	0.30510
Se_3		0.44640	¾	0.37130

Table 2.2 Crystal structure of Sb_2Se_3, with experimental values for atomic positions taken from [68].

The space group of Sb_2Se_3 may be described by the setting conventions of either *Pbnm* or *Pnma*, with each describing identical crystal structures, but assigning the Miller indices to different axes. The relation between the Miller indices, lattice parameter assignments, and interplanar spacings for the two setting conventions are shown in Table 2.3 to allow for simple and unambiguous comparison. Either setting convention is equally valid and both are widely applied. For example, [11] and [68] use *Pnma* while [53] and [55] use *Pbnm*. In this work, *Pbnm* is used in all cases, as it assigns the [001] crystal axis to covalently bonded axis with the short interplanar spacing, judged to make the best conceptual sense.

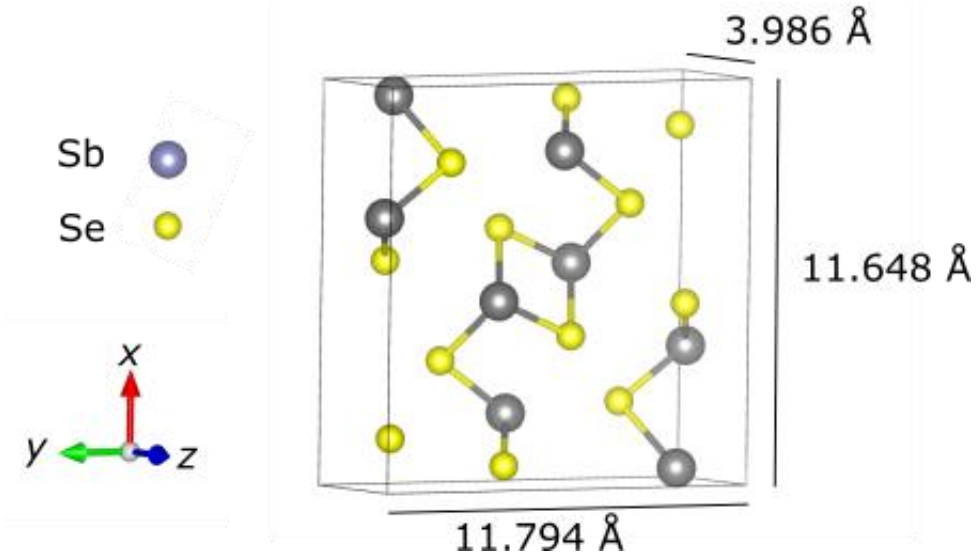

Fig. 2.9 Unit cell of Sb_2Se_3, orthorhombic *Pbnm* space group, with atoms and bonds shown. Images generated using Vesta software[41] from crystal structure in [53].

Plane Spacing (Å)	Lattice Parameters, Crystal Planes			
	Pbnm		*Pnma*	
$d_{100,\ 001}$ = 11.648	*a*	(100)	*c*	(001)
$d_{010,\ 100}$ = 11.794	*b*	(010)	*a*	(100)
$d_{001,\ 010}$ = 3.986	*c*	(001)	*b*	(010)

Table 2.3 Comparison of the two orthorhombic space group setting conventions used in the literature for Sb_2Se_3.

b) – *Vibrational modes of Sb_2Se_3*

The low symmetry of Sb_2Se_3 results in a large number of predicted vibrational modes, with the irreducible representation for the Raman active modes of Sb_2Se_3 given as: $\Gamma = 10A_g + 5B_{1g} + 10B_{2g} + 5B_{3g}$, 30 in total[69]. These are calculated at the Brillouin zone centre, as the wavelength of visible

light (~ 500 nm) is large compared to atomic spacing (0.4 – 1 nm), meaning *k*-values of incident photons are small. Relatively little work has been carried out to assign the Raman-active vibrational modes of Sb_2Se_3, with Vidal-Fuentes *et al.*[70] being the most comprehensive to date. In that work, polarised Raman spectroscopy of a Sb_2Se_3 single crystal was used to distinguish closely spaced, overlapping peaks, as the anisotropy of Sb_2Se_3 means that peaks may appear with different intensities in orthogonally-polarised spectra. Several Raman modes were assigned this way, but there was some ambiguity, as the crystal itself was not large enough to allow orientation by XRD or a similar method, and so the specific crystal axes were unknown and the $B_{1g,\ 2g,\ 3g}$ modes could not be individually assigned (these are therefore denoted B_{xg} in [70]). Nevertheless, the association of Raman modes with crystal axes indicates a means to 'fingerprint' the crystal orientation of Sb_2Se_3 grains in a thin film, as has been carried out previously for $CuInSe_2$ in the work Schmid *et al.*[71]

c) – *Identification of Possible Ambiguity from Oxides in the Raman Spectra of Sb_2Se_3*

Ambiguity also exists in the literature over which Raman peaks correspond to the Sb_2Se_3 phase, with the often-cited work by Liu *et al.*[50] attributing peaks at 190 and 253 cm^{-1} to Sb_2Se_3, while Shongalova *et al.*[72] identifies the 253 cm^{-1} peak as belonging to Sb_2O_3 instead, while the 190 cm^{-1} may belong to either.

d) – *Extended defects in van der Waals materials*

2D van der Waals materials exhibit distinctly different mechanical properties from covalently-bonded crystals, with buckling and rippling of monolayers a common feature when under stress. Sb_2Se_3 closely resembles ordered 2D materials, despite its 1D nature, and so it may be expected to undergo similar deformations. One defect observed in van der Waals materials is the extended 'ripplocation' defect that was only defined as recently as 2015 by the work of Kushima *et al.*[73]. These defects result when strain within a van der Waals material is relieved through the rippling and wrinkling of atomic layers without any covalent bonds being broken, in contrast to slip-plane dislocations in covalently bonded crystals. 'Ripplocations' may be temporary or permanent, often accumulating to form extended macroscopic crystal defects[73,74], and have been observed in

the 2D material MoS_2[73] as well as phyllosilicate minerals[74] and Ti_3SiC_2[75]. However, they have not been reported in Sb_2Se_3. While extreme ripplocations can lead to layers folding over entirely, such features are distinct from the lammelae formed in polymer crystals, as they represent a break in long-range order due to stress, as opposed to an ordering phenomenon whereby layered crystals are formed in polymers. There are no reports to date of ripplocations appearing in polymer crystals, but polymer crystals are usually more disordered than inorganic 1D or 2D materials. This could make the systematic buckling of oriented polymer chains under stress much more difficult to detect in polymers compared to inorganic materials.

2.4.4 Point Defects in Sb_2Se_3

An understanding of the point defects present in a semiconductor is necessary to address the issues of carrier recombination that limit V_{OC}, but such work is in the early stages for Sb_2Se_3. DFT calculations suggest that the low symmetry of Sb_2Se_3 means a large number of point defects are possible across the five unique atomic sites[64,76]. Attempts to detect and assign deep level defects have been made on Sb_2Se_3 thin films via temperature-dependent conductivity[77], admittance spectroscopy[78] and deep-level transient spectroscopy (DLTS)[79]. Meanwhile the work of Grossberg *et al.*[80] provides the only comprehensive photoluminescence (PL) study of Sb_2Se_3, analysing bulk polycrystalline material with the aim of characterising shallow-level defects. PL is not reported widely for Sb_2Se_3 due to its low luminescence yield[80], possibly due to the indirect conduction band minimum[48,81].

2.4.5 Grain Boundaries in Sb_2Se_3 and Single Crystals

The PL study of Sb_2Se_3 by Grossberg *et al.*[80] ascribes a prominent peak to the effect of grain boundaries, suggesting electrically active defects. Meanwhile the work of Zhou *et al.*[55] suggests many grain boundaries of Sb_2Se_3 are, in fact, electrically benign, specifically where grain boundaries line up with the van der Waals-bonded crystal planes. Therefore, producing thin films with columnar grains where the covalently bonded axis runs from the back-contact to the partner layer allows this characteristic to be exploited. Characterisation of electrically active defects within Sb_2Se_3 single crystals, eliminating the influence of grain boundaries, has not been carried out to date, but work on point defects in CdTe by Nagaoka *et al.*[82] has demonstrated the advantages single crystals offer in this regard.

Indeed, reports of the growth and characterisation of Sb_2Se_3 single crystals are limited. Growth was carried out several decades ago by the vertical Bridgman[83,84] and the liquid-encapsulated Bridgman-Stockbarger (method described in [85]) solidification methods[65], and what little work has been reported more recently concerns topological insulators rather than PV[86].

2.4.7 Opportunities for Further Work

The literature for Sb_2Se_3 signposts several key areas that may provide opportunities for productive future investigations. For one thing, little of the work so far described was carried out on single crystals, so attempts to grow single crystals of Sb_2Se_3 may provide superior compositional control, purity, elimination of grain boundaries and flat, optically favourable crystal facets of a known orientation. This may enable the gathering of definitive evidence into the origins of conductivity within Sb_2Se_3, whether native or due to extrinsic impurities. Following on from this, an investigation into the efficiency of extrinsic doping of Sb_2Se_3 with different elements, both p-type and n-type, and the effects upon photovoltaic performance, could be carried out. Other investigations could attempt the detection of deep-level point defects with deep-level transient spectroscopy, with photoluminescence permitting investigation of shallow defect levels. Furthermore, crystallographic measurements with electron-backscattered diffractometry (EBSD) could detect stress-induced long-range defects in Sb_2Se_3 and establish what form they take. Raman measurements could also be carried out on facets of known orientation to examine anisotropies in the spectra that result.

Moving beyond single crystals in isolation, the nature of contact barriers in Sb_2Se_3 could be investigated further to inform the study of back-contact barriers in solar cells and to allow capacitive profiling of Schottky junctions. The fabrication of Sb_2Se_3 single crystal solar cells may also be possible, allowing PV working parameters to be characterised in the absence of grain boundaries.

More generally, further evidence of the signature of Sb_2O_3 in Raman spectra would be desirable to aid phase identification and determine the extent of oxidisation within thin films. Finally, an investigation into the phase stability of $Sb_2(S,Se)_3$ compounds may inform the choice of thermal regimes used for device processing, with the measurement of a Vegard relation aiding compositional determination.

All of these areas have the potential to inform the production of higher-performing Sb_2Se_3 solar cells, and many have been addressed in this thesis.

2.5 References

[1] D. G. Callister, William D. Rethwisch, *Materials Science and Engineering*, 8th ed. Hoboken, N. J: John Wiley & Sons, 2011.

[2] J. Nelson, *The Physics of Solar Cells*, 1st ed. London: Imperial College Press, 2003.

[3] N. G. Dhere, "Toward GW/year of CIGS production within the next decade," *Sol. Energy Mater. Sol. Cells*, vol. 91, no. 15–16, pp. 1376–1382, 2007.

[4] C. Chen *et al.*, "6.5% certified efficiency Sb_2Se_3 solar cells using PbS colloidal quantum dot film as hole-transporting layer," *ACS Energy Lett.*, vol. 2, pp. 2125–2132, 2017.

[5] O. S. Hutter, L. J. Phillips, K. Durose, and J. D. Major, "6.6% efficient antimony selenide solar cells using grain structure control and an organic contact layer," *Sol. Energy Mater. Sol. Cells*, vol. 188, no. May, pp. 177–181, 2018.

[6] B. L. Sharma and R. K. Purohit, *Semiconductor Heterojunctions*, 1st ed. Oxford: Pergamon Press, 1974.

[7] H. Ji *et al.*, "Self-assembly of a lateral quasi-Ohmic $CuInSe_2$/InSe isotype heterojunction for flexible devices by pulsed laser deposition," *Appl. Phys. Lett.*, vol. 115, no. 16, pp. 1–6, 2019.

[8] H. J. Pauwels, "Analysis and evaluation of isotype heterojunction solar cells," *Solid State Electron.*, vol. 22, pp. 988–990, 1979.

[9] O. S. Hutter, L. J. Phillips, K. Durose, and J. D. Major, "6.6% efficient antimony selenide solar cells using grain structure control and an organic contact layer," *Sol. Energy Mater. Sol. Cells*, vol. 188, no. August, pp. 177–181, 2018.

[10] Y. Cao *et al.*, "Towards high efficiency inverted Sb_2Se_3 thin film solar cells," *Sol. Energy Mater. Sol. Cells*, vol. 200, p. 109945, 2019.

[11] K. Zeng, D.-J. Xue, and J. Tang, "Antimony selenide thin-film solar cells," *Semicond. Sci. Technol.*, vol. 31, pp. 1–13, 2016.

[12] J. Mullins, "DLTS study of recombination active defects in solar silicon," PhD Thesis, School of Electrical and Electronic Engineering, University of Manchester, 2018.

[13] S. M. Sze and K. K. Ng, *Physics of Semiconductor Devices*, 3rd ed. Hoboken, N.J: John Wiley & Sons, 2007.

[14] K. Ito, *Copper Zinc Tin Sulfide-Based Thin-Film Solar Cells*, 1st ed. Nagano: John Wiley and Sons, 2015.

[15] J. D. Major, R. E. Treharne, L. J. Phillips, and K. Durose, "A low-cost non-toxic post-growth activation step for CdTe solar cells," *Nature*, vol. 511, no. 7509, pp. 334–337, 2014.

[16] M. A. Green, E. D. Dunlop, J. Hohl-Ebinger, M. Yoshita, N. Kopidakis, and A. W. Y. Ho-Baillie, "Solar cell efficiency tables (Version 55)," *Prog. Photovoltaics Res. Appl.*, vol. 28, no. 1, pp. 3–15, 2020.

[17] S. Mariotti, O. S. Hutter, L. J. Phillips, P. J. Yates, B. Kundu, and K. Durose, "Stability and performance of $CsPbI_2Br$ thin films and solar cell devices," *Appl. Mater. Interfaces*, vol. 10, pp. 3750–3760, 2018.

[18] National Renewable Energy Laboratory, "Best Research-Cell Efficiency Chart," 2020. [Online]. Available: https://www.nrel.gov/pv/cell-efficiency.html. [Accessed: 21-Apr-2020].

[19] K. Kaur, N. Kumar, and M. Kumar, "Strategic review of interface carrier recombination in Earth abundant Cu–Zn–Sn–S–Se solar cells: current challenges and future prospects," *J. Mater. Chem. A*, vol. 5, no. 7, pp. 3069–3090, 2017.

[20] Z. Shi, D. Attygalle, and A. H. Jayatissa, "Kesterite-based next generation high performance thin film solar cell: current progress and future prospects," *J. Mater. Sci. Mater. Electron.*, vol. 28, no. 2, pp. 1–17, 2016.

[21] M. Kumar, A. Dubey, N. Adhikari, S. Venkatesan, and Q. Qiao, "Strategic review of secondary phases, defects and defect-complexes in kesterite CZTS-Se solar cells," *Energy Environ. Sci.*, no. 8, pp. 3134–3159, 2015.

[22] S. Bourdais *et al.*, "Is the Cu/Zn disorder the main culprit for the voltage deficit in kesterite solar cells?," *Adv. Energy Mater.*, vol. 6, no. 12, p. 1502276, 2016.

[23] I. L. Repins *et al.*, "Kesterite successes , ongoing work , and challenges : a perspective from vacuum deposition," *IEEE J. Photovoltaics*, vol. 3, no. 1, pp. 1–7, 2012.

[24] A. Walsh, "The steady rise of kesterite solar cells," *ACS Energy Lett.*, vol. 2, pp. 776–779, 2017.

[25] S. Rao, A. Morankar, H. Verma, and P. Goswami, "Emerging photovoltaics: organic, copper zinc tin sulphide and perovskite-based solar cells," *J. Appl. Chem.*, vol. 2016, pp. 1–20, 2016.

[26] M. Kumar, A. Dubey, and N. Adhikari, "Strategic review of secondary phases, defects and defect-complexes in kesterite CZTS–Se solar cells," *Energy Environ. Sci.*, vol. 8, pp. 3134–3159, 2015.

[27] A. Lafond, L. Choubrac, C. Guillot-deudon, P. Deniard, and S. Jobic, "Crystal structures of photovoltaic chalcogenides, an intricate puzzle to solve: the cases of CIGSe and CZTS materials," *J. Inorg. Gen. Chem.*, vol. 638, no. 15, pp. 2571–2577, 2012.

[28] L. Choubrac, M. Paris, A. Lafond, C. Guillot-Deudon, X. Rocquefelte, and S. Jobic, "Multinuclear (67Zn, 119Sn and 65Cu) NMR spectroscopy – an ideal technique to probe the cationic ordering in Cu_2ZnSnS_4 photovoltaic materials," *phys*, vol. 15, pp. 10722–10725, 2013.

[29] T. Taskesen *et al.*, "Device characteristics of an 11.4% CZTSe solar cell fabricated from sputtered precursors," *Adv. Energy Mater.*, vol. 8, p. 1703295, 2018.

[30] T. J. Huang, X. Yin, G. Qi, and H. Gong, "CZTS-based materials and interfaces and their effects on the performance of thin film solar cells," *Phys. Status Solidi*, vol. 762, no. 9, pp. 735–762, 2014.

[31] M. Grossberg, J. Krustok, J. Raudoja, K. Timmo, M. Altosaar, and T. Raadik, "Photoluminescence and Raman study of $Cu_2ZnSn(Se_xS_{1-x})_4$ monograins for photovoltaic applications," *Thin Solid Films*, vol. 519, pp. 7403–7406, 2011.

[32] B. G. Mendis, M. C. J. Goodman, J. D. Major, A. A. Taylor, K. Durose, and D. P. Halliday, "The role of secondary phase precipitation on grain boundary electrical activity in Cu_2ZnSnS_4 (CZTS) photovoltaic absorber layer material," *J. Appl. Phys.*, vol. 124508, pp. 1–11, 2012.

[33] W. Wang *et al.*, "Device characteristics of CZTSSe thin-film solar cells with 12.6% efficiency," *Adv. Energy Mater.*, vol. 4, no. 7, 2014.

[34] Y. Sun *et al.*, "Novel non-hydrazine solution processing of earth-abundant $Cu_2ZnSn(S,Se)_4$ absorbers for thin-film solar cells," *J. Mater. Chem. A*, vol. 1, pp. 6880–6887, 2013.

[35] S. Abermann, "Non-vacuum processed next generation thin film photovoltaics: Towards marketable efficiency and production of CZTS based solar cells," *Sol. Energy*, vol. 94, pp. 37–70, 2013.

[36] A. Lafond, C. Guillot-deudon, P. Fertey, M. Evain, and S. Jobic, "X-ray resonant single-crystal diffraction technique , a powerful tool to investigate the kesterite structure of the photovoltaic Cu 2 ZnSnS 4 compound research papers," *Acta Crystallogr. Sect. B Struct. Sci. Cryst. Eng. Mater.*, vol. 70, pp. 390–394, 2014.

[37] A. Ritscher, J. Just, O. Dolotko, S. Schorr, and M. Lerch, "A mechanochemical route to single phase Cu_2ZnSnS_4 powder," *J. Alloys Compd.*, vol. 670, no. 82, pp. 289–296, 2016.

[38] G. Rey *et al.*, "The band gap of $Cu_2ZnSnSe_4$: Effect of order-disorder," *Appl. Phys. Lett.*, vol. 105, no. 11, p. 112106, 2014.

[39] T. Raadik *et al.*, "Low temperature time resolved photoluminescence in ordered and disordered Cu_2ZnSnS_4 single crystals," *Phys. B Condens. Matter*, vol. 508, no. November 2016, pp. 47–50, 2016.

[40] K. Timmo *et al.*, "Influence of order-disorder in Cu_2ZnSnS_4 powders on the performance of monograin layer solar cells," *Thin Solid Films*, pp. 2–6, 2016.

[41] K. Momma and F. Izumi, "VESTA 3 for three-dimensional visualization of crystal, volumetric and morphology data," *J. Appl. Cryst*, vol. 44, pp. 1272–1276, 2011.

[42] A. Nagaoka, R. Katsube, S. Nakatsuka, and K. Yoshino, "Growth and characterization of $Cu_2ZnSn(S_xSe_{1-x})_4$ single crystal grown by traveling heater method," *J. Cryst. Growth*, vol. 423, pp. 9–15, 2015.

[43] D.-L. Mai, H.-J. Park, and I.-H. Choi, "Growth of Cu_2ZnSnS_4 crystals by the directional freezing method with an induction heater," *J. Cryst. Growth*, vol. 402, pp. 104–108, 2014.

[44] A. Nagaoka, K. Yoshino, H. Taniguchi, and T. Taniyama, "Growth and characterization of $Cu_2ZnSn(S_xSe_{1-x})_4$ alloys grown by the melting method," *J. Cryst. Growth*, vol. 386, pp. 204–207, 2014.

[45] A. S. Ionkin, B. M. Fish, W. J. Marshall, and R. H. Senigo, "Use of inorganic fluxes to control morphology and purity of crystalline késterite and related quaternary chalcogenides," *Sol. Energy Mater. Sol. Cells*, vol. 104, pp. 23–31, 2012.

[46] J. He, L. Sun, S. Chen, Y. Chen, P. Yang, and J. Chu, "Composition dependence of structure and optical properties of $Cu_2ZnSn(S,Se)_4$ solid solutions: An experimental study," *J. Alloys Compd.*, vol. 511, pp. 129–132, 2011.

[47] S. Wu *et al.*, "High-efficiency $Cu_2ZnSn(S,Se)_4$ solar cells fabricated through a low-cost solution process and a two-step heat treatment," *Prog. Photovolt Res. Appl.*, no. September 2016, pp. 58–66, 2017.

[48] K. Zeng, D.-J. Xue, and J. Tang, "Antimony selenide thin-film solar cells," *Semicond. Sci. Technol.*, vol. 31, pp. 1–13, 2016.

[49] X. Wang, R. Tang, C. Wu, C. Zhu, and T. Chen, "Development of antimony sulfide–selenide $Sb_2(S,Se)_3$-based solar cells," *J. Energy Chem.*, vol. 27, no. 3, pp. 713–721, May 2018.

[50] X. Liu *et al.*, "Thermal evaporation and characterization of Sb_2Se_3 thin film for substrate Sb_2Se_3/CdS solar cells," *ACS Appl. Mater. Interfaces*, vol. 6, no. 13, pp. 10687–10695, 2014.

[51] M. Birkett *et al.*, "Band gap temperature-dependence of close-space sublimation grown Sb_2Se_3 by photo-reflectance," *APL Mater.*, vol. 6, p. 84901, 2018.

[52] G. Ghosh, "The Sb-Se (antimony-selenium) system," *J. Phase Equilibria*, vol. 14, no. 6, pp. 753–754, 1993.

[53] N. W. Tideswell, F. H. Kruse, and J. D. McCullough, "The crystal structure of antimony selenide, Sb_2Se_3," *Acta Cryst*, vol. 10, pp. 99–102, 1957.

[54] H. Song *et al.*, "Highly anisotropic Sb_2Se_3 nanosheets: gentle exfoliation from the bulk precursors possessing 1D crystal structure," *Adv. Mater.*, vol. 29, no. 29, pp. 1–7, 2017.

[55] Y. Zhou *et al.*, "Thin-film Sb_2Se_3 photovoltaics with oriented one-dimensional ribbons and benign grain boundaries," *Nat. Photonics*, vol. 9, no. 6, pp. 409–415, 2015.

[56] M. Grossberg, O. Volobujeva, A. Penežko, R. Kaupmees, T. Raadik, and J. Krustok, "Origin of photoluminescence from antimony selenide," *J. Alloys Compd.*, vol. 817, p. 152716, Oct. 2019.

[57] S. Messina, M. T. S. Nair, and P. K. Nair, "Antimony selenide absorber thin films in all-chemically deposited solar cells," *J. Electrochem. Soc.*, vol. 156, no. 5, pp. H327-332, 2009.

[58] Z. Li *et al.*, "9.2%-efficient core-shell structured antimony selenide nanorod array solar cells," *Nat. Commun.*, vol. 10, no. 1, pp. 1–10, 2019.

[59] Y. Zhou *et al.*, "Buried homojunction in CdS/Sb_2Se_3 thin film photovoltaics generated by interfacial diffusion," *Appl. Phys. Lett*, vol. 111, no. 10, p. 13901, 2017.

[60] L. J. Phillips *et al.*, "A scaleable synthesis approach to antimony selenide solar cells," *Submitt. to Nat. Commun.*, 2018.

[61] L. J. Phillips *et al.*, "Current enhancement via a TiO_2 window layer for CSS Sb_2Se_3 solar cells: performance limits and high Voc," *IEEE J. Photovoltaics*, vol. 9, no. 2, pp. 544–551, 2019.

[62] H. Shiel *et al.*, "Chemical etching of Sb_2Se_3 solar cells: surface chemistry and back contact behaviour," *J. Phys. Energy*, vol. 1, p. 045001, 2019.

[63] F. De Bray Sánchez, M. T. S. Nair, and P. K. Nair, "Optimum chemical composition of antimony sulfide selenide for thin film solar cells," *Appl. Surf. Sci.*, vol. 454, pp. 305–312, 2018.

[64] C. N. Savory and D. O. Scanlon, "The complex defect chemistry of antimony selenide," *J. Mater. Chem. A*, vol. 7, no. 17, pp. 10739–10744, 2019.

[65] R. Bacewicz and T. F. Ciszek, "Liquid encapsulated crystal growth and electrical properties of Sb_2Se_3 and Bi_2S_3," *J. Cryst. Growth*, vol. 109, pp. 133–136, 1991.

[66] A. Stoliaroff *et al.*, "Deciphering the role of key defects in Sb_2Se_3, a promising candidate for chalcogenide based solar cells," *ACS Appl. Energy Mater.*, vol. 3, no. 3, pp. 2496–2509, 2020.

[67] R. Vadapoo, S. Krishnan, H. Yilmaz, and C. Marin, "Electronic structure of antimony selenide (Sb_2Se_3) from GW calculations," *Phys. Status Solidi Basic Res.*, vol. 248, no. 3, pp. 700–705, 2011.

[68] R. Caracas and X. Gonze, "First-principles study of the electronic properties of A_2B_3 minerals, with A = Bi, Sb and B = S, Se," *Phys. Chem. Miner.*, vol. 32, pp. 295–300, 2005.

[69] I. Efthimiopoulos, J. Zhang, M. Kucway, C. Park, R. C. Ewing, and Y. Wang, "Sb_2Se_3 under pressure," *Sci. Rep.*, vol. 3, p. 2665, 2013.

[70] P. Vidal-Fuentes *et al.*, "Multiwavelength excitation Raman scattering study of Sb_2Se_3 compound: fundamental vibrational properties and secondary phases detection," *2D Mater.*, vol. 6, p. 045054, 2019.

[71] T. Schmid, N. Schäfer, S. Levcenko, T. Rissom, and D. Abou-Ras, "Orientation-distribution mapping of polycrystalline materials by Raman microspectroscopy," *Sci. Rep.*, vol. 5, pp. 1–7, 2015.

[72] A. Shongalova, M. R. Correia, B. Vermang, J. M. V Cunha, P. M. P. Salome, and P. A. Fernandes, "On the identification of Sb_2Se_3 using Raman scattering," *MRS Commun.*, vol. 8,

pp. 865–870, 2018.

[73] A. Kushima, X. Qian, P. Zhao, S. Zhang, and J. Li, "Ripplocations in van der Waals layers," *Nano Lett.*, vol. 2, no. 15, pp. 1302–1308, 2015.

[74] J. Aslin, E. Mariani, K. Dawson, and M. W. Barsoum, "Ripplocations provide a new mechanism for the deformation of phyllosilicates in the lithosphere," *Nat. Commun.*, vol. 10, p. 686, 2019.

[75] J. Gruber, A. C. Lang, J. Griggs, M. L. Taheri, G. J. Tucker, and M. W. Barsoum, "Evidence for bulk ripplocations in layered solids," *Sci. Rep.*, vol. 6, 2016.

[76] M. Huang, P. Xu, D. Han, J. Tang, and S. Chen, "Complicated and unconventional defect properties of the quasi-one-dimensional photovoltaic semiconductor Sb_2Se_3," *ACS Appl. Mater. Interfaces*, vol. 11, no. 17, pp. 15564–15572, 2019.

[77] C. Chen *et al.*, "Characterization of basic physical properties of Sb_2Se_3," *Front. Optoelectron.*, vol. 10, no. 1, pp. 18–30, 2017.

[78] X. Hu *et al.*, "Investigation of electrically-active defects in Sb_2Se_3 thin-film solar cells with up to 5.91% efficiency via admittance spectroscopy," *Sol. Energy Mater. Sol. Cells*, vol. 186, no. July, pp. 324–329, 2018.

[79] X. Wen *et al.*, "Vapor transport deposition of antimony selenide thin film solar cells with 7.6% efficiency," *Nat. Commun.*, vol. 9, p. 2179, 2018.

[80] M. Grossberg, O. Volobujeva, A. Penežko, R. Kaupmees, T. Raadik, and J. Krustok, "Origin of photoluminescence from antimony selenide," *J. Alloys Compd.*, vol. 817, p. 152716, Oct. 2019.

[81] J. J. Carey, J. P. Allen, D. O. Scanlon, and G. W. Watson, "The electronic structure of the antimony chalcogenide series: Prospects for optoelectronic applications," *J. Solid State Chem.*, vol. 213, pp. 116–125, 2014.

[82] A. Nagaoka, D. Kuciauskas, J. Mccoy, and M. A. Scarpulla, "High p-type doping, mobility, and photocarrier lifetime in arsenic-doped CdTe single crystals," *Cit. Appl. Phys. Lett*, vol. 112, p. 192101, 2018.

[83] J. Black, E. M. Conwbll, L. Seigle, and C. W. Spencer, "Electrical and optical properties of some $M_2^{V\text{-}B}N_3^{VI\text{-}B}$ semiconductors," *J. Phys. Chem. Solids*, vol. 2, pp. 240–251, 1957.

[84] B. R. Chakraborty, R. Bhattacharya, and A. K. Dutta, "Magnetic and electric properties of antimony selenide (Sb_2Se_3) crystals," *J. Phys. Chem. Solids*, vol. 41, pp. 913–917, 1980.

[85] T. F. Ciszek, "Melt growth and some properties of $Cu_xAg_{1-x}InSe_2$ and $CuIn_yGa_{1-y}Se_2$ chalcopyrite solid solution crystals," *J. Cryst. Growth*, vol. 79, pp. 689–694, 1986.

[86] P. P. Kong *et al.*, "Superconductivity in strong spin orbital coupling compound Sb_2Se_3," *Sci. Rep.*, vol. 4, p. 6679, 2014.

3. Experimental Methods

3.1 Introduction and Scope

This chapter details the theory and practice of the experimental techniques employed in this thesis, as well as specific details of the equipment and parameters applied. Methods of sample preparation are covered in Section 3.2, including details of the synthesis and crystal growth methods for CZTSSe (Sections 3.2.1, 3.2.2 and 3.2.5.2) and Sb_2Se_3 and $Sb_2S_{3x}Se_{3(1-x)}$ (Sections 3.2.3, 3.2.4, 3.2.5.1, 3.2.6, 3.2.7 and 3.2.8). Methods and details of physical characterisation are described in Section 3.3, chemical analysis in Section 3.4, while characterisation methods for the electrical properties of Sb_2Se_3 crystals and solar cells are described in Section 3.5.

3.2 Crystal Synthesis and Fabrication Methods

3.2.1 Direct Synthesis of CZTSSe Feedstock

Polycrystalline $Cu_2ZnSn(S,Se)_4$ (CZTSSe) 'feedstock' was synthesised via direct synthesis from powdered elements with constant metal (cation) proportions and varying proportions of sulphur to selenium. The quantity x was defined as $x = S/(Se+S)$, i.e. $x = 0$ corresponds to CZTSe and $x = 1$ corresponds to CZTS. Elemental powders were weighed on an ADAM PW 124 analytical balance with a precision of 0.1 mg.

Samples with x - values from 0 to 1 in steps of 0.1 were synthesised. Elements of purity Cu-3N, Zn-5N, Sn-3N, S-3N and Se-5N, from Alfa Aesar were used in stoichiometric proportions of metals to chalcogens, determined by weighing. Powders were loaded into 16 mm diameter quartz tubes and flushed three times by evacuating to 10^{-2} mbar then filling with 900 mbar of Ar before evacuating to 10^{-5} mbar, and sealed at a length of 12 cm. Ampoules were heated to 800°C at 1.5°C min^{-1}, the heating rate being selected to allow sulphurisation/selenisation of the elements to avoid large vapour pressures, and held for 24hrs to allow for full reaction and homogenisation. They were then cooled at 0.5°C min^{-1} to 350°C to allow for crystallisation, after which the furnace was switched off and the ampoules were left to free cool in the furnace. As 350°C lies above the reported

order/disorder transition for CZTS at 260°C[1] and CZTSe at 200°C[2], this material was expected to take the form of partially disordered kesterite.

3.2.2 Growth of Crystallised CZTSSe from Molten Salts

CZTSSe feedstock was reground for the crystallisation process, where powdered feedstock and the solvent, a NaCl/KCl mix, were loaded into a 16 mm diameter quartz tube. NaCl/KCl was selected for its non-toxicity, with its suitability as a solvent for CZTSSe already demonstrated in other works (see Section 2.3.4). It was used for the whole composition range $0 \leq x \leq 1$ of feedstock, with the salts dried beforehand, and a 16 mm diameter tube used. The molar ratio of salts NaCl:KCl used was 1:1.

A DSC scan for the NaCl/KCl mixture itself (1:1 molar ratio, with no CZTSSe added) is shown in fig. 3.1 and a large endotherm peak is observed., indicating a eutectic point where the solid mixture transitions to a single-phase liquid. The peak exhibits two components, at 655°C and 660 °C, most likely indicating some uneven melting of the solid salt particles. The deeper minimum at of 660 °C was taken as the eutectic point, as it was assumed that more complete mixing was achieved at the higher temperature. Having established that the NaCl/KCl mix is liquid above 660°C, this liquid served as the solvent for CZTSSe. The molar ratios of CZTSSe to the salt-mix solvent used were 1:8, 1:16 and 1:32. Tubes were evacuated to 10^{-2} mbar then filled with 900 mbar of Ar, then evacuated again, three times, before evacuation to 10^{-5} mbar.

The sealed ampoules were placed in a two-zone horizontal tube furnace where the temperature profile varied with time as follows: Both zones of the furnace were heated to a peak temperature of 785°C for CZTSe ($x = 0$), 875°C for CZTS ($x = 1$), and to temperatures interpolated between these values for the samples with intermediate composition ($0 \leq x \leq 1$). This linear interpolation was influenced by DSC taken from the feedstock series (Section 4.2.2) where a decomposition transition (expected to correlate with melting point) was observed to follow a linear trend with x from 778°C to 866°C. It was also influenced by the original investigation in the literature,

where a top temperature of 750°C was used for CZTS (see Section 2.3.4). In that case, however, source elements, rather than pre-synthesised CZTS, were added to the solvent, so in this work, higher temperatures were expected to be necessary for melting as opposed to reaction (Pure CZTS melts at 986°C but, as evidenced by the results in Section 4.2.1, will form from reaction at 800°C). With both zones at the peak temperature, the temperature of one zone, where the tube tip was situated, was lowered by 10°C, establishing a temperature gradient of around 1°C cm^{-1} along the ampoule length. Both zones were then cooled simultaneously at a rate of 0.4°C hr^{-1}, lowering the overall temperature profile of the furnace over a window of 55°C. The window was selected as preliminary investigations with CZTS (not shown) demonstrated larger crystal grains if slower cooling was used in this range, suggesting that the solidification point lies within this window. A square quartz seed plate 10 x 10 mm in size was placed near to the tube tip for some crystallisation runs to encourage nucleation and growth of flat samples. All crystals grown from solution in molten salts were cleaned by soaking in DI water prior to characterisation.

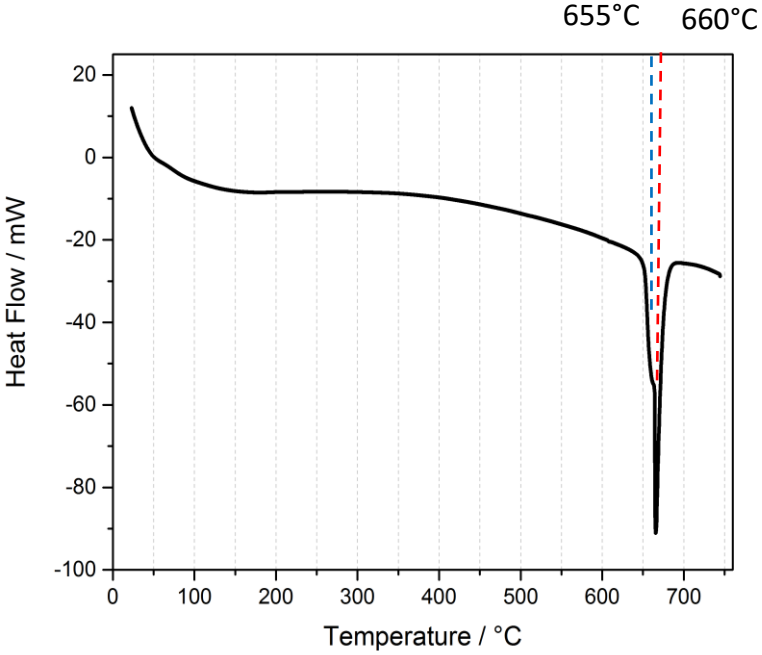

Fig. 3.1. DSC heat flow (during heating at 5°C min^{-1}) against temperature plot for NaCl/KCl only, with a molar ratio NaCl:KCl of 1:1. The large peak with the deeper minimum at 660°C represents an endotherm, indicating melting of the eutectic mixture (see text for a discussion of the shoulder at 655°C).

3.2.3 Direct Synthesis of Sb_2Se_3 and $Sb_2S_{3x}Se_{3(1-x)}$

Direct synthesis of doped and undoped Sb_2Se_3 from the elements was carried out by loading elemental Sb (Alfa Aesar 6N) and Se (Alfa Aesar 5N) shot having a total mass of 8g, into a 16 mm internal diameter quartz tube. Stoichiometry was controlled by weighing, with 'stoichiometric' composition being defined as < 0.01 at% deviation, while 'Se-poor' and 'Se-rich' are defined as deviations of 0.1 at%. Given the masses of Sb and Se used, and the precision of the balance being 0.1 mg, the precision of the weighing method was ~0.0013 at%, allowing these deviations from stoichiometry to be chosen at the weighing stage. The deviations from stoichiometry were judged too small to detect with the post-growth chemical analysis techniques available, so this was not done and the weighed ratios were assumed to carry-through into the processed samples. For some samples, Sn (3N Alfa Aesar) was included as an extrinsic dopant, with a concentration of 0.1 at% determined by weighing, meaning that a Sn concentration of 7×10^{-18} cm^{-3} was expected in the synthesised material. As before, the tubes were evacuated and flushed with argon, repeated three times, evacuated to 10^{-5} mbar and sealed. The ampoules were placed in the centre of a single-zone horizontal tube furnace and heated to 615°C, held for 24 hrs, before cooling to 300°C at a rate of 1.5°C min^{-1}. The furnace was then turned off, with the ampoules left to cool naturally. Given the high vapour pressure of Sb_2Se_3, it was assumed that the samples would be effectively homogenised through mixing in the vapour phase while being held at 615°C, so additional grinding and reaction steps were not used. When used as source material for growth runs, this material was powdered a second time.

Direct synthesis of $Sb_2S_{3x}Se_{3(1-x)}$ from compounds was carried out by loading commercial pre-synthesised Sb_2Se_3 (Alfa Aesar 5N) and Sb_2S_3 granulate (Alfa Aesar 5N), at a total mass of 5 g, into a 16 mm internal diameter quartz tube. The ratio of sulphur to selenium, the x – value, was based on the weighed quantities of Sb_2Se_3 and Sb_2S_3, and x – values of 0.2 and 0.5 were used. The evacuation and sealing procedure for the tubes was as before. The ampoules were placed in the centre of a single-zone horizontal tube furnace and heated to 630°C, held for 24 hrs, before cooling to 300°C at a rate of 1.5°C min^{-1}. The furnace was then turned off, with the ampoules left to cool naturally. Homogenisation was also expected to occur through the vapour phase, as Sb_2S_3 similarly has a high

vapour pressure[3] so only one step was used for synthesis, rather than the material being powdered and reacted again.

3.2.4 Vapour Growth Methods for Sb_2Se_3

The Piper-Polich and self-selecting vapour growth (SSVG) techniques both make use of thermal gradients to drive vapour transport within ampoules sealed at low pressure, and to promote growth, but otherwise work in quite different ways.

3.2.4.1 Piper-Polich Growth

In the Piper-Polich method[4], the growth tube is filled at one end with the source material, which is placed at the centre of a single-zone furnace. The vapourised material then diffuses from the high-pressure region at the hot end of the tube to the lower pressure region at the cold (growth tip) end. As such, this process utilises the natural horizontal temperature gradient as shown in fig. 3.2a. The fastest-growing crystal orientations are expected to dominate, and growth is seedless.

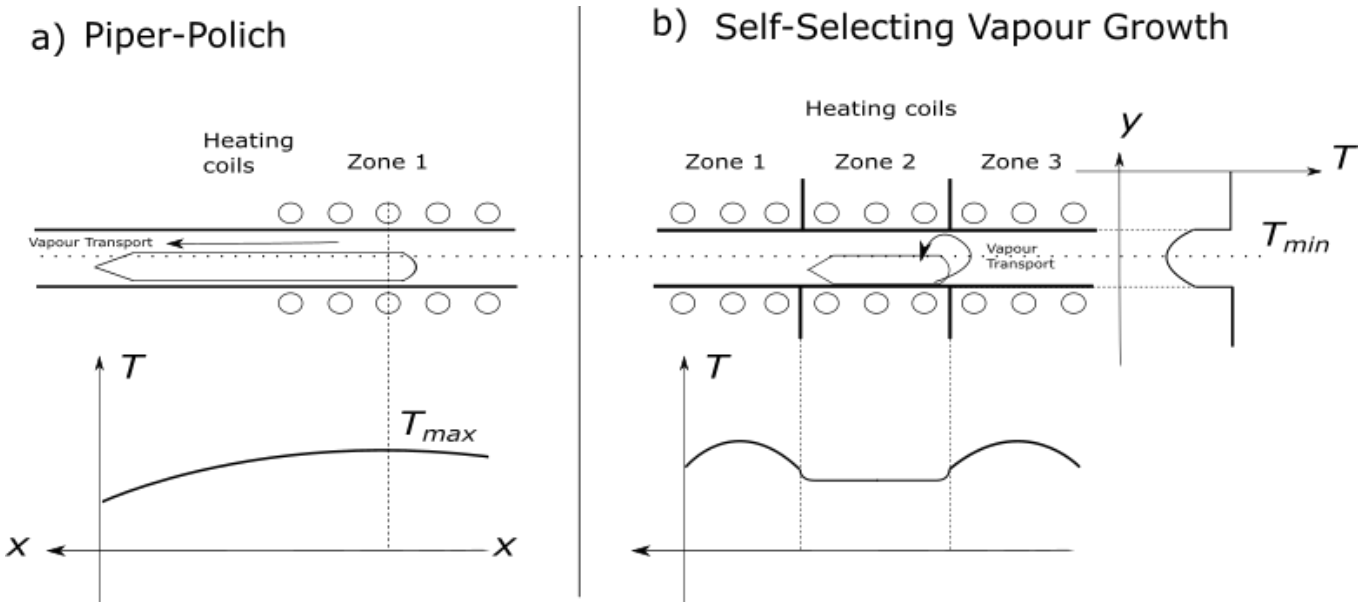

Fig. 3.2 Schematic diagrams of the vapour-growth processes a) Piper-Polich growth and b) self-selecting vapour growth, with ideal horizontal temperature profiles underneath.

In this work, Piper-Polich growth was carried out by loading a quartz tube of 10 mm internal diameter, closed at one end with a pointed growth tip, with ~ 5 g of commercial Sb_2Se_3 granulate (Alfa Aesar 5N). Flushing with argon and evacuation was as above, with a 5.5 cm active length. Ampoules were placed in a single-zone horizontal furnace with the charge at one end, in the furnace centre, and heated to 605°C. The thermal profile for the single-zone horizontal furnace was not measured directly, but it was assumed to be of the roughly parabolic form observed for the single-zone vertical furnace (see fig. 3.5), with a level region at the furnace centre. The temperature at the growth tip, 5.5 cm from the furnace centre, was measured as 523°C, so an approximate temperature gradient of ~ 15°C cm^{-1} was assumed in the region between the charge and the growth tip. The tube was left at the growth temperature for 10-14 days before the furnace setpoint was cooled to 300°C at 5°C min^{-1}, and the tube left to cool naturally in the furnace after switching off.

3.2.4.2 Self-Selecting Vapour Growth

In contrast to Piper-Polich growth, SSVG utilises the radial temperature gradient present in a horizontal tube furnace [5,6], with the temperature minimum at the axis of the tube and a continuous increase as far as the tube walls. At the tube walls, a discontinuous temperature increase results at the point of contact with the furnace walls – the result of moving from a radiative heating regime to conductive heating. This situation is illustrated in fig. 3.2b.

The radial temperature gradient results in vapourisation of a polycrystalline source where it is in contact with the bottom of the tube, encouraging transport to the axial, cooler part of the tube. Here, vapour growth is seeded by the crystals at the top of the source and condenses, increasing the crystals' size. In this process, the fastest-growing crystal orientations at the top are favoured, and as the material at the bottom of the tube is vapourised, the large crystals at the top progressively make up a greater proportion of the overall mass. Therefore, if conditions are right, the larger single crystals will begin to dominate, with the mass they lose to vapourisation underneath being constantly replenished by condensation at the top[5]. The ideal temperature configuration for SSVG is shown in fig. 3.2b and makes use of a three-zone horizontal tube furnace, with the central zone at a lower temperature than the outer zones. This is to prevent vapour transporting away from the centre of the tube where SSVG is favoured. It ensures that the central zone profile is as flat as possible, again to prevent horizontal transport of vapour and encourage the vertical vapour transport required for SSVG.

For self-selecting vapour growth in this work (SSVG), 5 g of Alfa Aesar (5N) Sb_2Se_3 was loaded into a 10 mm internal diameter quartz tube. Flushed with argon, evacuated to 10^{-5} mbar and sealed at a length of 7.5 cm. Ampoules were placed with the centre of the tube aligned with the (horizontal) centre of an open-ended single-zone horizontal tube furnace, the same furnace as was used for Piper-Polich growth (Section 3.2.4.1) at a temperature setpoint of 605°C. The thermal profile for the single-zone horizontal furnace was not measured directly, but it was also assumed to be roughly parabolic, as observed for the single-zone vertical furnace (see fig. 3.5). This inferred temperature profile, as represented in fig. 3.3, differed from the ideal temperature profile required for SSVG, but a more level temperature profile was expected in the furnace centre where the tube was

placed (as observed for the single-zone vertical furnace in fig. 3.5), and growth exploiting the radial temperature profile was still expected.

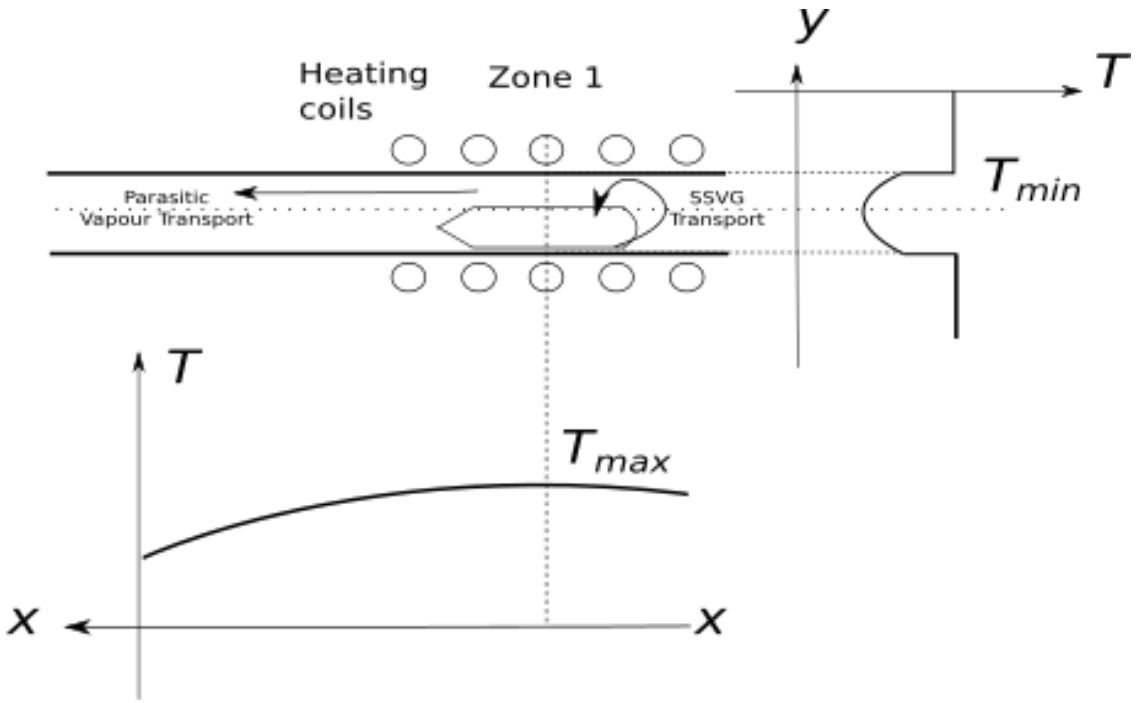

Fig. 3.3 Diagram of the single-zone furnace setup applied in this work to carry out SSVG of Sb_2Se_3. This differs from the ideal furnace setup for SSVG (see fig. 3.2b) in the form of the horizontal temperature profile, which came as a result of using a single-zone furnace rather than the three zones required for the ideal profile. SSVG is still expected to occur due to the presence of the radial temperature profile.

3.2.5 Vertical Bridgman and Directional Freezing Methods

The vertical Bridgman method is a technique for growing large single crystals which is well established for binary compounds. It involves the transport of a sealed crucible filled with molten material through a vertical temperature gradient[7]. The ampoule may be raised or lowered, with the crystallisation proceeding in the opposite direction to the motion of the crucible. Through slow movement as well as rotation of the crucible, conditions close to equilibrium are achieved. The growth of existing crystals from the melt (often a seed crystal is placed in the bottom of the crucible)

is favoured over further nucleation within the melt. An illustration of the process of vertical Bridgman for a single-zone vertical furnace is shown in fig. 3.4.

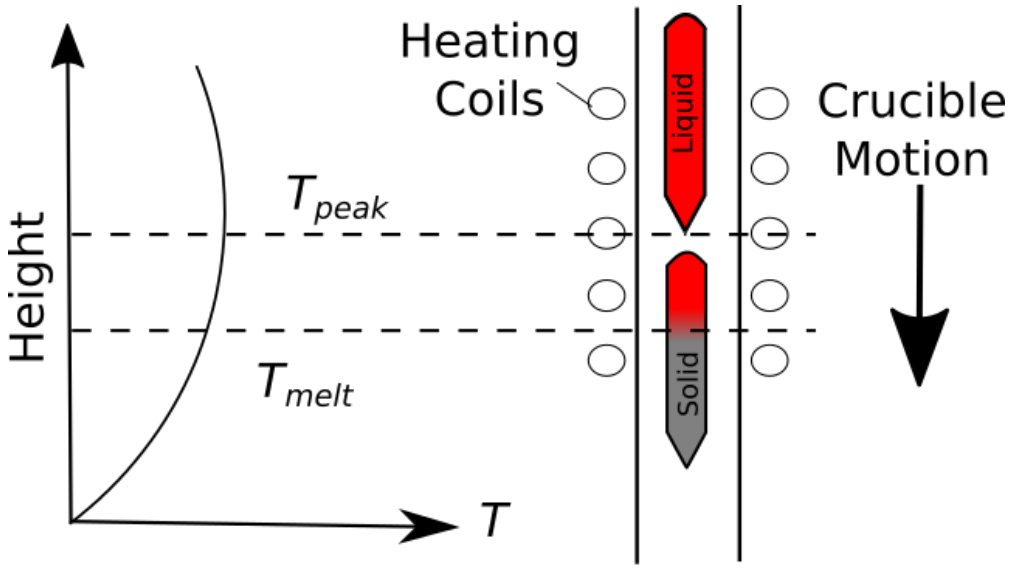

Fig. 3.4 Illustration of the vertical Bridgman technique for a single-zone vertical furnace.

A technique similar to vertical Bridgman, the directional freezing method[8] works on the same thermal principles i.e. an ampoule is moved slowly through a vertical temperature gradient to encourage crystal growth. However, while vertical Bridgman uses a pure melt, the directional freezing method uses the target compound in solution with another material, in order to reach the liquid phase at lower temperatures.

3.2.5.1 Vertical Bridgman Growth of Doped and Undoped Sb_2Se_3 Single Crystals

The vertical Bridgman growth (Section 3.2.2) of Sb_2Se_3 crystals proceeded as follows: ~ 6 g of powderised Sb_2Se_3 source material was loaded into quartz tubes of either 4 mm or 10 mm internal diameter and 20 cm long. The source material used included both Alfa Aesar (5N) Sb_2Se_3 and Sb_2Se_3 synthesised directly from the elements, the latter being either stoichiometric (<0.01 at% deviation from stoichiometry), Se-rich or Se-poor (both ~0.1 at% deviation from stoichiometry), with this stoichiometry inferred from the proportion of weighed elements used for synthesis. The precision of

stoichiometric control at the weighing stage was ± 0.0013 at%. Given the small differences in composition between these sample types, the difference was not expected to be discernible through post-growth chemical analysis, so this was not done. The samples were either left undoped or doped through the addition of elemental Sn powder (3N Alfa Aesar) or $MgCl_2$ powder (3N Sigma Aldrich). Quantities of 0.1 at% dopants were weighed and mixed into the Sb_2Se_3 powder before loading the growth tube. Based on these quantities, atomic densities of 7 x 10^{18} cm^{-3} Sn or 7 x 10^{18} cm^{-3} Mg and 1.4 x 10^{19} cm^{-3} Cl were expected in the doped crystals (assuming full incorporation). These were expected to provide sufficient concentrations for high carrier densities if activation occurred.

Once the tubes were filled, the powder was pressed manually to ensure it stayed in place, but mechanical packing was not carried out and so a high-density powder was not expected. After flushing with argon and sealing either under 10^{-5} or 100 mbar argon, ampoules were placed in a single-zone vertical tube furnace starting with the lower tip of the tube at the maximum temperature point of the furnace. The static thermal profile for the furnace during this process is shown in fig. 3.5a. The thermal profile was directly measured at a temperature setpoint of 610°C (shown in blue), where the actual peak temperature was found to be 605°C. As this was too low to melt the powdered Sb_2Se_3 (melting point 611°C), the temperature setpoint was raised to 630°C for the growth runs in this work. The profile was not measured directly at this setpoint, but it was assumed to have similar form to the profile for a 610°C setpoint, with the peak temperature expected to be similarly ~5 °C below the setpoint, i.e. 625°C. This scaled profile is also shown in fig. 3.5a (in red) and is assumed to hold for the Sb_2Se_3 growth runs discussed, with the expected thermal gradient in the working range based off this profile.

In each case, the growth ampoule was heated to the peak temperature (625°C) and left for several hours, before dropping at 1.15 mm/hr, rotating at ~ 1 revolution per minute. The ampoule was thus moved vertically through the natural temperature gradient of the furnace, as inferred from the temperature profiles in fig. 3.5a to be 0.6°C/ mm, over a period of 7 days, after which the furnace was turned off, and the ampoule left to cool naturally. Each growth run passed through the thermal gradient only once, with the slow growth speed expected to provide good homogeneity.

The vapour pressure of Sb_2Se_3 was measured by Liu *et al.* [9] based on eq. 3.1:

$$\log_{10}(P) = A - \frac{B}{T} \tag{3.1}$$

where P is pressure in mmHg, T is temperature in K, and A and B are estimated from experimental data as A = 8.7906 and B = 6432.6 K.

Based on this, an ampoule sealed under vacuum would be expected to contain an atmosphere of Sb_2Se_3 of 52 mbar at 898 K (the top temperature expected). Meanwhile, an ampoule sealed under an Ar pressure of 100 mbar at 300 K would be expected (from the ideal gas law) to have an Ar pressure of 298 mbar at 898 K, almost 6x larger than the vapour pressure of Sb_2Se_3 expected at this temperature. As a result, the Ar pressure of 100 mbar applied during sealing at 300 K was expected to suppress major vaporisation of Sb_2Se_3 at the highest growth temperature and prevent boiling of the melt where applied.

3.2.5.2 Growth of CZTS Crystals from Sn by Directional Gradient Freeze Technique

Sn was used as the solvent for the crystallisation of CZTS (x = 1) only, using a 10 mm diameter tube. The tube was loaded with powdered CZTS feedstock and elemental Sn powder in a ratio of 70 mol% CZTS to 30 mol% Sn, matching the compositions used for crystal growth of CZTS in the literature[8]. The tubes were evacuated and flushed three times with argon before evacuation to 10^{-5} mbar. The directional gradient freeze technique was applied with the intent of growing large single crystals of CZTS, utilising a single-zone vertical tube furnace at a peak temperature of 900°C, as measured directly from the thermal profile of the furnace at a 915°C setpoint, shown in fig. 3.5b. Ampoules were lowered though the furnace at 0.6 mm hr^{-1}, with the temperature gradient of the furnace estimated as 1.3°C mm^{-1} in the working range, based on the measured thermal profile (fig.

3.5b). Upon removal from the growth tube, the ingot was cut to remove the solvent Sn which had segregated to the top of the growth tube.

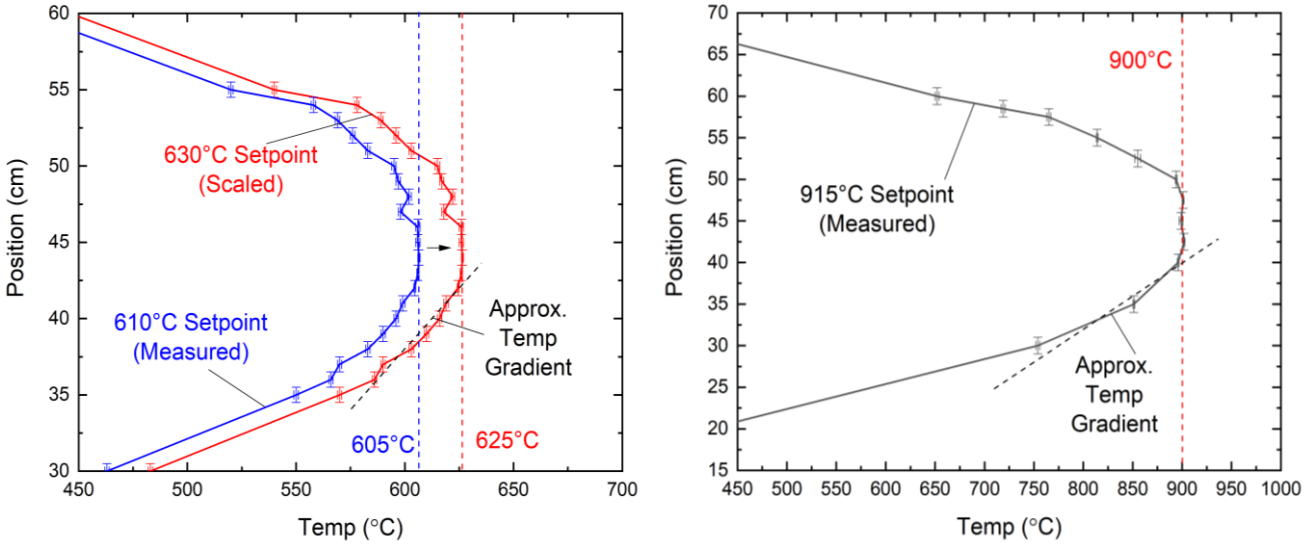

Fig. 3.5 Thermal profiles of vertical furnace used for vertical Bridgman and directional gradient freeze growth. a) thermal profile measured at a setpoint temperature of 610°C (blue) and the same profile scaled to that expected for a setpoint of 630°C (red). b) thermal profile measured at a setpoint of 915°C.

3.2.6 Thermal Evaporation of Semiconductor Thin Films and Metals

Thermal evaporation provides a quick and simple method to deposit thin layers of semiconductors or elemental metals. Source material is loaded into a crucible or boat in a chamber evacuated to low pressure (10^{-4} mbar). The substrate is placed within the line-of-sight of the crucible which is heated to high temperature to vapourise the source. The thickness of deposited layers is monitored by a quartz microbalance, allowing a fine degree of control over the thickness of the layers. Depending on the material and whether the substrate is heated, post-growth annealing may be required to influence the crystallinity of the thin films.

In this work, thermally evaporated Sb_2Se_3 devices were fabricated in superstrate configuration. 10 x 10 cm^2 squares of TEC-10 (sheet resistance = 10 Ω / □) FTO-coated glass were used as the superstrate (NSG Pilkington). CdS was sputtered onto it in an AJA International ATC Orion sputtering system under 5 mTorr Ar, with a substrate temperature of 200°C at a power of 60 W for 24 mins, resulting in a layer 80 nm thick.

Commercial Alfa Aesar (5N) Sb_2Se_3 and Sb_2Se_3 produced by direct synthesis from elements with stoichiometric undoped and Se-rich Sn-doped compositions were used as source material to deposit the Sb_2Se_3 absorber layer. Separate crucibles were used for each source to prevent contamination by elemental impurities, and a Moorfield Minilab 080 thermal evaporator was used with an Infinicon SQC-310C deposition controller. 800 nm of Sb_2Se_3 was deposited in each case with the substrate at room temperature.

The coated squares were broken into eight 2.5 x 5 cm^2 pieces, and each was individually annealed on a Fisher Scientific Isotemp hotplate inside a Jacomex GP Campus N_2 glovebox at 300°C for 10, 20, 25, 30 or 40 mins. Poly(3-hexylthiophene) (P3HT), with a concentration of 4 mg/ml in chloroform was deposited onto the Sb_2Se_3 by spin coating at 5000 rpm, and was intended to act as a hole transport layer (i.e. p-type) at the back contact and improve baseline efficiency. 28 Au contacts 0.1 cm^2 in size and 50 nm thick were deposited through a mask by thermal evaporation. One 2.5 x 5 cm^2 device plate having 28 individual cells was fabricated for each doping type and anneal time.

Measurements of working parameters for all cells were averaged and standard deviation taken for the device as a whole. Since solar cell performance will vary across a given device, the cell with the highest efficiency was reported as the ‘champion’ cell, representing the best possible performance for the device, although such cells did not represent the distribution across the whole device.

3.2.7 Close-Space Sublimation of Semiconductor Material

Close-space sublimation (CSS) is used for the production of semiconductor thin films, but in contrast to thermal evaporation, it takes place under higher pressures (~ 1 mbar) and the source and substrate are placed in close (~ 1 mm) proximity. Additionally, the source material granulate is placed in a source tray having an area equal to that of the substrate, allowing for efficient materials transfer. Annealing within the chamber, combined with carefully controlled source-temperatures and pressures, all allow for a greater degree of control over the crystallisation of semiconductor thin films than for thermal evaporation, with larger crystal grains produced.

In this work, Sb_2Se_3 thin films were synthesised via a two-stage close-space sublimation (CSS) process. TEC-10 (sheet resistance = 10 Ω / □) FTO-coated glass sections were used as the substrate (NSG Pilkington). In the first growth step, lasting 2 mins, a source temperature of 340°C and pressure of 0.05 mbar was used, followed by in-situ annealing for 10 mins in 260 mbar N_2. In the second growth step, lasting 15 mins, a source temperature of 460°C and 13 mbar pressure was used. This two-stage process was used in order to achieve a similar film morphology to what has been used in highly-efficient Sb_2Se_3 solar cells, where the first growth step deposits a densely-packed 'seed-layer' which allows the larger grains grown in the second step to remain densely-packed[10]. This process was used so that the samples measured in this work would have applicability in the context of solar cells. After growth, the substrate was split into four sections, with one section unannealed (CSS-5NAA-Un-25) and the other three annealed in air on a hotplate at 100 (CSS-5NAA-Un-100), 200 (CSS-5NAA-Un-200) and 400°C (CSS-5NAA-Un-400).

3.2.8 Fabrication of Sb_2Se_3 Single Crystal Substrate Devices

Single crystal substrate devices were formed from cleaved sections of Sb_2Se_3 single crystals grown by vertical Bridgman. Both n-type and p-type crystals were used, with areas of ~ 4 x 4 mm^2, and thicknesses in the range 0.2 - 0.5 mm. Au contacts were first evaporated onto the crystal sections and then sputtering of CdS onto the opposite face was carried out in a AJA international ATC Orion system with the substrate crystals at 200°C, under 5 mTorr of Ar and 60W power for 24 minutes, yielding layers ~80 nm thick. Some crystals were removed at this point, while others then had a layer of tin-doped indium oxide (ITO) sputtered within the same chamber (without breaking vacuum) using a power of 60W, pressure of 5 mTorr, and substrate temperature of 200°C for 2hrs, producing a film around 200 nm thick with a sheet resistance of ~ 10 Ω / □. Crystals without ITO deposited had a bead of Ag paste placed directly on the CdS to act as the top contact. Crystals with ITO had a smaller bead of Ag paste placed on the edge of the ITO for the top contact. All crystals were then mounted on glass slides with a line of Ag paste which formed an accessible electrical connection to the Au back contact.

J-V measurements were taken with Au-wire probes, placed on the rear and front Ag paste contacts so as to complete the circuit. Diagrams of the devices are shown in figs. 6.16a-b.

3.3 Characterisation Methods for Physical Properties

3.3.1 Cutting, Mounting and Polishing

A diamond saw with a translation stage and a goniometer was used to cut the samples which were first fixed to glass microscope slides using Crystalbond mounting wax.

Slices of the polycrystalline CZTSSe boules as well as the Sb_2Se_3 polycrystal grown by the Piper-Polich method were cut axially to provide samples for characterisation. The CZTS polycrystal grown from the directional gradient freeze technique was cut radially. Oriented slices of Sb_2Se_3 with (100), (010) and (001) surfaces were prepared through visual alignment (using an optical microscope, see next section) to the cleavage steps on the (010) plane of the crystals followed by cutting, as discussed in Section 5.6.2. Cutting had an uncertainty of ± 1°.

To prepare the cut surfaces for further studies, the CZTS, CZTSSe and Sb_2Se_3 slices were mounted in Epofix resin blocks, ground with silicon carbide paper, and mechanically polished progressively with 3, 1 and 0.3 μm alumina particles in DI water. The CZTS polycrystal grown from Sn solution, and the crystallised CZTSSe solid solutions, were then subjected to a chemical treatment with 2 vol% Br in MeOH for 30 s to etch the surface.

3.3.2 Optical Microscopy

Optical microscopy was carried out with a Nikon Eclipse LV100 microscope in bright field mode at 5x magnification. Grain size estimates were based on optical micrographs of an area 1.8 x 2.4 mm in size. For each image, 4 horizontal and 6 vertical, evenly spaced lines were traced across the image. Each line was then divided into sections wherever it intersected a grain boundary. The length of the grains intersected by a line was then measured based on the image scale bar, as shown in fig.

3.6, with all of these lengths averaged to produce an estimate for the average grain size in the image. The uncertainty is quoted as the variance in each case.

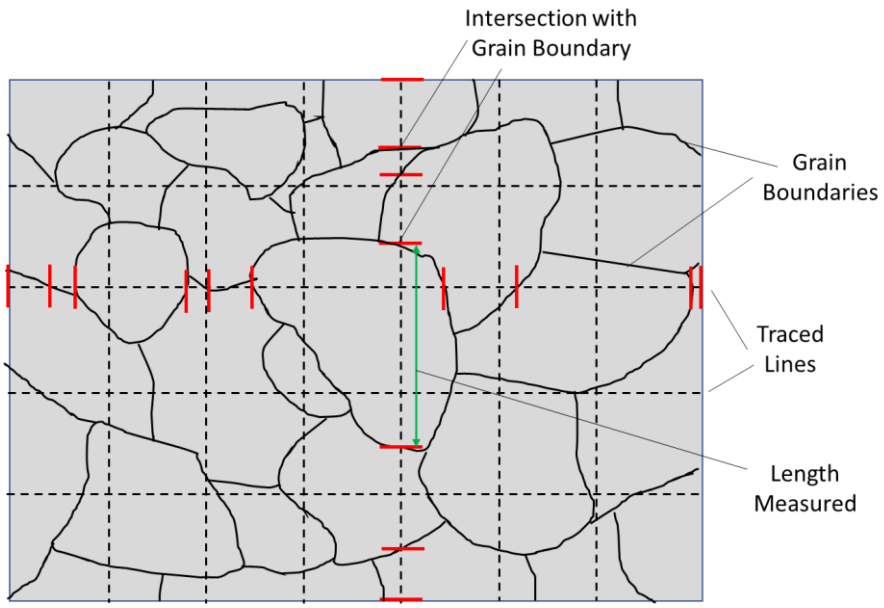

Fig. 3.6 Illustration of the method applied to estimate average grain size from optical micrographs, with the intersections with grain boundaries being shown for one vertical and one horizontal line.

3.3.2.1 Differential Interference Contrast Microscopy

Differential interference contrast (DIC) microscopy is as method for enhancing the contrast of images viewed through an optical microscope. The method works by splitting the incident light from the illumination source image using a polariser and a Normarski prism that displaces two orthogonally polarised images by a small distance, or 'shear', typically ~ 1 μm. When the two beams encounter a gradient in the sample surface, they are reflected back with slightly different phases. The two beams are then recombined in the same Nomarski prism, and if the change in the path length of the light across the shear distance is close to a half-wavelength of the incident light, destructive interference will occur, and the region will appear dark on the DIC image. As a result, the brightness levels in DIC images correspond to gradients on the sample surface on the order of the illumination wavelength. As a result, DIC allows the topography of relatively flat samples that would be otherwise appear featureless to be observed[11]. In this work, DIC microscopy was carried out with the same equipment as the standard optical microscopy.

3.3.3 X-ray Diffraction

X-ray diffraction (XRD) is the subject of book length reviews, e.g. [12]. Briefly, for diffraction to occur, the Bragg condition (eq. 3.2) must be satisfied.

$$n\lambda = 2d_{hkl}\sin\theta \tag{3.2}$$

where λ is the wavelength of the incoming x-rays, *n* is the order of diffraction, θ is the angle between the atomic plane and the incident beam, and d_{hkl} is the interplanar spacing. The factor *n* means that for a single crystal plane, multiple reflections, *hkl*, may be expected, where *h*, *k* and *l* are the Miller indices. In order to avoid the need to determine *n* explicitly, it is usually accounted for by adjusting the Miller indices of the reflection. This convention is equivalent to interpreting the patterns assuming that *n* = 1, and indeed the term *n* is often omitted from equation 3.2.

The relation of d_{hkl} to the specific lattice parameters of a crystal will vary depending on the symmetry of the crystal lattice. For a tetragonal crystal system, such as CZTSSe, the interplanar spacing d_{hkl} may be related to the Miller indices and unit cell parameters by eq. 3.3.

$$\frac{1}{{d_{hkl}}^2} = \frac{1}{n^2}\left(\frac{h^2+k^2}{a^2} + \frac{l^2}{c^2}\right) \tag{3.3}$$

where *a* and *c* are the lattice parameters of the crystal.

For an orthorhombic system such as Sb_2Se_3, the interplanar spacing is defined by eq. 3.4.

$$\frac{1}{{d_{hkl}}^2} = \frac{1}{n^2}\left(\frac{h^2}{a^2} + \frac{k^2}{b^2} + \frac{l^2}{c^2}\right) \tag{3.4}$$

where *a*, *b* and *c* are the crystal lattice parameters. In order to avoid the need to determine *n* explicitly, it is usually accounted for by adjusting the Miller indices of the reflection. For example, the notation d_{200} represents the 2nd-order reflection from the crystal plane (100), while d_{100} is the 1st-order reflection.

In this work, samples were analysed in the parallel-beam θ-2θ configuration as shown in fig. 3.7. The parallel-beam geometry is functionally similar to the well-established Bragg-Brentano

geometry, but differs in that it utilises a collimated beam of x-rays, rather than a focussed beam, with the beam size defined by an aperture. This allows for more freedom in the distance from source to sample and sample to detector compared to Bragg-Brentano geometry[13]. Both methods allow scanning over a large range of Bragg θ and hence the measurement of the full set of *d*-spacing presented by the samples investigated. This *d*-spacing measurement ultimately allows the diffracting planes to be indexed using eqs. 3.3 and 3.4[12]. As the angle between source and sample is changed, the area of the footprint of the collimated beam on the sample, (and therefore the sampled area) will also change, but this was not corrected for in this work, because all samples, as measured, were assumed to be uniform.

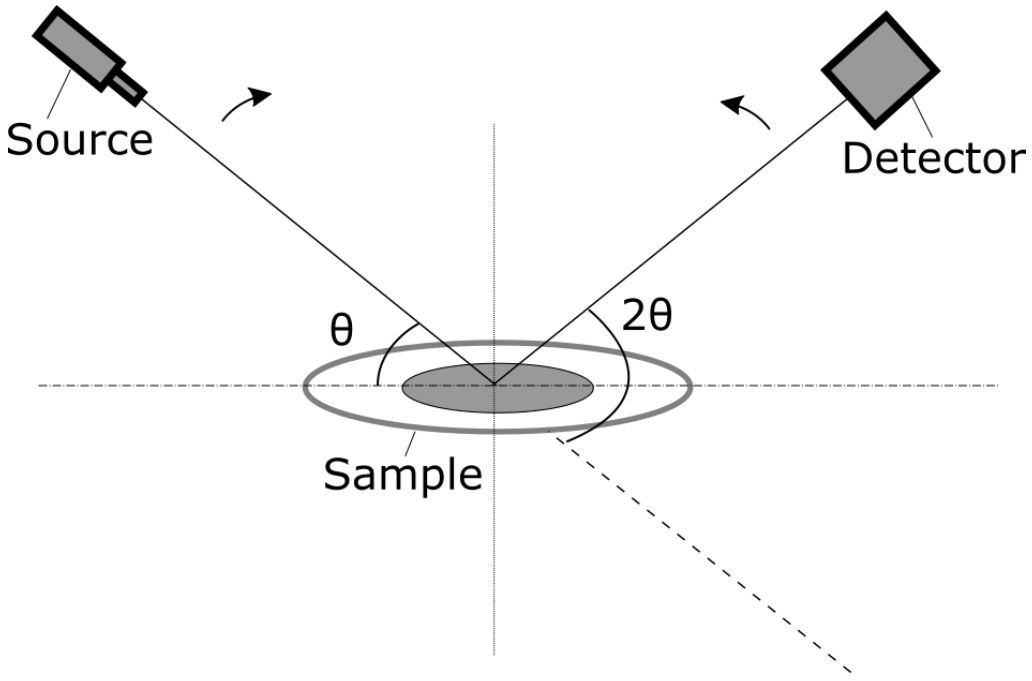

Fig. 3.7 Illustration of the relationship between the sample, source and detector in an XRD θ-2θ (parallel beam) scan. At the scan start, 2θ = θ = 0, and source both and detector are moved synchronously and stepwise to scan the 2θ axis of a diffraction pattern.

XRD was employed for three main uses in this work: the identification of a specific crystal phase; the measurement of lattice parameters; and the determination of the crystal orientation of a

sample surface. For the former two, samples were examined in powderised form (powder XRD), while solid single crystal sections were used for the last.

Powder XRD ensures that individual crystalline particles are randomly oriented, and a large number of particles ensures that every possible set of crystal planes is available for diffraction. However, for the θ-2θ geometry shown in fig. 3.7 only the subset of grains having planes parallel to the sample holder plate can meet the Bragg condition (eq. 3.2) and hence contribute to the diffracted intensity. For powder samples, the set of specific spacings of the peaks acts as a structural 'fingerprint' for a given material, allowing for unambiguous phase identification from a 2θ scan, although CZTSSe is an exception to this (Section 2.3.3).

A more randomised overall crystal orientation for a powder is achieved by grinding for a longer period of time, while grinding for a shorter time may result in a 'preferred orientation' where scattering from some crystal planes is more likely than others. This means that certain peaks in the 2θ scan will have higher intensities than would be expected for a fully random condition.

Powder XRD patterns are commonly analysed through the process of Rietveld refinement, which generates a modelled diffraction pattern based on a set of initial structural parameters including lattice parameters, and which use literature data as the starting point. These structural parameters may then be iteratively refined until the modelled diffraction pattern matches most closely with the experimentally observed pattern[14]. The goodness-of-fit is determined by the minimisation of the conventional Rietveld parameters.

There are several Rietveld parameters, all of which define goodness-of-fit in different ways, but no single parameter is a definitive quantification of fit quality. A detailed discussion of all of the Rietveld parameters is not included in this work, but may be found in [15].

Of the conventional Rietveld parameters, the chi-square statistic (χ^2) is a reasonable quantification of the goodness of fit[15], and one that is commonly quoted, provided that the other parameters have small values. It is used throughout this work.

In contrast to powders, when a single crystal is examined under XRD in θ-2θ geometry, only the single set of crystal planes that is parallel to the substrate holder will produce diffraction peaks, meaning that only a single peak and its higher order reflections may be expected. If no crystal planes are aligned with the plane of measurement, no peaks will appear. Therefore the appearance of a single diffraction peak and its higher orders provides evidence for a single crystal, with its planar orientation indicated by the angular position of the peak. However, there are limitations to this approach, not least because a single θ-2θ scan is insensitive to rotations about the axis of the diffraction plane, and so cannot distinguish a single crystal from a polycrystalline material with the grains presenting the same crystal plane, but rotated axially relative to one another (i.e. a preferred orientation). Furthermore, given the alignment criterion for Bragg reflection, secondary crystallites may be 'invisible' to the scan if they do not happen to be aligned appropriately. Because of these factors, a polycrystalline sample may appear monocrystalline in a θ-2θ scan, so other identification techniques, such as a rocking-curve, imaging of Kossel patterns, or inspection of the sample's cleavage behaviour, may be necessary to confirm monocrystallinity.

3.3.3.1 Diffractometer Conditions

In this work, x-ray diffraction (XRD) θ-2θ measurements for all samples were taken with a Rigaku Smartlab x-ray diffractometer with a step size of 0.01° for 2θ. Where powders were used, they were dried at 70°C and mounted on the sample stage with vacuum grease. As the parallel beam geometry was used, the collimated beam was defined at a constant width throughout the scan by an aperture. The sampled area was expected to change with the angle between the source and sample, but this was not corrected for as samples were expected to be uniform.

The following aperture width and radiation selections were used:

a) CZTSSe ($0 \leq x \leq 1$) feedstock, powderised: Cu $K\alpha_{1,2}$ and 10 mm aperture
b) CZTSSe ($0 \leq x \leq 1$) crystals, powderised: monochromated Cu $K\alpha_1$ and 10 mm aperture
c) Large-grained polycrystal CZTSSe: Cu $K\alpha_{1,2}$ and 2 mm aperture
d) Sb_2Se_3 and $Sb_2S_{3x}Se_{3(1-x)}$, powderised: Cu $K\alpha_{1,2}$ and 10 mm aperture
e) Large-grained Piper-Polich Sb_2Se_3 polycrystal: Cu $K\alpha_{1,2}$ and 10 mm aperture
f) Single crystal Bridgman Sb_2Se_3: monochromated Cu $K\alpha_1$ and 5 mm aperture

In the case of the Sb_2Se_3 single crystals, 4 measurements were taken with the sample rotated axially (about the vertical axis in fig. 3.7) by 45° on the measurement plate between scans. This was to account for small misalignments with the plane of measurement and ensure that it was as closely aligned with a crystal plan as possible to maximise diffraction peak intensity, with the highest-intensity scan used in analysis. These rotations were not carried out for other samples. Scans recorded early in the project were recorded with unmonochromated Cu $K\alpha_{1,2}$ emission lines, but for later work a monochromator was used since it simplified the analysis of the diffraction patterns.

3.3.3.2 Rietveld Refinement of Powder XRD Patterns

Rietveld refinement of all powder XRD patterns was carried out with the Fullprof software suite[16], with peaks fitted using the pseudo-Voigt line-shape and a 2θ step size of 0.01°.

For CZTSSe, the initial crystal structure was based on the *I*-4 space group for a kesterite structure, with the positions of atoms in the unit cell based on the work of Ritscher and Nozakia[17,18] and shown in Table 3.1. This assumes that Se and S (anions) occupy the same sites. For the case of disordered kesterite, Cu or Zn may occupy the 2c and 2d sites at random, but they also have very similar x-ray scattering factors, meaning that distinguishing between the ordered and disordered phases of CZTSSe with conventional XRD is unfeasible. As a result, the Cu and Zn atoms of the 2a 2c and 2d Wyckoff sites were treated as equivalent. The initial lattice parameters and anion positions were taken from Choubrac *et al.* for CZTSe ($x = 0$)[19] and Ritscher *et al.* for CZTS ($x = 1$)[17]. The overall occupancy for all atoms was fixed at 1 with the occupancy ratios based on stoichiometric proportions of metals to anions, with the ratio of sulphur to selenium atoms based on the weighed proportions (x – value). The lattice parameters of the intermediate compositions were interpolated between the values for CZTSe and CZTS, as expressed in Table 3.1.

Atom	Wyckoff Site	x Position	y Position	z Position	B_{Iso} (Å^2)	Occupancy
Cu/Zn	2a	0	0	0	0.1	0.125
Cu/Zn	2c	0	1/2	1/4	0.1	0.125
Cu/Zn	2d	0	1/2	3/4	0.1	0.125
Sn	2b	0	0	1/2	0.1	0.125
Se	8g	0.755	0.757	0.8718	0.1	$0.5\cdot(1-x)$
S	8g	0.755	0.757	0.8718	0.1	$0.5\cdot x$

Initial Lattice Parameters:	a (Å) = $-0.262x + 5.6965$ c (Å) = $-0.0497x + 11.3394$

Table 3.1 Initial structural parameters for Rietveld refinement of the CZTSSe solid solution series $0 \leq x \leq 1$.

For Sb_2Se_3, the initial structural parameters were based on the orthorhombic crystal structure reported in Caracas and Gonze [20]. Although Caracas and Gonze apply the *Pnma* convention in their work, the *Pbnm* convention was used in all reporting within this work (see Section 2.4.3 for explanation). For $Sb_2S_{3x}Se_{3(1-x)}$, the initial lattice parameters were interpolated between the values for Sb_2Se_3 reported in Caracas and Gonze[20], and the values for Sb_2S_3 reported in Kyono and Kimata [21]. The initial atomic positions from Caracas and Gonze, as shown in Table 2.2 were used.

In analysing the powder XRD patterns, a fully randomised overall orientation was assumed, and an 8-coefficient polynomial function was used to fit the background. The process of Rietveld refinement was carried out in the following order where possible:

1. Refine scale factor and first 6 polynomial coefficients
2. Refine lattice parameters and instrument zero
3. Refine atomic positions
4. Fix atomic positions and refine overall isotropic thermal parameter B_{Iso}
5. Refine both atomic positions and B_{Iso}
6. Refine 7th background coefficient
7. Refine peak shape parameters and all 4 asymmetry parameters
8. Refine 8th background coefficient

3.3.4 Differential Scanning Calorimetry and Thermogravimetric Analysis

Differential scanning calorimetry (DSC) is a technique able to determine the temperatures at which phase transitions occur. The heat flow to a sample is measured against temperature, which may be either increasing or decreasing experimentally. Abrupt peaks in the magnitude of heat flow indicate phase transitions, such as melting points or other similar transitions, with negative peaks indicating endothermic transitions and positive peaks exothermic. DSC is therefore useful in determining the phase transition temperatures of mixed materials, such as alloys and solid solutions, especially where data for a specific mixture has not been documented previously[22]. DSC is often carried out in

conjunction with thermogravimetric analysis (TGA) which tracks the mass of a sample against temperature, allowing material loss during the process (due to vapourisation) to be observed.

In this work, DSC and TGA measurements were taken using a TA Instruments SDT-Q600 system for the feedstock series end members CZTSe ($x = 0$) and CZTS ($x = 1$) and intermediate compositions of $x = 0.1$, 0.2, 0.4, 0.5, 0.6, 0.8 and 0.9, at a heating rate of 5°C min^{-1}, with around 5 mg of material used in each case.

3.3.5 Raman Spectroscopy

Raman scattering occurs when a photon (conventionally from a laser) incident on a material interacts with phonons within it. The photon may gain energy from a phonon in the material (anti-Stokes scattering) or lose it through the excitation of a phonon (Stokes scattering), with the latter process being more likely than the former. The gain, or loss, in energy of the scattered photon results in a small shift from the frequency of the incident light, usually expressed as the wavenumber $\tilde{\nu}$, in units of cm^{-1}[23]. The two Raman scattering processes are illustrated in fig. 3.8.

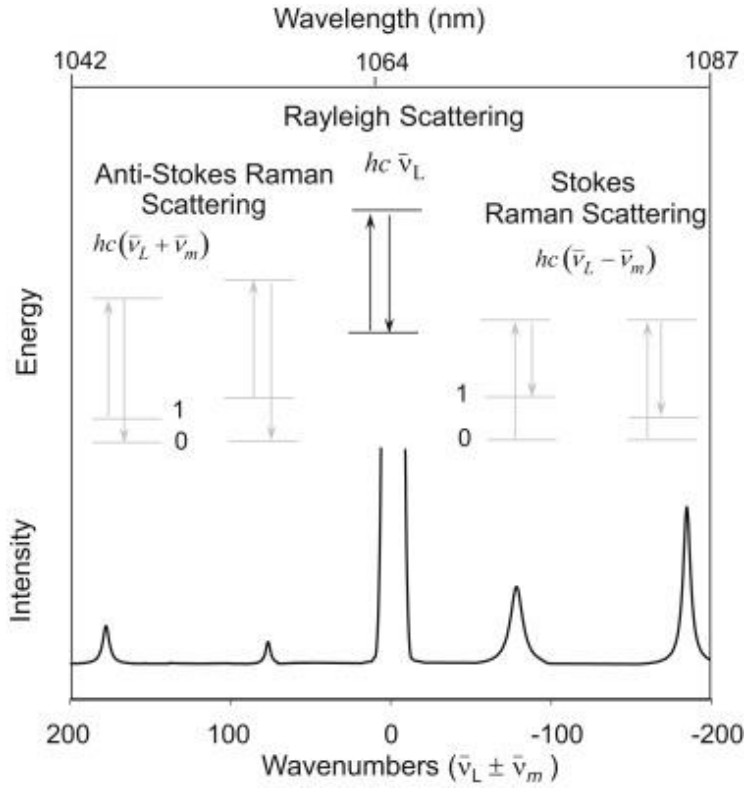

Fig. 3.8 Illustration of the basic principles of Raman scattering, reproduced from [23], where $\tilde{\nu}_L$ is the wavenumber of the incident photon, $\tilde{\nu}_m$ is the wavenumber of the phonon, h is Planck's constant and c is the speed of light.

The wavenumber of a spectral peak resulting from Raman scattering depends upon the energy of the vibrational mode of the crystal that produced the shift, while the vibrational modes that may exist in a crystal are constrained by the symmetry of the lattice as defined by the space group. The space group consists of all the symmetry operations required to fully define a crystal lattice, including translations in space, rotations and reflections, and which may be expressed in terms of 'representations', square matrices that produce equivalent transformations to the symmetry operations. The matrix form of representations aids the task of solving physical problems, with an 'irreducible representation' (Γ) being the group of lowest dimensional matrices required to fully describe the symmetry of a system[24]. The symmetry modes constituting the irreducible

representation of a crystal may be expressed in Mulliken notation as *A*, *B* or *E*. *A* and *B* modes are non-degenerate (i.e. one energy value for each symmetry mode), while *E* is doubly degenerate (two symmetry modes will have the same energy). *A* modes are symmetric under rotation in the principal axis (i.e. the direction of the vibration) while *B* modes are antisymmetric under this rotation. Additionally, the subscript *g* indicates that a mode is symmetric under inversion, while modes with a *u* subscript are antisymmetric under inversion. Finally, the number subscripts 1, 2 or 3 indicate modes are symmetric under rotation in the z, *y* or *x* axes respectively[25]. Group theory using irreducible representations allows the Raman-active symmetry modes in a material to be predicted, but not the energies or peak intensities[24].

The energy of a vibrational mode depends on the interatomic spacing, force constants and atomic mass of the bonded atoms involved[23]. Raman spectroscopy therefore provides a means of phase identification, as observed peaks will be influenced by crystal properties specific to a given material and crystal structure. It also provides a means to characterise such properties, like the inter-atomic spacing, as well as the arrangement of atoms within the crystal, making Raman sensitive to atomic disorder. Furthermore, if polarised excitation and collection of scattered light is employed, the angular dependence of these properties may also be examined.

In this work, Raman measurements were taken on the polished surface of the crystallised CZTSSe solid solutions ($0 \leq x \leq 1$) using a Renishaw in-Via microscope with 532 nm illumination laser, 50x long working distance objective lens and 1800 lines mm^{-1} grating. The laser spot diameter was 2 μm and the laser power was 1 mW.

The Raman spectra for the Sb_2Se_3 {100} crystal planes were measured with a Horiba Xplorer Plus Raman microscope with 532 nm laser, 1800 lines mm^{-1} grating, 1.3 μm spot size and 1 mW laser power. A single-mode fibre ran from the laser output to a 10x magnification objective lens. As a result, the incident laser was expected to maintain its initial polarisation, even though polarisers were not used in the optical path. Acquisition times of 240 s were used.

3.3.6 Secondary Electron Imaging and Energy Dispersive X-ray Spectroscopy in a Scanning Electron Microscope

Scanning electron microscopy (SEM) works through scanning a sample with a beam of electrons, accelerated to high energy (keV range). Where the beam impinges on the sample surface, secondary electrons are ejected and collected by the detector. The secondary electron counts at each site are reconstructed to form a topographic image of the sample with sub-micron resolution.

An additional consequence of the ejection of core electrons by the incident beam is that electrons from higher energy orbitals drop into the orbitals of those ejected, producing x-rays detectable with an energy-dispersive x-ray (EDX) spectrometer. The x-ray peaks produced from this process are unique to specific elements and their intensity relates to the quantity of an element present in the sample. Translating the peak intensities into elemental proportions requires a matrix correction method to account for factors such as the attenuation of x-rays by the sample itself, as well as fluorescence from the sample. With an appropriate matrix correction applied, EDX is a means to measure the elemental proportions present in a sample, working in the uncertainty range of ~ ± 1 at%. The depth from which core x-rays are generated may be controlled by the acceleration voltage of the incident electron beam. The methods are reviewed in book form by Goodhew, Humphreys and Beanland[26].

Scanning electron microscopy (SEM) and energy dispersive x-ray spectroscopy (EDX) were carried out with a JEOL-7001 FEGSEM or a JEOL-6610 electron microscope on the CZTSSe feedstock and crystals and the $Sb_2S_{3x}Se_{3(1-x)}$. Typically, up to 12 sites, each measuring 20 x 20 μm^2 were measured from an area of approximately 1 x 1 mm^2.

EDX on the CZTSSe polycrystalline feedstock was carried out for several samples across the $0 \leq x \leq 1$ composition range, with 2 - 12 sites per sample. The scan areas were around 20 x 20 μm^2 in size. EDX on the crystallised CZTSSe solid solutions was also carried out across the composition range $0 \leq x \leq 1$, where a 1 x 1 mm^2 analysis area was used for each sample with 3-11 sites measured. For the $Sb_2S_{3x}Se_{3(1-x)}$ samples examined, two analysis areas, each 1 x 1 mm^2 in size, had measurements taken at 7-10 sites. In all cases the compositions from the sites were averaged, with the

variance of the dataset reported as the uncertainty on the value (with a random natural variation assumed).

3.3.7 Electron Backscattered Diffraction

Electron backscattered diffraction (EBSD) is another technique that utilises an electron beam within a scanning electron microscope. As a crystalline sample is scanned, some of the incident beam electrons are backscattered from within the sample and diffracted by the crystal lattice according to Bragg's law. These electrons may be detected with a phosphor screen, producing visible diffraction patterns known as Kikuchi patterns and resembling Kossel patterns in x-ray diffraction. The patterns are then recorded with a camera and image processing software used to compare the observed patterns to models based on an existing dataset of crystal structural parameters. Based on the form and orientation of the Kikuchi patterns, specific crystal orientations may be assigned to the sites scanned[28]. This means that EBSD is able to map the orientation of a crystal or set of crystals, as well as quantifying their misorientation with the measurement (reference) plane.

EBSD was carried out with a Philips XL30 tungsten filament SEM on a carbon coated sample of a 5N Sb_2Se_3 single crystal grown by the vertical Bridgman technique. Structural parameters for Sb_2Se_3 based on Caracas and Gonze[20] were applied to fit the observed Kikuchi patterns and provide orientation data. The beam acceleration voltage was 15 kV.

3.4 Chemical Analysis Techniques

3.4.1 Inductively-coupled Plasma Methods

Inductively-coupled plasma optical emission spectroscopy and mass spectrometry (ICP-OES and ICP-MS) both make use of a plasma formed from the ionisation of a gas (usually Ar) excited by an induction coil. Typically, materials for analysis must be digested in acid and diluted in a solvent (often DI water) in order to be analysed by either method. The solution is introduced to the plasma in droplet form or as aerosol particles, at which point the elemental constituents become ionised.

The ionised elements within the plasma luminesce, producing sharp atomic emission lines which are exploited in ICP-OES. The optical emission lines are characteristic of a given element and may be used to detect their presence in the sample through measurement with a spectrometer. Furthermore, the intensities of the atomic emission lines may be used to quantify the concentration of a given element in the sample. This is done by comparing the intensity of the emission lines to a set of calibration standards with known concentrations. In ICP-MS, by contrast, the ionised atoms are directed from the plasma to a mass spectrometer, where ions are separated by mass, allowing the concentrations of the elements to be determined by counts.

Both techniques allow for the detection of elements that exist at the parts-per-million (ppm) level and below, making them invaluable for determining the level of elemental impurities present in different samples. ICP scans can quantify elemental concentrations to high precision, or a survey scan can be carried to simply detect the presence of a large number of elements . Survey scans may often use only one elemental concentration and a pure water ‘blank’ to calibrate, while a quantitative scan will use several concentrations of the element.

3.4.1.1 Inductively-Coupled Plasma Optical Emission Spectroscopy (ICP-OES)

ICP-OES scans were carried out with an Agilent 5110 ICP-OES spectrometer. For the quantitative scans carried out on CZTSSe samples, the intensity of each emission line was linearly calibrated against elemental standards at 5 known levels of concentration, for all elements. For the

survey scans carried out on Sb_2Se_3 samples, emission line intensity was calibrated using a single known concentration and a blank (pure DI water) for each element.

Quantitative scans were carried out on digested samples of CZTSSe solid solutions ($0 \leq x \leq 1$) to determine the atomic ratios of Cu Zn, Sn, S and Se. Samples were digested as follows: ~ 100 mg of material was added to 2 ml of concentrated HNO_3 (70% conc.) and 1 ml of HCl (37% conc.) and stirred at room temperature until fully dissolved after around 1 hr. 1 ml of the acid mixture was added to 13 ml DI water, resulting in an acid concentration of 4 vol%.

Survey scans were carried out on Sb_2Se_3 single crystal samples grown by the vertical Bridgman technique. The acid dissolution was as follows: 5 mg of Sb_2Se_3 was added to 3 ml of concentrated HNO_3 (70% conc.) and stirred at room temperature. After 1 hour, the acid had turned yellow, but small particles of Sb_2Se_3 remained, while after 18 hours, they had fully dissolved. 1 ml of the acid was added to 13 ml DI water, resulting in an acid concentration of 5 vol%. The process of dilution did not cause precipitation, indicating that this concentration was suitable for ICP-OES. Despite this, the concentration of Sb_2Se_3 in the diluted solution remained small (114 mg / l), meaning that the concentration of trace (<0.1 at%) elements were expected to be at levels < 0.1 ppm in the solution, this being close to the detection limit for some elements.

Samples of DI water (the ‘blank’) and diluted acid were also analysed in all cases to determine background levels of the relevant elements in the solutions.

3.4.1.2 Inductively-Coupled Plasma Mass Spectrometry (ICP-MS)

Survey ICP-MS scans (Section 3.4.1) were carried out on digested samples of Sb_2Se_3 single crystals grown by vertical Bridgman using a high-resolution Element 2 ICP-MS system. Samples were digested in 2 ml HNO_3 (70% conc.) and 1 ml of HCl (37% conc.) at 150 °C.

3.4.2 Secondary Ion Mass Spectrometry

Secondary ion mass spectrometry (SIMS) is capable of depth profiling the elemental composition of a sample and measuring trace impurities. The central process stems from a high-energy (keV) beam of ions (primary beam) accelerated onto the sample surface (examples being O^- and Cs^+). The impact of the beam ionises the atoms in the sample (secondary ionisation) and ejects them from the surface (sputtering).

In one variant, quadrupole SIMS, the secondary ions are directed to a quadrupole mass filter, where electric fields are adjusted to allow only ions with a specific charge-mass ratio to pass. A count of the secondary ions, corresponding to a specific ionised isotope, may then be recorded. By this method, the relative concentration of a given element may be determined from the mass count, allowing for the measurement of both impurity and major element concentrations.

As the surface is sputtered, secondary ions from deeper within the sample are ejected, meaning that the sputtering time relates to the depth of the sample being probed[28]. This allows depth profiling.

Quadrupole SIMS measurements were carried out with a Hidden Analytical gas ion gun and quadrupole detector. O^{2-} ions were used in the beam and the ion energy was set at 5 keV with a beam current of 300 nA. The scanning area was approximately 0.5 x 0.5mm^2.

3.5 Characterisation Methods for Electrical Properties

3.5.1 Hot-Probe Technique

The hot-probe technique utilises a temperature gradient to induce current flow of the majority carriers in a semiconductor. This happens as the elevated temperature (increasing kT) excites a greater number of electrons into the conduction band (or holes into the valence band) relative to the room temperature ‘cold’ probe. These carriers then diffuse from the high density region to the low density, resulting in a flow of electric current, or a potential difference. Since the majority carriers will always diffuse from the hot to the cold probe, the polarity of the measured current indicates the majority

carrier type[29]. The magnitude of the observed current is strongly influenced by the doping level of the material but will also depend on carrier mobility.

Hot probe measurements were carried out with gold probes connected to a Keithley 2400 source meter, with a soldering iron used as a heat source and K-type thermocouple to monitor temperature. Current, rather than voltage, was measured as it produced more consistent results.

Reference polarity checks were carried out as follows: monocrystalline samples of p-CdTe and n-InSb were contacted with Au, then measured with the hot probe (fig. 3.9). The p-type reference exhibited an increasing positive current with increasing temperature gradient, while the n-type exhibited a negative current. In both cases, the thermally-induced currents increased in an exponential fashion with temperature gradient, as evidenced by the current increasing rapidly at ≥ 30 °C / cm for the p-CdTe, while this rapid increase resulted in the ammeter saturating at -105 μA at a temperature gradient of ≥ 30 °C / cm for the n-InSb (fig. 3.9b). The value of 30 °C / cm is otherwise not physically significant and these features are coincidental. Reversal of the electrodes (not shown) resulted in currents of similar magnitude and opposite polarity, confirming that a positive current is expected in a p-type semiconductor, while a negative current is expected in n-type.

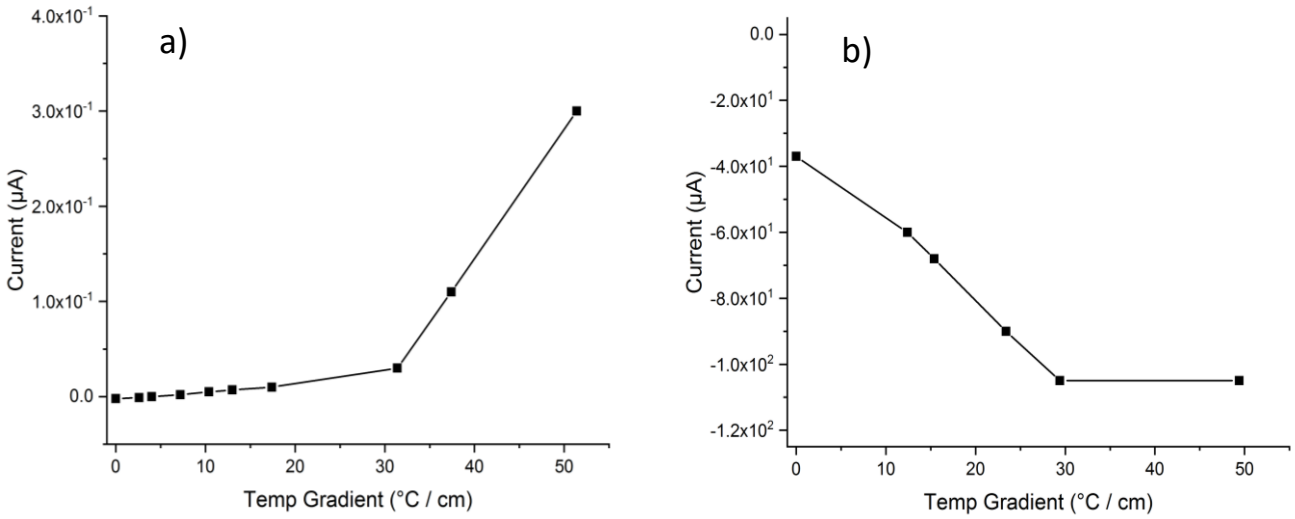

Fig. 3.9 Thermally-induced currents for p- and n-type reference samples p-CdTe (a) and n-InSb (b). The ammeter was saturated at -105 μA for large temperature gradients in measurements of the InSb (b).

3.5.2 Hall Effect

The Hall effect provides a means of measuring the carrier type, density and mobility within a sample. This occurs as carriers flowing in a current are deflected by an applied magnetic field to produce an additional (Hall) voltage across the sample. It is possible to observe the Hall effect and measure the Hall coefficient, R_H using van der Pauw geometry. Ideal van der Pauw geometry requires edge contacts, but this not always practical, and in this work, contacts were placed in a square as illustrated in fig. 3.10. This is expected to introduce additional uncertainties as, for instance, the non-zero contact widths may produce additional potential gradients across the sample, complicating the measurement of Hall voltage. Nevertheless this approximate van der Pauw geometry is usually considered adequate for the first trials in research work.

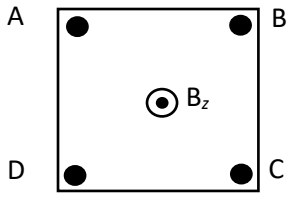

Fig. 3.10 Illustration of contacts placed in an approximate van der Pauw geometry, where A, B, C, D are electrodes and B_z is the magnetic field vector and points out of the page.

For a sample measured in van der Pauw geometry, the change in resistance due to magnetic field is defined by eq. 3.5[30].

$$R_H = \frac{w}{B_z}\Delta R_{BDAC} \tag{3.5}$$

where R_H is the Hall coefficient, B_z is the magnetic induction field (applied orthogonal to page), w is the sample thickness, and ΔR_{BDAC} is the change in resistance between diagonal contacts (A-C and B-D), for a given magnetic field. This diagonal measurement scheme is in contrast to a van der Pauw resistivity measurement, where adjacent contacts are used.

Additionally, the term Hall conductance, G_{xy}, is defined in eq. 3.6.

$$G_{xy} = \frac{\Delta R_{BDAC}}{{R_0}^2} \tag{3.6}$$

where R_0 is the sheet resistance measured at zero magnetic field in the conventional van der Pauw scheme (adjacent contacts). Given the non-ideal geometry used in this work (see fig. 3.10) additional potential gradients may be expected, causing a non-zero parasitic sheet resistance value to be measured with diagonal contacts and zero magnetic field. This may be corrected for in analysis by setting G_{xy} to zero at zero magnetic field.

In order to extract the Hall coefficient, eq. 3.6 may be rearranged as eq. 3.7.

$$G_{xy} = \frac{R_H \mu_0}{w{R_0}^2} H_z \tag{3.7}$$

where H_z is the auxiliary magnetic field and μ_0 is the permeability of free space. By setting G_{xy} to zero where the field H_z is zero, parasitic sheet resistance may be neglected and symmetrical data plotted. From eq. 3.7 it is clear that a linear fit of G_{xy} against H_z allows the Hall coefficient to be derived. The Hall coefficient may be related to carrier density as defined in eq. 3.8.

$$R_H = \frac{1}{\mathrm{e}N_S} \tag{3.8}$$

where N_S is the carrier density and e is the charge on an electron.

The carrier mobility may then be calculated based on the carrier density and sheet resistance from eq. 3.9.

$$\mu = \frac{wR_0}{N_S} \tag{3.9}$$

In this work, Hall measurements were carried out on Sb_2Se_3 single crystals growth by vertical Bridgman from Alfa Aesar (5N) Sb_2Se_3 on square cleaved samples of around 3 x 3 mm area. Given that the hot probe results for crystals of this type suggested n-type conductivity, In contacts were used to ensure an Ohmic contact and eliminate contact barriers which could complicate the measurement

(if p-type conductivity were suspected, Au contacts would have been used to ensure Ohmic contacts). The contacts were soldered to the surface in a square configuration to approximate van der Pauw geometry (see fig. 3.10). R_0 and G_{xy} were measured using a Keithley 2400 source meter and a Quantum Design Physical Property Measurement System (PPMS). Auxillary magnetic field strengths of up to 60 or 90 kOe were used and all measurements were taken at 300 K (The PPMS instrument is a modular multi-functional measurement platform but in this case it was simply used to provide the magnetic field for the Hall measurements).

3.5.3 Barrier Height Estimation from *I-V-T* Measurements

The barrier height of a Schottky barrier at the back-contact of a solar cell may be estimated from the temperature-dependent series resistance, measured via *I-V* profiling. The expression in eq. 3.10[31] indicates the relationship between series resistance and Schottky barrier height:

$$R_s = R_{\Omega 0} + \frac{\partial R_{\Omega 0}}{\partial T} T + \frac{C}{T^2} \exp\left(\frac{\Phi_B}{kT}\right) \tag{3.10}$$

Where T is temperature, k is the Boltzmann constant, R_s is series resistance, $R_{\Omega 0}$ is resistance at 0°C, $\partial R_{\Omega 0}/\partial T$ is the Ohmic temperature coefficient, Φ_B is barrier height, and C is a constant. The exponential part of equation 3.11 is assumed to dominate the form of the curve if $\Phi_B >> kT$ in the temperature range, and as such, is linearised as eq. 3.11, allowing barrier height to be extracted from a linear plot of $\ln(R_S T^2)$ against $1/T$.

$$\ln\left(R_s T^2\right) = \frac{\Phi_B}{kT} + \ln(C) \tag{3.11}$$

This allows the barrier height of a Schottky diode to be estimated from measurements of R_s against temperature.

Current-voltage (*I-V*) measurements for Sb_2Se_3 single crystals were taken using a Keithley 2400 source meter. Room-temperature measurements were taken in air and temperature dependent measurements were taken in a CTI Cryogenics Model 22 Cryodine Refrigerator closed cycle helium

cryostat under 10^{-2} mbar pressure, with a Lakeshore 331 temperature controller. A temperature range of 290-380 K was applied for the p-type single crystal (Sn-doped, grown from 5N Sb_2Se_3), and a range of 220-320 K was used for the n-type Sb_2Se_3 single crystals (consisting of $MgCl_2$-doped Se-rich and both undoped and $MgCl_2$-doped crystals grown from 5N Sb_2Se_3). Temperature increments of 10 K were used in all cases.

3.5.4 *C-f* Measurements and 'Roll-Off' at High-Frequency

Capacitance-frequency (*C-f*) profiling provides a means to assess the reliability of carrier densities measured using capacitance-voltage at a given frequency. *C-V* measurements taken at low AC frequencies have the issue that the capacitance may be strongly influenced by the presence of carrier traps[30], which will have a strong frequency dependence determined by the emission rates of the defects, typically on the order of ms[30]. As a result, high frequency measurements (>1kHz) are preferred. However, there is a drop-off in measured capacitance at high-frequencies, as described by the relationship shown in eq. 3.12[30].

$$C_{meas} = \frac{C_{true}}{(1 + (\omega C_{true} R_s)^2)} \tag{3.12}$$

Here, C_{meas} is the measured capacitance, C_{true} is the true diode capacitance, ω is the measurement frequency, and R_s is the series resistance of the diode. As can be seen, the larger the measurement frequency, the more the measured capacitance will underestimate the true capacitance. Essentially, the diode acts as a low pass filter to the AC voltage signal. Therefore, a region with a minimal variation of capacitance with frequency will indicate the regime where $\omega C_{true} R_s << 1$ and therefore $C_{meas} \approx C_{true}$. The "roll-off" effect will have a lower frequency cut-off the larger the series resistance of the diode, meaning that for more resistive samples, the frequency-window in which $C_{meas} \approx C_{true}$, but frequency is also high enough to ignore traps, is narrowed.

In this work, capacitance-frequency (*C-f*) measurements were taken in the dark using a Solartron 1260 Frequency Response Analyser and 1296 Dielectric Interface. AC frequency was varied from 1 to 1 MHz and DC bias varied from –1 V to +1 V.

3.5.5 *C-V* Measurements and Carrier Density

The capacitance of a rectifying junction, assuming the 'one-sided junction' approximation, may be expressed by eq. 3.13[30]:

$$C = A\left(\frac{\varepsilon_r \varepsilon_0 q N_S}{2}\right)^{\frac{1}{2}}\left(V - \frac{\mathrm{k}T}{\mathrm{e}}\right)^{\frac{1}{2}} \tag{3.13}$$

where N_S is carrier density (shallow doping density), A is contact area, ε_r is relative dielectric permittivity of Sb_2Se_3, ε_0 is the permittivity of free space, V is applied DC bias. The width of the space charge region is given by eq. 3.14:

$$x_d = \frac{\varepsilon_r \varepsilon_0 A}{C} \tag{3.14}$$

Taking the expression in eq. 3.13 [30] and re-arranging to eq. 3.15 means that carrier density may be estimated from a plot of C^{-2} against voltage (Mott-Schottky plot).

$$N_S = \frac{2}{qA^2 \varepsilon_r \varepsilon_0 \frac{d(C^{-2})}{dV}} \tag{3.15}$$

For resistive samples, the phenomenon of frequency-dependent roll-off may affect the carrier density that is measured, leading to inaccuracies. The dependence of the measured carrier density on AC frequency may be described in eq. 3.16[30] as:

$$N_{S(meas)} = \frac{N_{S(true)}}{1 - (\omega C_{true} R_s)^4} \tag{3.16}$$

indicating a very strong dependence of the measured carrier density upon frequency when $\omega C_{true} R_s$ is close to a value of 1, and effectively no dependence when $\omega C_{true} R_s << 1$. It can also be seen that for any $\omega C_{true} R_s$ values greater than 1, the measured value of N_A will very rapidly drop relative to the

true value, i.e. as $\propto \omega^{-4}$. Estimating the value of $\omega C_{true} R_s$ is therefore important to assess the reliability of carrier density measurements.

C-V measurements were taken with the same equipment as the *C-f* measurements, at AC frequencies from 100 Hz to 1 MHz, with DC bias ranging from -1 to 1 V.

3.5.6 Deep-Level Transient Spectroscopy

Deep-level transient spectroscopy (DLTS) works using the principle that if a voltage pulse is applied to a junction, e.g. a Schottky diode, deep-level traps in the space-charge region will populate with majority charge carriers and then depopulate in the time following the pulse. This depopulation will cause a transient decay in the capacitance, with the form of the transient given by eq. 3.17[32]:

$$C(t) = C_R - \Delta C \exp\left(-\frac{t}{\tau_e}\right) \tag{3.17}$$

where C_R is the capacitance observed during the pulse, due to the movement of free-carriers, while τ_e is the time constant of the decay and ΔC is the magnitude of capacitance change due to the presence of deep-level carrier traps. ΔC is related to the density of deep-level traps N_T as expressed in eq. 3.18[32]:

$$\Delta C \approx C_R \frac{N_T}{2N_S} \tag{3.18}$$

assuming all of the impurities in the space charge region are occupied.

The transient emission time constant τ_e may be related to the energy level and capture cross section of a charge carrier (electron or hole) trap with eq. 3.19[32]:

$$\tau_e = \left(\sigma_n \nu_{th} \chi_n N_{C,V} \exp\left(-\frac{E_A}{kT}\right)\right)^{-1} \tag{3.19}$$

where σ_n is the capture cross section, ν_{th} is the charge carrier thermal velocity, χ_n is the entropy factor, $N_{C,V}$ is the density of states in the conduction band for n-type doping, or the density of states in the valence band for p-type doping. E_A is the activation energy, where for n-type conductivity $E_A = E_C$ -

E_T, and for p-type, $E_A = E_T - E_V$. E_C is the energy level of the conduction band, E_v is the energy level of the valence band and E_T is the trap energy level. The expression in eq. 3.19 may then be linearised to produce eq. 3.20:

$$\ln\left(\tau_e v_{th} N_{C,V}\right) = \frac{E_A}{\mathrm{k}}\frac{1}{T} - \ln(\chi_\mathrm{n}\sigma_\mathrm{n}) \tag{3.20}$$

meaning that for a linear plot of $\ln(\tau_e v_{th} N_{C,V})$ against $1/T$ (Arrhenius plot), the activation energy of the trap may be determined from the gradient, while the capture cross section may be determined from the intercept.

A typical DLTS scan is performed by measuring the change in the magnitude of the transient signal over a range of temperatures and for varied measurement period widths. For a given decay time constant, τ_e there will be a specific temperature at which the magnitude change of the transient will peak (see fig. 3.11), and it is this temperature which is applied in the Arrhenius plot. Typically, temperature sweeps are repeated with variation of the time constant to construct the Arrhenius plot and extract E_A and σ_A values.

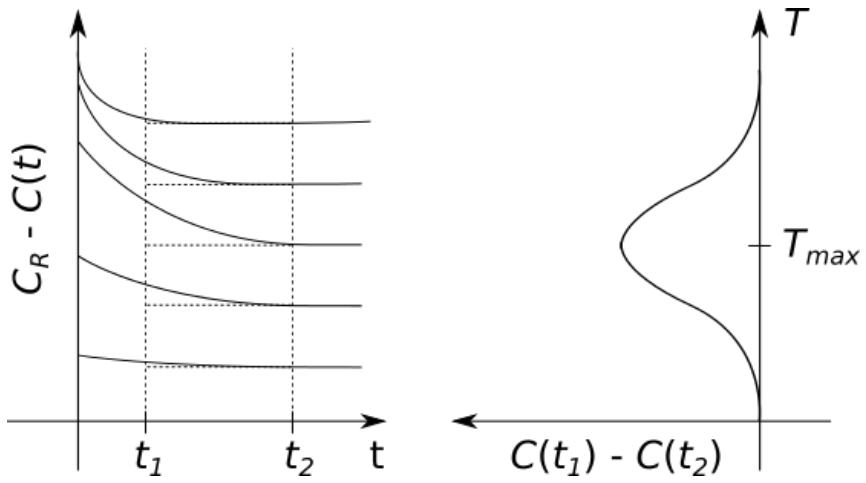

Fig. 3.11 Illustration of the change in capacitance transient with temperature, and the magnitude of change in the measured capacitance $C(t_1)$ - $C(t_1)$ for a given rate window $t_1 - t_2$.

In earlier experiments, due to equipment limitations, the transient signal was sampled only twice per measurement, with time constant defined by a specific 'rate window'. The magnitude change of the transient was determined from the difference in single values of capacitance measured at the start and end of the rate window. As the rate window defined the value of τ_e, multiple temperature sweeps with different rate windows were then required to produce Arrhenius plots. This method is often referred to as 'classical DLTS'.

More recently, the method of 'deep-level transient Fourier spectroscopy' (DLTFS) has become standard, as advances in digital signal processing allow an entire transient to be sampled at high time resolution. The signal may then be processed with a discrete Fourier transform to generate the series of Fourier coefficients c_n^D that constitute the signal, eliminating the need for multiple temperature sweeps to produce an Arrhenius plot. The magnitude of these coefficients, such as the frequently-used sinusoidal correlation function b_1, is a measure of the capacitance change in the transient, so may be expressed more simply as ΔC, and each Fourier coefficient will have a specific emission time constant associated, depending on measurement period width. This means that DLTFS works on the same principles as classical DLTS, and may be understood in similar terms. Full details

of the signal processing are not included in this work, but a more detailed discussion can be found in [32].

Based on eq. 3.19, ΔC peak positions will shift with temperature depending on the time constant of the Fourier coefficient. The position of a given peak may then be plotted in Arrhenius form against the time constants used. In this way, a single temperature-transient scan may be employed to produce an Arrhenius plot for any peaks that appear in the scan, from which values of activation energy and capture cross-section may be estimated. The amplitude of the peaks may also be used to determine the value ΔC, from which trap density may be estimated using eq. 3.18.

DLTS measurements in this work were carried out on n-type Sb_2Se_3 single crystal samples using a Phys Tech HERA FT1030 system. An $MgCl_2$-doped selenium-rich single crystal and an undoped crystal grown from 5N Sb_2Se_3 were examined, both with two evaporated Au contacts 0.1 cm^2 in size. A pulse width of 1 ms and a measurement time of 19.2 ms was used, with a temperature range of 150-400 K. Temperature increments of 1 K were used for the $MgCl_2$-doped crystal and 2 K for the 5N crystal.

3.5.7 Photoluminescence

Photoluminescence (PL) works through laser excitation of a semiconductor sample with a photon energy greater than the bandgap of the semiconductor. This process excites electrons from the valence to the conduction band, where they thermalise to the band minimum. Carriers may then recombine through non-radiative or radiative channels, the latter producing luminescence radiation which is observed as peaks in a spectrum. Besides simple band-to-band recombination (where the peak energy matches the bandgap), there are many possible radiative recombination channels following PL excitation, which may be mediated by defects that lie within the band gap of the semiconductor. This means that PL peaks of energy smaller than the bandgap may appear in the spectra.

The type of transition taking place may be inferred from measurements of PL intensity with different excitation power, based on the relation in eq. 3.21[33]:

$$PL \sim P^m \tag{3.21}$$

where *PL* is the photoluminescence intensity and *P* is the laser power. The exponent *m* is influenced by the type of recombination present in the sample, meaning that a log-log (Schmidt) plot of PL intensity against laser power allows the recombination type to inferred from the value of *m*[33].

The PL peak intensities will also vary with temperature, as expressed in eq. 3.22[34]:

$$\Phi(T) = \frac{\Phi_0}{1 + \alpha_1 T^{3/2} + \alpha_2 T^{3/2} \exp(-E_T/\mathrm{k}T)} \tag{3.22}$$

where E_T is the thermal activation energy, T is temperature, α_1 and α_2 are the process rate parameters and Φ is integrated intensity[34].

Photoluminescence measurements were carried out on undoped stoichiometric, Se-rich Sn-doped, Se-rich $MgCl_2$-doped and undoped 5N Sb_2Se_3 single crystals grown by vertical Bridgman. The 442 nm line of a He-Cd laser at a range of power levels from 0.27 mW to 37 mW, with a spot size of 100 μm diameter, monochromated using a 0.64 m focal length single grating of 600mm^{-1}, was used as the excitation source. A Hamamatsu InGaAs photomultiplier tube was used as detector. Measurements were taken within a closed-cycle helium cryostat in order to avoid laser-induced oxidisation of the sample surface, as well as controlling temperatures from 10 K to 300 K.

3.5.8 *J-V* Curves and Photovoltaic Working Parameters

Of central importance to the study of solar cells is the power-conversion efficiency, or PCE (η), which for a photovoltaic cell under illumination, is given by eq. 3.23[35].

$$\eta = \frac{J_{SC} V_{OC} FF}{P_S} \tag{3.23}$$

where J_{SC} is the short-circuit current density (current density that flows when $V = 0$), V_{OC} is the open-circuit voltage (the bias at which $J = 0$), P_S is the power density of a standardised illumination source usually having the AM1.5 spectrum and an intensity of 1000 Wm^{-2}, and FF is the fill factor, a measure of the 'squareness' of the J-V curve. FF is defined by eq. 3.24:

$$FF = \frac{J_{max} V_{max}}{J_{SC} V_{OC}} \tag{3.24}$$

where J_{max} and V_{max} are the current density and voltage at the maximum power point (where the product of J and V is largest). FF is strongly affected by the values of shunt resistance R_{sh} (resistance where $V = 0$) and series resistance R_s (resistance where $J = 0$), with larger values of R_{sh} producing a larger FF and larger values of R_s decreasing FF.

J_{SC}, V_{OC}, FF, R_s and R_{sh} are therefore all key working parameters that determine the power conversion efficiency of a solar cell, each with dependences upon different properties of the solar cell[35]. Conveniently, all of these working parameters may be derived from a J-V curve of a solar cell, making J-V measurements crucial in measuring the performance of a solar cell. Measuring J-V is as simple as taking an I-V measurement of a solar cell with a back contact of a defined area.

J-V measurements for the single-crystal and thermally evaporated Sb_2Se_3 devices were taken in the dark and under AM1.5 illumination using a TS Space Systems AAA100 solar simulator calibrated with a PV Measurements photodiode. Individual cells for the thermally evaporated Sb_2Se_3 devices were identified as being shorted if the resistance measured using the source meter was below 1 kΩ for a 10 μA probe current.

3.5.9 External Quantum Efficiency

External quantum efficiency (EQE) quantifies the carrier yield of a device compared to the number of incident photons for each wavelength across a scan range, i.e. the probability of an incident

photon of a given wavelength generating an electron which is collected by the circuit, with the expression for EQE in eq. 3.25:

$$EQE = \frac{I \cdot \mathrm{h}\nu}{\mathrm{e} \cdot P} \tag{3.25}$$

where I is device current, hν is photon energy and P is the power of the incident light. As such, the EQE spectrum of a solar cell is independent of a specific illumination spectrum (such as AM1.5), allowing the conversion efficiency of specific wavelengths to be known. An EQE spectrum may be compared to the absorption edge of solar cell materials as well as that of expected secondary phases to identify absorption features.

External quantum efficiency (EQE) measurements were carried out with a Bentham PVE300 EQE system with a TMC300 Monochromator and Bentham 605 power supply. White light bias was applied.

3.6 References

[1] T. Raadik *et al.*, "Low temperature time resolved photoluminescence in ordered and disordered Cu_2ZnSnS_4 single crystals," *Phys. B Condens. Matter*, vol. 508, no. November 2016, pp. 47–50, 2016.

[2] G. Rey *et al.*, "The band gap of $Cu_2ZnSnSe_4$: Effect of order-disorder," *Appl. Phys. Lett.*, vol. 105, no. 11, p. 112106, 2014.

[3] W. M. Haynes, *CRC Handbook of Chemistry and Physics*, 95th ed. London, New York: CRC Press, Taylor & Francis Group, 2014.

[4] W. W. Piper and S. J. Polich, "Vapor-phase growth of single crystals of II–VI compounds," *J. Appl. Phys. Appl. Phys. Lett.*, vol. 32, no. 62, pp. 1278–2851, 1961.

[5] A. Szczerbakow and K. Durose, "Self-selecting vapour growth of bulk crystals - Principles and applicability," *Prog. Cryst. Growth Characterisation Mater.*, vol. 51, pp. 81–108, 2005.

[6] A. Szczerbakow, "Model of the temperature field in tube furnaces and its application to a system of 'contactless' crystal growth from the vapour," *J. Cryst. Growth*, vol. 257, pp. 31–41, 2003.

[7] M. Jurisch, S. Eichler, and M. Bruder, *Handbook of Crystal Growth: Bulk Crystal Growth*, 2nd ed. Amsterdam: Elsevier, 2015.

[8] D. Mai, H. Park, and I. Choi, "Growth of Cu_2ZnSnS_4 crystals by the directional freezing method with an induction heater," *J. Cryst. Growth*, vol. 402, pp. 104–108, 2014.

[9] X. Liu *et al.*, "Thermal evaporation and characterization of Sb_2Se_3 thin film for substrate

Sb_2Se_3/CdS solar cells," *ACS Appl. Mater. Interfaces*, vol. 6, no. 13, pp. 10687–10695, 2014.

[10] L. J. Phillips *et al.*, "Current enhancement via a TiO_2 window layer for CSS Sb_2Se_3 solar cells: performance limits and high Voc," *IEEE J. Photovoltaics*, vol. 9, no. 2, pp. 544–551, 2019.

[11] D. B. Murphy, E. D. Salmon, K. R. Spring, M. Abramowitz, and M. W. Davidson, "Fundamental concepts in DIC microscopy," *Olympus Microscopy Resource Centre*, 2020. [Online]. Available: http://www.olympusmicro.com/primer/techniques/dic/dicintro.html. [Accessed: 01-Mar-2020].

[12] D. G. Callister, William D. Rethwisch, *Materials Science and Engineering*, 8th ed. Hoboken, N. J: John Wiley & Sons, 2011.

[13] XOS, "Parallel Beam Geometry for Powder XRD Technique," 2020. [Online]. Available: https://www.xos.com/Parallel-Beam-XRD-Powder. [Accessed: 09-Jul-2020].

[14] J. Rodríguez-Carvajal, "Recent advances in magnetic structure determination by neutron powder diffraction," *Phys. B Condens. Matter*, vol. 192, no. 1–2, pp. 55–69, Oct. 1993.

[15] W. I. F. David, "Powder diffraction: Least-squares and beyond," *J. Res. Natl. Inst. Stand. Technol.*, vol. 109, no. 1, p. 107, 2004.

[16] J. Rodríguez-Carvajal, "Recent advances in magnetic structure determination by neutron powder diffraction," *Phys. B Condens. Matter*, vol. 192, no. 1–2, pp. 55–69, Oct. 1993.

[17] A. Ritscher, J. Just, O. Dolotko, S. Schorr, and M. Lerch, "A mechanochemical route to single phase Cu_2ZnSnS_4 powder," *J. Alloys Compd.*, vol. 670, no. 82, pp. 289–296, 2016.

[18] H. Nozaki, T. Fukano, S. Ohta, Y. Seno, H. Katagiri, and K. Jimbo, "Crystal structure determination of solar cell materials: Cu_2ZnSnS_4 thin films using X-ray anomalous dispersion," *J. Alloys Compd.*, vol. 524, pp. 22–25, 2012.

[19] L. Choubrac, A. Lafond, M. Paris, C. Guillot-Deudon, and S. Jobic, "The stability domain of the selenide kesterite photovoltaic materials and NMR investigation of the Cu/Zn disorder in $Cu_2ZnSnSe_4$ (CZTSe)," *Phys. Chem. Chem. Phys.*, vol. 17, no. 23, pp. 15088–15092, 2015.

[20] R. Caracas and X. Gonze, "First-principles study of the electronic properties of A_2B_3 minerals, with A = Bi, Sb and B = S, Se," *Phys. Chem. Miner.*, vol. 32, pp. 295–300, 2005.

[21] A. Kyono and M. Kimata, "Structural variations induced by difference of the inert pair effect in the stibnite-bismuthinite solid solution series $(Sb,Bi)_2S_3$," *Am. Minerol.*, vol. 89, no. February, pp. 932–940, 2004.

[22] S. M. Khopkar, *Basic Concepts of Analytical Chemistry*, 3rd ed. New Delhi: New Academic Science, 2008.

[23] P. J. Larkin, *Infrared and Raman Spectroscopy: Principles and Spectral Interpretation*, 2nd ed. Solvay, Stamford, CT, United States: Elsevier, 2018.

[24] M. S. Dresselhaus, G. Dresseulhaus, and A. Jorio, *Group Theory Application to the Physics of Condensed Matter*. Berlin: Springer-Verlag, 2008.

[25] R. S. Mulliken, "Report on notation for spectra of diatomic molecules," *Phys. Rev.*, vol. 23, p. 1997, 1955.

[26] R. Goodhew, P J; Humphreys, F J; Beanland, *Electron Microscopy and Analysis*, 3rd ed. London: Taylor & Francis, 2001.

[27] V. Randle, "Electron backscatter diffraction: Strategies for reliable data acquisition and processing," *Mater. Charact.*, vol. 60, pp. 913–922, 2009.

[28] Paul van der Heide, *Secondary Ion Mass Spectrometry: An Introduction to Principles and*

Practices, 1st ed. John Wiley and Sons, 2012.

[29] G. Golan, A. Axelevitch, B. Gorenstein, and V. Manevych, "Hot-probe method for evaluation of impurities concentration in semiconductors," *Microelectronics J.*, vol. 37, no. 9, pp. 910–915, 2006.

[30] P. Blood and J. W. Orton, *The Electrical Characterization of Semiconductors: Majority Carriers and Electron States*, 1st ed. London: Academic Press Limited, 1992.

[31] D. L. Bätzner, M. E. Öszan, D. Bonnet, and K. Bücher, "Device analysis methods for physical cell parameters of CdTe/CdS solar cells," *Thin Solid Films*, vol. 362, pp. 288–292, 2000.

[32] S. Weiss, "Semiconductor investigations with the DLTFS (deep–level transient fourier spectroscopy) method," PhD Thesis, Department of Physics, University of Kassel, Hesse, 1991.

[33] T. Schmidt, K. Lischka, and W. Zulehner, "Excitation-power dependence of the near-band-edge photoluminescence of semiconductors," *Phys. Rev. B*, vol. 45, no. 16, pp. 8989–8994, 1992.

[34] J. Krustok, H. Collan, and K. Hjelt, "Does the low-temperature Arrhenius plot of the photoluminescence intensity in CdTe point towards an erroneous activation energy?," *J. Appl. Phys.*, vol. 81, no. 3, pp. 1442–1445, 1997.

[35] J. Nelson, *The Physics of Solar Cells*, 1st ed. London: Imperial College Press, 2003.

4. Vegard Relation and Raman Mode Evolution for the Kesterite Solid Solution Series $Cu_2ZnSnS_{4x}Se_{4(1-x)}$

4.1 Introduction

This chapter details work carried out on the synthesis, crystallisation and properties of the kesterite solid solutions $Cu_2SnSnS_{4x}Se_{4(1-x)}$, specifically, the lattice parameters, Raman mode frequencies and control of sulphur-selenium content (defined by the value of x, where $x = 0$ for $Cu_2ZnSnSe_4$ and $x = 1$ for Cu_2ZnSnS_4). It was motivated by the high efficiencies that have been achieved for thin films utilising solid solutions of CZTSe and CZTS, relative to the pure end members, as well as the difficulty in knowing the compositions of these films to high accuracy (Section 2.3.3). Additionally, an initial aim was the production of single crystals of CZTSSe in order to carry out electrical characterisation of point defects, although this was not ultimately achieved.

Section 4.2 describes the outcomes of direct synthesis from the elements (DSE) and crystal growth from solution in either Sn or a NaCl/KCl mix. Sn-based solution growth through the vertical gradient freeze technique was intended to produce CZTS single crystals, while the NaCl/KCl mix was used to produce monograin crystals across the composition range of $Cu_2ZnSnS_{4x}Se_{4(1-x)}$ from $x = 0$ (CZTSe) to $x = 1$ (CZTS) in steps of 0.1, with the nucleation of thick plates onto a quartz seed plate also investigated. Metallographic analysis, scanning electron microscopy (SEM), optical microscopy and single-crystal x-ray diffraction (XRD) were applied to determine crystal grain sizes in the crystallised material, while energy dispersive x-ray spectroscopy (EDX) and inductively-coupled plasma optical emission spectroscopy (ICP-OES) were employed to measure precise elemental proportions. The combination of chemical analysis methods was hoped to reveal sources of systematic error and allow for a more accurate assessment of composition. Such a combination of techniques to measure crystal structure and composition simultaneously is difficult to achieve with thin films because while EDX is a frequently-applied non-destructive method of chemical analysis, ICP-OES

requires destruction of the film. Chemical analysis of thin films may also be complicated by the presence of substrate layers. For instance, samples grown on Mo and analysed with EDX may overestimate the quantity of sulphur as the S K (2.47 keV) and Mo L (2.52-2.87 keV)[1] emission lines may interfere. Additionally, direct comparison between separate thin film samples is difficult as small variations in homogeneity and processing conditions can introduce significant differences.

In contrast to the problems encountered with thin films, a batch of well-homogenised bulk material may, in principle, be separated into multiple samples, each with a different characterisation method applied, and the results applicable to the batch as a whole. In this work, such an approach is intended to allow direct relation of lattice parameters, Raman band positions and compositions as determined from comparison of weighed source elements, EDX and ICP-OES. Section 4.3 details powder XRD measurements and subsequent Rietveld refinement, carried out to provide a precise estimate for the crystal lattice parameters at each composition and determine the Vegard relation. Section 4.4 reports a set of Raman spectra measured from samples across the solid solution series $Cu_2ZnSnS_{4x}Se_{4(1-x)}$, which indicates linear two-mode Raman band evolution, as well as a shift in the ordering of the kesterite phase that is sensitive to the crystallisation process. Metallography and XRD suggested that large monograins were produced in the growth process, thereby allowing Raman measurements on individual crystals, eliminating the influence of grain boundaries. While both the Vegard relation and Raman mode evolution have been characterised previously (Section 2.3.5), with Raman measurements also taken of CZTSSe monograins, a relatively small number of data points were examined in those studies, and so the intention of this work was to provide a higher density of data points, to provide greater precision than in previous work[1].

[1] The experimental results presented in this chapter formed the basis of Article 1 detailed in the List of Publications at the end of this thesis.

4.2 Synthesis and Crystal Growth Outcomes

4.2.1 Direct Synthesis of Polycrystalline CZTSSe 'Feedstock' from the Elements

Samples of polycrystalline $Cu_2ZnSnS_{4x}Se_{4(1-x)}$ (CZTSSe) feedstock with compositions in the range $0 \leq x \leq 1$ were successfully synthesised directly from the elements (DSE) as described in Section 3.2.1 and confirmed by powder XRD and Raman spectroscopy as described later in this chapter. The synthesised material was black and powdery, matching the expected form of CZTSSe, with a homogenous appearance. SEM images were taken of these samples, with an image for the x = 0.5 sample being shown in fig. 4.1. This image shows sharp-edged, irregular shaped features ~ 1 μm in size, suggesting a polycrystalline structure, as opposed to an amorphous state, which would produce a relatively featureless image, perhaps with smooth undulations. This suggests that synthesis and crystallisation of CZTSSe both occurred, although other techniques, such as x-ray diffraction and Raman, were necessary to fully confirm crystallisation and phase purity.

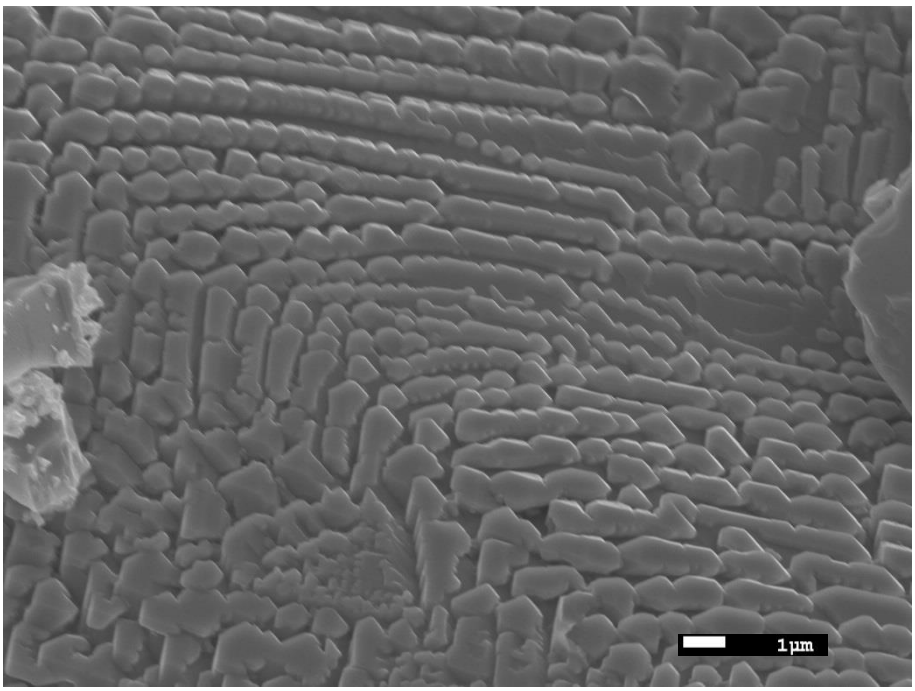

Fig. 4.1 SEM image of polycrystalline CZTSSe feedstock of composition (x = 0.5), with features consistent with crystal grains ~ 1 μm in size demonstrated.

EDX scans were carried out on the CZTSSe feedstock across the composition range $0 \leq x \leq 1$, with the number of measurements for each composition ranging from 2-12. These results are shown in Table 4.1, compared to weighed quantities, and are seen to be broadly consistent. It may therefore be inferred that the synthesis process preserved the weighed ratios of the elements in the compounds.

x-value	Cu At%	Zn At%	Sn At%	S At%	Se At%	N	Cu/ (Zn+Sn)	Cu/Zn	Cu/Sn	Zn/Sn
Feedstock - Weighed										
0	25 ± 0.01	12.5 ± 0.01	12.5 ± 0.01	0[2]	50 ± 0.01		1	2	2	1
0.1	25 ± 0.01	12.5 ± 0.01	12.5 ± 0.01	5 ± 0.01	45 ± 0.01		1	2	2	1
0.2	25 ± 0.01	12.5 ± 0.01	12.5 ± 0.01	10 ± 0.01	40 ± 0.01		1	2	2	1
0.3	25 ± 0.01	12.5 ± 0.01	12.5 ± 0.01	15 ± 0.01	35 ± 0.01		1	2	2	1
0.4	25 ± 0.01	12.5 ± 0.01	12.5 ± 0.01	20 ± 0.01	30 ± 0.01		1	2	2	1
0.5	25 ± 0.01	12.5 ± 0.01	12.5 ± 0.01	25 ± 0.01	25 ± 0.01		1	2	2	1
0.6	25 ± 0.01	12.5 ± 0.01	12.5 ± 0.01	30 ± 0.01	20 ± 0.01		1	2	2	1
0.7	25 ± 0.01	12.5 ± 0.01	12.5 ± 0.01	35 ± 0.01	15 ± 0.01		1	2	2	1
0.8	25 ± 0.01	12.5 ± 0.01	12.5 ± 0.01	40 ± 0.01	10 ± 0.01		1	2	2	1
1	25 ± 0.01	12.5 ± 0.01	12.5 ± 0.01	50 ± 0.01	0[2]		1	2	2	1
Feedstock -EDX										
0	30.10 ± 0.09	12.71 ± 0.16	11.30 ± 0.09	0[2]	45.92 ± 0.25	4	1.254	2.370	2.664	1.124
0.1	27.3 ± 1.0	12.6 ± 0.5	15.8 ± 1.4	7.3 ± 1.0	37.3 ± 1.0	9	0.961	2.167	1.728	0.797
0.3	27.3 ± 0.5	12.2 ± 0.5	12.0 ± 0.5	20.8 ± 2.0	27.8 ± 0.6	7	1.128	2.238	2.275	1.017
0.5	28.1 ± 0.6	11.6 ± 0.5	15.8 ± 1.7	26.0 ± 0.6	18.6 ± 0.5	12	1.026	2.422	1.778	0.734
0.6	28.32 ± 0.16	13.04 ± 0.25	14.0 ± 1.4	28.5 ± 0.4	16.11 ± 0.25	9	1.048	2.177	2.021	0.929
0.7	28.0 ± 1.4	14.29 ± 0.04	13.3 ± 1.2	32.8 ± 0.4	11 ± 4	2	1.015	1.959	2.105	1.074
0.9	23 ± 6	20 ± 6	9.93 ± 0.16	42.3 ± 1.4	3.73 ± 0.16	2	0.759	1.120	2.354	2.101
1	25.4 ± 1.7	17.4 ± 2.3	10.90 ± 0.02	46.31 ± 0.16	0[2]	2	0.898	1.460	2.330	1.596

Table 4.1 Measurements of the proportions of elements present in the $Cu_2ZnSnS_{4x}Se_{4-4x}$ feedstock, with compositions determined by weighing and EDX. The errors on EDX values are the variance, with up to 12 sites per sample being measured.

[2] Values of zero were given as the element was not added to the growth tube, so if detected in EDX spectra, a false positive was thought more likely than contamination of the growth tube, and the element was excluded from analysis.

4.2.2 Growth of Large-Grained Crystalline CZTSSe Solid Solutions from KCl/NaCl Molten Salts

In order to grow crystalline CZTSSe from solution in the NaCl/KCl mix, an estimate of the melting point for each composition of feedstock in the series was desired, in order to select an appropriate temperature range for solution growth. Differential scanning calorimetry (DSC) of feedstock samples were taken across the whole composition range with several of these scans shown in fig. 4.2. In all cases, an endotherm was observed in the vicinity of 800°C on the heating curve (heating at a rate of 5°C min^{-1}), in some cases consisting of a single clear peak, such as for CZTS (fig. 4.2f), and seeming to consist of multiple peaks in others, such as for $x = 0.4$ (fig. 4.2c).

What is interesting to note about these results is that, in the scan shown in 4.2f, a peak was not observed at the expected melting point of CZTS, at 986°C, (reported in the phase diagram by Nagaoka in [4]) despite this material having been confirmed as CZTS by Raman spectroscopy later in this work (Section 4.4.1). In addition, all the endotherms seen in fig. 4.2 coincided with a significant loss of mass, which continued as the temperatures increased (note the green TGA curve), suggesting that these are sublimation rather than melting transitions. If this is the case, these transitions are likely to involve the loss of sulphur and/or selenium, due to their high vapour pressures[1]. In all cases, the remaining mass after heating was ~ 50 % which, for the pure-selenide sample (fig. 4.2a) would be consistent with complete Se loss. However, this is not a convincing explanation for the pure-sulphide sample (fig. 4.2f) which lost ~ 45% of its mass despite consisting of only ~ 30% sulphur by weight, so the nature of these transitions is still not fully understood. Regardless of the exact process at work, this dramatic vaporisation may have occurred because a small quantity (~ 5 mg) of CZTSSe was analysed under vacuum in a comparatively large chamber, meaning that vaporised material did not increase the pressure sufficiently to prevent further sublimation, and a large enough quantity of material was lost to change the phase of the analysed material. CZTSSe was not expected to decompose at these temperatures, being significantly below the melting point, but it seems the most likely explanation, especially as endotherms matching the expected melting points do not appear at higher temperatures. Additionally, the endotherms that are seen during heating do not appear on the cooling curves, suggesting a change in chemical composition.

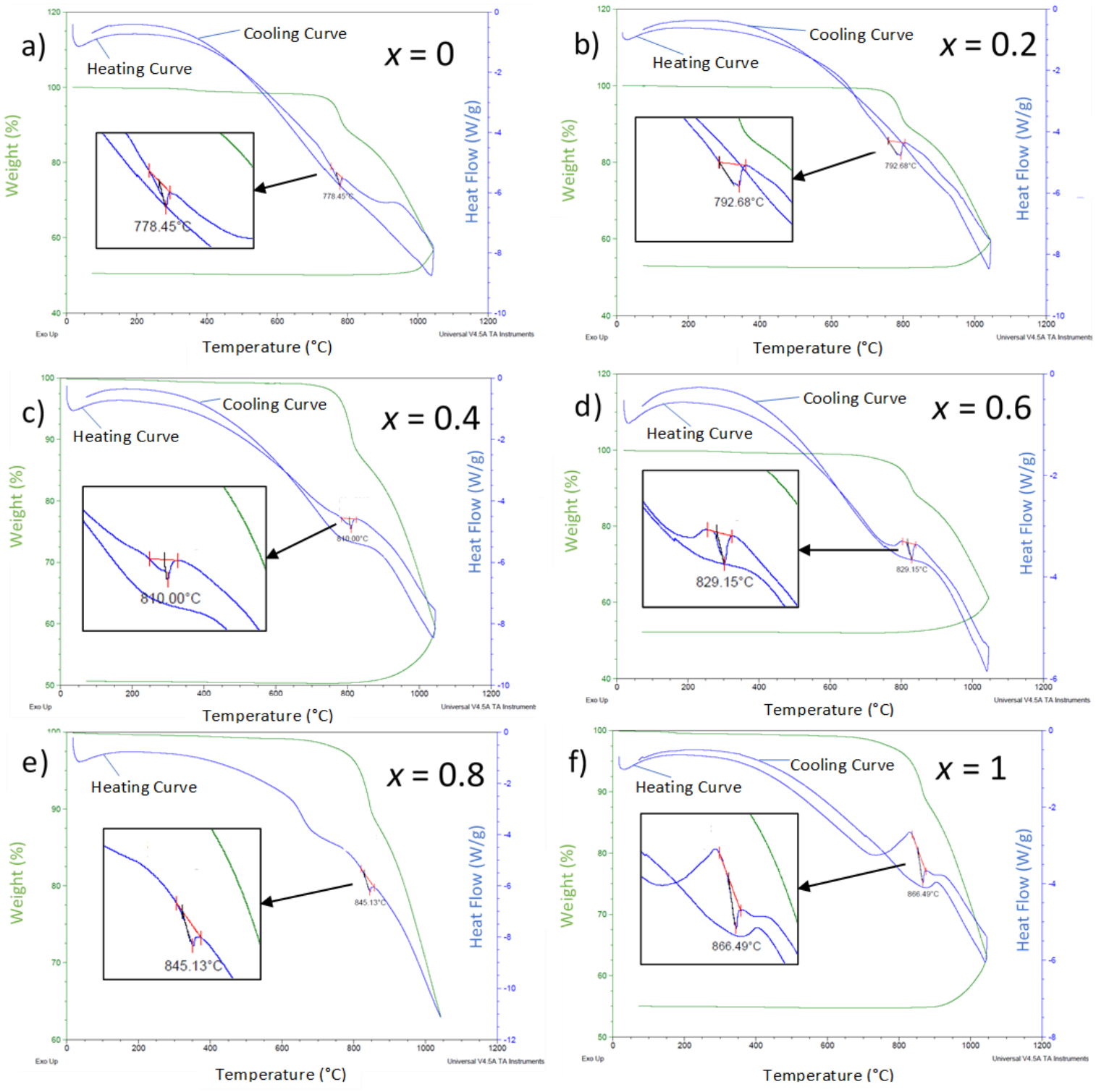

Fig. 4.2 DSC (right axis, blue) and TGA (left axis, green) plots for a series of CZTSSe samples in the range $0 \leq x \leq 1$, with x equal to a) 0, b) 0.2, c) 0.4, d) 0.6, e) 0.8, f) 1, with endotherms highlighted.

Additionally, while the endotherm peaks for CZTSe and CZTS (figs. 4.2a and f) looked to consist of a single peaks, some intermediate compositions such as the $x = 0.2$ and $x = 0.4$ samples (figs. 4.2b and c) exhibited multiple-component peaks, which may reflect both S and Se being lost, rather than only one of these elements for the series end members.

Despite this, one important thing to note about of these curves is that prior to the mass loss during heating, additional endotherm peaks corresponding to the melting points of sulphur, selenium, zinc or tin (115, 685, 420 and 232°C respectively[1]) were not observed on the heating curve, suggesting that in their initial form, the directly synthesised CZTSSe samples were effectively homogenised, with no significant quantities of source elements remaining.

Fig. 4.3 shows the position of the observed sublimation endotherms (position taken from the higher-temperature, deeper minimum) plotted against the weighed *x*-values for the feedstock. These results indicate a linear relationship between weighed *x*-value and the endotherm temperature, across the whole range, with fitting estimating a trend of $T_{endotherm}(°C) = 87.9x + 775.6$. As the exact nature of the sublimation transition is not known, the reason for linear behaviour is also unknown, but it likely relates to the fact that CZTS has a higher reported melting point (986°C) than CZTSe (801°C)[4]. This may have caused the sulphur-rich samples to decompose at higher temperatures, despite S having a higher vapour pressure than Se. If we can assume therefore that the temperatures of these decompositions correlate with the melting point, these results would provide (indirect) evidence that the melting point of CZTSSe follows a linear trend with *x*.

This investigation did not succeed in identifying the melting points of the feedstock series, but nonetheless influenced the choice of temperatures used for the growth of crystallised CZTSSe in NaCl/KCl, where the top temperature followed a linear rule with *x*-value from 785°C ($x = 0$) to 875°C ($x = 1$). This choice of temperature was also influenced by literature reports using the same solution (see Section 3.2.2). Evidence for complete melting at these temperatures across the whole series was provided by the results of these crystallisation runs (see below).

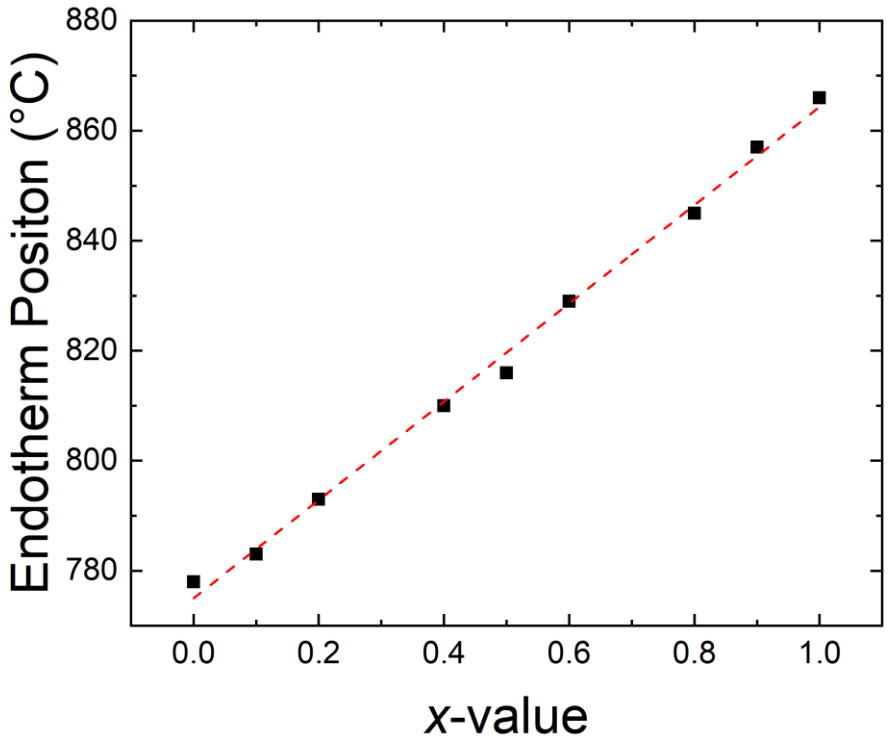

Fig. 4.3 Positions of endotherms associated with decomposition of CZTSSe ($0 \leq x \leq 1$) measured by DSC. A linear relationship between endotherm position and weighed x - value is observed.

Crystallisation of CZTSSe from the solution formed of CZTSSe feedstock and the NaCl/KCl salt mix was successful for 10 compositions across the range $0 \leq x \leq 1$. Evidence for this was provided through characterisation with EDX, XRD, Raman and ICP-OES, which were all consistent with the formation of CZTSSe solid solutions, with XRD and Raman demonstrating the samples were crystallised. This re-crystallisation offers evidence that full melting of the samples occurred at the top temperatures used (see Section 3.2.2). XRD results are covered in Section 4.3, with Raman covered in Section 4.4. The results of the analysis with EDX and ICP-OES techniques are as follows:

EDX measurements were taken to determine the composition of the crystallised samples for each x-value at 3-11 sites, with the results shown in Table 4.2. These results indicate better agreement with weighed proportions than were observed for the CZTSSe feedstock. The increased match most likely results from the long homogenisation time of the liquid solution phase followed by slow

cooling at 0.4°C hr^{-1}. In contrast, the feedstock synthesis relied upon vapour-solid and solid-solid diffusion for homogenisation, with a relatively rapid cooling rate of 30°C hr^{-1}. Additionally, the EDX measurements of the crystallised solid solutions were taken from flat, polished faces while those for the feedstock were taken from rough surfaces which could lead to errors. This provides additional evidence that both the synthesis and growth processes preserved the weighed ratios of elements. ICP-OES measurements were also carried out on the crystallised series, with results shown in Table 4.2.

x-value	Cu At%	Zn At%	Sn At%	S At%	Se At%	N	Cu/ (Zn+Sn)	Cu/Zn	Cu/Sn	Zn/Sn
Crystallised-EDX										
0	25.48 ± 0.05	12.11 ± 0.06	13.00 ± 0.01	0[3]	49.41 ± 0.08	9	1.014	2.104	1.960	0.931
0.3	24.72 ± 0.16	13.65 ± 0.04	12.62 ± 0.03	15.60 ± 0.08	33.45 ± 0.08	6	0.940	1.809	1.957	1.081
0.5	24.97 ± 0.04	11.89 ± 0.03	12.74 ± 0.02	26.96 ± 0.05	23.43 ± 0.15	7	1.013	2.100	1.959	0.933
0.6	27.7 ± 1.2	13.8 ± 0.6	12.4 ± 0.8	28.6 ± 0.4	17.5 ± 0.8	3	1.057	2.007	2.233	1.112
0.7	24.82 ± 0.27	12.00 ± 0.04	13.17 ± 0.09	37.02 ± 0.04	12.98 ± 0.06	8	0.986	2.068	1.884	0.911
1	24.58 ± 0.02	11.61 ± 0.03	12.75 ± 0.02	51.06 ± 0.07	0[3]	11	1.009	2.117	1.927	0.910
Crystallised-ICP-OES										
0	27.11 ± 0.03	11.44 ± 0.03	12.480 ± 0.007	0[3]	49.96 ± 0.16	3	1.132	2.368	2.171	0.917
0.1	27.54 ± 0.05	12.278 ± 0.005	12.318 ± 0.003	4.808 ± 0.007	43.05 ± 0.05	3	1.119	2.243	2.236	0.996
0.2	26.653 ± 0.011	13.344 ± 0.012	12.06 ± 0.021	9.87 ± 0.07	38.1 ± 0.1	3	1.049	1.997	2.210	1.106
0.3	27.24 ± 0.06	12.961 ± 0.006	12.120 ± 0.005	14.78 ± 0.03	32.911 ± 0.022	3	1.085	2.101	2.247	1.069
0.4	27.294 ± 0.016	12.987 ± 0.016	12.139 ± 0.007	20.388 ± 0.014	27.202 ± 0.014	3	1.085	2.100	2.247	1.069
0.5	27.750 ± 0.016	12.452 ± 0.009	12.186 ± 0.005	24.50 ± 0.05	23.11 ± 0.04	3	1.126	2.228	2.277	1.021
0.6	27.579 ± 0.009	12.3975 ± 0.0023	12.137 ± 0.055	29.62 ± 0.14	18.27 ± 0.06	3	1.124	2.224	2.272	1.021
0.7	28.1713 ± 0.0012	12.28 ± 0.04	12.290 ± 0.010	33.45 ± 0.16	13.7 ± 0.01	3	1.146	2.294	2.292	0.999
0.8	27.883 ± 0.007	12.413 ± 0.010	12.253 ± 0.009	38.6 ± 0.4	8.857 ± 0.021	3	1.130	2.246	2.276	1.013
1	26.74 ± 0.04	12.66 ± 0.04	12.138 ± 0.009	48.462 ± 0.017	0[3]	3	1.07	2.111	2.202	1.043

Table 4.2 Measurements of the proportions of elements present in the $Cu_2ZnSnS_{4x}Se_{4-4x}$ solid solutions crystallised from the NaCl/KCl mix, with compositions determined by weighing, by EDX and ICP-OES. The errors are variance with up to 11 sites per sample being measured by EDX and the ICP-OES compositions being the average of measurements taken using three different wavelengths.

[3] Values of zero were given as the element was not added to the growth tube, so if detected in EDX spectra, a false positive was thought more likely than contamination of the growth tube, and so the element was excluded from analysis.

The results of the EDX and ICP-OES measurements of the CZTSSe solid solutions are compared to the weighed quantities of the elements in fig. 4.4 for the anions Se (a) and S (b), where good agreement is found for both methods with the weighed quantities. The values of Se and S concentration from EDX and ICP-OES were used to calculate the *x* – values of the series, which also demonstrated good agreement with the weighed quantities (fig. 4.4c). The strong agreement between analysis methods supports these conclusions, suggesting that both methods provided accurate values, while indicating that the weighed quantities were reliably carried through into the final compositions via the direct synthesis from elements and crystal growth processes.

ICP-OES and EDX results are presented in fig. 4.5 for the cation (metal) constituents of the crystallised CZTSSe series (a-c), as well as the total quantities of anion elements Se and S (c). Values are presented for copper (a), zinc (b), tin (c) and anions [Se + S] (d). Given that, within experimental uncertainty, the EDX and ICP-OES support the interpretation that the weighed concentrations are carried through to the crystallised samples, the weighed values of *x* were used in the plot. These plots demonstrate consistency of all measured elements with the weighed quantities, except that the ICP-OES measurements indicate a copper excess of ~ 2 at% (fig. 4.5a), which accounts for the overall anion deficiency (fig. 4.5d). This is in disagreement with the values measured with EDX and represents a deviation from the stoichiometric proportions observed at the weighing stage.

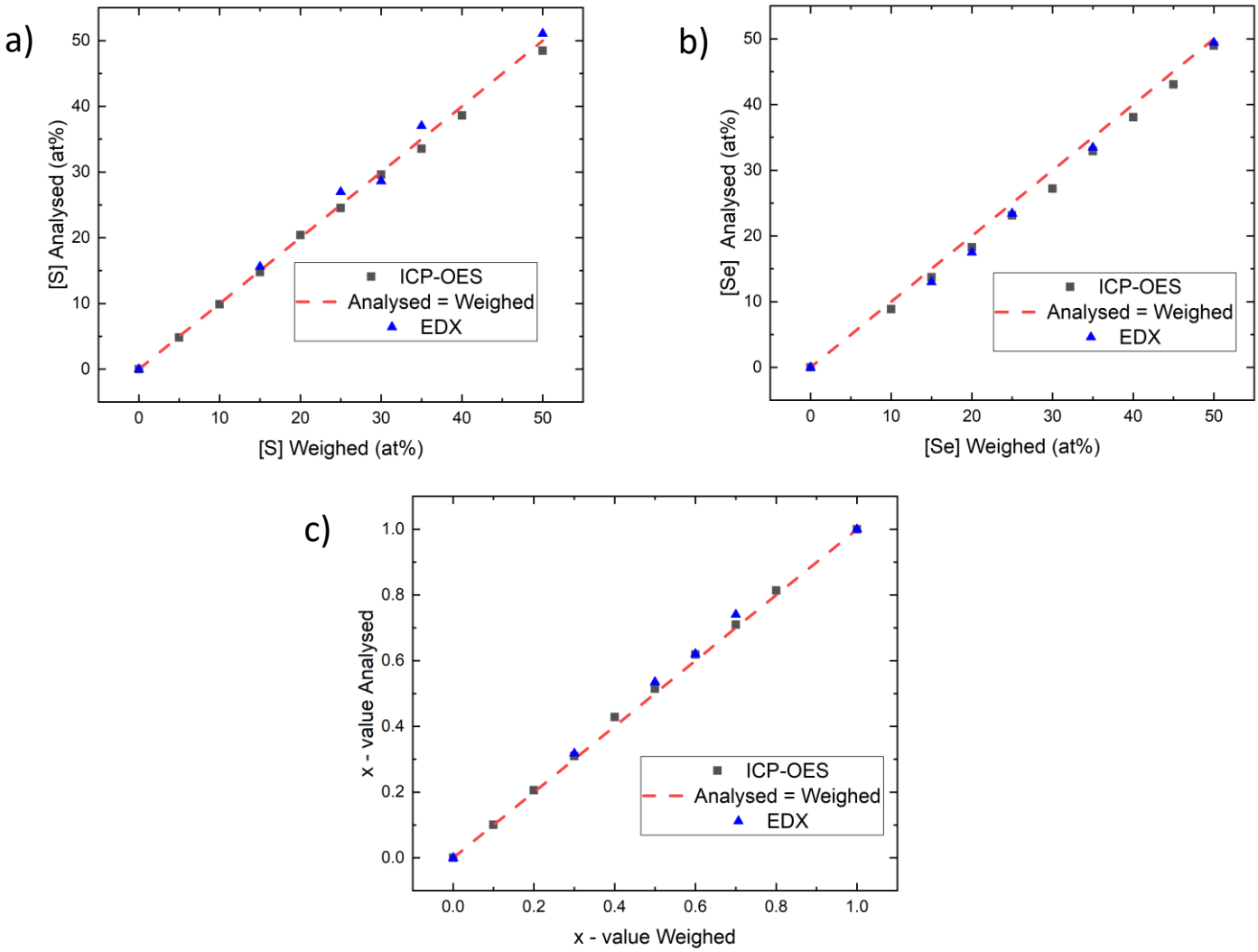

Fig. 4.4 Chemical analysis of anion (Se and S) concentrations in CZTSSe crystallised solid solutions, with the results of EDX and ICP-OES compared to the weighed compositions of the samples, for a) selenium, b) sulphur and c) *x*-value. Weighed compositions were found to be consistent with both EDX and ICP-OES in all cases, with the dashed lines having a slope of 1.

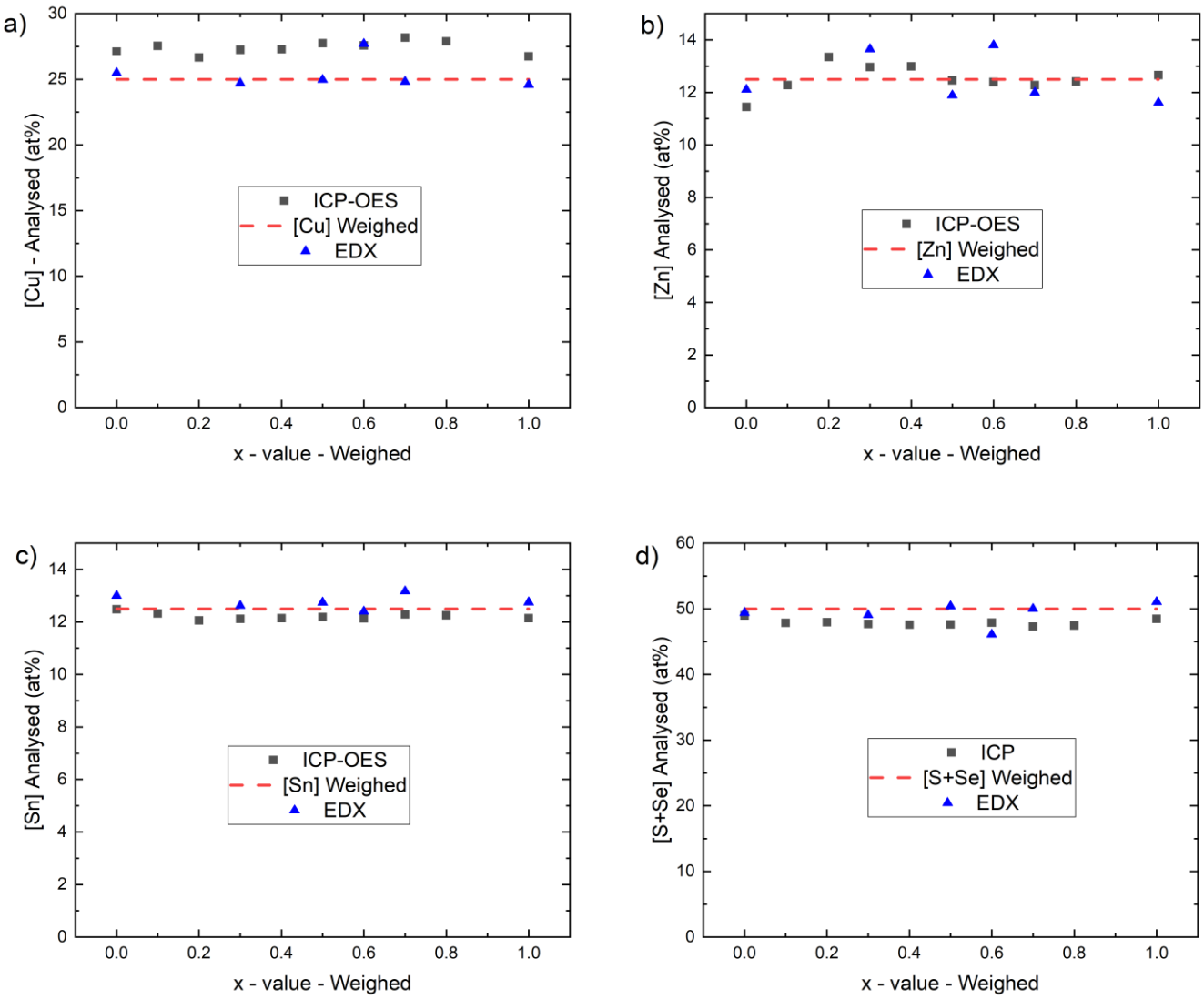

Fig. 4.5 Chemical analysis of cation (metals) and anion (Se and S) concentrations in crystalline CZTSSe solid solutions, with the results of EDX and ICP-OES compared to the weighed compositions, as shown by the dashed lines. The *x*-values were based on weighing prior to synthesis. Results are shown for a) copper, b) zinc, c) tin and d) total content of anions Se and S.

Given that the EDX and ICP-OES results agree with the weighed quantities in all other respects, the apparent copper excess is taken to be a systematic error in the ICP-OES measurement, with the weighed Cu concentration considered more reliable. A systematic error in Cu concentration

measured by ICP-OES would most likely result from uncertainties in the fitting of the Cu calibration curve. Based on this series of measurements, the weighed quantities of elements before synthesis provide a reliable estimate for elemental concentrations in the crystallised samples, and have the highest precision, so are used in subsequent analysis.

Two crystal types were observed in the ingots of CZTSSe solid solutions crystallised in the NaCl/KCl mix: a hard, densely packed shell deposited on the surface of the growth tube; and loosely packed, larger monograins inside the shell, grown within the solution volume. The hard shell was ~ 0.5 mm thick and had a smooth, black surface, with an optical microscope image of a mechanically polished (Section 3.3.1) section treated with Br-MeOH shown in fig 4.6a, for the sample where x = 0.3. The Br-MeOH treatment revealed dark grain boundaries, consistent with crystal grains ~ 100 μm in size and providing evidence that this treatment worked as a chemical etch. The grain sizes for all solid solutions in the series, determined as described in Section 3.3.2, are plotted against x - value in fig. 4.6c, demonstrating that there were variations in the average size of the crystal grains with x-value, ranging from 100-200 μm., This scatter was slightly larger than the standard deviation for a given sample (represented by the error bars), but there were no clear trends relating grain sizes to x-value, suggesting crystallisation occurred similarly across the series. These crystal grains likely formed by heterogenous nucleation of CZTSSe on the surface of the growth tube, resulting in a high density of grains, as a given grain's growth terminated as soon as it encountered another.

Apart from the hard shell formed of dense crystal grains on the walls of the growth tubes, the CZTSSe solid solutions crystallised in the NaCl/KCl mix also consisted of an assembly of crystal monograins, nucleated within the solution volume, rather than seeded by the tube walls. The polished surfaces of several of these monograins in the case of CZTS (x = 1) are imaged with optical microscopy in fig. 4.6d.

These monograins were larger than the dense grains found in sections of the hard shell, being up to 700 μm in size. The size difference was most likely because grains in the melt volume require homogenous nucleation sites, of which a lower density would be expected than the heterogenous nucleation sites on the tube walls, so grains within the melt volume were able to grow to a larger size

before encountering another grain. Straight boundaries on the surface of the monograins separating bright and dark regions of the image are suggestive of twin defects.

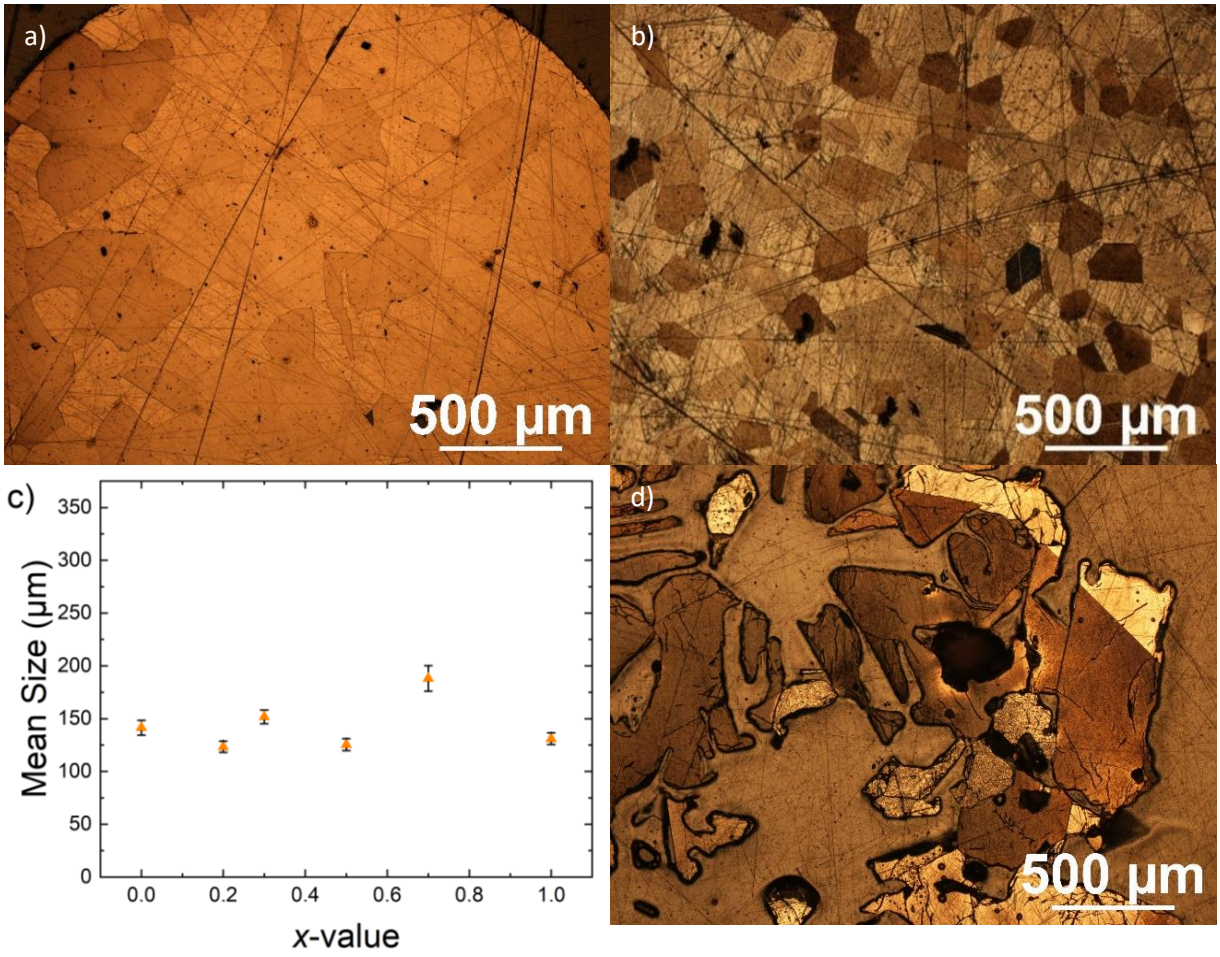

Fig. 4.6 a) Optical microscope image of a polished section of the hard shell of the CZTSSe ingot crystallised from solution in the NaCl/KCl mix, where x = 0.3. b) Optical microscope image of polished surface of compact crystalline CZTS (x = 1) section grown on a quartz seed plate. c) Graph of grain size vs composition. d) Polished surface of crystal monograins of CZTS (x = 1) formed within the solution volume, at < 700 µm in size.

Both these large monograins and the densely-packed grains comprising the hard shell of the samples were significantly larger than the crystal grains observed in the feedstock (fig. 4.1), at ~ 1 µm. This demonstrates that the crystallisation process from solution in the NaCl/KCl mix was

effective in producing larger crystals compared to the direct synthesis method. This is to be expected, given the slow cooling rates of 0.4°C hr^{-1} (Section 3.2.2) and the long homogenisation times.

XRD was carried out on the polished surface of the monograin samples, with the results shown in fig. 4.7a (middle and bottom). These scans indicate only one prominent diffraction peak in each case, the 112 peak for the CZTS (x = 1) sample, and the 220 peak for the CZTSSe sample where x = 0.6. This offers evidence that the individual monograins were indeed single crystals, although as mentioned in Section 3.3.3, XRD measurements can only confirm the presence of a single plane, and are insensitive to a columnar growth situation with strong preferred orientation, where grains may share a plane, but are rotated relative to one another. The etching may not pick up on this if adjacent grains share a planar orientation, so it remains a possibility. Additionally, other crystal orientations may be present, but will not show up in the XRD scan if the planes are not lined up with the substrate holder. Full confirmation would require an imaging method such as Laue diffraction or EBSD.

If it can be assumed that the grains revealed by the etch were single crystals of CZTSSe, they were large enough to characterise with Raman spectroscopy, as the laser spot size in the Renishaw instrument is ~ 1 - 2 μm (Section 3.3.5). Results of powder XRD and Raman measurements of the crystallised solid solution series are presented in Sections 4.3 and 4.4.

4.2.3 Growth of Thick-Film Polycrystalline CZTSSe Using Quartz Seed Plates

Since crystallisation from molten salts could be seeded by the quartz surface of the tube, a flat seed plate 10 x 10 mm in size was also placed within the tube for some growth runs to encourage this form of nucleation. The result was a deposit of CZTSSe ~ 0.5 mm thick and 10 x 10 mm in size, with the same appearance as the hard black shell deposited on the walls of the growth tube. The size and flatness of these sections meant that they provided a practical surface for optical characterisation techniques such as Raman spectroscopy. An optical microscope image of the mechanically polished surface of the CZTS sample crystallised this way, etched with the Br-MeOH treatment, is shown in fig. 4.6b, where etching revealed crystal grains ~ 100 μm in size. This is consistent with the growth results for the hard shell (fig. 4.6a) indicating that the same form of growth occurred.

4.2.4 Directional Gradient Freeze Growth of CZTS Crystals from Sn

The growth of CZTS crystals from a solution of CZTS (x = 1) and Sn via the directional freezing method produced an ingot around 15 mm long. Cutting and polishing produced the surface shown in fig. 4.7b, where orientation-selective etching by the Br-MeOH treatment revealed columnar grains 10 mm long and 2 mm wide, oriented along the growth axis. Fig, 4.7a (top) shows XRD measurements taken for single grains on the polished surface in the same way as for the monograin samples grown in the NaCl/KCl mix (Section 4.2.2). The 415 diffraction peak is the only significant peak observed for the Sn-grown CZTS, offering strong evidence that the grains shown fig. 4.7b (outlined in red) are single crystal grains.

Despite large crystal grains being evidenced, single crystals were not ultimately grown through this method, greatly reducing the possibility of examining the electrical and point defect properties of CZTSSe, one of the original aims of this work. As a result, focus was shifted into investigating the structural properties of the CZTSe-CZTS series using the sample series grown in the NaCl/KCl mix, as described in the following sections.

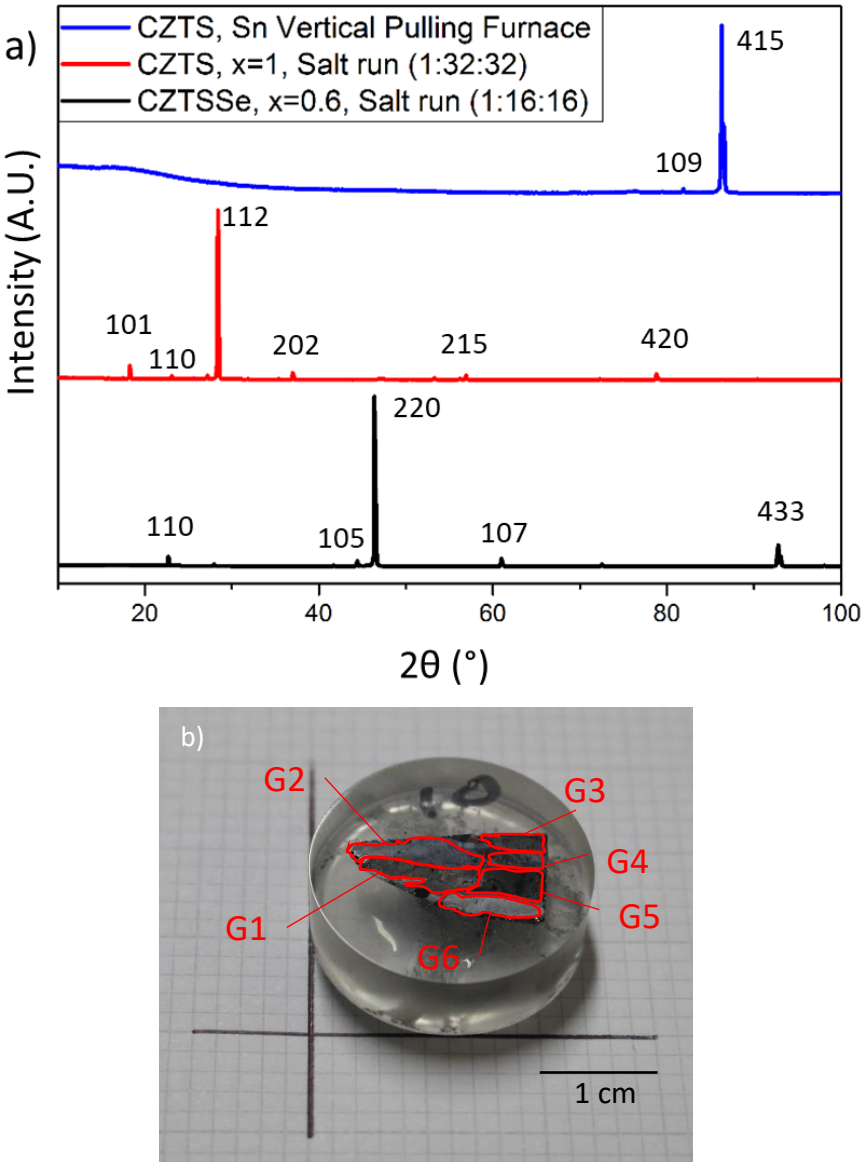

Fig. 4.7 a) XRD measurements (linear y-axis) taken from the polished surface of: i) crystallised CZTSSe solid solution grown with a ratio CZTSSe:NaCl:KCl of 1:16:16, where x = 0.6 (bottom); ii) crystallised CZTS (x = 1) grown by the same method with a ratio of CZTSSe:NaCl:KCl of 1:32:32 (middle); iii) Crystalline CZTS (x = 1) grown by the directional gradient freeze method in solution with Sn. Observed diffraction peaks are assigned on the plot. b) Photograph of the cut, polished and etched surface of the same CZTS polycrystal, with grain boundaries outlined in red.

4.3 Powder XRD Investigation

This section reports determination of the Vegard relations for CZTSSe for both the feedstock material and that crystallised from molten salts.

4.3.1 Diffraction Patterns

θ-2θ powder XRD measurements were taken for powderised sections of the CZTSSe feedstock directly synthesised from the elements and for the CZTSSe solid solutions crystallised in NaCl/KCl mix, as shown in figs. 4.8 and 4.9 respectively. The strong, sharp peaks observed in all scans offer further confirmation of the successful crystallisation of CZTSe, CZTS and intermediate solid solutions by both methods. The peaks at 27.14°, 45.05° and 53.44° correspond to the 112, 220 and 332 diffraction peaks for CZTSe, while these shift to 28.46°, 47.36° and 56.15° for CZTS.
It should be noted that ZnS/Se may also produce these peaks (see Section 2.3.3)[2]. However, the Raman study of these samples (Section 4.4) indicates that ZnS/Se is not present in significant quantities, meaning that these peaks may be attributed to CZTS/Se. For the solid solutions as a whole, the XRD scans exhibited a linear shift in peak positions from low to high with increasing *x*, suggesting that the lattice parameter shifted similarly from large to smaller values. This provides confirmation that the intermediate compositions are, in fact, solid solutions, rather than phase-separated CZTSe and CZTS. This behaviour is observed for both the feedstock series and the CZTSSe solid solutions crystallised in NaCl/KCl. As is usual for conventional XRD in the study of CZTSSe, these measurements were unable to assess the relative ordering of Cu and Zn atoms in the two series (see Section 2.3.3). However, it has been suggested[3] that order and disorder have an impact on the value of the unit cell volume as a result of shifts in the *c* parameter.

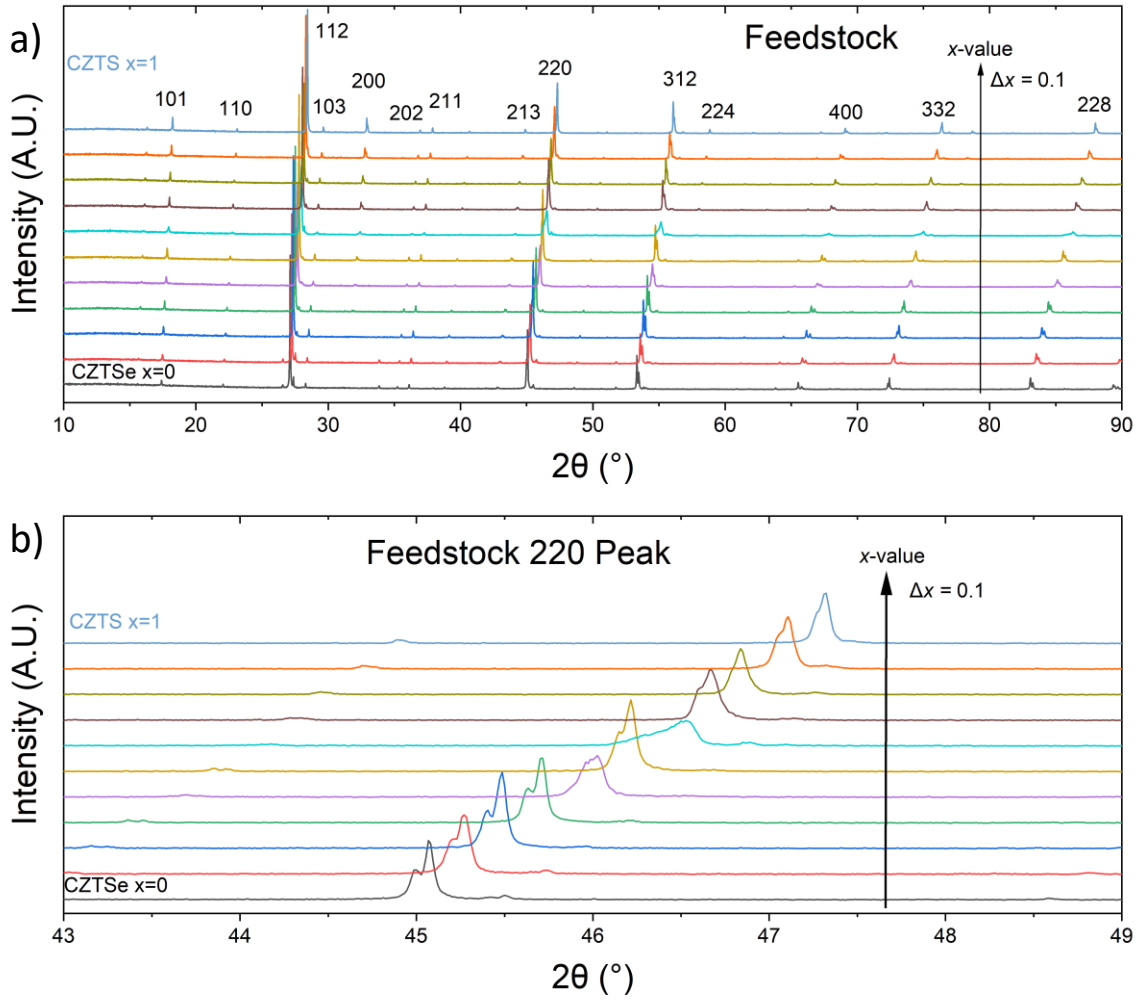

Fig. 4.8 XRD θ-2θ scans (linear y-axis) for a) CZTSSe feedstock for the composition range $0 \leq x \leq 1$ in increments of 0.1 (weighed x - values) with all peaks indexed. b) Same sample set, showing the shift in the 220 peak with x to higher angles, a doublet peak as both the Cu K-α_1 and K-α_2 lines were used.

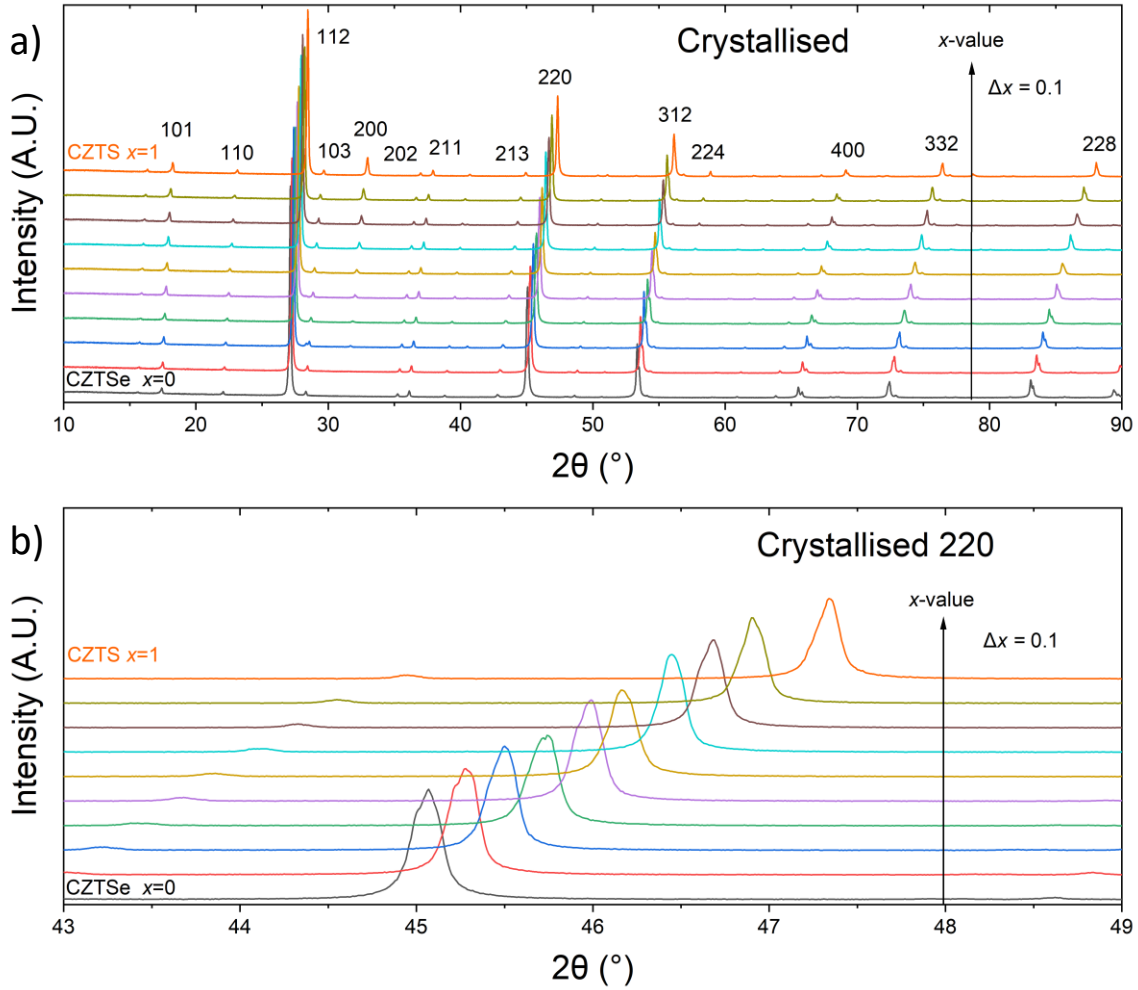

Fig. 4.9 XRD θ-2θ scans (linear y-axis) of: a) CZTSSe solid solutions crystallised in NaCl/KCl mix. b) Same sample set, showing the shift in the 220 peak, a singlet peak as the monochromated Cu *K*- α_1 line was used. a) shows prominent 112, 220 and 332 peaks, with all peaks assigned. Peaks shift to higher angles in all cases with increasing *x*.

4.3.2 Rietveld Refinement

Example plots of the Rietveld refinement of the patterns for crystallised CZTSSe (same patterns as shown in fig. 4.9) are shown in fig. 4.10 for *x* – values of a) 0, b) 0.4, c) 0.6 and d) 1. The small residuals (blue line) shown in fig. 4.10 provide indication of a good fit between the model and experiment.

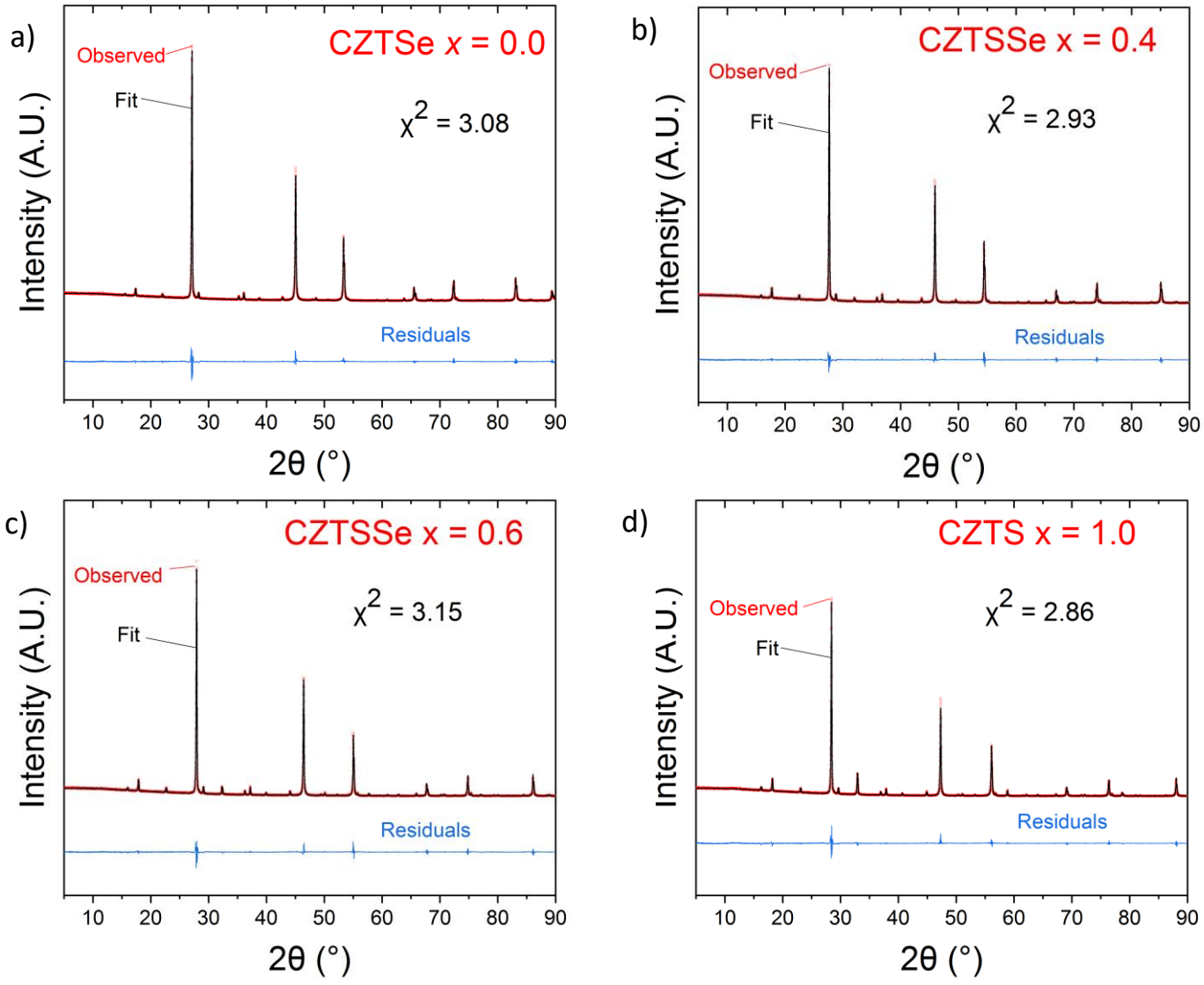

Fig. 4.10 Results of the Rietveld refinement (linear y-axis) carried out on the powder XRD patterns for the CZTSSe solid solutions crystallised in NaCl/KCl mix, with *x* - values of a) 0, b) 0.4, c) 0.6 and d) 1. The observed patterns (red circles), the fit (black line), and the residuals (blue line) are shown.

Table 4.3 shows that values of χ^2 ranging from 2 to 4 were found for the Rietveld refinement across the composition range of crystallised CZTSSe, demonstrating a good fit between the model and the experiment (see Section 3.3.3), while small values of the other conventional Rietveld parameters (not shown) were found.

4.3.3 Lattice Parameters

Table 4.3 presents the structural parameters determined by the Rietveld refinement process for the full composition series of the crystallised CZTSSe solid solutions: lattice parameters, atomic position and the overall isotropic thermal parameter B_{Iso}. B_{Iso} is a quantification of the average volume occupied by the atoms in the unit cell due to thermal motion, as measurements were taken at room temperature (the value of B_{Iso} , in units of $Å^2$, corresponds to the area of the circular cross-section of the sphere occupied by the atom), which causes broadening of the diffraction peaks.

Table 4.4 presents the lattice parameters determined in this work from Rietveld refinement for the feedstock and crystallised sample series, for the series end members CZTSe (x = 0) and CZTS (x = 1). These values are presented with the cation (metals) ratios based on weighing prior to synthesis and compared to lattice parameter values taken from the literature on CZTSe and CZTS.

***x* – value (Weighed):**	**0**	**0.1**	**0.2**	**0.3**	**0.4**
Lattice parameters (Å)					
a	5.69258(3)	5.67077(3)	5.64406(3)	5.61520(3)	5.58530(3)
c	11.34351(8)	11.29954(8)	11.24646(8)	11.1876(8)	11.13394(7)
Anion positions					
x	0.765(5)	0.7574(11)	0.7544(7)	0.7567(9)	0.7505(6)
y	0.755(4)	0.7645(8)	0.7677(5)	0.7669(7)	0.7710(4)
z	0.87047(16)	0.87033(17)	0.87049(18)	0.87003(18)	0.86964(19)
B_{Iso} (Å^2)	0.953(19)	0.941(21)	1.184(22)	0.996(21)	0.949(21)
χ^2	3.08	3.47	3.36	2.74	2.93
***x* – value (Weighed):**	**0.5**	**0.6**	**0.7**	**0.8**	**1**
Lattice parameters (Å)					
a	5.56237(4)	5.53041(3)	5.50522(3)	5.47855(3)	5.43170(3)
c	11.09142(9)	11.03185(8)	10.98109(7)	10.92823(7)	10.83919(8)
Anion positions					
x	0.7527(7)	0.7518(7)	0.7503(7)	0.75040(8)	0.7674(15)
y	0.7701(5)	0.7711(5)	0.7735(5)	0.7727(6)	0.7551(17)
z	0.86993(21)	0.86949(22)	0.86992(24)	0.86973(28)	0.8701(3)
B_{Iso} (Å^2)	1.298(21)	1.011(22)	1.053(22)	0.677(23)	0.819(22)
χ^2	2.64	3.15	2.66	2.96	2.86

Table 4.3 Crystal structure parameters for the CZTSSe solid solution series, determined from the Rietveld refinement process: lattice parameter; positions of the anions (Se and S); and the overall isotropic thermal parameter B_{Iso}. The '*x* - value' in the column headers refers to composition based on

weighed quantities, while the values of '*x*' presented under 'Anion positions' refer to the position of the anions in space. χ^2 values indicate the goodness-of-fit.

Sample Set		**Composition**	
		CZTSe (*x* = 0)	**CZTS (*x* = 1)**
This work: feedstock	*a* / Å	5.69193(5)	5.43296(8)
	c / Å	11.34416(15)	10.84387(22)
	Cell volume / Å^3	367.529(7)	320.079(9)
This work: material crystallised in NaCl/KCl mix	*a* / Å	5.69258(3)	5.43170(3)
	c / Å	11.34351(8)	10.83919(8)
	Cell volume / Å^3	367.591(7)	319.792(6)
	Cu/(Zn+Sn)	1[4]	1[4]
	Zn/Sn	1[4]	1[4]
Adachi[4] – **compiled data**	*a* / Å	5.688	5.430
	c / Å	11.341	10.845
	Cell volume / Å^3	366.92	319.76
Sample #3 – Lafond[5]	*a* / Å		5.43006
	c / Å		10.8222
	Cell volume / Å^3		319.098
	Cu/(Zn+Sn)		0.79
	Zn/Sn		1.19
Sample #4 – Lafond[5]	*a* / Å		**5.43097**
	c / Å		10.8415
	Cell volume / Å^3		**319.777**
	Cu/(Zn+Sn)		0.95
	Zn/Sn		1.08
Sample #6 – Lafond[5]	*a* / Å		5.42936
	c / Å		**10.8391**
	Cell volume / Å^3		319.53
	Cu/(Zn+Sn)		1.14
	Zn/Sn		0.8

Table 4.4 Crystal unit cell lattice parameters and cell volumes for the CZTSe and CZTS samples directly synthesised from the elements and grown from solution in a NaCl/KCl melt. Averaged

[4] Ratio based upon weighed proportions of elements before synthesis, where precision is < 0.001 at%

experimental values reported by Adachi in [4], as well as to the values reported by Lafond *et al.*[5], which investigated cation composition, are included. Lattice parameter values from the latter study which most closely match our values are shown in bold.

These results show good agreement with the values for CZTSe and CZTS averaged by Adachi in [4] from several sources of published data. The feedstock and crystallised series from this work exhibit a small difference in cell volumes, with the volume for the CZTS feedstock sample larger, at 320.08 $Å^3$, than for the crystallised CZTS, at 319.79 $Å^3$. Based on work reported in Choubrac *et al.*[3] this would suggest that the crystallised CZTS sample was more highly-ordered than the CZTS feedstock, as that work reported cell volumes of 319.80 $Å^3$ for an ordered sample, and 320.10 $Å^3$ for a disordered sample. Choubrac *et al.* argues that the observed change in cell volume resulted solely from changes to the *c* parameter, but this was not found to be the case for the CZTS samples in this work, where the *c* parameter shifted by ~ 0.04% but the *a* parameter also shifted by ~ 0.02%. The difference was in spite of the fact that the crystallised samples in this work were demonstrated to have compositions in line with the stoichiometric proportions engineered at the weighing stage (fig. 4.5a), matching closely with the composition of samples reported on in Choubrac *et al.*[3]. The difference may therefore result from the different processing methods used. In our work, samples were crystallised between 820°C and 875°C then cooled from 820°C, while the samples in Choubrac *et al.* were annealed at 750°C before cooling.

There is no comparable change in the unit cell volumes found for the CZTSe samples, with a volume of 367.53 $Å^3$ for the CZTSe feedstock and 367.59 $Å^3$ for the crystallised CZTSe. The ordering effect within CZTS and CZTSe may be characterised with Raman spectroscopy (Section 4.4) providing a more direct assessment of ordering in these samples.

The lattice parameters in CZTSSe are sensitive to cation ratios, as well as anion ratios, as is reported in the work of Lafond *et al.*[5]. Lattice parameters for several samples of CZTS from that work, where close matches were found, are compared to our values in Table 4.4, with the cation ratios in each case also presented. For the case where the *a* values match most closely (Lafond sample #4), the metals stoichiometry is very similar to our sample, however the closest match for *c* is found with a

sample (Lafond sample #6) with significantly different stoichiometry, demonstrating that the relationship between lattice parameters and metals stoichiometry is complicated, with no simple trends forthcoming based on these datasets.

Fig. 4.11 shows the lattice parameter values for the whole CZTSSe compositions series ($0 \leq x \leq 1$), for directly synthesised feedstock (fig. 4.11a-b) and CZTSSe solid solutions crystallised in NaCl/KCl mix (fig. 4.11c-d). All datasets demonstrated linear Vegard relationships, with the series fitted linearly to produce trends of: a (Å) = -0.264(7)x + 5.691(4) and c (Å) = -0.504(6)x + 11.343(4) for the feedstock. Meanwhile, a trend where: a (Å) = -0.268(3)x + 5.6949(17) and c (Å) = -0.516(6)x + 11.345(3) was found for the crystallised series. Uncertainty values were determined based on the goodness of the linear fits, with the no. of significant figures in the coefficients reflecting this. These results may be compared to the trends identified by Nagaoka *et al.*[6] as a (Å) = -0.26x + 5.71 and c (Å) = -0.53x + 11.45), while He *et al.*[7] reported trends of a (Å) = -0.28x + 5.68 and c (Å) = -0.55x + 11.38. These trends are compared in fig. 4.12, where the values of a (fig. 4.12a) and c (fig. 4.12b) parameters showed close agreement between the feedstock and crystallised sample sets in this work. However, the samples reported in Nagaoka *et al.*[6] demonstrated lattice parameters of systematically higher values than those reported in this work for both a and c, with shifts across the whole composition series of approximately + 0.02 Å in the a-value and + 0.01 Å in the c-value. In comparison, the values reported by He *et al.*[7] were smaller for a, with a shift of -0.01 Å at x = 0 and -0.03 Å at x = 1, but larger for c, with a shift of +0.04 Å at x = 0, converging on our value at x = 1. It should be noted that the series for a in this work was situated directly in the middle of the two series from the literature, placing it firmly within the range of flexibility that may be expected based on prior work.

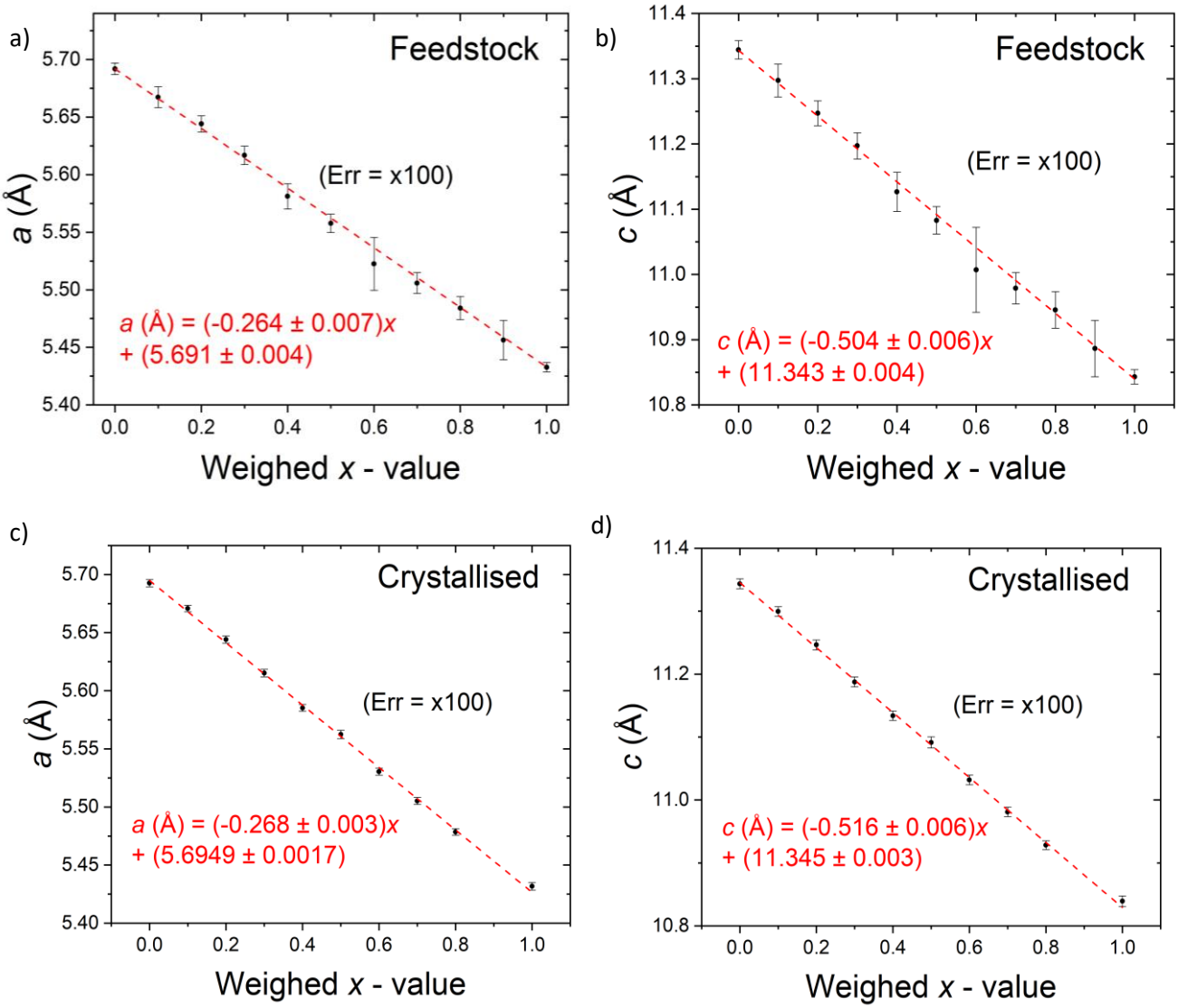

Fig. 4.11 Plots showing the lattice parameter values for the whole CZTSSe compositions series ($0 \leq x \leq 1$), with results shown for directly-synthesised feedstock for the a) *a* parameter and b) *c* parameter. Results are shown for the CZTSSe solid solutions crystallised in NaCl/KCl mix for the c) *a* parameter and d) *c* parameter. All are plotted against weighed quantities before synthesis. Linear fits are shown with the dashed lines, and the uncertainties on the lattice parameter values were multiplied by 100 in the error bars.

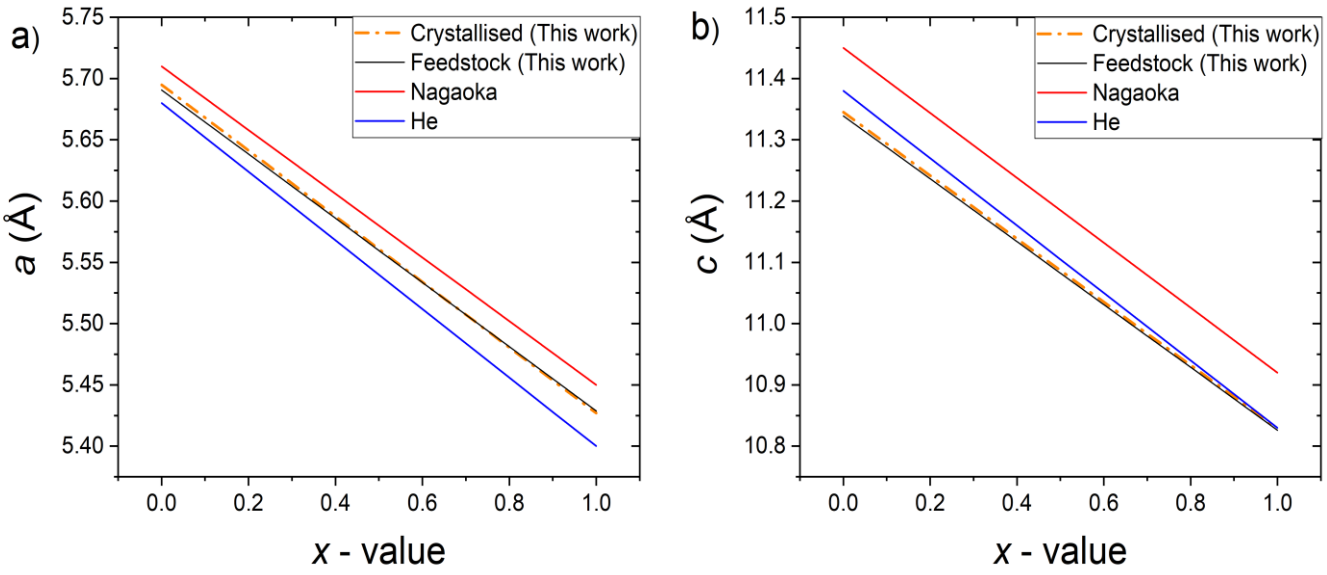

Fig. 4.12 Vegard plots for the linear trends in a) *a* and b) *c* lattice parameters determined in this work, compared to Nagaoka *et al.*[6] and He *et al.*[7]. The lines for both the CZTSSe feedstock crystallised material match closely, but differ from the literature data. See text for details.

One of the key uses for a comprehensive set of Vegard data is the ability to back-correlate material stoichiometry from the lattice parameters. However, the discrepancies in fig. 4.12 demonstrate that there are issues with this approach. For example, if the lattice parameter *c* were used to determine composition, with a value of $x = 0.5$ determined from our data, the data from Nagaoka *et al.* [6] would provide a value of $x = 0.69$, while the data from He *et al.*[7] would mostly agree with ours. Similarly, if the lattice parameter *a* were used, the trend from Nagaoka *et al.* would estimate a value of $x = 0.58$ and He *et al*. would provide an estimate of $x = 0.43$.

The reason for the difference in linear trends between studies is most likely down to deviations from stoichiometry in the ratio of metals, which are known to influence lattice parameters[5]. Furthermore, there was a strong similarity between the Vegard trends for the CZTSSe feedstock and crystallised solid solutions produced in this work (fig. 4.12), despite very different processing conditions, with the similarity lying in the elemental compositions (Tables 4.1 and 4.2). Given that CZTSSe has been shown to support large deviations from stoichiometry (Table 4.4), this

leaves room for significant variations in lattice parameter as a result. In this case, the samples characterised in Nagaoka *et al.* had metal ratios where 0.91 < Cu/(Zn+Sn) < 0.96, 1.69 < Cu/Zn < 1.76 and 1.13 < Zn/Sn < 1.26, whereas metals ratios of Cu/(Zn+Sn) = 1, Cu/Zn = 2 and Zn/Sn = 1 were chosen for the crystallised samples in this work (Table 4.2). Further investigation with varied metal ratios is required to fully understand the origins of the systematic error, although we can have high confidence in the self-consistency of the values of lattice parameter reported in this work. This is due to the large number of closely-spaced data points and small errors on the linear coefficients, which allow reporting to three or four decimal places. Meanwhile, earlier works plotted lattice parameter values but did not provide numerical values, meaning that results may only be read-off to two decimal places. Additionally, it may be argued that the Zn-rich stoichiometry in Nagaoka *et al.* primarily caused a constant shift in the linear trend compared to our values, opening up the possibility of corrections in cases where metal ratios vary. Besides the cation issue, it may be that strain within the material influenced the lattice parameters and contributed to observed discrepancies. The samples in Nagaoka *et al.* were cooled naturally from 1100°C to room temperature, while very slow cooling over a 55°C window < 875°C was employed for the crystallised samples in this work, and the feedstock was cooled from 800°C to 350°C at 0.5°C / min, assumed to be slower than natural cooling. As a result, reduced strain may be expected for the samples in this work compared to those in Nagaoka *et al.*, contributing to a difference in lattice parameters.

4.4 Raman Spectroscopy Investigation

Raman spectroscopy was carried out for the CZTSSe feedstock and CZTSSe crystallised in the NaCl/KCl mix on the series end members CZTSe ($x = 0$) and CZTSe ($x = 1$), while Raman was carried out across the whole composition series ($0 \leq x \leq 1$) for the crystallised CZTSSe solid solutions. Sample fragments were set in epoxy blocks and polished to provide suitably flat surfaces for measurement.

4.4.1 Raman of the Series End Members CZTSe and CZTS (x = 0 and 1)

Fig. 4.13 shows the Raman spectra for the CZTSSe series end members CZTSe and CZTS in the form of both the feedstock (a and c) and after crystallisation (b and d).

Prominent peaks centred on 170.9 and 194.3 cm^{-1} were observed in the spectrum for the CZTSe (x = 0) feedstock (fig. 4.13a), with a smaller peak at 233.6 cm^{-1}. All of these peaks were consistent with the values reported for solution-processed CZTSe thin films, such as those fabricated by electrodeposition[8] and by spray pyrolysis[9], where the smaller peak is placed at 235 cm^{-1}. These values may also be compared to the averages reported by Adachi in [4], where the vibrational symmetry modes A_1, A_1 and B_1 were assigned to the peaks 170, 195 and 231 cm^{-1}. These peak positions are consistent with the values in our work, further confirming the synthesis of the CZTSe phase, and suggesting that the peaks in fig. 4.13a may be assigned to modes with symmetry A_1 (170.9 cm^{-1}), A_1 (194.3 cm^{-1}) and B_1 (233.6 cm^{-1}). In addition to representing CZTSe, the peak at 233.6 cm^{-1} may also contain a small peak indicating the secondary phase Cu_2SnS_3 at 236 cm^{-1} although since the resolution of the spectrum was ~ 1 cm^{-1}, additional peaks of this kind were not distinguishable. A contribution at 232 cm^{-1} corresponding to pure selenium (Rruff ID: R060137.2), may also be present, although it also cannot be resolved given the resolution of these scans. Furthermore, surface selenium was not expected on the polished sample, and the low laser irradiance of 0.3 mW μm^{-2} was not expected to induce degradation of the CZTSe surface.

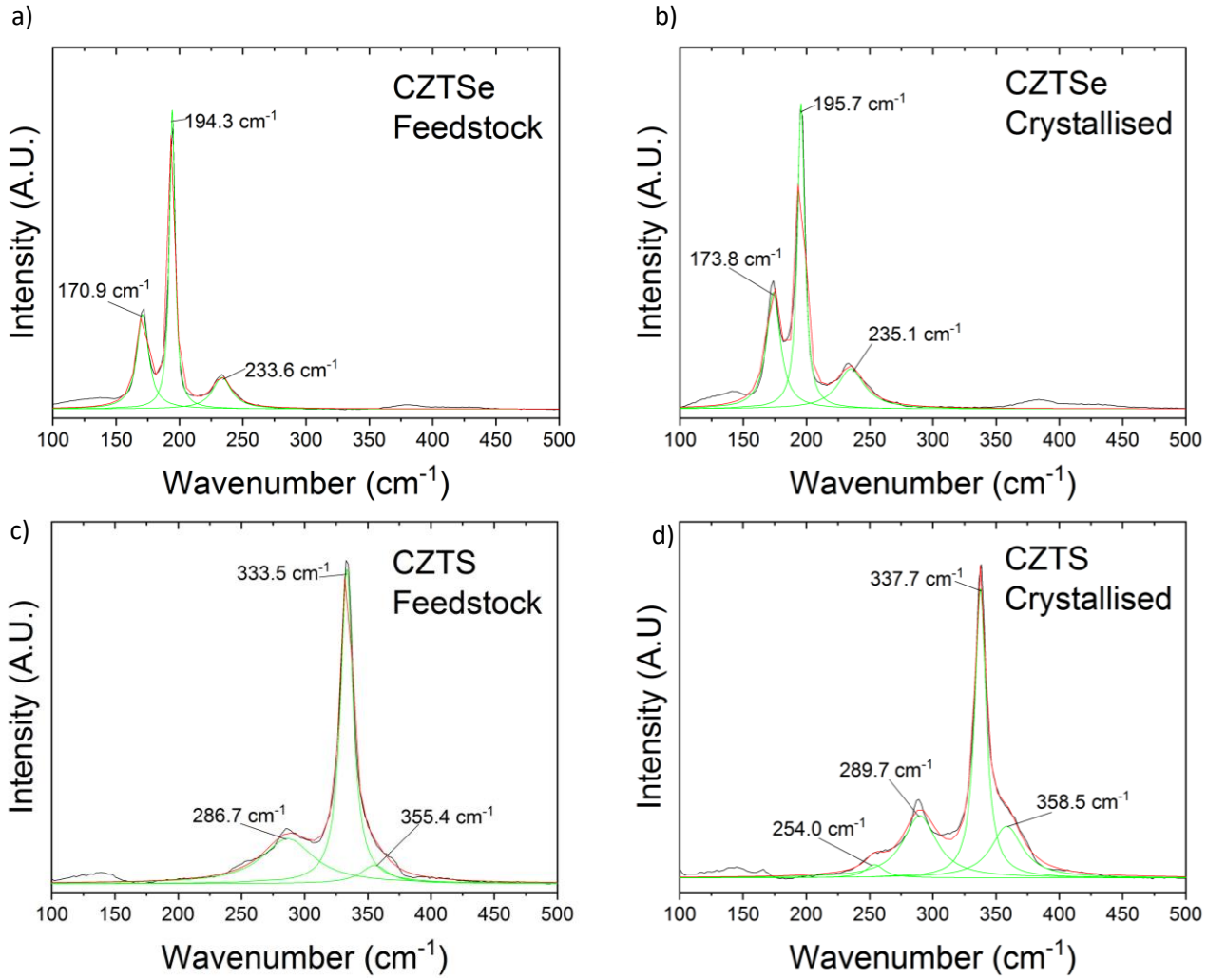

Fig. 4.13 Raman spectra for feedstock series end members a) CZTSe and c) CZTS, and after crystallisation of b) CZTSe and d) CZTS. Small additional peaks in the CZTS spectra (c-d) suggest the presence of secondary phases. Peaks shift to higher wavenumber in the crystallised compared to the feedstock spectra.

The Raman spectrum for the crystallised CZTSe (fig. 4.13b) exhibited peaks similar to those observed in the feedstock, except that all peaks were shifted to a higher wavenumber, to 173.8, 195.7 and 235.1 cm^{-1}. This upward shift is in line with that reported by Rey *et al.*[10], where a shift from 194.5 to 196.4 cm^{-1} was associated with a transition from disordered (194.5 cm^{-1}) to ordered (196.4

cm^{-1}) kesterite phases. Furthermore, theoretical work reported in Khare *et al.*[11] predicts a higher wavenumber value for the kesterite *A* symmetry mode in CZTSe compared to the A_1 symmetry mode for disordered kesterite. As a result, we assigned the symmetry modes *A* (173.8 cm^{-1}), *A* (195.7 cm^{-1}) and *B* (235.1 cm^{-1}) to the peaks observed in this spectrum. Just as for the CZTSe feedstock, small secondary phase peaks may be present in the 235.1 cm^{-1} peak in addition to the peak representing the CZTSe *B* mode. If so, their proportions are likely to be small, as the observed shift suggests that the CZTSe *B* mode dominates this peak (secondary phase peaks would not be expected to shift also).

Fig. 4.13c shows the Raman spectrum for the CZTS feedstock sample, where prominent peaks centred on 286.7 cm^{-1} and 333.5 cm^{-1} are observed, as well as a small shoulder at 355.4 cm^{-1}. The 286.7 cm^{-1} peak is consistent with kesterite CZTS[12], while the 355.4 cm^{-1} peak may result from the secondary phases ZnS[8] or Cu_2SnS_3[13]. Peaks associated with elemental sulfur (154, 220, 436 and 473 cm^{-1}) (Rruff ID: R040135.2) were generally not observed, although the 247 cm^{-1} sulfur peak may be responsible for the small bump observed at 250 cm^{-1} in the spectrum. Either way, the spectrum is not dominated by sulfur peaks, consistent with the low laser irradiance, which would not be expected to induce surface degradation. The prominent peak at 333.5 cm^{-1} is intermediate between the 331 cm^{-1} peak associated with the disordered kesterite A_1 symmetry mode[14] and the 337 cm^{-1} peak associated with the ordered kesterite *A* mode[15]. This peak therefore indicates the formation of partially disordered kesterite, where the Cu and Zn atoms are distributed on the 2c and 2d Wyckoff sites in a regime intermediate between fully random and fully ordered. The work of Grossberg *et al.*[15] reports on a CZTS spectrum containing coexisting kesterite *A* and disordered kesterite A_1 modes, supporting this interpretation.

In the Raman spectrum for CZTS crystallised in the NaCl/KCl mix, shown in fig. 4.13d, large peaks appear at 289.7 and 337.7 cm^{-1}, with smaller shoulder peaks at 254.0 and 358.5 cm^{-1}. This represents a shift to higher wavenumbers compared to the feedstock (fig. 4.13c), similar to the phenomenon observed in the CZTSe (fig. 4.13a-b). This suggests that the CZTS similarly transitioned to a more ordered kesterite configuration in the crystallised sample, justifying the assignment of the kesterite *A* symmetry mode to the 289.7[12] and 337.7 cm^{-1} peaks[15]. The peak at 254.0 cm^{-1} was

also associated with the CZTS phase, but a symmetry assignment was not found[16]. The additional peak at 358.5 cm^{-1} may indicate the presence of ZnS[12], Cu_2SnS_3[13], or both, suggesting that despite improved ordering, secondary phases were still present in the crystallised material, although the fact that this peak also shifted compared to feedstock suggests that CZTS dominates the spectrum.

Improved ordering was evidenced in the crystallised samples despite the slow-cooling step (0.4°C hr^{-1}) taking place at temperatures of > 730°C (Section 3.2.2), significantly higher than the reported order-disorder transitions for CZTSe at 200°C[17] and CZTS at 260°C[18]. This may suggest that during the natural cooling step (after the slow-cooling) while at temperatures below the order-disorder transition temperature (< 200°C), the material experienced an effective anneal which influenced the ordering. The rate of natural cooling was not known, so it is unclear how long the samples remained at temperatures close to (but below) the order-disorder transitions temperature. However, crystallised samples may have stayed at these temperatures for a longer period than the CZTSSe feedstock due to heat retention by the large mass of salt in the growth tube, offering an explanation for the differing levels of ordering.

4.4.2 Raman of the Full Composition Series $0 \leq x \leq 1$

The Raman spectra for the whole composition series ($0 \leq x \leq 1$) of the CZTSSe crystallised in the NaCl/KCl mix are shown in fig. 4.14a. The assumed single crystal nature of the monograins (Section 4.2.2) likely produced the clean spectra with strong Lorentzian peaks .

Fig. 4.14a shows the Raman spectra for the crystallised series ($0 \leq x \leq 1$). For the series end members CZTSe and CZTS, one large, principal peak (assigned to kesterite *A* symmetry mode) was observed in each spectrum, while for the intermediate compositions ($0 < x < 1$), two principal peaks were observed in each spectrum, with wavenumber values similar to the principal CZTSe and CZTS peaks, so were described as ‘CZTSe-like’ and ‘CZTS-like’. Fig. 4.15 presents their FWHMs vs. x determined from weighing. The larger peak widths found at intermediate x - values (compared to the series end members) most likely result from increased disorder in the placement of the Se and S anions.

In addition to the broadening that occurred at intermediate *x* - values, the CZTSe-like and CZTS-like peaks, representing the kesterite *A* mode, both shifted to larger wavenumbers (represented by ω in this work) with increasing *x* - value. Figs. 4.14b-c plot the positions of the CZTSe peak (fig. 4.41b) and CZTS peak (fig. 4.41b) against *x* - value determined from weighing, and show a linear shift in each case.

The Raman measurements of the crystallised CZTSSe solid solutions clearly exhibit 'two-mode' behaviour, with separate vibrational modes associated with either selenium or sulfur atoms coexisting, rather than the selenium mode smoothly transitioning into the sulfur mode, as for 'one-mode' behaviour. The two-mode behaviour is in line with the results reported by Grossberg *et al.*[19] and by Adachi in [4].

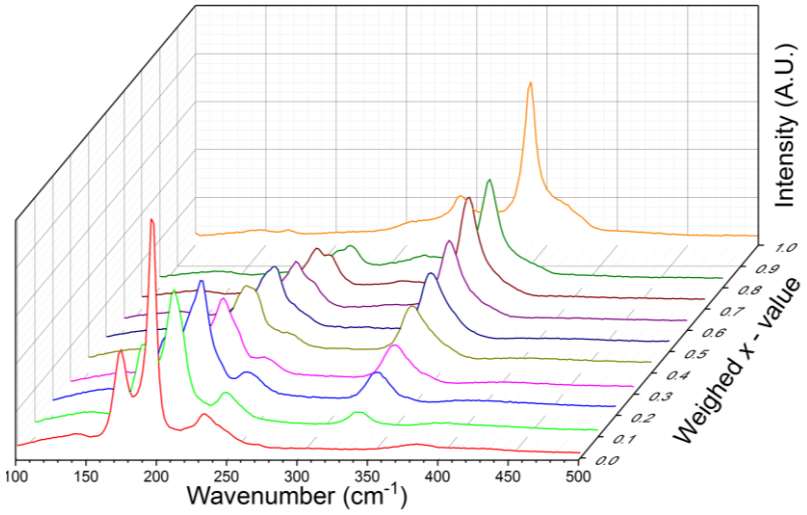
Intensity (A.U.)
Weighed x - value
1.0
0.9
0.8
0.7
0.6
0.5
0.4
0.3
0.2
0.1
0.0
100
150
200
250
300
350
400
450
500
Wavenumber (cm-1)

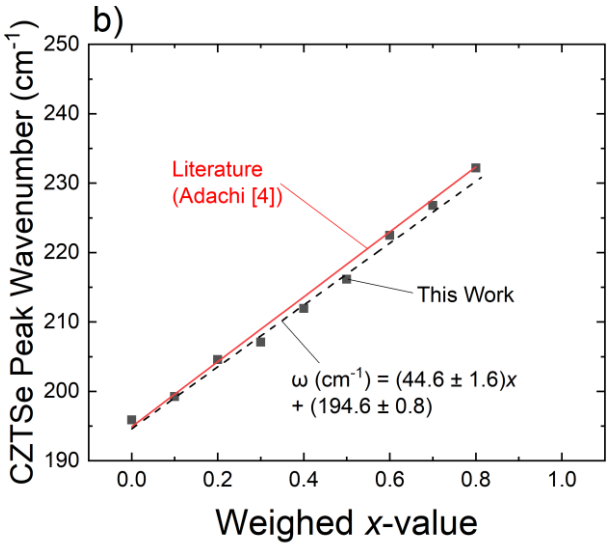
b)
CZTSe Peak Wavenumber (cm-1)
250
240
230
220
210
200
190
Literature
(Adachi [4])
This Work
ω (cm-1) = (44.6 ± 1.6)x
+ (194.6 ± 0.8)
0.0
0.2
0.4
0.6
0.8
1.0
Weighed x-value

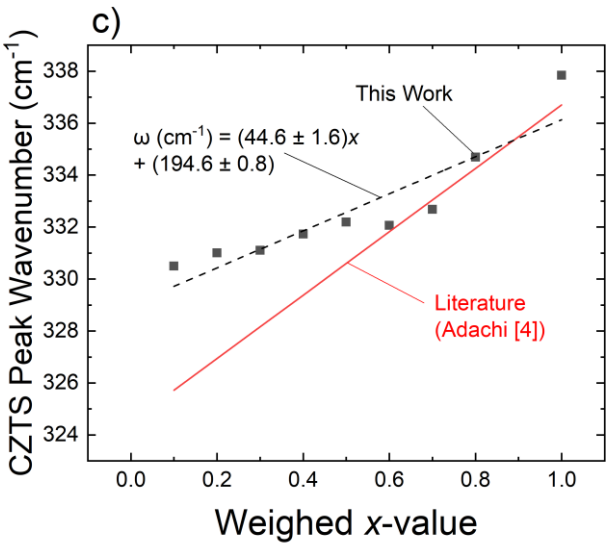
c)
CZTS Peak Wavenumber (cm-1)
338
336
334
332
330
328
326
324
This Work
ω (cm-1) = (44.6 ± 1.6)x
+ (194.6 ± 0.8)
Literature
(Adachi [4])
0.0
0.2
0.4
0.6
0.8
1.0
Weighed x-value

Fig. 4.14 a) Raman spectra taken for every CZTSSe composition crystallised from NaCl/KCl mix over range ($0 \leq x \leq 1$). Two principal Raman peaks are observed for each intermediate composition ($0 < x < 1$), each shifting to higher wavenumber with increasing x - value. b-c) Plotted positions of principal kesterite *A* mode peaks for crystallised b) CZTSe and c) CZTS against x - value (weighed). Linear trends for this work are shown with dashed black lines and compared to the linear trends reported in Adachi[4], shown with solid red lines.

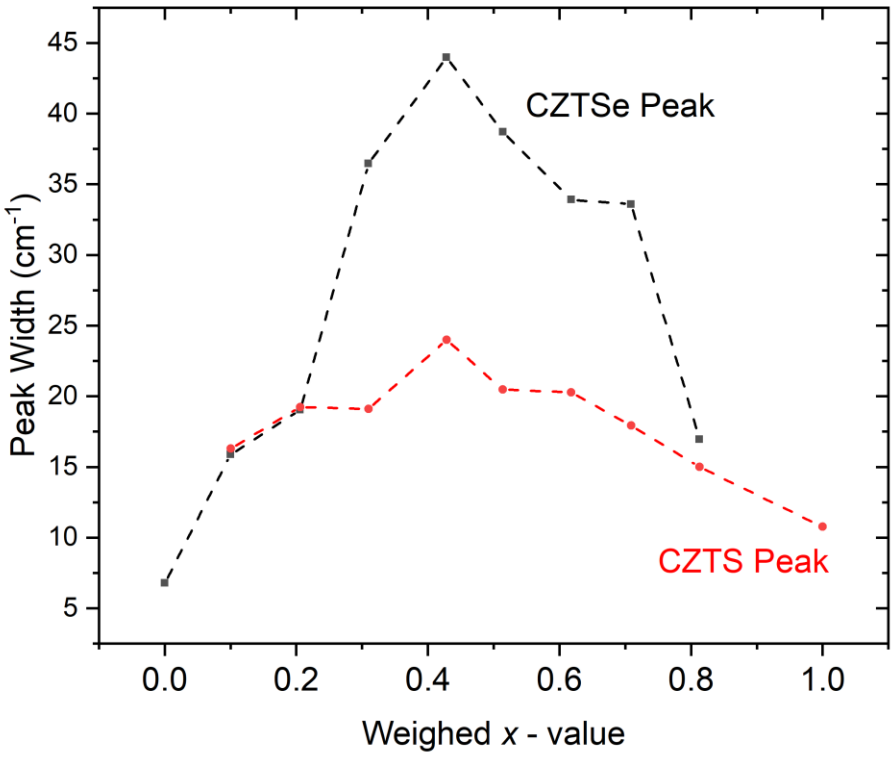

Fig. 4.15 Plot of the FWHM values for the 'CZTSe-like' and 'CZTS-like' peaks in the series of CZTSSe samples crystallised in the NaCl/KCl mix, against weighed x - value. Peaks experience broadening for intermediate compositions.

The modified random-element isodisplacement model, outlined by Chang and Mitra[20], forms the theoretical framework for the two-mode evolution. The model considers a mixture of two binary compounds, so CZTSe and CZTS are treated as pseudobinary compounds, with the CZTSSe solid solutions a mixture of the two. The CZTSe-CZTS system may be defined as AB_xC_{1-x} where *A* is Cu_2ZnSn, with a mass of $M_{Cu2ZnSn} = M_{Cu2} + M_{Zn} + M_{Sn}$, while *B* is defined as S_4 and *C* as Se_4. The criterion for two-mode behaviour is that the mass of *B* is smaller than the reduced mass for the A-C system, i.e. $M_B < \mu_{AC}$ where μ_{AC} is the reduced mass of the *A*-*C* system. As reported by Adachi in [4], the CZTSe-CZTS system is expected to exhibit two-mode behaviour as defined by this model, because the mass of sulphur is smaller than the reduced mass of $M_{Cu2ZnSn}$ and M_{Se}. The Raman results presented in this work (fig. 4.14b) therefore provide confirmation of this.

Given that the two-mode system predicts linear shifts in peak positions, the linear fit applied in fig. 4.14b is valid, producing expressions for the trend in Raman mode evolution with *x* – value. The CZTSe-like *A* mode shifted as: ω_{CZTSe} (cm^{-1}) = (44.6 ± 1.6)*x* + (194.6 ± 0.8) while the CZTS-like A mode shifted as: ω_{CZTS} (cm^{-1}) = (7.1 ± 1.3)*x* + (329.0 ± 0.8). The review in by Adachi in [4] combines the data presented in Grossberg *et al.*[19] and He *et al.*[7] to report a trend in the Raman mode evolution of the CZTSe-like *A* mode of: ω_{CZTSe} (cm^{-1}) = 46.8*x* + 194.9 and for the CZTS-like *A* mode of: ω_{CZTS} (cm^{-1}) = 12.2*x* + 324.5. These trends are consistent with our values for the CZTSe-like *A* mode, as can be seen from the comparison in fig. 4.14b, but with some difference for the CZTS-like A mode, where we observed a less rapid variation in the peak position with *x* – value: a total shift of 7.1 cm^{-1} over the range as opposed to 12.2 cm^{-1} for Adachi. This difference is clear to see in fig. 4.14c. Much of this discrepancy may be put down to the larger value of ω_{CZTS} at *x* = 0 estimated in this work, at 329.0 cm^{-1} compared to 324.5 cm^{-1} for Adachi. In both cases this value is an extrapolation, as no CZTS-like mode appears in pure CZTSe. We may have confidence in our extrapolation given the large number of data points, although there was more scatter about the linear trendline for ω_{CZTS} than for ω_{CZTSe}.

It should also be noted that the sample sets covered by Adachi in [4] by way of Grossberg *et al.*[19] and He *et al.* were copper-poor, something that has been demonstrated to affect lattice

parameters[5], which followed a different trend with x – value in He *et al.*[7], as compared to our data in fig. 4.12. The differing cation ratios may therefore be responsible for the value of ω_{CZTS} at $x = 0$ while simultaneously producing a shift in the value of c. The good agreement of the CZTSe-like peak with literature suggests that this series may be less sensitive to metals stoichiometry than lattice parameters while the good linear fit achieved suggests it may be applied in an analogous way to the lattice parameters to determine the anion ratio in a thin film, especially as the CZTSe *A* mode is less sensitive to ordering than the CZTS *A* mode (see fig. 4.13). This also offers some advantage over using lattice parameters because refining the XRD pattern for a thin film to extract lattice parameters is often complicated by preferred crystal orientations. Raman also allows the characterisation of sites 1 – 2 μm in size, while conventional XRD provides an average over an area of at least several square mm. It should be noted, however, that as these results were derived from highly-crystalline bulk samples, they are most applicable to highly-crystalline CZTSSe thin films, and have less relevance for amorphous or poorly crystalline films, as non-crystalline material would not be identifiable with XRD or Raman. Additionally, given the possibility of lattice strain influencing lattice parameters, these results may be less useful for films grown under highly non-equilibrium conditions.

4.5 Conclusions

While an original aim of this work was to produce single crystals of CZTSSe to examine point defects, as well as structural properties, this was not ultimately achieved. Instead, a key synthesis result presented in this chapter is the growth of crystal monograins of CZTSSe ~ 100 μm in size from solution in a NaCl/KCl salt mix with controlled stoichiometry and strong evidence of ordering. This was achieved across the composition range $0 \leq x \leq 1$ to a precision of $\Delta x = 0.1$. Due to these sample synthesis results, more focus was placed on measuring the structural properties of this series to high precision, rather than continuing attempts to grow single crystals, with results as follows.

XRD measurements provided a linear Vegard relation where relations a (Å) = -0.268(3)x + 5.6949(17) and c (Å) = -0.516(6)x + 11.345(3) were determined, while Raman mode evolution data was produced for the same sample set, where two-mode behaviour was clearly observed. The evolution of the CZTSe-like and CZTS-like *A* Raman modes were determined as ω_{CZTSe} (cm^{-1}) = (44.6 ± 1.6)x + (194.6 ± 0.8) and ω_{CZTS} (cm^{-1}) = (7.1 ± 1.3)x + (329.0 ± 0.8) respectively. Meanwhile, accurate determination of the cation and anion content of the sample series was carried out, allowing the lattice parameters and Raman data to be examined in the context of precise stoichiometric ratios. The gathering of fundamental reference data for CZTSSe has utility in the fabrication of highly crystalline thin films, for instance, in allowing the back-correlation of anion composition based on lattice parameters and/or Raman mode position. Determination of composition using these techniques offers advantages over EDX, as no matrix correction step (and associated systematic errors) is necessary, while XRD and Raman are also non-destructive, in contrast to secondary ion mass spectrometry or ICP-based chemical analysis methods. However, they have the disadvantage of being less applicable to amorphous or poorly-crystalline samples, as an amorphous material will not produce a clear contribution to the signal observed with these methods, even if it, in fact, dominates the sample.

These results provide a higher level of precision in the compositional control than previous studies of this type, and probe a regime with different stoichiometry in the cations (metals). This

allows additional confidence to be placed in these trends, as well as demonstrating the differences (and similarities) that emerge when cation ratios are different. Additionally, the results presented in this work add to the body of evidence on the effects of ordering within CZTSSe, demonstrating a transition from a disordered to a more ordered kesterite phase. While the mechanism behind this improved ordering is not known for certain, it is possible that ordering occurred while the sample was being cooled, if it remained close to, but below, the order-disorder transition temperature (~200°C) for an extended period of time. As well as providing reference data for experimentalists, it is hoped that theorists will find utility in these results to inform their models, for instance, in modelling the impact of the *a* and *c* lattice parameters on the frequency of vibrational modes.

4.6 References

[1] W. M. Haynes, *CRC Handbook of Chemistry and Physics*, 95th ed. London, New York: CRC Press, Taylor & Francis Group, 2014.

[2] S. Schorr, "Crystallographic Aspects of Cu_2ZnSnS_4 (CZTS)," in *Copper Zinc Tin Sulfide-Based Thin-Film Solar Cells*, 1st ed., K. Ito, Ed. Chichester: John Wiley and Sons, 2015, pp. 55–74.

[3] L. Choubrac, M. Paris, A. Lafond, C. Guillot-Deudon, X. Rocquefelte, and S. Jobic, "Multinuclear (67Zn, 119Sn and 65Cu) NMR spectroscopy – an ideal technique to probe the cationic ordering in Cu_2ZnSnS_4 photovoltaic materials," *phys*, vol. 15, pp. 10722–10725, 2013.

[4] K. Ito, *Copper Zinc Tin Sulfide-Based Thin-Film Solar Cells*, 1st ed. Nagano: John Wiley and Sons, 2015.

[5] A. Lafond, L. Choubrac, C. Guillot-deudon, P. Deniard, and S. Jobic, "Crystal structures of photovoltaic chalcogenides, an intricate puzzle to solve: the cases of CIGSe and CZTS materials," *J. Inorg. Gen. Chem.*, vol. 638, no. 15, pp. 2571–2577, 2012.

[6] A. Nagaoka, K. Yoshino, H. Taniguchi, and T. Taniyama, "Growth and characterization of $Cu_2ZnSn(S_xSe_{1-x})_4$ alloys grown by the melting method," *J. Cryst. Growth*, vol. 386, pp. 204–207, 2014.

[7] J. He, L. Sun, S. Chen, Y. Chen, P. Yang, and J. Chu, "Composition dependence of structure and optical properties of $Cu_2ZnSn(S,Se)_4$ solid solutions: An experimental study," *J. Alloys Compd.*, vol. 511, pp. 129–132, 2011.

[8] L. Guo *et al.*, "Electrodeposited $Cu_2ZnSnSe_4$ thin film solar cell with 7% power conversion efficiency," *Prog. Photovolt Res. Appl.*, vol. 22, pp. 58–68, 2014.

[9] X. Zeng *et al.*, "$Cu_2ZnSn(S,Se)_4$ kesterite solar cell with 5.1% efficiency using spray pyrolysis of aqueous precursor solution followed by selenization," *Sol. Energy Mater. Sol. Cells*, vol. 124, pp. 55–60, 2014.

[10] G. Rey *et al.*, "The band gap of $Cu_2ZnSnSe_4$: Effect of order-disorder," *Appl. Phys. Lett.*, vol. 105, no. 11, 2014.

[11] A. Khare, B. Himmetoglu, M. Johnson, D. J. Norris, M. Cococcioni, and E. S. Aydil, "Calculation of the lattice dynamics and Raman spectra of copper zinc tin chalcogenides and comparison to experiments," *J. Appl. Phys*, vol. 111, p. 83707, 2012.

[12] E. M. Mkawi, K. Ibrahim, M. K. M. Ali, M. A. Farrukh, and N. K. Allam, "Influence of precursor thin films stacking order on the properties of Cu_2ZnSnS_4 thin films fabricated by electrochemical deposition method," *Superlattices Microstruct.*, vol. 76, pp. 339–348, 2014.

[13] O. Vigil-Galán, M. Courel, M. Espindola-Rodriguez, V. Izquierdo-Roca, E. Saucedo, and A. Fairbrother, "Toward a high Cu_2ZnSnS_4 solar cell efficiency processed by spray pyrolysis method," *J. Renew. Sustain. Energy*, vol. 5, no. 5, 2013.

[14] M. Y. Valakh *et al.*, "Raman scattering and disorder effect in Cu_2ZnSnS_4," *Phys. Status Solidi*, vol. 7, no. 4, pp. 258–261, 2013.

[15] M. Grossberg, J. Krustok, J. Raudoja, and T. Raadik, "The role of structural properties on deep defect states in Cu_2ZnSnS_4 studied by photoluminescence spectroscopy," *Appl. Phys. Lett*, vol. 101, p. 102102, 2012.

[16] O. Vigil-galán *et al.*, "Secondary phases dependence on composition ratio in sprayed Cu_2ZnSnS_4 thin films and its impact on the high power conversion efficiency," *Sol. Energy Mater. Sol. Cells*, vol. 117, pp. 246–250, 2013.

[17] G. Rey *et al.*, "The band gap of $Cu_2ZnSnSe_4$: Effect of order-disorder," *Appl. Phys. Lett.*, vol. 105, no. 11, p. 112106, 2014.

[18] T. Raadik *et al.*, "Low temperature time resolved photoluminescence in ordered and disordered Cu_2ZnSnS_4 single crystals," *Phys. B Condens. Matter*, vol. 508, no. November 2016, pp. 47–50, 2016.

[19] M. Grossberg, J. Krustok, J. Raudoja, K. Timmo, M. Altosaar, and T. Raadik, "Photoluminescence and Raman study of $Cu_2ZnSn(Se_xS_{1-x})_4$ monograins for photovoltaic applications," *Thin Solid Films*, vol. 519, pp. 7403–7406, 2011.

[20] I. F. Chang and S. S. Mitra, "Application of a modified random-element-isodisplacement model to long-wave optic phonons of mixed crystals," *Phys. Rev.*, vol. 172, no. 3, pp. 924–933, 1968.

5. Growth and Physical Characterisation of Doped Crystalline Sb_2Se_3 and $Sb_2S_{3x}Se_{3(1-x)}$

5.1 Introduction

This chapter details work carried out to investigate the growth of bulk crystalline samples of Sb_2Se_3 and $Sb_2S_{3x}Se_{3(1-x)}$ solid solutions. Sb_2Se_3 was synthesised from elemental Sb and Se with controlled stoichiometry, both with and without extrinsic dopants, and used as source material for crystal growth. Commercial Sb_2Se_3 source material was also used. Additionally, the formation of solid solutions of $Sb_2S_{3x}Se_{3(1-x)}$ was investigated. These crystals allowed examination of the lattice parameters and Raman modes. Another key motivation of the crystal growth studies was to determine the most effective methods to produce single crystals suitable for electrical characterisation (see Chapter 6).

In Sections 5.2-5.6, the use of several techniques to prepare crystals of Sb_2Se_3 is reported (details may be found in Sections 3.2.4 and 3.2.5). These were: direct synthesis from elements (DSE) or from compounds (DS) in a sealed tube, Piper-Polich (PP) growth, self-selecting vapour growth (SSVG) and vertical Bridgman (VB) growth.

The process of direct synthesis of Sb_2Se_3 from the elements used elemental Sb (6N purity) and Se (5N purity) shot as the source material. The Piper-Polich, SSVG and vertical Bridgman techniques utilised either commercial 5N Sb_2Se_3 or Sb_2Se_3 directly synthesised in-house from the elements, as above. The largest single crystals were produced via the vertical Bridgman method and these proved to be the most suitable for further characterisation. As a result, small quantities of extrinsic dopant elements were incorporated into some growth runs, with their impact on electronic properties covered in Chapter 6.

In Section 5.5, direct synthesis from compounds was employed to investigate the formation of sulfo-selenide solid solutions $Sb_2S_{3x}Se_{3(1-x)}$. Commercial 5N Sb_2Se_3 and Sb_2S_3 (x = 0 and 1 respectively) were used to synthesise the solid solutions.

All samples prepared by these techniques were examined with optical microscopy, powder x-ray diffraction (XRD), scanning electron microscopy (SEM) and energy-dispersive x-ray spectroscopy (EDX) to evaluate the phase, composition and crystallite size. For the $Sb_2S_{3x}Se_{3(1-x)}$ solid solutions, these techniques were also used to determine the extent of intermixing and measure the Vegard relation.

Section 5.6 reports the physical properties of Sb_2Se_3 single crystals grown by the vertical Bridgman method using XRD, differential interference contrast (DIC) microscopy, electron backscattered diffraction (EBSD) and Raman spectroscopy.

Section 5.7 reports chemical analysis by inductively-coupled plasma optical emission spectroscopy (ICP-OES) mass spectrometry (ICP-MS), and secondary ion mass spectrometry (SIMS). The successful incorporation of Sn and Mg from extrinsic doping is demonstrated, and a significant quantity of Cl is found in the 5N Sb_2Se_3 source material, both of which have great relevance to the electrical properties of Sb_2Se_3 as investigated in Chapter 6.

Table 5.1 details all of the sample types synthesised in this work, with sample codes applied in this and the following chapter (Chapter 6). The deviation from stoichiometry in the samples synthesised from the elements (DSE) was controlled by weighing, while the exact stoichiometry of the commercial 5N Sb_2Se_3 was not known. The stoichiometry and percentage of extrinsic dopants in the vertical Bridgman crystals (where relevant) were inferred from the stoichiometry of the source material and the mass of dopant measured during weighing. For most sample types, several individual samples were synthesised.

Growth Technique	Source Material	Stoichiometry	Extrinsic Dopants	Sample Code
Piper-Polich growth - **PP**	Commercial pre-synthesised Sb_2Se_3 – **5NAA**		Undoped - **Un**	**PP-5NAA-Un**
Self-selecting vapour growth – **SSVG**	Commercial pre-synthesised Sb_2Se_3 – **5NAA**		Undoped – **Un**	**SSVG-5NAA-Un**
Direct synthesis from elements (Sb_2Se_3) - **DSE**	Elemental Sb shot, Elemental Se shot – **6NSb5NSe**	Stoichiometric (< 0.01 at% variation) - **St**	Undoped – **Un**	**DSE-St-Un**
		Se – poor (> 0.1 at% variation) – **SeP**	Undoped – **Un**	**DSE-SeP-Un**
		Se – rich (> 0.1 at% variation) - **SeR**	Undoped - **Un**	**DSE-SeR-Un**
			Sn-doped (~0.1 at%) – **Sn**	**DSE-SeR-Sn**
Direct synthesis from compounds Sb_2S_3 and Sb_2Se_3 ($Sb_2S_{3x}Se_{3(1-x)}$) - **DS**	Commercial pre-synthesised Sb_2Se_3 – **5NAA**, Commercial pre-synthesised Sb_2S_3	$Sb_2S_{0.6}Se_{2.4}$		**DS-x02**
		$Sb_2S_{1.5}Se_{1.5}$		**DS-x05**

(Continued)

Vertical Bridgman - **VB**	Commercial pre-synthesised Sb_2Se_3 – **5NAA**		Undoped - **Un**	**VB-5NAA**
			Sn-doped (~0.1 at%) – **Sn**	**VB-5NAA-Sn**
			$MgCl_2$-doped (~0.1 at%) – **MgCl2**	**VB-5NAA-MgCl2**
	Direct synthesis from elements (**DSE**)	Stoichiometric (< 0.01 at% variation) - **St** Se – poor (> 0.1 at% variation) - **SeP**	Undoped - **Un**	**VB-St-Un**
			Undoped - **Un**	**VB-SeP-Un**
			Sn-doped (~0.1 at%) – **Sn**	**VB-SeP-Sn**
			$MgCl_2$-doped (~0.1 at%) – **MgCl2**	**VB-SeP-MgCl2**
		Se – rich (> 0.1 at% variation) - **SeR**	Undoped - **Un**	**VB-SeR-Un**
			Sn-doped (~0.1 at%) – **Sn**	**VB-SeR-Sn**
			$MgCl_2$-doped (~0.1 at%) – **MgCl2**	**VB-SeR-MgCl2**
Close-space sublimation – **CSS**	Commercial pre-synthesised Sb_2Se_3 – **5NAA**		Undoped - **Un**	**CSS-5NAA-Un**

Table 5.1 Details of the growth technique, source material, stoichiometry (where controlled) and extrinsic dopants for all samples investigated in this work. Sample codes are given in bold.

5.2 Piper-Polich Growth of Sb_2Se_3

Piper-Polich growth (Section 3.2.4.1) was carried out using 5N Sb_2Se_3 source material and sealed under vacuum. This growth method was feasible due to the high vapour pressure of Sb_2Se_3[1].

6.2.1 Piper-Polich Crystal Growth Outcomes

Typical results of Piper-Polich growth are shown in Fig. 5.1, indicating an ingot of Sb_2Se_3 formed from vapour transport of material from the charge end (now empty) where temperature was high, to the growth tip, where the temperature was lowest. The process formed a polycrystal around 15 mm long and up to 10 mm wide. It bore similar lustre and colour to the source material with no clear signs of segregation. The clean transport suggests that congruent vaporisation of the Sb_2Se_3 occurred. The majority of the Sb_2Se_3 was deposited on the cooler top-side of the tube interior, as shown in fig. 5.1a. This results from lower temperatures expected at the upper edge of the ampoule, closer to the axis of the furnace tube, as explained in Section 3.2.4.1.

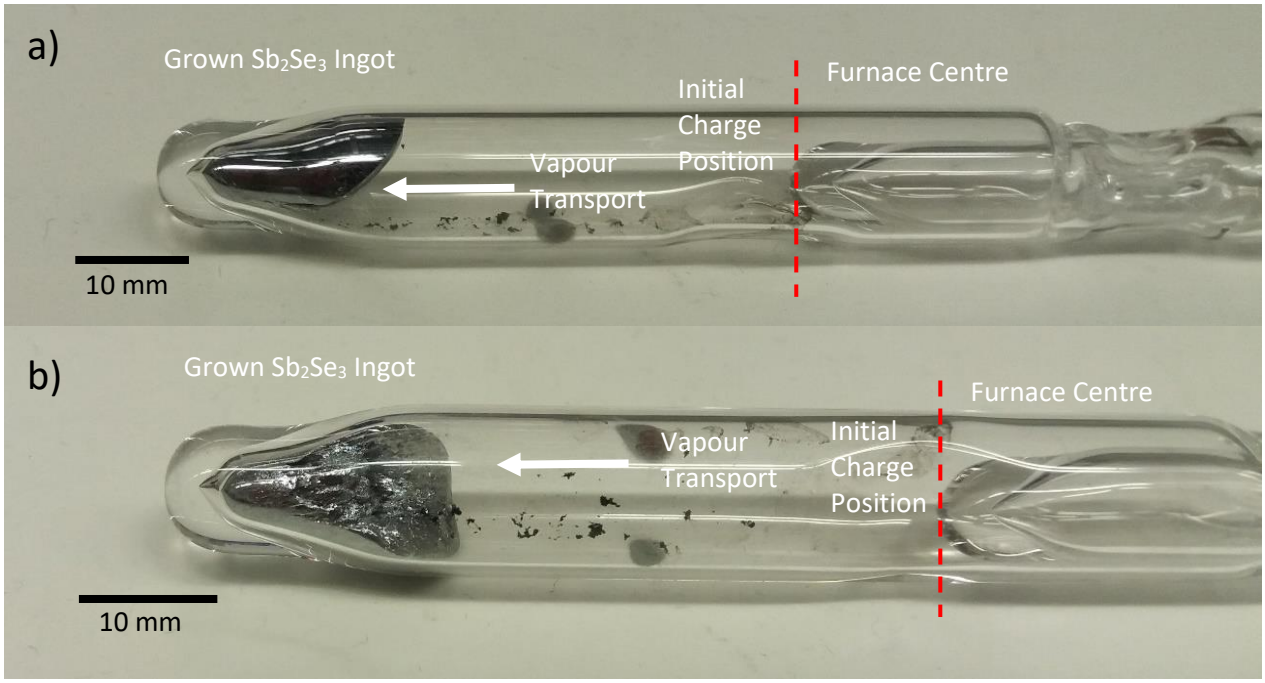

Fig. 5.1 Photographs of Sb_2Se_3 polycrystal grown via the Piper-Polich method from 5N Sb_2Se_3 source material (PP-5NAA-Un), within quartz growth tube, showing: a) position as during growth and b) same sample upturned to present the growth surface. The charge region of tubes (right hand side) is now empty of material and the vapour transport has proceeded from right to left.

5.2.2 XRD Evaluation of Piper-Polich-Grown Sb_2Se_3

A fragment of the polycrystal grown using the Piper-Polich method (PP-5NAA-Un) was finely ground and powder XRD was carried out. The θ-2θ scan was compared to a control from the unprocessed 5N Sb_2Se_3 source material and fig. 5.2 shows the results of both scans.

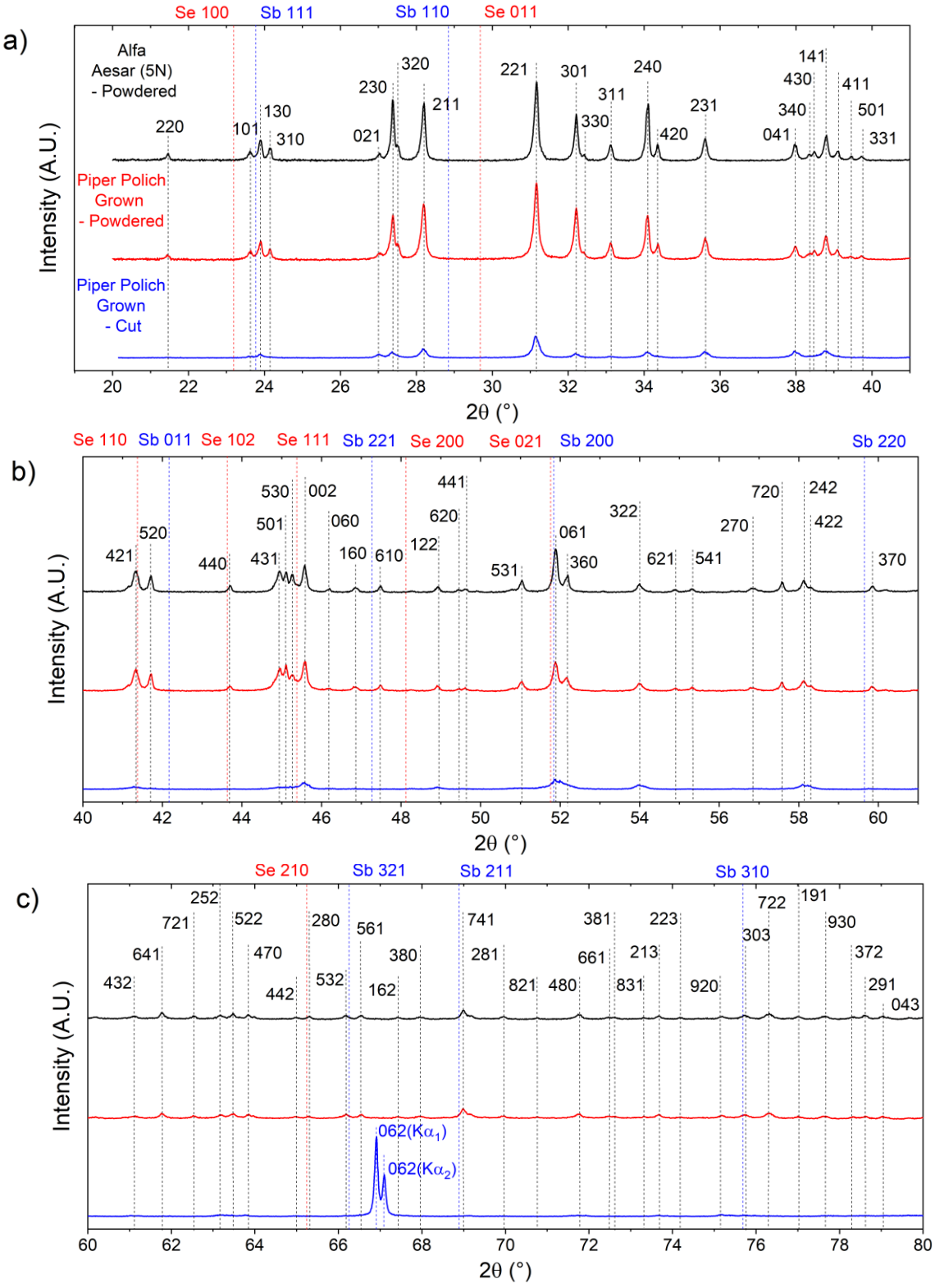

Fig. 5.2 XRD θ-2θ scans (linear intensity scale) for: (black) powdered unprocessed 5N source material, (red) powdered fragment of Piper-Polich-grown polycrystal (PP-5NAA), (blue) polished surface of polycrystal cut orthogonal to growth direction. Covering angular range a) 20-40°, b) 40-60°, c) 60-80°, with all Sb_2Se_3 peaks indexed, and expected positions for Sb and Se peaks also shown.

The two patterns very closely match, with no peaks appearing for the polycrystal that were not also present for the source material, the only difference being in peak intensity. For both patterns, the 121 and 221 peaks (dashed lines) are the most prominent. For both samples, every peak that appears may be indexed to a reflection associated with Sb_2Se_3, indicating that Sb_2Se_3 is present in both cases. Additionally, peaks associated with elemental Sb and Se (positions shown in fig. 5.2) do not appear, except at positions where they overlap with possible Sb_2Se_3 peaks, such as for the Sb 111, 200, 321 and 310 peaks; and for the Se 110, 021 and 210 peaks. As a result, the presence of the elements is unlikely, but cannot be entirely ruled out.

Furthermore, in both cases Rietveld refinement (fig. 5.3) indicated that the patterns matched the orthorhombic *Pbnm* structure of Sb_2Se_3[2]. The differences in relative peak intensity are likely to be due to a preferred orientation, while the lattice parameters calculated for the 5N source material are: *a* (Å) = 11.6393(3) *b* (Å) = 11.78897(26) *c* (Å) = 3.97913(8) and for the polycrystal grown by Piper-Polich are: *a* (Å) = 11.63061(21) *b* (Å) = 11.78079(20) *c* (Å) = 3.97648(7).

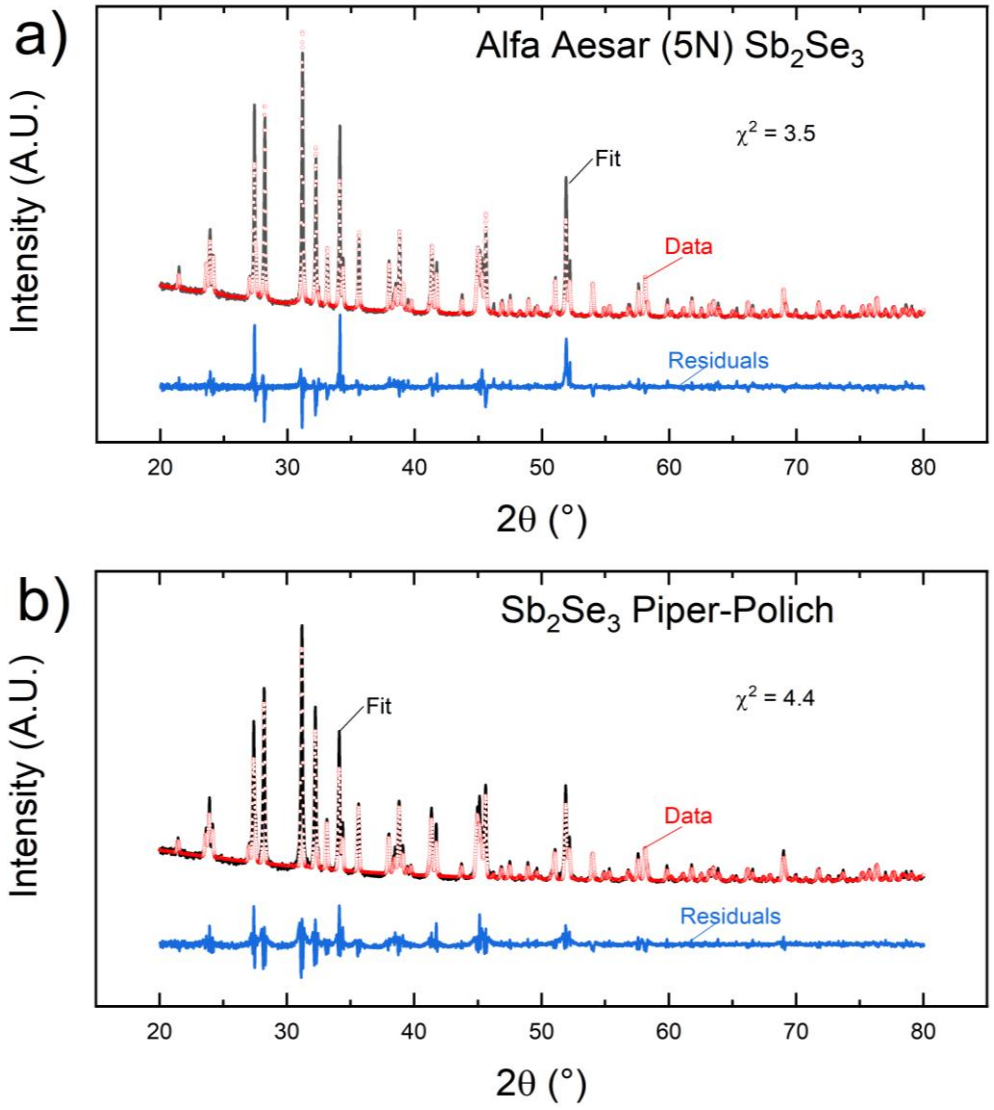

Fig. 5.3 a) Rietveld refinement results (linear intensity scale) for the 5N Sb_2Se_3, showing a good match to the *Pbmn* crystal structure[2]. b) Rietveld refinement for the powderised polycrystal grown from Piper-Polich, also showing a good match to the *Pbmn* crystal structure.

In order to assess crystallinity and growth axis, material was cut orthogonal to the growth direction and polished. A θ-2θ scan was carried out (fig. 5.2 blue) which exhibits several small peaks, as well as a prominent peak at 66.8°, split into the K-α_1 and K-α_2 diffraction lines, and indexed as 062. All peaks in the crystallised material were present in the source material, with peak assignments

shown in fig. 5.2, but the large peak for 062 indicated a polycrystalline sample with a strong preferred orientation towards the [062] axis. This suggests preferential growth along [062], although the sample is evidently polycrystalline and it cannot be confirmed from this single observation that this orientation is generally preferred for vapour-transport experiments.

The congruent vaporisation and transport of Sb_2Se_3 demonstrated in these results means that other vapour-based techniques, such as self-selecting vapour growth (SSVG), may be carried out without the issue of elemental segregation.

5.3 Self-Selecting Vapour Growth of Sb_2Se_3

Self-selecting vapour growth (SSVG) was carried out using 5N Sb_2Se_3, with the details outlined in Section 3.2.4.2. As discussed, SSVG works by vapour transport, but utilises the radial temperature-gradient present in a horizontal tube furnace, rather than the horizontal gradient as for Piper-Polich (see fig. 3.2).

5.3.1 Optical Microscopy

Following the SSVG process, the Sb_2Se_3 formed a solid ingot on the bottom surface of the growth tube (fig. 5.4a). The top-facing side of one of the ingots had visible crystal habit planes. These pieces cleaved crystallographically to reveal reflective cleavage facets.

The distribution of the material in the tube (fig. 5.4a) comes as a consequence of the radial temperature profile in the furnace tube, as is intended for SSVG. However, the horizontal distribution indicates that the horizontal temperature profile was not ideal, with material having transported from right to left. This is to be expected for a single zone furnace, as in our setup (fig. 3.3). Specialist SSVG furnaces have a three-zone design with a cool centre zone to confine the material to the centre of the furnace (Section 3.2.4.2).

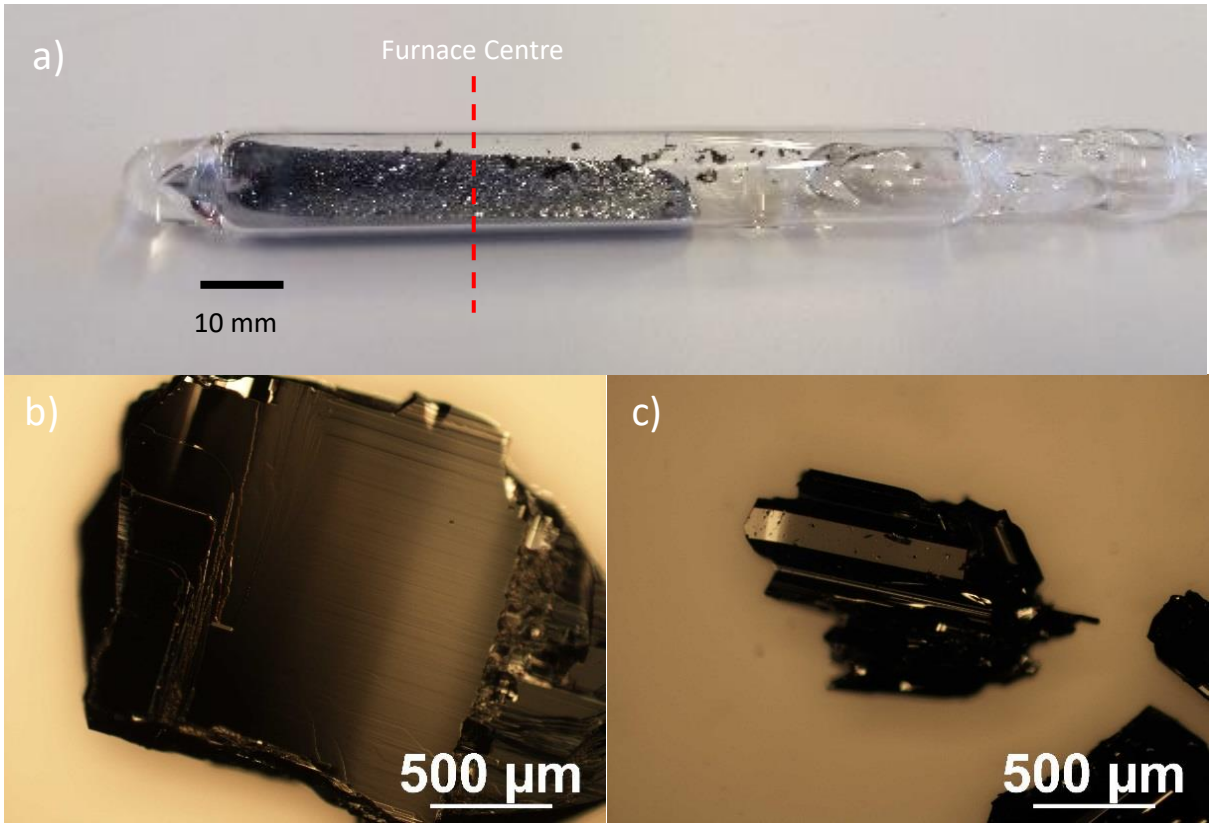

Fig. 5.4 a) Photograph showing a Sb_2Se_3 ingot grown by SSVG, within growth tube, with position of furnace centre (i.e. horizontal temperature peak) shown by the red dashed line. b) Optical micrograph of a cleaved face of the crystal showing cleavage steps. c) Optical micrograph of a narrow, needle-like Sb_2Se_3 crystal extracted from the free volume of the growth ampoule and showing crystal habit planes.

5.3.2 Scanning Electron Microscopy

Ingots were cleaved manually and imaged by optical microscopy (fig. 5.4b and c). The largest single crystal (fig. 5.4b) exhibited cleavage planes and a large square facet around 1 x 1.5 mm in size and had parallel cleavage steps. Another fragment of the ingot contained a narrow, columnar crystallite (fig. 5.4c) several hundred µm long. These secondary crystallites are a known feature of the SSVG method[3].

Figs. 5.5a-b show crystallites of unprocessed 5N source material ranging from 0.5 to 10 μm in size with no clear long-range order. In contrast, the images of the sample grown from SSVG (SSVG-5NAA) (fig. 5.5c-d) indicate larger crystals, up to 400 μm in size (fig. 5.5c) and showing crystallographic cleavage.

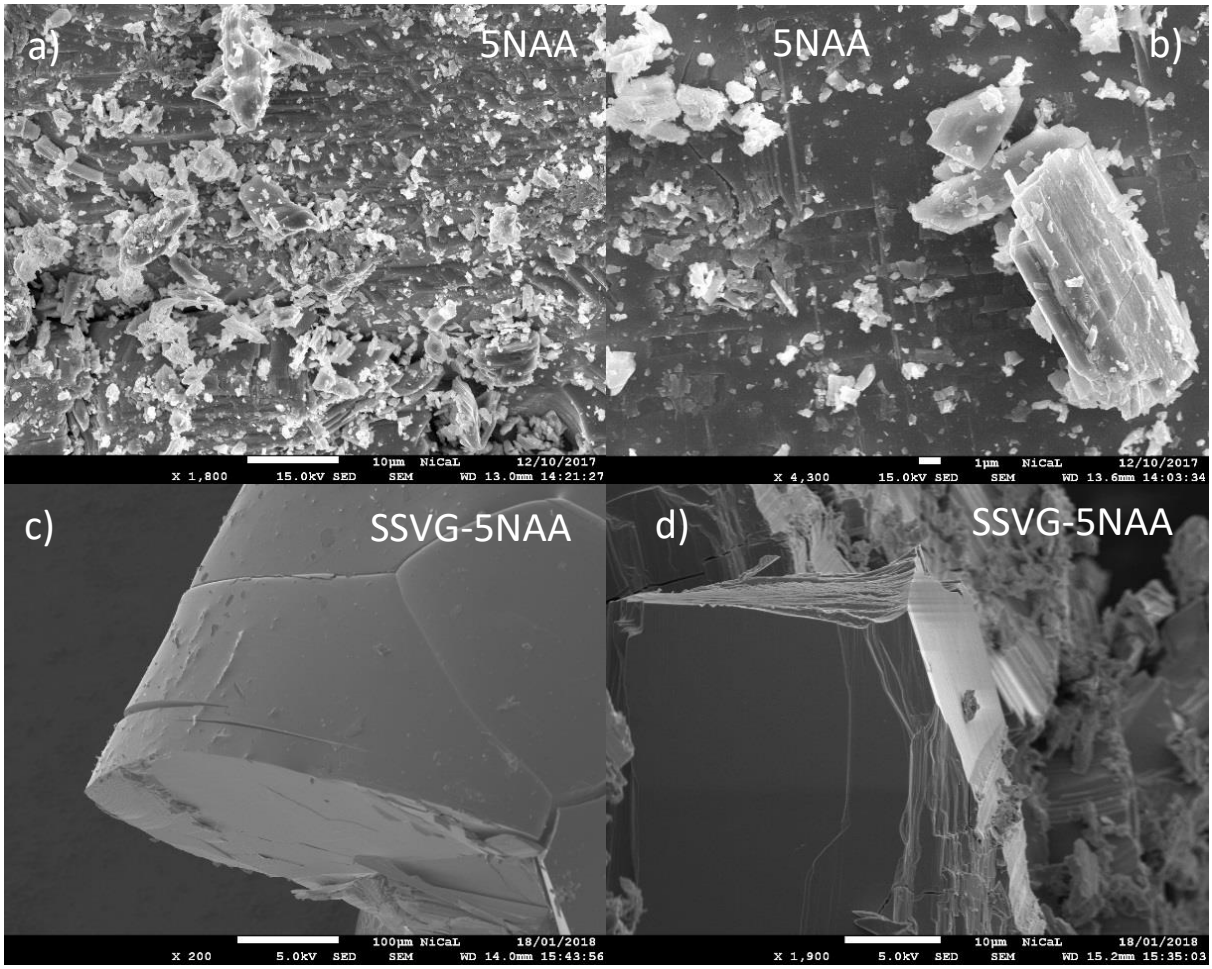

Fig. 5.5 a-b) Scanning electron microscope images of 5N Sb_2Se_3 source material (5NAA) and (c-d) crystallites grown by SSVG (SSVG-5NAA) showing an increase in grain size from 0.5- 10 μm (a-b) up to 400 μm (c-d) in size. This confirms that the SSVG process stimulates crystal growth.

The grains formed in these samples (fig. 5.5c-d) demonstrate a significant increase in size compared to the unprocessed source material following growth over a timescale of weeks (fig. 5.5a-

b), with clearly observed grain boundaries and cleavage planes indicating individual crystal grains. These millimetre-scale grains demonstrate the success of the SSVG method, but the grains remain fairly small, despite the long time periods (2 weeks) involved in processing, with the crystals shown in figs. 5.4b and c likely to be at the upper limit of size without changes to the thermal conditions. It is concluded that other growth methods may produce larger single crystals, more suitable for characterisation.

5.4 Direct Synthesis of Doped and Undoped Sb_2Se_3 from the Elements

Direct synthesis of Sb_2Se_3 from the elements was carried out so as to allow preparation of material intentionally doped with Sn and $MgCl_2$, and also to provide source material having different and lower levels of impurities than the 5N Sb_2Se_3. Here, 6N Sb and 5N Se shot were reacted in sealed quartz tubes at 615°C for 24 hrs.

The reaction was expected to occur as follows:

1. Se vaporises under the high temperature and low pressure
2. Se vapour reacts with the surface of the Sb shot, forming Sb_2Se_3
3. Since Sb_2Se_3 has a higher vapour pressure than Sb, it evaporates from the surface of the shot
4. The surface of the Sb underneath is exposed, allowing further reaction between Sb and the Se vapour
5. The highly mobile Sb_2Se_3 vapour allows for the rapid mixing of Sb and Se-rich material, resulting in good homogeneity

Both stoichiometry and doping were controlled to the precision achievable by weighing (see Section 3.2.3).

5.4.1 Inspection

Photographs of undoped stoichiometric and Se-rich Sb_2Se_3 directly synthesised from the elements (DSE-St-Un and DSE-SeR-Un) are shown in figs. 5.6a and b respectively. For both, most of the synthesised material formed at the site of the source elements, close to the tube tip, and consisted of a mixture of dense material and thin, needle-like crystals. Further away from the tube tip, separate pieces of material formed, with a similar appearance to the sections closer to the tube tip.

This morphology most likely arises from the liquid and gas phases present in the ampoule. The long sections of Sb_2Se_3 away from the tube tip appear to have formed from solidified pools of liquid, which extend along the full length of the ingot. Meanwhile, the needle-like crystals most likely result from condensation of vaporised Sb_2Se_3. It is not known whether the needle-like crystals developed while the ampoule was held at high temperature, or whether they condensed only as the tube was cooled, or a combination of the two. Either way, it is likely that the radial temperature gradient of the tube furnace played a role. While the SSVG phenomenon was not intended during this growth process, these results may indicate that a large free volume encourages the growth of these needle-like crystals.

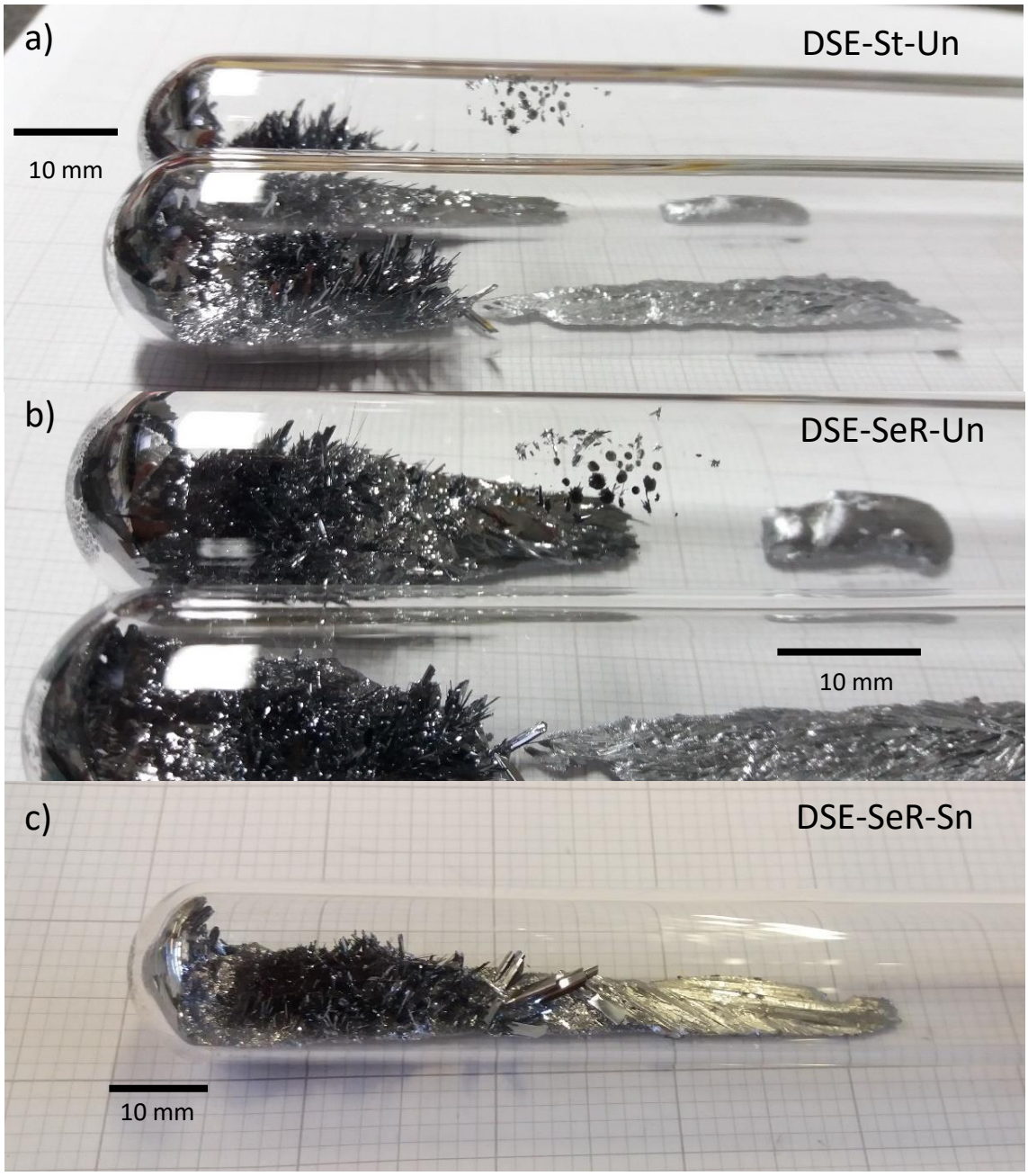

Fig. 5.6 Photographs of samples synthesised via direct synthesis from elements (DSE): a) undoped stoichiometric Sb_2Se_3, b) undoped Se-rich Sb_2Se_3, c) Sn-doped Se-rich Sb_2Se_3. The ingots consisted of dense, crystalline sections most likely resulting from solidified melt, coexisting with smaller, needle-like crystals, most likely formed from condensed Sb_2Se_3 vapour.

Although intended as a synthesis method, some of the material formed by direct synthesis from the elements contained grains large enough for electrical characterisation, without the need for further crystallisation. This is reported in Chapter 6.

5.4.2 Powder XRD of Sb_2Se_3 Directly Synthesised from the Elements

Powder XRD was carried out on powderised fragments of an undoped stoichiometric ingot directly synthesised from the elements, as shown in fig. 5.7 (black). The pattern matches well with the crystal diffraction pattern for the 5N source material (fig. 5.2, black). Rietveld refinement (fig. 5.8) indicates that this pattern matches closely with the *Pbnm* orthorhombic structure of Sb_2Se_3 and thus confirming formation of the compound. The lattice parameters were *a* (Å) = 11.63061(21), *b* (Å) = 11.78079(20), *c* (Å) = 3.97648(7).

A Se-rich Sn doped sample was also prepared by direct elemental synthesis with 0.1 at% Sn added. An ingot resulting from this process (DSE-SeR-Sn) is shown in fig. 5.6c. The appearance is very similar to the undoped samples, with small-needle-like crystals and dense underlying sections of the ingot.

Fig. 5.7 compares powder XRD of the Se-rich Sn-doped and the stoichiometric undoped samples. They are similar, the only notable difference being the presence of an additional peak at 28.64° for the Sn-doped sample (fig. 5.7a, blue arrow) which does not appear in the pattern for the stoichiometric undoped sample. Rietveld analysis is shown in fig. 5.8 and confirmed a match to the *Pbnm* crystal structure, with lattice parameters determined as: *a* (Å) = 11.63231(18), *b* (Å) = 11.78126(21), *c* (Å) = 3.97777(9). This represents a slight expansion of the unit cell volume compared to the undoped sample.

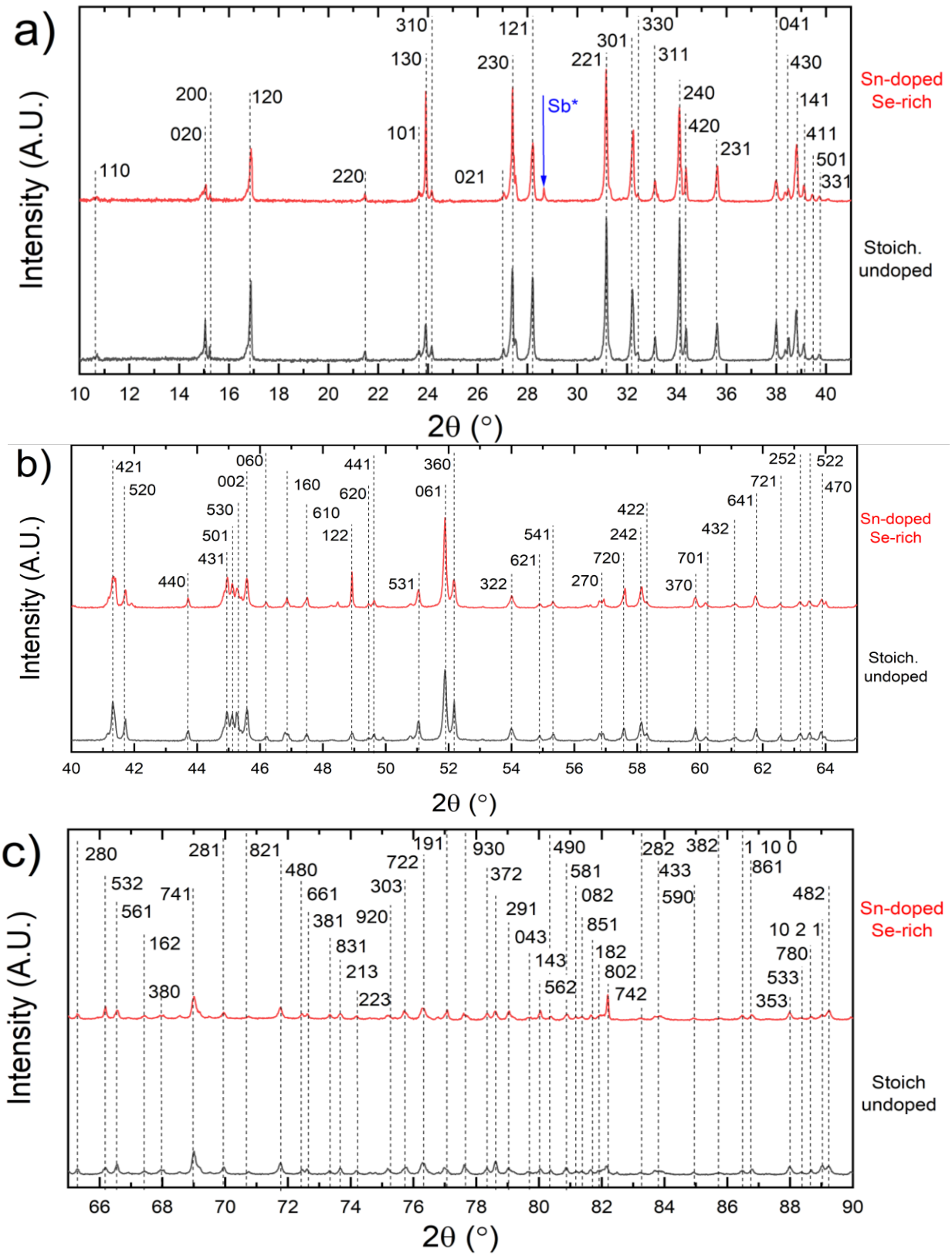

Fig. 5.7 θ-2θ scans (linear intensity scale) of powderised samples of undoped stoichiometric and Sn-doped Se-rich Sb_2Se_3. Apart from the peak that appears at 28.64° (Sb*), all peaks that appear are indexed to expected diffraction peaks for Sb_2Se_3.

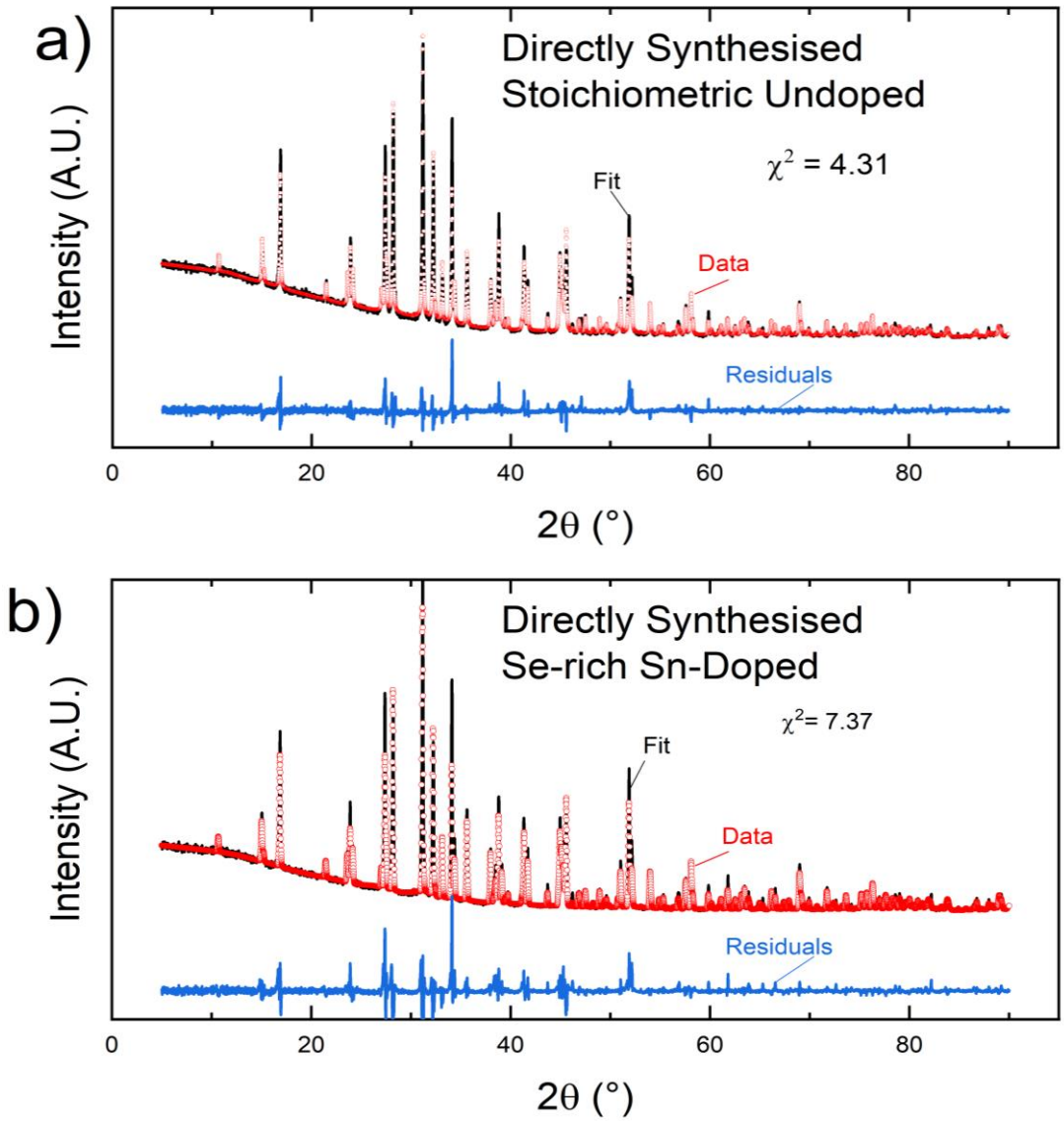

Fig. 5.8 Rietveld refinement (linear intensity scale) for the same patterns shown in fig. 5.7: a) undoped stoichiometric and b) Se-rich Sn-doped Sb_2Se_3 synthesised from elements.

The additional peak at 28.64° in fig. 5.7a is not easily assigned to any peak expected for Sb_2Se_3, nor may it be assigned to peaks expected from elemental Se, Sn or the compound SnSe. It is possible that it corresponds to the Sb 110 diffraction peak, although shifted slightly from its expected position at 28.8° [Rruff R050654]. A small Sb excess in the synthesised material may result, despite

the Se-excess in the source, from Sb being displaced by Sn during the reaction, so this assingment is plausible.

5.5 Direct synthesis of $Sb_2S_{3x}Se_{3(1-x)}$ Solid Solutions from Compounds

5.5.1 SEM and EDX

Samples of $Sb_2S_{3x}Se_{3(1-x)}$ were prepared with values of x of 0.2 and 0.5, by a combining 5N Sb_2Se_3 and Sb_2S_3 source material (Section 3.2.3). These ratios were chosen because the bandgap of Sb_2S_3, at 1.74 eV, is larger than the optimal bandgap for solar cells at 1-1.5 eV (see Section 2.2.6), so the selenium-rich side of the composition range was expected to be more technologically relevant. Furthermore, time pressures only permitted two samples to be synthesised, so these compositions were expected to effectively cover the technology-relevant compositional range. Upon removal from the tube, the ingots had a similar lustre and grey colour to the source materials, with no signs of segregation.

SEM images were taken of fragments of both samples and shown in fig. 5.9a-b, showing crystalline, columnar structures, which bore similar appearance to the 5N source material and crystals grown by SSVG (see fig. 5.6). EDX was carried by exposing two analysis areas to the electron beam, each around 1 x 1 mm^2 in size, for each sample, with measurements taken on 7-10 sites for each area. Typical spectra for these scans are shown in fig. 5.9c-d, where all expected elements produced peaks, and a more intense S peak relative to Se was seen in the x = 0.5 compared to the 0.2. The elemental concentrations derived from these scans are shown in Table 5.2 and indicated that the samples were sulphur-rich compared to the weighed quantities, with values of x = 0.28 for 0.2 weighed, and x = 0.55 for 0.5 weighed, with a homogeneity of ~ 2 at% across the sampled area. The sulphur excess compared to the weighed proportions is not expected, and would not be explained by selenium loss, as the total chalcogen ratio [S+Se] compared to Sb is at the level expected. With no clear physical explanation, it may be that the matrix correction step of the analysis was unable to accurately translate the EDX peak intensity into elemental ratios for these scans.

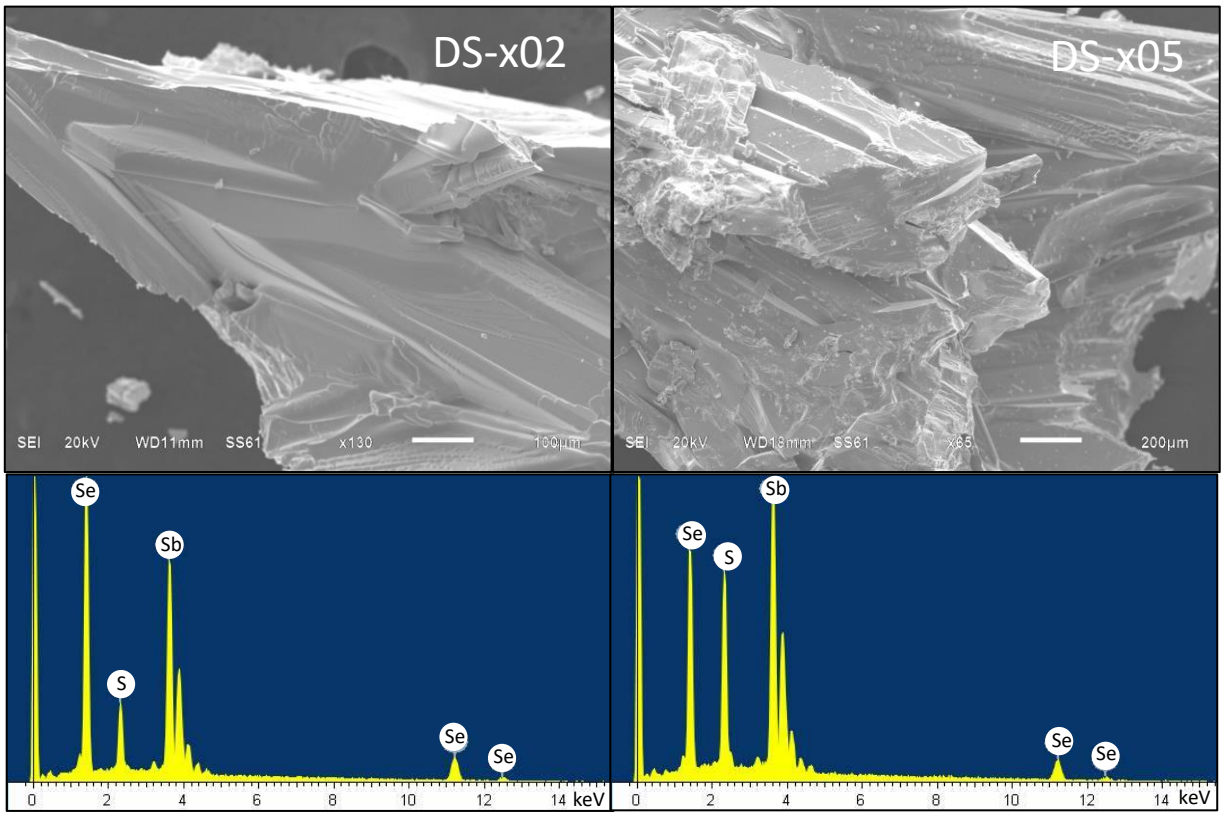

Fig. 5.9 a-b) SEM images of $Sb_2S_{3x}Se_{3(1-x)}$ samples synthesised by direct reaction of the compounds Sb_2Se_3 and Sb_2S_3 with weighed *x* - values of: a) 0.2 (DS-x02) and b) 0.5 (DS-x05). Images show columnar crystalline morphology with no evidence of segregation. c-d) Typical EDX spectra for compounds with weighed *x*-values of c) 0.2 (vertical scale is 2257 cts) and b) 0.5 (vertical scale is 1841 cts) demonstrating the presence of all key elements.

Weighed *x* – value:	0.2		0.5	
Appearance	Analysis Area 1 (*N*=10)	Analysis Area 2 (*N*=7)	Analysis Area 1 (*N*=10)	Analysis Area 2 (*N*=7)
Elements at%				
Sb	41 ± 2.5	40.2 ± 1.1	40.7 ± 1.7	40.8 ± 1.2
S	16.6 ± 0.6	15.7 ± 2.3	33.2 ± 1.8	31.9 ± 1.0
Se	42.6 ± 1.8	44.1 ± 2.0	26.9 ± 1.3	27.3 ± 0.7
Measured *x* - value	0.28	0.26	0.55	0.54

Table 5.2 Atomic percentage values measured by EDX for Sb, S and Se in the directly synthesised $Sb_2S_{3x}Se_{3(1-x)}$ samples with weighed *x* - value = 0.2 (DS-x02) and 0.5 (DS-x05). The *x* – value measured from EDX is also shown, indicating a higher S concentration than the weighed values. The number of measurement sites *N* is indicated for each area examined.

SEM and EDX results suggest that segregation has not occurred in the $Sb_2S_{3x}Se_{3(1-x)}$ samples, offering evidence for the formation of solid solutions. XRD was carried out to confirm this.

5.5.2 Powder XRD of $Sb_2S_{3x}Se_{3(1-x)}$

XRD of the $Sb_2S_{3x}Se_{3(1-x)}$ samples where $x = 0.28$ and $x = 0.55$, was compared to that of unprocessed 5N Sb_2Se_3, as well as literature data for Sb_2S_3 or 'stibnite' from Kyono and Kimata [4] as shown in fig. 5.10. All are similar, with the key difference being the expected shift in position of all XRD peaks to higher angles with increasing *x* – value, as indicated for the 221, 303, 311 240 and 420 peaks.

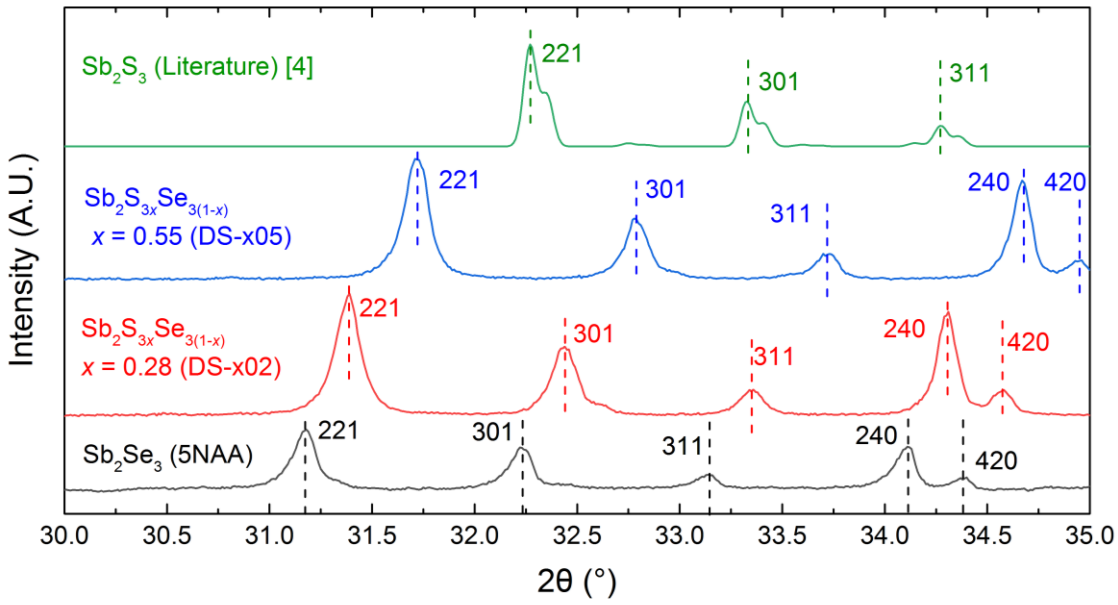

Fig. 5.10 θ - 2θ scans (linear intensity scale) of powderised fragments of 5N Sb_2Se_3 (5NAA, black), $Sb_2S_{3x}Se_{3(1-x)}$ with *x* values estimated from EDX as 0.28 (DS-x02, red), and 0.55 (DS-x05 blue) compared to a θ - 2θ scan for Sb_2S_3 [4] (green). The shift of the diffraction peaks to higher angle with increasing *x* - value can be observed.

The absence of new peaks and the shift in XRD peaks with *x* - value indicates the formation of a homogenous solid solution of Sb_2S_3 and Sb_2Se_3. The shift in peak position is consistent with the expected decrease in lattice parameters as Se is replaced with S.

Rietveld refinement (Section 3.3.3.2) results for the same XRD patterns are shown in figs. 5.11a and b respectively. The positions of the peaks matched well between the data and the modelled structure, providing a good fit to the structure expected for a $Sb_2S_{3x}Se_{3(1-x)}$ solid solution, assuming S replaces Se atoms in the unit cell, with starting lattice parameters interpolated between the values of lattice parameter for the end members Sb_2S_3 and Sb_2Se_3. However, the peak intensities had significant residuals, which were largest for peaks in the {010} plane family in both cases, suggesting a preferred orientation of the powder as deposited on the sample plate towards [010].

The lattice parameters for the solid solutions were estimated from the refinement as *a* (Å) = 11.56616(15), *b* (Å) = 11.71360(16), *c* (Å) = 3.94809(4) for $Sb_2S_{3x}Se_{3(1-x)}$ where $x = 0.28$ and *a* (Å) = 11.43982(20), *b* (Å) = 11.58394(19), *c* (Å) = 3.90251(5) for $Sb_2S_{3x}Se_{3(1-x)}$ where $x = 0.55$, with *x*-values determined from EDX. Plots of the lattice parameters derived from Rietveld refinement are plotted against *x* – value in fig. 5.11c-d. Values are included for undoped stoichiometric Sb_2Se_3 directly synthesised from the elements (Section 5.4.2) and from literature for Sb_2S_3[4].

The lattice parameters do not exhibit a linear Vegard relation, with slight upward bowing observed. A quadratic fit to the trends yielded relations as follows: *a* (Å) = 11.635(16) – 0.24(8)*x* – 0.179(7) x^2, *b* (Å) = 11.783(7) – 0.173(3)*x* – 0.33(3)x^2, *c* (Å) = 3.978(5) – 0.110(23)*x* – 0.039(22)x^2.

The shift in the lattice parameters with composition provides further evidence for the formation of solid solutions. Given the small number of data points, further investigation beyond the scope of the present work is necessary to confirm the extent of bowing. Uncertainty in the value of *x* as measured by EDX would also need to be addressed.

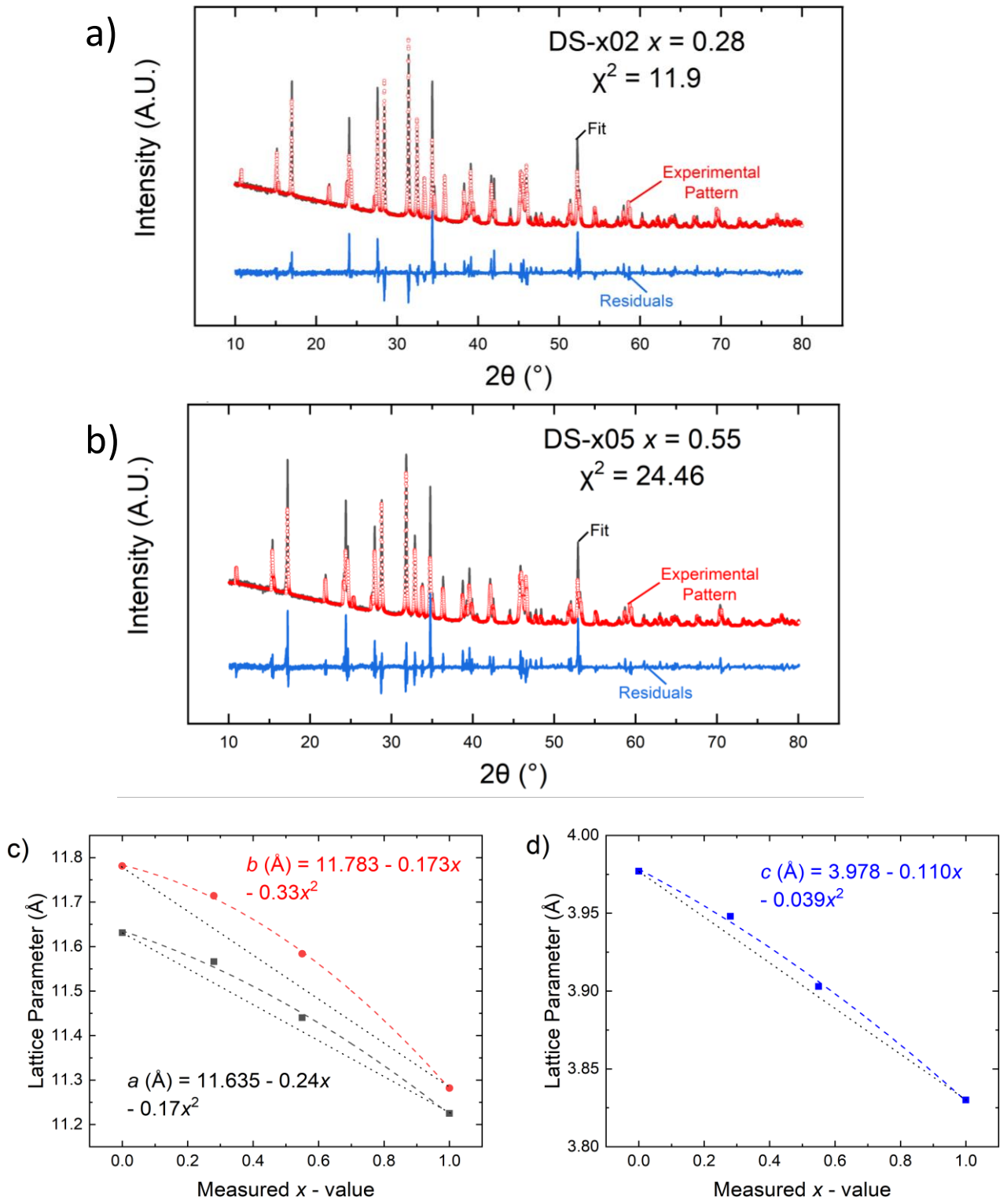

Fig. 5.11 a-b) Rietveld refinement (linear intensity scale) of the powder XRD patterns for $Sb_2S_{3x}Se_{3(1-x)}$ samples with x values of a) 0.28 (DS-x02) and b) 0.55 (DS-x05) as determined from EDX, with the measured XRD pattern shown in red, the fits in black and the residuals in blue. Fits and data matched well on peak position, but less well for peak intensity. c-d) Vegard plots (Sb_2S_3 data from [4]) showing a slight upward bowing from linear (dotted line) behaviour.

5.6 Vertical Bridgman Growth of Doped and Undoped Sb_2Se_3 Single Crystals

5.6.1 Crystal Growth Outcomes

Crystals grown by the vertical Bridgman technique are listed in Table 5.1 and included crystals grown from commercial 5N Sb_2Se_3 and from Sb_2Se_3 directly synthesised from the elements (DSE), the latter being either stoichiometric, Se-rich or Se-poor.

The samples prepared from the 5N Sb_2Se_3 source material were grown either under vacuum (1×10^{-5} mbar) or under an argon pressure of 100 mbar, both in tubes of 4 mm inner diameter, with samples denoted VB-4mm-5NAA-Vac and VB-4mm-5NAA-Ar.

The Sb_2Se_3 crystals grown by the vertical Bridgman method are photographed in fig. 5.12. in both cases the ingot consisted of multiple pieces, separated by voids, with a greater number of voids in the sample grown under vacuum than that grown under argon. The voids contained small, long thin crystals, with growth following a helical path, as illustrated by the sketches in figs. 5.12c-d.

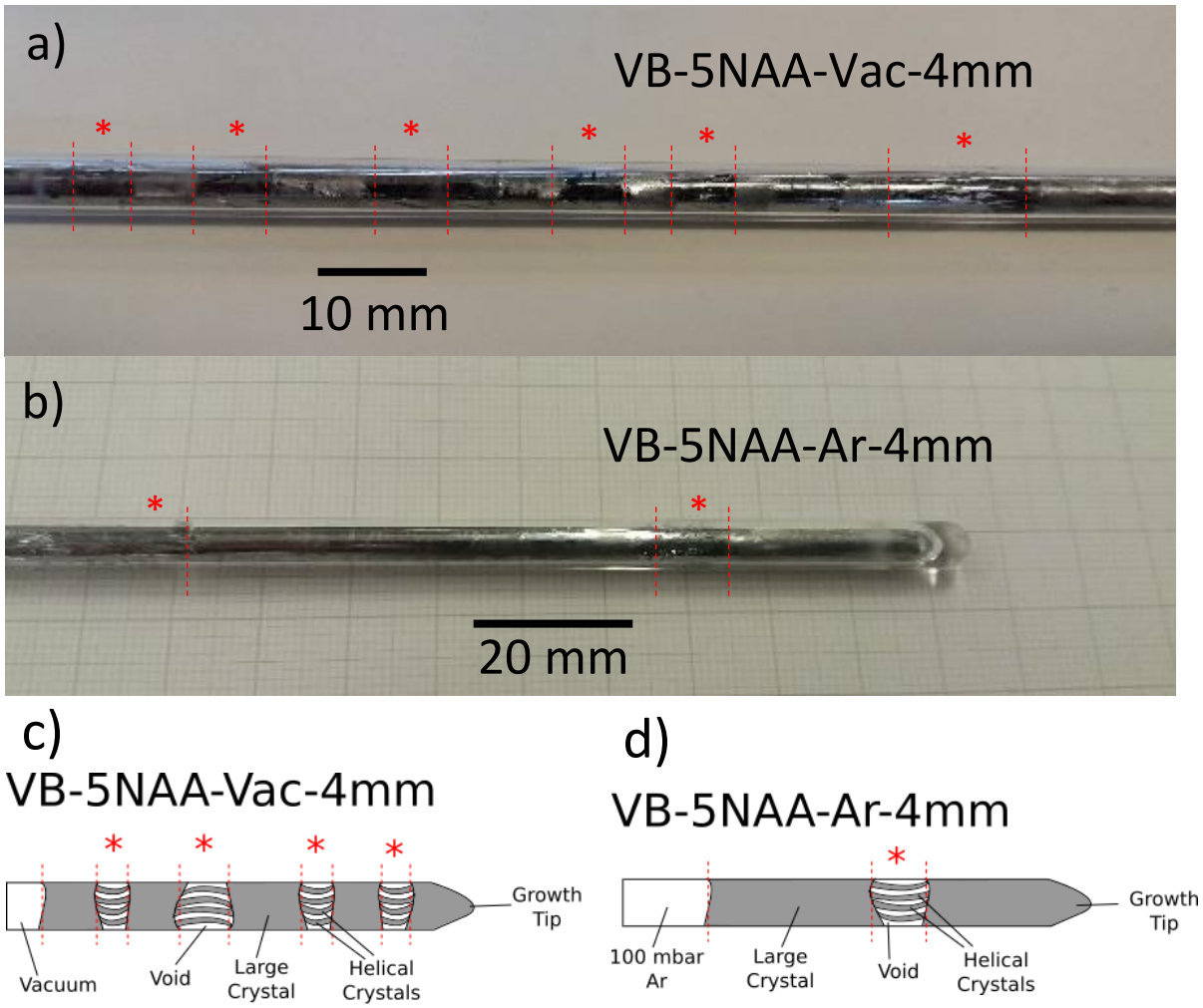

Fig. 5.12 a-b) Photographs showing Sb_2Se_3 crystals grown via vertical Bridgman in 4 mm tubes a) under vacuum (VB-5NAA-Vac-4mm) and b) under argon (VB-5NAA-Ar-4mm), within quartz growth tubes. Samples comprised solid portions separated by voids (indicated by red stars) inhabited by needles as shown in the diagrams in c) and d).

The greater prevalence of voids appearing under vacuum than under argon could be explained by greater sublimation of Sb_2Se_3 during the growth process, due to the lower pressure used, however under the argon pressure used, boiling of the Sb_2Se_3 is expected to be suppressed (see Section 3.2.5.1), so the formation of voids as bubbles is not a satisfactory explanation. More likely, therefore, is that the voids formed due to uneven melting of the powder, as the entire length of the tube would

not have been heated above the melting point of Sb_2Se_3 at one time. The powder was also not packed to high density prior to growth (see Section 3.2.5.1), so with melting and the resulting increase in density, grains are likely to have coalesced, with the adhesion of material to the tube walls allowing them to remain separate. Pre-melting of the entirety of the powder would most-likely prevent this from happening. The small crystals present within the voids most likely condensed from vapour, with the helical path resulting from the rotation of the ampoule during growth. These secondary crystals were too small to be of any value in further work.

Photographs of the same crystals after extraction from the growth tubes are shown in fig. 5.13. The assumption of single crystals was based on the cleavage behaviour of the solid pieces: Several large sections were found to very easily cleave along oriented parallel planes, as illustrated in fig. 5.13b and d. The cleaved surfaces were flat and reflective, and further cleavage allowed thin, flat sections of material to be separated, as shown in fig. 5.13c.

Figs. 5.13e-f) show a Sb_2Se_3 sample grown under 100 mbar Ar in a 10 mm diameter tube (VB-5NAA-Ar-10mm). This crystal fractured irregularly, with crystal facets (fig. 5.13e) becoming larger at greater distance from the bottom of the tube (along arrow of growth direction). An especially large facet is shown in fig. 5.13f, the size of which increased with distance from the bottom of the growth tube in tapering fashion. These features demonstrate that small grains formed at the growth tip expanded into larger crystals as the process progressed.

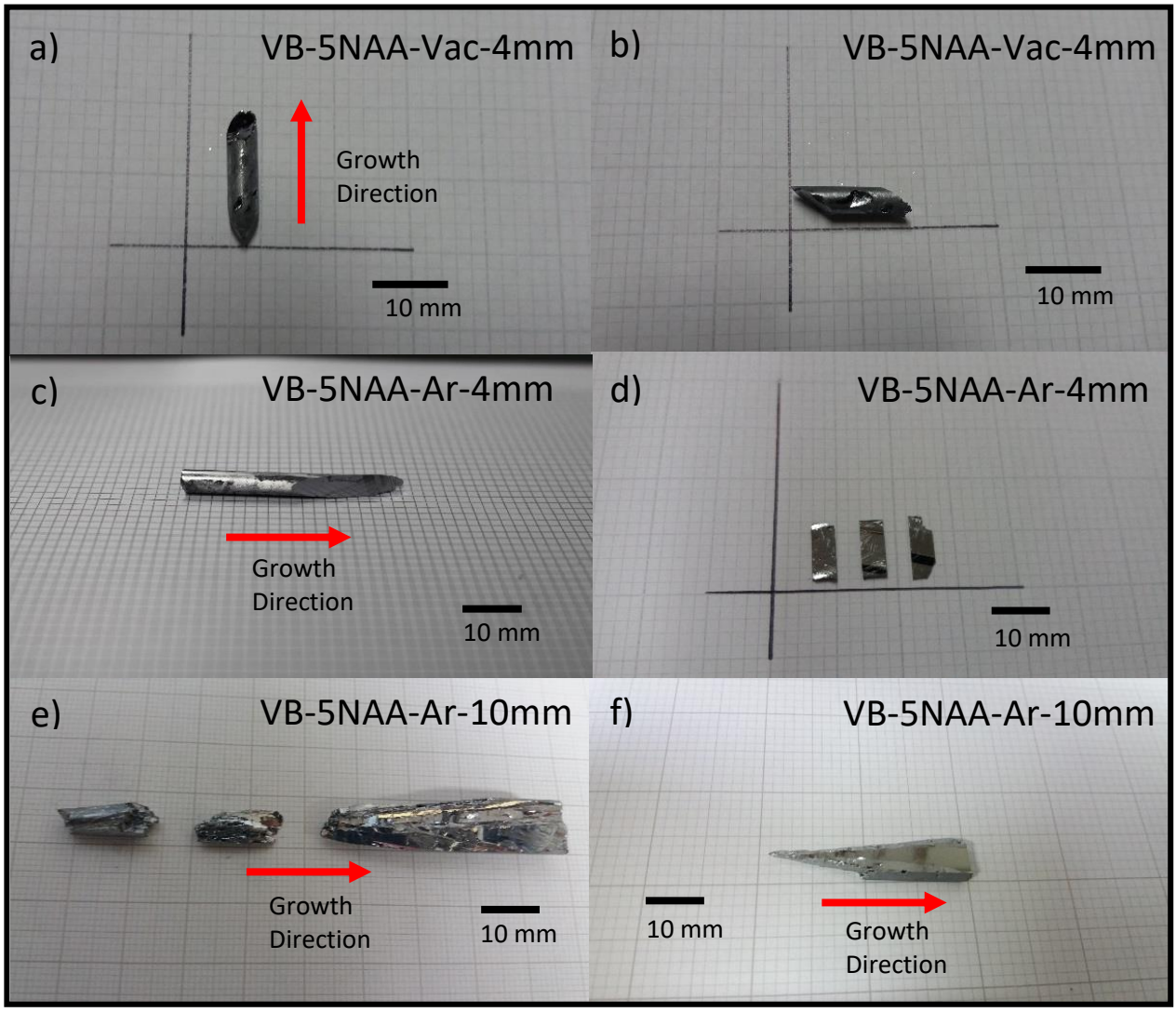

Fig. 5.13 Cleaved sections of Sb_2Se_3 crystals grown by vertical Bridgman a-b) under vacuum and c-f) under argon in a-c) 4 mm and e-f) 10 mm diameter tubes, with sample identifiers in the images. The red arrows indicate the direction of crystal growth, from the bottom to the top of the growth tube. The parallel cleavage planes in b-d demonstrate the extent of single crystal domains.

Based on these results, two growth mechanisms are proposed for the crystals grown by vertical Bridgman, shown in fig. 5.14. Fig. 5.14a concerns the growth mechanism for the sample in the larger, 10 mm diameter tube, where multiple nucleation points in the conical tube tip means that many grain orientations are present. However, a crystal grain having its fastest-growing crystal axis (most likely [001]) most-closely aligned with the tube axis will outgrow the surrounding crystals. As

this crystal grows, it is able to incorporate more of the melt until it is the only orientation present at the top of the tube. Fig. 5.14b proposes a growth mechanism for the 4 mm diameter samples, where the initial nucleation in the conical region of the tip proceeds in the same way, except that large voids filled with Sb_2Se_3 vapour may form, maintained by the surface tension of the melt within the smaller-diameter tube. Within these voids, vapour-solid growth of small, narrow crystals (similar to those observed in direct synthesis from the elements, see Section 5.4.1) follows, of which one or more may nucleate crystal growth in the melt above. This would explain why large voids often separate polycrystalline sections from single crystal sections in these samples, without gradual transitions as is observed for the growth regime proposed in fig. 5.14a. The abrupt appearance of single crystals for samples grown in 4 mm tubes means that this growth process provided a greater yield of single crystals for the initial mass of Sb_2Se_3 used.

These results would suggest that single crystals ~1 cm long and 4 mm wide may be grown by the vertical Bridgman method using 4 mm internal diameter tubes, a significantly larger size than those achieved in the Piper-Polich or SSVG methods (see Sections 5.2 and 5.3 respectively). Further evidence for monocrystalline nature is provided by XRD, carried out on the cleaved face of a Sb_2Se_3 single crystal grown under argon in a 4 mm tube, in Section 5.6.3, which suggested that the cleaved surface is (010). The XRD measurement alone does not provide proof of single crystals, as a columnar polycrystalline sample with strong preferred orientation would produce the same results. However, the narrow, intense diffraction peaks, combined with the observation of a continuous, clean reflective surface coming as a natural product of sample cleavage, provide consistency with single crystals. As a result, these samples are treated as single crystals in later analysis, even though this is not confirmed. Laue diffractometry would be necessary to unambiguously confirm single crystals, which could also be achieved through the imaging of Kikuchi patterns resulting from electron-backscattered diffraction. But the equipment was not available for the former and time constraints did not allow for the latter.

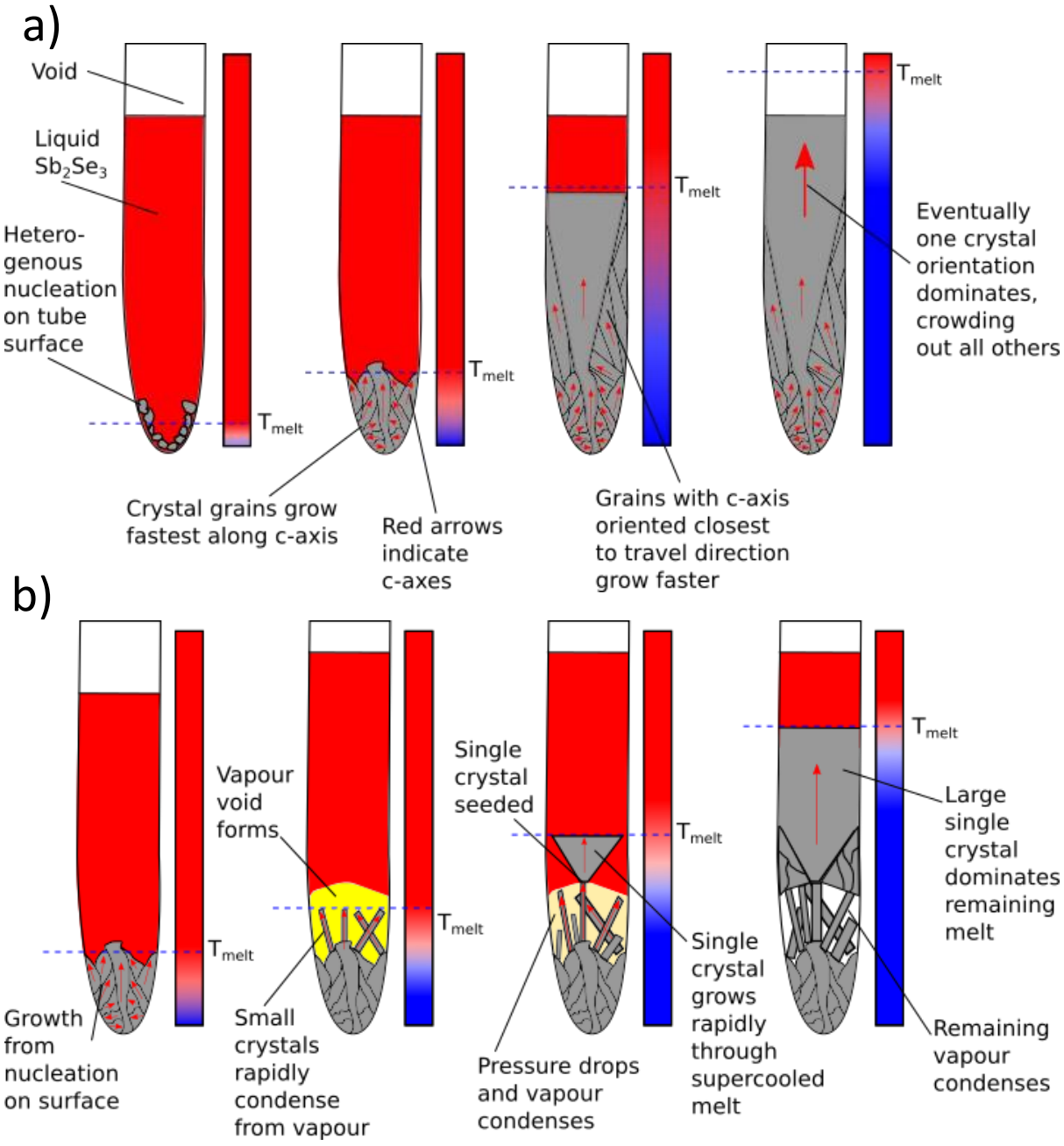

Fig. 5.14 Diagram of proposed growth processes for Sb_2Se_3 single crystals grown by vertical Bridgman method in a) 10 mm diameter and b) 4 mm diameter ampoules. For the case of 10 mm diameter ampoules (a) nucleation occurs in the region of the conical tube tip, with the crystal with fastest-growing crystal axis (most likely [001]) outgrowing the competing crystals. For the smaller diameter ampoules (b) vapour-filled voids may form due to uneven melting and grain coalescence, within which small, narrow crystals condense from vapour, and may then orient growth in the melt above them, leading to rapid growth of large single crystals.

5.6.2 Orientation of Indexed Faces by Visual Inspection

An optical micrograph of the cleaved surface of Sb_2Se_3 single crystal grown by vertical Bridgman under argon in a 4 mm tube (VB-5NAA-Ar-4mm) is shown in fig. 5.15a. This shows a flat, reflective surface with crystallographic cleavage steps. Sections of Sb_2Se_3 crystal were cut orthogonal to the cleaved surface ((010) plane), both parallel and perpendicular to these cleavage steps. These surfaces are shown in fig. 5.15c and d respectively. The cut and polished surfaces were flat and reflective, with some voids also being visible on both surfaces along with some lines from polishing damage and irregular crystallographic cracks.

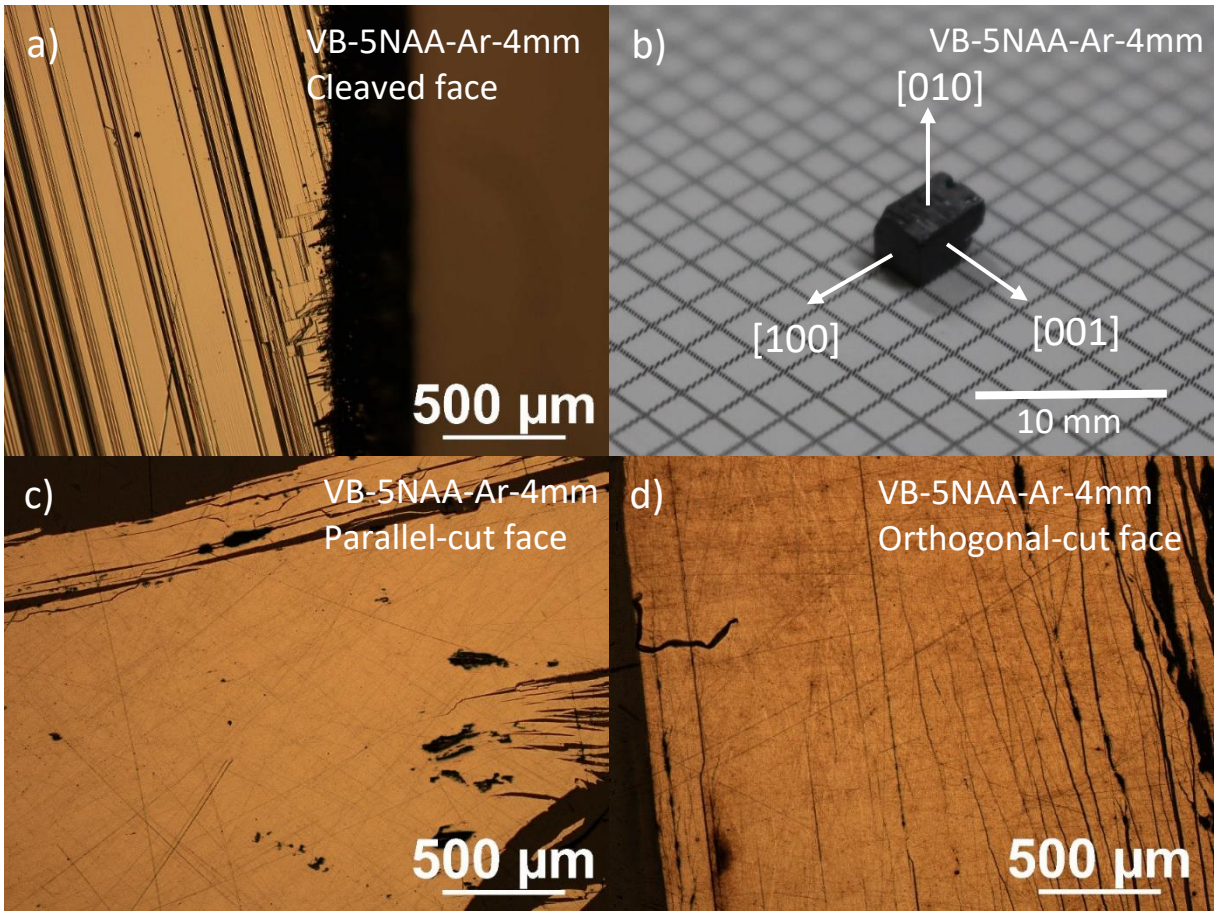

Fig. 5.15 a) Optical micrograph of a cleaved (010) surface of a Sb_2Se_3 crystal grown by vertical Bridgman (VB-5NAA-Ar-4mm). XRD results suggested that the cleavage steps lie parallel to [001]. b) Photograph of Sb_2Se_3 single crystal prepared by cleaving on (010) then cutting with a diamond saw both parallel and perpendicular to the cleavage steps, and perpendicular to the cleaved surface, so as to cut on (100) and (001). c-d) Optical micrographs of the (100) and (001) surfaces after mechanical polishing.

The cleavage steps observed on the (010) surface of the crystals (fig. 5.15a) are expected to run parallel to the [001] crystal axis, as Sb_2Se_3 is covalently bonded in this direction, with 1-dimensional molecular nanoribbons structured with van der Waals interactions in the [100] and [010] axes. This means that any secondary cleavage would be expected to involve (100) planes, leaving cleavage steps that lie perpendicular to both [100] and [010], i.e. parallel to the [001] axis. As the 1-dimensional nanoribbons lie along this axis, this provides a macroscopic indication of crystallographic orientation. These assumptions are supported by the XRD results in the following section.

5.6.3 Single Crystal XRD

XRD $\theta - 2\theta$ scans were carried out on the cleaved and cut planes of the Sb_2Se_3 single crystal grown by vertical Bridgman under argon, shown in fig. 5.16. All exhibit sharp peaks, which match very well with the positions expected from the Bragg formula (eq. 3.2 and 3.4) for the a) {100}, b) {010} and c) {001} families of planes, using the values of lattice parameter determined from powder XRD of Sb_2Se_3 (Section 5.4.2).

These results are consistent with the samples studied being single crystals, as the crystal orientations of planes at right-angles to each other would be unlikely to occur in a polycrystalline sample with a preferred orientation. Furthermore, they suggest that the plane cut parallel to the cleavage steps is (100), while the plane cut perpendicular to them is (001). This provides evidence that the cleavage steps do, in fact, run parallel to the covalent-bonded [001] crystal axis, as expected, and suggests that they may be used as a guide to orient the crystal without the need for Laue equipment, although the latter would provide more reliable information on orientation.

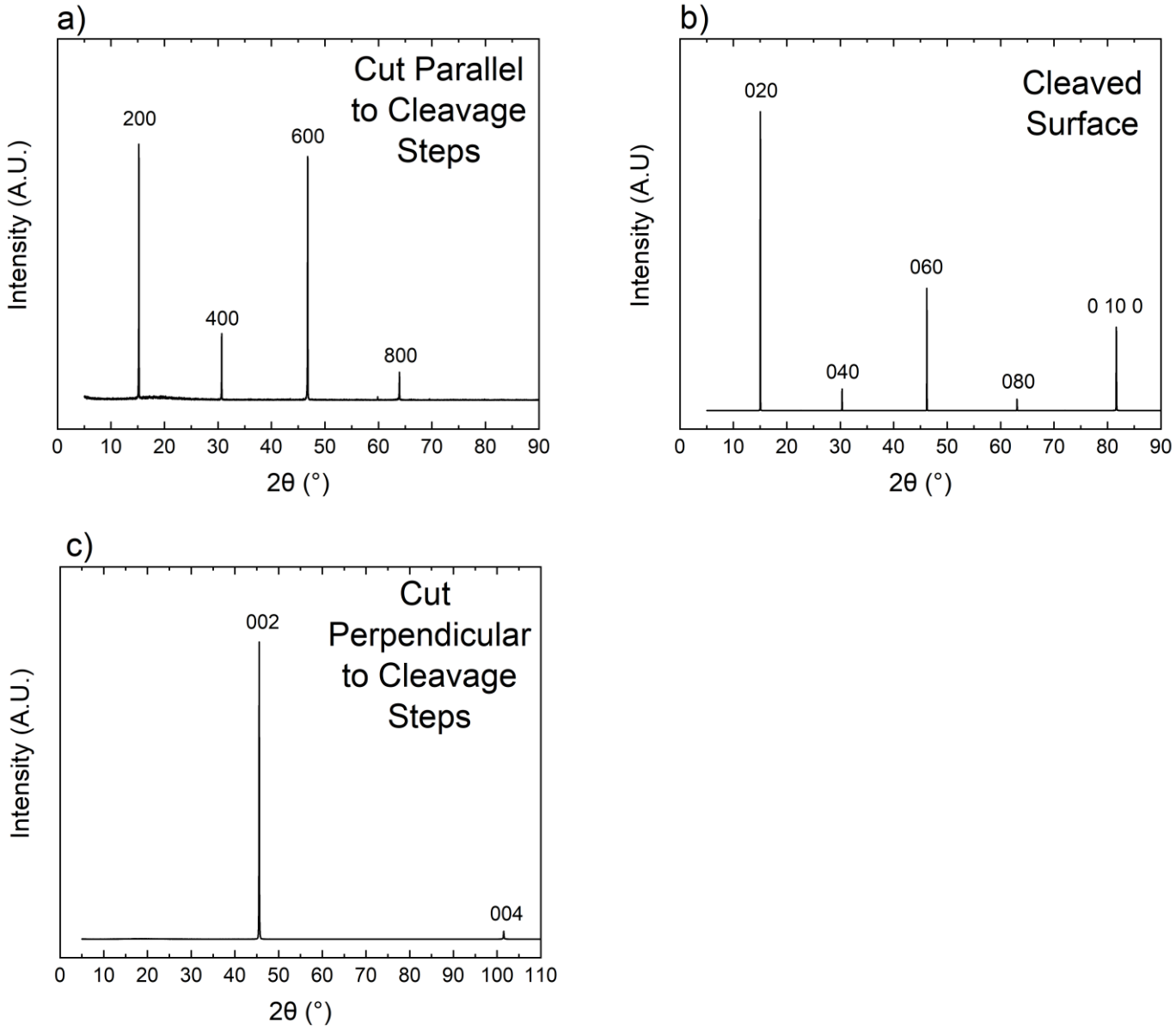

Fig. 5.16 XRD θ – 2θ scans (linear intensity scale) of cleaved and cut Sb_2Se_3 single crystal surfaces as shown in fig. 5.15, with a) the surface cut parallel to the cleavage steps (fig. 5.15c) and mechanically polished, b) the cleaved (010) plane (fig. 5.15a), c) the surface cut perpendicular to the cleavage steps (fig. 5.15d) and mechanically polished. The appearance of the even numbered peaks corresponding to planes in the: a) {100}, b) {010} and c) {001} plane families confirmed that these are the (100), (010) and (001) crystal planes respectively.

5.6.4 Low-Angle Boundary Defects in Sb_2Se_3

5.6.4.1 DIC Microscopy of a Deformed Sb_2Se_3 Crystal

Differential interference contrast (DIC) microscopy allows for the enhancement of the contrast in topographic features of a surface (Section 3.3.2.1). Figs. 5.17a-b show optical micrographs of a cleaved (010) surface of a Sb_2Se_3 single crystal sample grown by vertical Bridgman under Ar in a 4 mm diameter tube. In addition to the cleavage steps aligned with [001], there were dark and bright bands that ran perpendicular to them. The DIC micrographs of these areas (figs. 5.17c-d) show bands of high contrast running orthogonal to the [001] direction, confirming that these features are topographic.

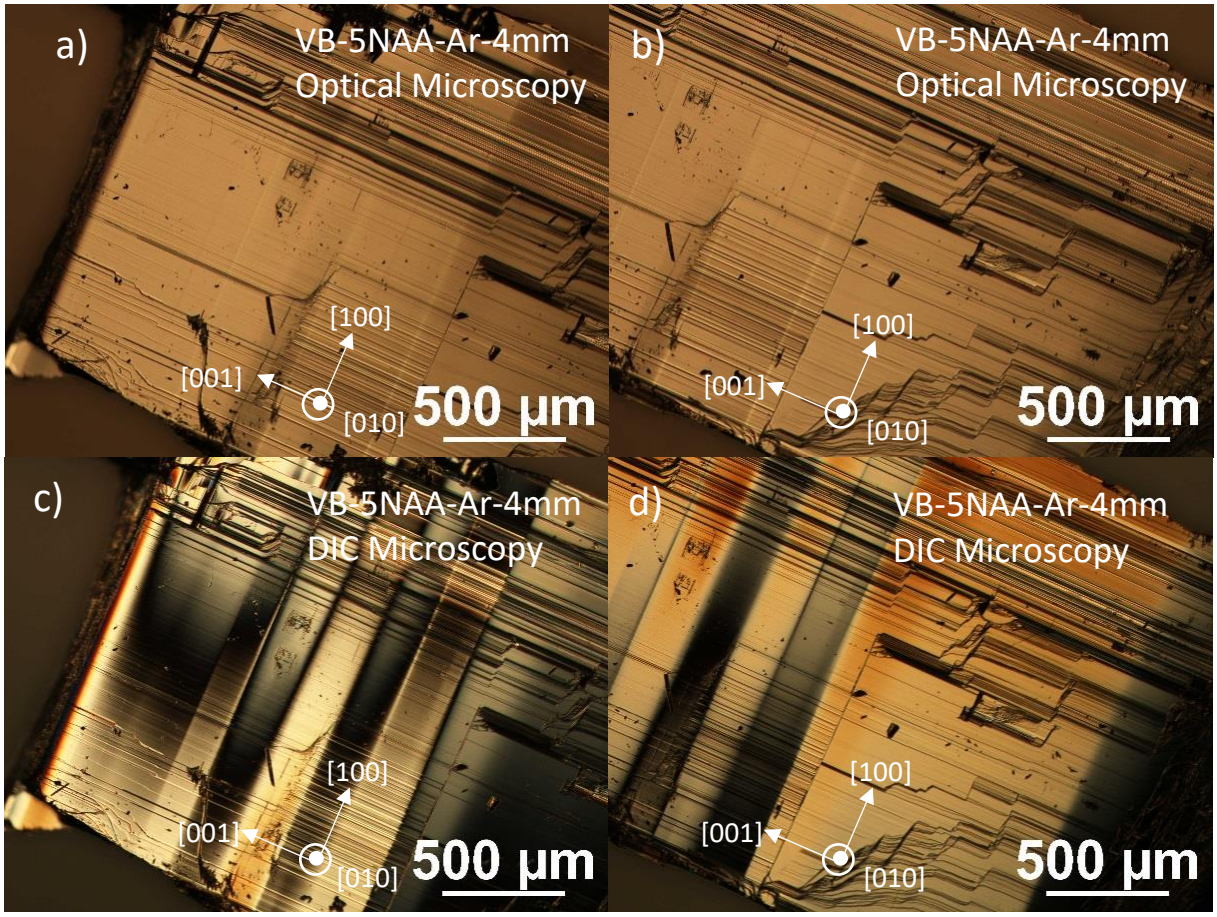

Fig. 5.17 a-b) Bright-field optical micrographs of cleaved (010) surface from Sb_2Se_3 single crystal sample grown by vertical Bridgman under Ar in 4 mm diameter tubes, with crystal axes indicated. Dark and bright bands orthogonal to cleavage steps are visible. c-d) DIC micrographs of the same locations, where shade represents the gradient of the surface and confirming that the dark and bright bands are topographic features.

These features correspond to abrupt undulations in the surface ~ 100-200 µm in width and, given that they are oriented parallel to [100] and perpendicular to [001] covalently-bonded chains, would represent a rotation about the [100] crystal axis. These distortions are evidently crystallographically aligned, and are associated with undulations in surface height. As such they do not resemble conventional defect structures that are known for metals and cubic semiconductors. For example, dislocation tilt boundaries (polygonization walls) can arise from arrays of dislocations and

they are never seen to be straight and parallel. Similarly large angle random grain boundaries are not straight. A case could be made that they constitute high symmetry grain boundaries, namely twins, which lie on distinct crystal planes with the twin bands lying parallel to one another. If this were the case, then each twin band would have a large and systematic crystal axis misorientation with its neighbour. However, since the structure of Sb_2Se_3 comprises covalent ribbons connected by van der Waals forces, an alternative defect type should be considered, namely, the 'kink-band' resulting from 'ripplocations', in which the ribbons systematically buckle in response to stress. These defects were introduced in Section 2.4.3 and are described in ref 5. This possibility is investigated further by EBSD reported in the following section.

5.6.4.2 Electron Backscattered Diffraction of Deformed Sb_2Se_3 Crystal

Electron backscattered diffraction (EBSD) was carried out (see Section 3.3.7) on the cleaved (010) face of a Sb_2Se_3 single crystal sample grown by vertical Bridgman in a 4 mm tube under Ar, but a different sample to that examined with DIC microscopy. A secondary electron SEM map is shown in fig. 5.18a, with a single band ~600 μm wide brighter than its surroundings, suggesting changing topography.

An orientation map of the same region, formed from the fitting of Kikuchi patterns of backscattered electrons for each pixel, is shown in fig. 5.18b. The blue areas correspond to regions where the (010) plane lies in the plane of measurement. It shows abrupt changes in orientation at two boundaries, with relatively constant orientations elsewhere. These form the boundaries of a band ~ 600 μm wide where the crystal orientation is rotated from the reference point (red cross) by up to 3°. The angular misorientation from the reference point along the line AB is plotted in fig. 5.18c. The misorientation profile suggests that low-angle crystallographic boundaries are present at 130 μm and 820 μm, corresponding to the boundaries in the orientation map. Fig. 5.18d represents the likely arrangement of the crystal planes based on the misorientation linescan, with low-angle boundaries included. The inferred topography resulting from this arrangement matches the features observed with

DIC microscopy (Section 5.6.4.1) meaning that both represent crystallographic distortions in the crystal, specifically a rotation about the [100] crystal axis. The deformation feature observed here is wider than the bands that appear in DIC microscopy, but otherwise matches their form, suggesting that these features do not have a characteristic wavelength and that the two low-angle boundaries observed here are independent.

The low-angle boundaries may be grain boundaries resulting from highly-oriented growth, explaining the straightness of the boundaries and the similar orientation either side, although the fact that they are found on the surface of what appears to be a continuous, otherwise clean cleavage facet makes this possibility less convincing. Twin boundaries also look relatively unlikely as an explanation, as they usually represent a significant rotation of the crystal lattice, rather than the small-angle rotation observed here. Twin boundaries may also be expected to be abrupt, i.e. occurring within only a few crystal planes, while the boundaries observed here are ~ 100 nm in extent. These features make the presence of kink-bands resulting from ripplocations a possibility, although it does not provide direct observation of ripplocations, which are usually smaller-scale than kink bands (which may result from their accumulation). Analysis employing transmission electron microscopy, such as that employed in [5] may be necessary to confirm the presence of ripplocations.

If the low-angle boundaries result from stress in the crystal, it could mean that Sb_2Se_3 in general relieves stress through similar mechanisms to 2D van der Waals crystals, through rippling and buckling of crystal monolayers, rather than through slip of dislocations, with the deformation process possibly mediated by ripplocations . Since the sample was not under stress during examination, these would be permanent kink-bands, and not the reversible type[6]. Given that ripplocations do not involve the breaking of covalent bonds, while slip-plane dislocations do, this could be an advantage to Sb_2Se_3 as a photovoltaic material, as dangling bonds may form sites for carrier recombination. Further consideration of benign boundaries is given in Section 5.8.4.

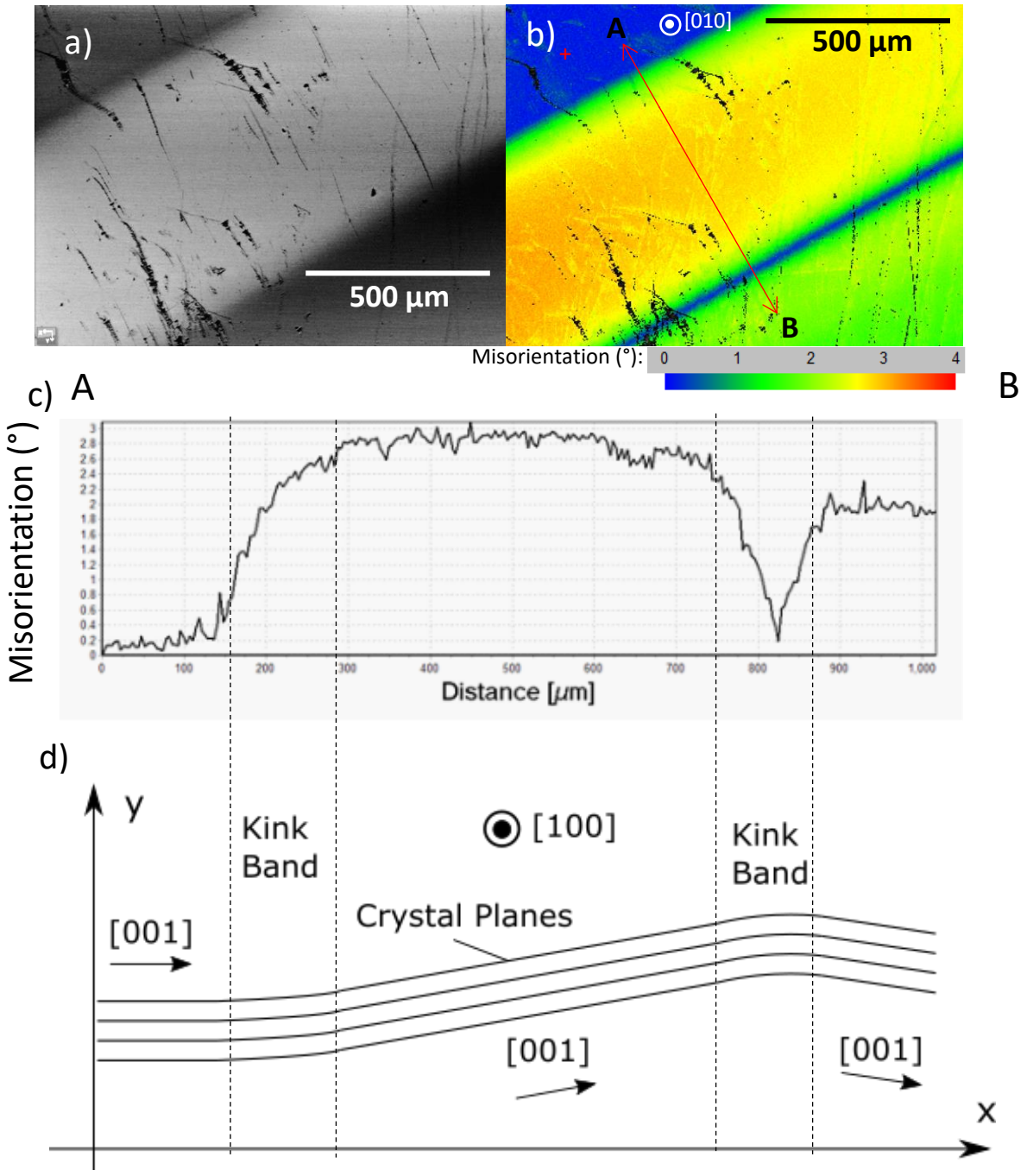

Fig. 5.18 SEM and EBSD images of a deformed Sb_2Se_3 single crystal a) secondary electron image b) EBSD misorientation map where blue represents zero tilt of the (010) plane. c) Misorientation line scan of the map section A-B. d) Representation of the crystal planes as inferred from the misorientation map, with undulating topography.

5.6.5 Raman Spectroscopy

Raman spectroscopy was employed to confirm the phase purity of the Sb_2Se_3 single crystals and to investigate differences in the spectra that result from anisotropy. Oxidisation of Sb_2Se_3 to Sb_2O_3 was also investigated by air annealing experiments.

5.6.5.1 Identification of the Sb_2Se_3 Phase and Sb_2O_3

The Raman spectrum for a (010) plane of the Sb_2Se_3 single crystal grown by vertical Bridgman under Ar is shown in fig. 5.19a. It exhibits prominent peaks at 190 and 212 cm^{-1}, with smaller peaks appearing at 104, 124 and 150 cm^{-1}. In addition to the single crystal, Raman was carried out on four films synthesised via close-space sublimation (see Section 3.2.7) which were either unannealed or air-annealed for 30 mins at 100, 200 and 400°C, in order to examine the process of oxidisation. The intensity-normalised Raman spectra for these samples are shown in fig. 5.19b, where there are strong similarities between the unannealed sample and the samples annealed at 100, and 200°C. Prominent peaks were observed at 190 and 212 cm^{-1}, and smaller ones at 100, 120 and 155 cm^{-1}. The sample annealed at 400°C exhibited clear differences from the other spectra: while peaks were also observed at 191 and 120 cm^{-1}, the peaks at 100 and 155 and 212 cm^{-1} peaks were absent.

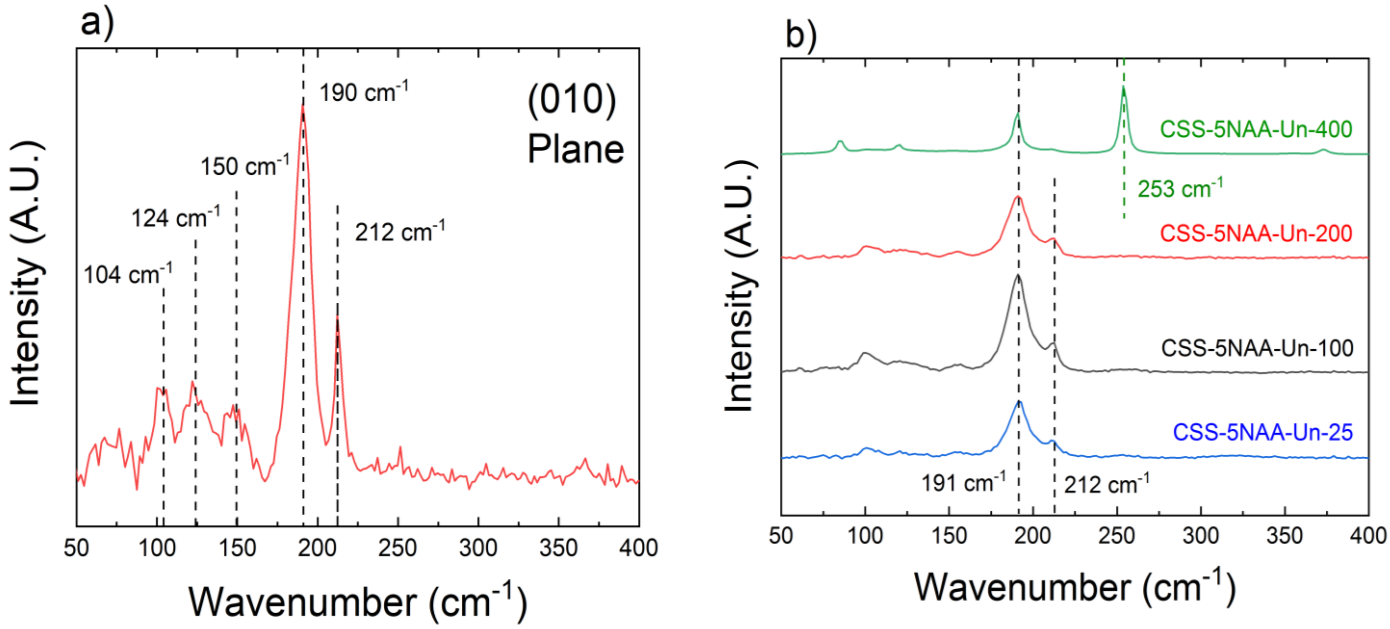

Fig. 5.19 a) Raman spectrum for cleaved (010) plane of Sb_2Se_3 single crystal grown by vertical Bridgman under Ar. Prominent peaks at 190 and 212 cm^{-1} with smaller peaks at 104, 124 and 150 cm^{-1}, are observed. b) Raman spectra for Sb_2Se_3 thin films synthesised by close-space sublimation, unannealed (CSS-5NAA-Un-25), or air-annealed at 100, 200 and 400°C (CSS-5NAA-Un-100, 200, 400) for 30 mins.

Meanwhile, a very strong peak was present at 253 cm^{-1}, together with a small peak at 85 cm^{-1}, neither of which appear in the other spectra.

The Raman spectra for single crystal and thin film samples are compared to one another and to literature peak positions in Table 5.3. There is good agreement between the peaks observed for the Sb_2Se_3 single crystal and Sb_2Se_3 in the literature.

Sb_2Se_3 Symmetry Modes [7]	Peak Position (cm^{-1})				
	Literature		This Work		
	Peaks for Sb_2Se_3 [7]	Peaks for Sb_2O_3 [8]	Single Crystal VB-5NAA-Ar-4mm (010) Plane	CSS Film – 25, 100 and 200 °C (CSS-5NAA-Un-25,-100,-200)	CSS Film – 400°C (CSS-5NAA-Un-400)
B_{xg}	102.6	82	104	100	85
B_{xg}	109.3				
A_g	118.7		124	120	120
B_{xg}	127.5				
B_{xg}	132.2				
B_{xg}	154.4		150	155	
A_g	184.7				
A_g	191.5	189	190	191	191
-	207.8				
A_g	212.8		212	212	
		254			253

Table 5.3 Literature values of Raman peak position for Sb_2Se_3 and Sb_2O_3 compared to experimental values observed for the (010) Sb_2Se_3 plane and also for annealed and unannealed Sb_2Se_3 films synthesised by CSS. *B* symmetry modes are subscripted with '*xg*' as ref 7 was unable to distinguish the symmetry modes B_{1g}, B_{2g} etc.

For the CSS films, with the exception of the 400°C annealed sample, there was good agreement between spectra and the literature, confirming the dominance of Sb_2Se_3 in these samples. The 400°C annealed film meanwhile provides strong agreement with the peaks reported for Sb_2O_3.

This suggests that the CSS film annealed at 400°C was highly oxidised, while those annealed at lower temperatures remained Sb_2Se_3. The plots in fig. 5.19 were normalised, but the counts per second for the 400°C annealed film were ~ 20x larger than for the other samples (for the same laser power), suggesting that Raman scattering is more efficient for Sb_2O_3. The Sb_2Se_3 films appear to withstand temperatures of up to 200°C in air without significant oxidisation after 30 mins. There is a small spike in the vicinity of 250 cm^{-1} in the spectrum for the single crystal also (fig. 5.19a), but this is comparable to the noise level and is too narrow to match the Raman peak at 253 cm^{-1} in fig. 5.19b, so is unlikely to represent the formation of Sb_2O_3, although its presence would not be surprising. Shongalova *et al.*[8] investigated the oxidisation of Sb_2Se_3, demonstrating that Sb_2O_3 will form under high laser powers in air. That study also demonstrated that Sb_2O_3 formed even under vacuum, though in much reduced quantity, with the only probable oxygen source being atoms previously adsorbed onto the surface. It seems likely, therefore, that Sb_2O_3 on the surface of Sb_2Se_3 may be detected in Raman spectra.

Finally, the results from Vidal-Fuentes *et al.*[7] presented in Table 5.3, report a greater number of peaks for Sb_2Se_3 than those observed here, suggesting that multiple closely-spaced (overlapping) peaks are present, especially at low wavenumber. The subscript '*xg*' in the table is used as the axes of the crystal studied in [7] were not known, so the specific symmetries of the B_{xg} modes could not be fully assigned. Vidal-Fuentes *et al.* argues that due to the strongly-anisotropic structure of Sb_2Se_3, different peaks will be prominent depending on the angular relationship between the crystal axes and the polarisation of the excitation laser. This may explain why peaks reported in Vidal-Fuentes *et al.*, such as the 184.7 cm^{-1} peak, are not present in fig. 5.19a. The effects of crystal anisotropy on the Raman spectra are explored further in the following section.

5.6.5.2 Results when Rotating Cut/Cleaved Planes 90°

Raman spectra are shown in fig. 5.20 for the cut and polished a) (100) and b) (001) planes, and cleaved c) (010) plane of Sb_2Se_3. Measurements were taken for a given (arbitrary) orientation, then after rotating axially by 90°. Polarised laser excitation was expected (see Section 3.3.5), but the relative angle between the laser polarisation and the crystal axes was not known, and the scattered light did not pass through a polariser. Nevertheless, significant differences in the observed spectra were observed, due to the anisotropy of Sb_2Se_3. The main peaks identified in each spectrum are shown with dashed lines on the figure, with the positions for all peaks being shown in Table 5.4.

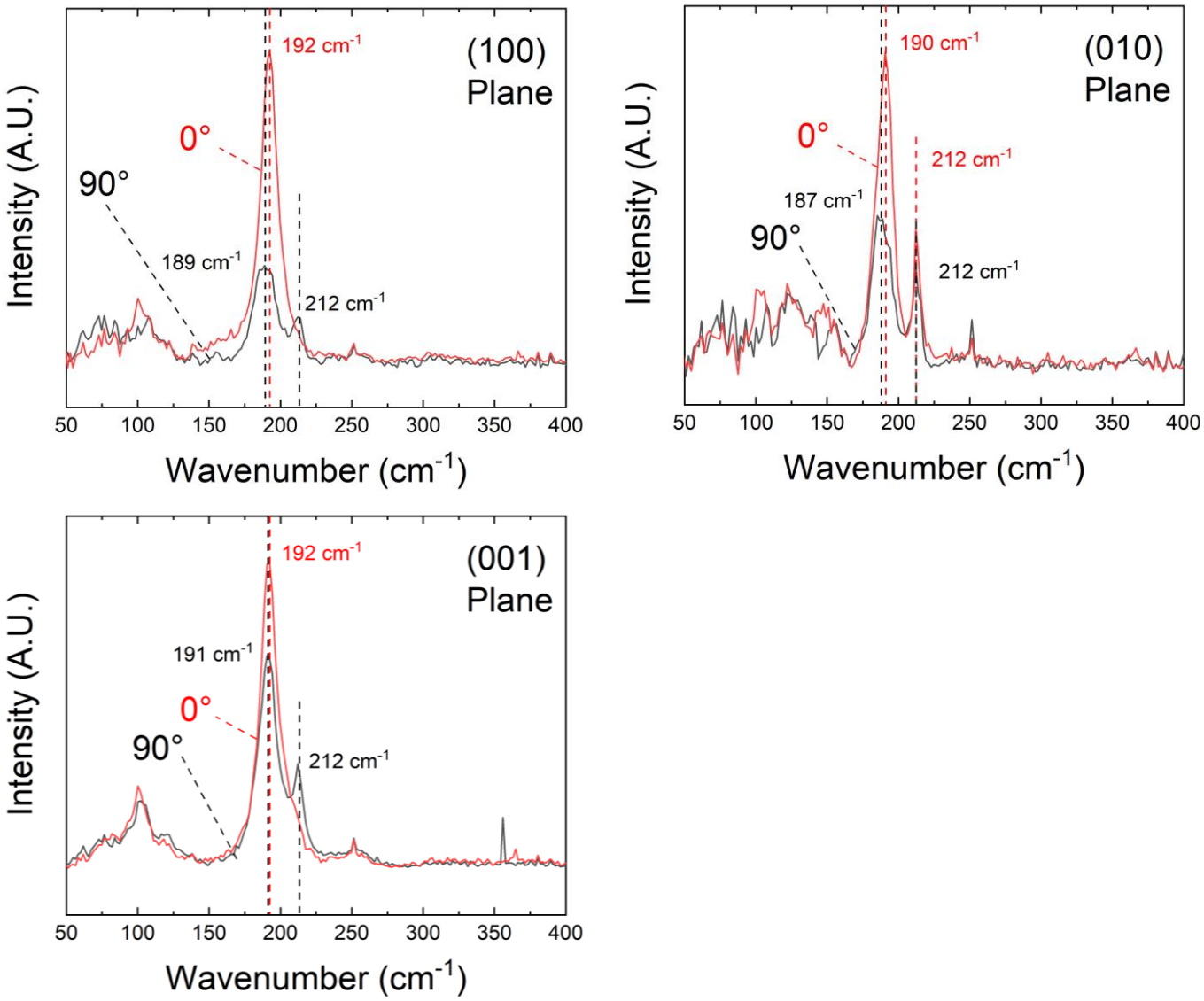

Fig. 5.20 Raman spectra for the crystal planes: cut and polished a) (100) plane, b) cleaved (010) plane and c) cut and polished (001) plane. All exhibit strong peaks at around 190 cm^{-1}, but with shifts resulting from the rotation of the samples by 90°. All peaks exhibit changes in intensity with rotation.

Peak Position (cm^{-1})							
Literature [7]		This Work					
		(100) plane		(010) plane		(001) plane	
Sb_2Se_3 Symmetry Modes	Peaks for Sb_2Se_3	0°	90°	0°	90°	0°	90°
B_{xg}	102.6	100		104		104	104
B_{xg}	109.3						
A_g	118.7		120	124			
B_{xg}	127.5						
B_{xg}	132.2						
B_{xg}	154.4			150	155		
A_g	184.7		189		187		
A_g	191.5	192		190	190	192	191
-	207.8						
A_g	212.8	212	212	212	212	212	

Table 5.4 Positions of Raman peaks observed in this work for the Sb_2Se_3 crystal planes (100), (010) and (001) taken at 0° and 90° orientations and compared to literature values for Sb_2Se_3 single crystals[7]. '*xg*' subscript could be 1*g*, 2*g* or 3*g*.

The spectra were all taken under the same laser power (1 mW) and acquisition time, with flat surfaces, meaning that the intensities are expected to be comparable. These results therefore indicate that the intensities of certain Raman modes are sensitive to the axial rotation of the sample, even when a polariser is not used (the polarisation of the laser being responsible for the difference). These results indicate that more of the peaks reported for Sb_2Se_3 single crystals in the literature[7] (mainly peaks in the range 187-9 cm^{-1}) may be observed if several different sample orientations are used. Moreover, this orientation sensitivity may be exploited to determine preferred orientations in thin films, as discussed in Section 5.8.3.

5.7 Chemical Analysis of Sb_2Se_3 Single Crystals (Doped and Undoped)

In this section, the results of chemical analysis for samples of Sb_2Se_3 single crystals grown by vertical Bridgman are reported. This was motivated by the fact that the primary origin of conductivity in Sb_2Se_3 has not been definitively pinned down (Section 2.4.2). Inductively-coupled plasma optical emission spectroscopy (ICP-OES), inductively-coupled mass spectrometry (ICP-MS) and secondary-ion mass spectrometry (SIMS) were carried out on samples of Sb_2Se_3 grown by vertical Bridgman from Alfa Aesar (5N) Sb_2Se_3 (VB-5NAA-Un), stoichiometric undoped (VB-St-Un), and Se-rich undoped (VB-SeR-Un) source material synthesised directly from the elements.

5.7.1 ICP-OES

For inductively-coupled plasma optical emission spectroscopy (ICP-OES), a survey (Section 3.4.1.1) was carried out for all detectable elements, with a single elemental reference concentration and a blank (i.e. a sample of pure DI water without no acid or material added, with negligible concentrations of impurity elements expected) used to calibrate emission intensity. The blank samples used in this work indicated a concentration of <0.0001 ppm of all elements examined, based on the intensity of emission, scaled to the single elemental reference used. Therefore, these concentrations are listed as 0 ppm for the level of precision used in Table 5.5. For the samples measured, the concentration of Sb_2Se_3 in the diluted solution was estimated at around 100 mg / l in each case, meaning that the concentration of trace (<0.1 at%) elements was expected to be at levels < 0.1 ppm in the solution. The acid solution itself was also analysed as a control.

Table 5.5 shows the results of the ICP-OES survey measurements. Given that concentration was determined based on the intensity of two characteristic emission wavelengths for each element (Section 3.4.1.1), the concentrations are listed for the two emission lines used, together with the mean. The at% concentration of each element was determined relative to the mean concentration of Sb_2Se_3. Sb was used to estimate the level of Sb_2Se_3, as the intensity of emission was higher for Sb than for Se, giving a reduced uncertainty.

		Concentration (ppm)					Concentration (at%) – Relative to Sb_2Se_3 Based on Sb Conc.		
Element	Emission Wavelength / nm	Blank	Acid Solution	VB-St-Un	VB-5NAA-Un	VB-SeR-Un	VB-St-Un	VB-5NAA-Un	VB-SeR-Un
Ca	393.366	0.0000	0.123	0.339	0.393	0.329	0.215	0.219	0.304
	396.847	0.0000	0.159	0.436	0.506	0.423	0.276	0.281	0.390
	Mean	0.0000	0.141	0.387	0.449	0.376	0.245	0.250	0.347
Cu	324.754	0.0000	0.009	0.009	0.007	0.024	0.003	0.004	0.014
	327.395	0.0000	0.005	0.005	0.004	0.018	0.001	0.002	0.010
	Mean	0.0000	0.007	0.007	0.005	0.021	0.002	0.003	0.012
Fe	238.204	0.0000	0.003	0.003	0.009	0.003	0.004	0.001	0.002
	259.940	0.0000	0.007	0.007	0.015	0.007	0.006	0.003	0.005
	Mean	0.0000	0.005	0.005	0.012	0.005	0.005	0.002	0.003
K	766.491	0.0000	0.148	0.512	0.552	0.463	0.309	0.339	0.439
	769.897	0.0000	0.402	0.762	0.808	0.728	0.452	0.504	0.690
	Mean	0.0000	0.275	0.637	0.680	0.596	0.381	0.422	0.564
Mg	279.553	0.0000	0.022	0.096	0.115	0.077	0.105	0.104	0.119
	280.270	0.0000	0.022	0.097	0.116	0.079	0.106	0.105	0.121
	Mean	0.0000	0.022	0.097	0.116	0.078	0.105	0.104	0.120
Na	588.995	0.0000	1.034	2.431	2.824	2.645	2.681	2.729	4.249
	589.592	0.0000	0.982	2.342	2.731	2.545	2.593	2.630	4.090
	Mean	0.0000	1.008	2.387	2.778	2.595	2.637	2.680	4.169
Sn	189.925	0.0000	0.000	0.000	0.000	0.000	0.000	0.000	0.000
	283.998	0.0000	0.000	0.000	0.000	0.000	0.000	0.000	0.000
	Mean	0.0000	0.000	0.000	0.000	0.000	0.000	0.000	0.000
Sr	407.771	0.0000	0.001	0.003	0.006	0.003	0.001	0.001	0.001
	421.552	0.0000	0.001	0.002	0.005	0.003	0.001	0.001	0.001
	Mean	0.0000	0.001	0.003	0.005	0.003	0.001	0.001	0.001

(continued)

Sb	206.834	0.0000	0.000	231.178	273.716	161.500	
	217.582	0.0000	0.000	146.761	173.310	102.620	
	Mean	0.0000	0.000	**188.969**	**223.513**	**132.060**	
Se	196.026	0.0000	0.000	128.449	154.343	121.659	
	203.985	0.0000	0.000	107.202	131.094	100.600	
	Mean	0.0000	0.000	**117.825**	**142.719**	**111.130**	

Table 5.5 ICP-OES concentrations of elements in Sb_2Se_3 crystals grown by vertical Bridgman from: 5N undoped (VB-5NAA-Un), stoichiometric undoped (VB-St-Un) and Se-rich undoped (VB-SeR-Un) source material and also a sample of the digestion acid. Results are shown for two emission wavelengths and their average. Concentrations in at% were calculated relative to Sb. Values for blank (Pure DI water) indicated no concentration of element detected at level of precision shown.

It should be noted that the atomic ratio of Sb to Se was not 2:3, as would be expected (even though all of the Sb_2Se_3 was digested for these samples), but ranged from 3:4 to 1:1 instead. This discrepancy is expected for the survey scans, as the intensity calibration curves were based on a single concentration and a blank for each element, rather than multiple concentrations (Section 3.4.1.1). Based upon this, the concentrations of impurity elements may vary by ±20% compared to the true values. While a very broad range of elements were studied in the scan, most peaks had an intensity below the level seen for the blank (pure DI water) used, and are therefore treated as indistinguishable from background levels (conc. = 0). The elements listed in Table 5.5 had detectable concentrations. Sn (not present) was included in the table as it is relevant to the doping study in Chapter 6.

The metals Cu, Fe and Sr were detected in all Sb_2Se_3 samples at very small quantities (~0.001 at%), while slightly higher quantities of Ca, K and Mg (0.01-0.1 at%) were also observed, and large concentrations of Na, at 2-4 at%. However, these metals were also detected in the acid sample at the same order of magnitude, and given the large uncertainties it is not clear that these metals originated in the Sb_2Se_3, rather than from the acid. Even assuming these metals originated in the Sb_2Se_3 samples,

their concentration was independent of the type of source material used, meaning that they are unlikely to produce significant differences in the electronic properties of the single crystals examined in Chapter 6. Finally, detectable levels of Sn ≥ 0.001 at% (shown in Chapter 6 to be a p-type dopant) were not found in any of these undoped samples.

5.7.2 ICP-MS

ICP-MS was carried out (Section 3.4.1.2) on digested Sb_2Se_3 crystals grown by the vertical Bridgman method, from undoped 5N Sb_2Se_3 and stoichiometric Sb_2Se_3 directly synthesised from the elements. Crystals doped with Sn and $MgCl_2$ (~0.1 at% by weight), grown from source material directly synthesised from the elements, were also included in the study. The results are shown in Table 5.6 with concentrations presented in units of ppm (μg of element per g of Sb_2Se_3) and atomic percentage (at%). For each sample and element, the measurement was taken twice. The 'blank' used was pure DI water, as for the ICP-OES, and it indicated no concentration of the elements (based on emission intensities scaled to the elemental references) at the level of precision used in Table 5.6.

The ICP-MS results suggest the presence of small quantities of Mg, P, V, Fe, Ge, Sn, Te, Cs, Au, Hg and Pb in all samples. Of these, Mg, P, V, Fe, Ge, Sn, Te and Au are detected in quantities ≥ 0.001 at% in some samples. The impurity content of the samples was found to be independent of source material type, with similar impurity levels observed in 5N crystals as in those grown from in-house source material directly synthesised from the elements, in line with what was observed with ICP-OES.

Additionally, these results indicate the presence of Mg in the $MgCl_2$-doped crystal, at a concentration of ~ 0.1 at%, in line with the quantity added before growth. Similar quantities of Mg were also detected in the Sn-doped crystal, which was not expected, but may result from the interference of C_2-ions (as they have the same mass as Mg ions). Sn was observed in the Sn-doped crystal for one of the measurements taken, at a concentration of 0.1 at% and so matching the quantity added before growth. This concentration was not observed in the other measurement, which may

result from the difficulty in resolving the signal of Sn from that of SeCl, especially if the latter is also produced during the analysis, leading to the Sn-signal being discounted as interference. Worth noting is that the average of these two values was still significantly larger than the Sn-content in any of the other samples. The Sn signal in the Sn-doped crystal was at risk of interference from SeCl, but this also holds for the other samples, where significant quantities of ions matching the mass of Sn and SeCl were not observed.

	Concentration – ppm (µg/g)					Concentration (at%)				
Element	**Blank**	**VB-5NAA-Un**	**VB-St-Un**	**VB-SeP-Sn**	**VB-SeR-MgCl2**	**VB-5NAA-Un**	**VB-St-Un**	**VB-SeP-Sn**	**VB-SeR-MgCl2**	**Possible Interferences**
Mg	0.00	0.00	0.00	60.14	**63.64**	0.000	0.000	0.119	**0.126**	C_2
	0.00	0.00	0.00	0.00	**49.79**	0.000	0.000	0.000	**0.098**	
P	0.00	0.00	0.42	0.00	0.00	0.000	0.001	0.000	0.000	
	0.00	0.00	0.40	0.00	1.01	0.000	0.001	0.000	0.002	
V	0.00	0.00	0.00	12.21	11.14	0.000	0.000	0.012	0.011	ClO
	0.00	0.00	0.00	2.46	16.37	0.000	0.000	0.002	0.015	
Fe	0.00	0.00	13.14	2.65	14.07	0.000	0.011	0.002	0.012	ArO
	0.00	0.00	6.97	0.00	0.00	0.000	0.006	0.000	0.000	
Ge	0.00	0.04	0.26	0.54	0.59	0.000	0.000	0.000	0.000	ClCl
	0.00	0.00	0.14	0.97	0.76	0.000	0.000	0.001	0.001	
Sn	0.00	0.13	0.66	**0.23**	0.21	0.000	0.000	**0.000**	0.000	SeCl
	0.00	0.55	0.12	**270.75**	0.21	0.000	0.000	**0.110**	0.000	
Te	0.00	7.59	1.07	3.78	4.57	0.003	0.000	0.001	0.002	
	0.00	6.53	1.07	0.66	3.80	0.002	0.000	0.000	0.001	
Cs	0.00	0.38	0.00	0.02	0.03	0.000	0.000	0.000	0.000	
	0.00	0.00	0.00	0.09	0.25	0.000	0.000	0.000	0.000	
Au	0.00	2.44	4.74	6.50	8.54	0.001	0.001	0.002	0.002	
	0.00	1.10	4.62	7.56	21.31	0.000	0.001	0.002	0.005	
Hg	0.00	0.00	0.00	0.37	0.00	0.000	0.000	0.000	0.000	
	0.00	0.33	0.95	0.65	0.00	0.000	0.000	0.000	0.000	
Pb	0.00	0.07	0.36	0.15	0.13	0.000	0.000	0.000	0.000	

Table 5.6 ICP-MS measurements of Sb_2Se_3 single crystals grown by vertical Bridgman from: 5N undoped (VB-5NAA-Un), stoichiometric undoped (VB-St-Un), Se-poor Sn-doped (VB-SeP-Sn) and Se-rich $MgCl_2$-doped (VB-SeR-MgCl2) source material, for detected elements. Concentrations are reported in ppm (µg of element per g or Sb_2Se_3) and at%. Elements in bold are extrinsic dopants added before growth. Values for blank (pure DI water) indicate no concentration of element detected at level of precision shown.

These results indicate that the impurity elements have been incorporated into the Sb_2Se_3 crystals. The Sb_2Se_3 single crystals doped with Sn and $MgCl_2$ may be expected to contain a density of Sn and Mg atoms of around 7×10^{18} cm^{-3}. The ICP methods cannot detect Cl, although an atomic density of 1.4×10^{19} cm^{-3} may be inferred in the $MgCl_2$-doped crystal from the Mg concentration. Despite evidence for incorporation, it is not known from chemical analysis whether the impurity atoms actually contribute towards extrinsic doping and, if so, what carrier density they may produce, as this depends on their electrical activation. Electrical measurements to address this question are reported in Chapter 6. While these results imply that Cl may be incorporated into Sb_2Se_3, SIMS measurements are necessary to directly detect Cl in samples of Sb_2Se_3, as well as other halogens which may be present as impurities, as presented in the next section.

5.7.3 SIMS

Quadrupole SIMS (Section 3.4.2) was employed in order to search for trace levels of Sn, halogens and oxygen in Sb_2Se_3 samples grown by vertical Bridgman. The detection of halogens was especially important, because as group-VII elements, they may be expected to act as n-type dopants if they occupied the Se (group-VI) site. Depth profiles showing the concentration of the elements ^{121}Sb, ^{78}Se, ^{120}Sn, ^{35}Cl, ^{127}I and ^{16}O measured by SIMS are shown in fig. 5.21, with all of the scans showing a plasma start-up artefact.

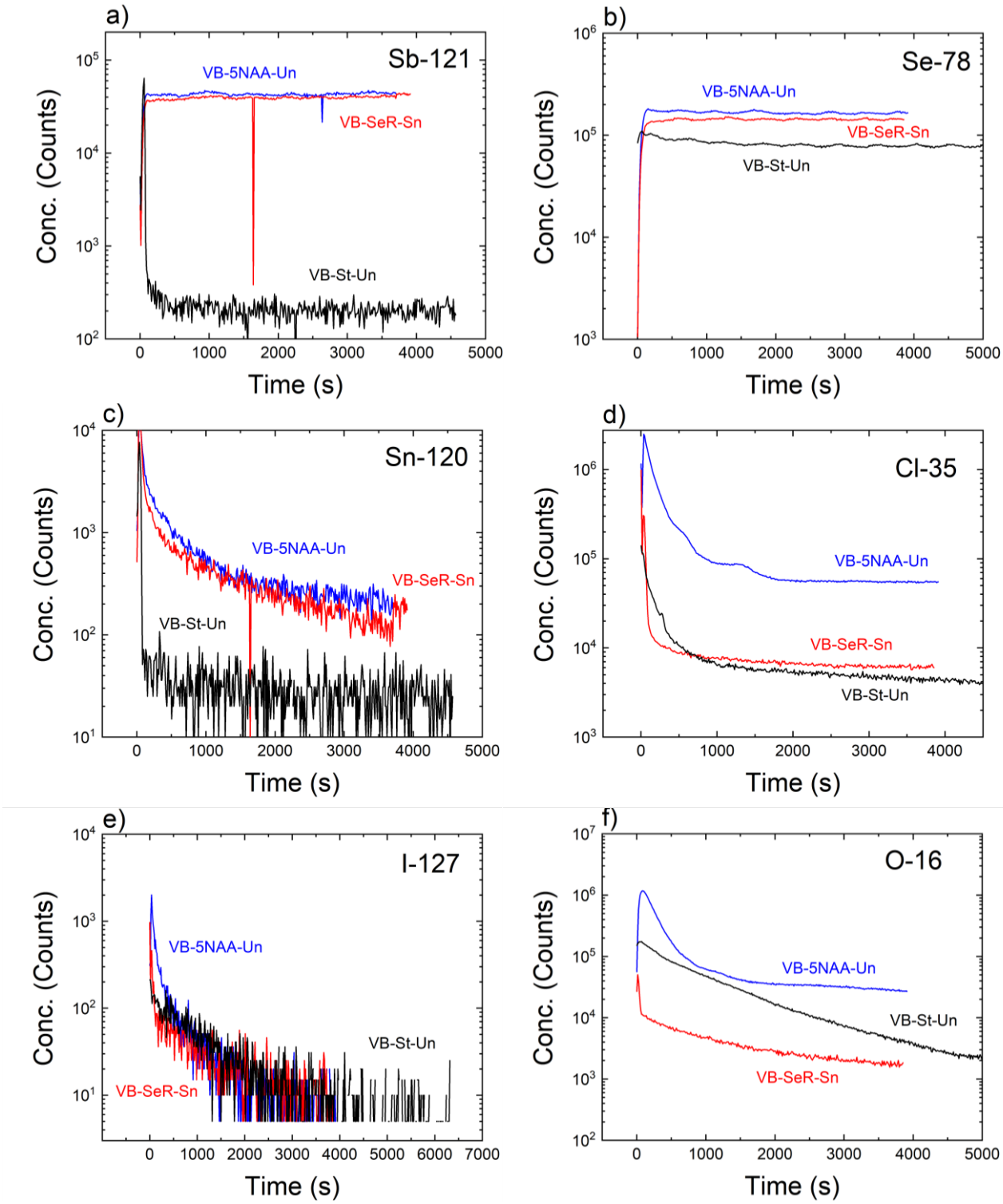

Fig. 5.21 SIMS profiles (logarithmic y-axis) of the Sb_2Se_3 single crystals grown by vertical Bridgman from: 5N undoped (VB-5NAA-Un), Se-rich Sn-doped (VB-SeR-Sn) and stoichiometric undoped (VB-St-Un) source material. Ion counts are plotted against sputtering time (analogue for depth) for the following ions: a) ^{121}Sb b) ^{78}Se, c) ^{120}Sn, d) ^{35}Cl, e) ^{127}I, f) ^{16}O.

The chemical information in the scans, in the same order as presented in fig. 5.20, is as follows:

i) The measured quantities of antimony (fig. 5.20a) were consistent across the 5N crystal and the Sn-doped Se-rich crystal but were much lower for the undoped stoichiometric crystal. The latter result was not expected, and given the difference is several orders of magnitude (note the logarithmic scale) for very similar samples, it is unlikely to be a physical result, and is more likely to be a measurement error. This may result from a negative charge building up in the sample and deflecting the O^{2-} ion beam, while also preventing the ejection of the positive Sb ions. Charging could occur if the undoped stoichiometric crystal has low conductivity compared to the other samples, as is confirmed in Chapter 6.

ii) For selenium (fig. 5.20b) the results were similar to Sb, with high counts in the 5N crystal and Sn doped crystal, but lower counts in the stoichiometric undoped crystal, possibly due to deflection of the ion beam by the charged sample. The lower levels of Se in the undoped stoichiometric crystal are less dramatic than Sb, possibly because the negative charge of Se ions meant they were ejected more easily from a negatively charged crystal.

iii) The magnitude of the tin concentration indicated in fig. 5.20c is < 1% of the levels of Sb and Se observed in the 5N undoped crystal and the Se-rich Sn-doped crystal, while the levels for the stoichiometric undoped crystal are significantly lower. The Sn quantity observed in the 5N crystal contradicts the ICP measurements (Tables 5.5 and 5.6) and may be an overestimate (see iv) or result from a greater concentration of Sn near the crystal surface. Meanwhile as Sn is a positive ion, its prevalence may be underestimated in the undoped stoichiometric sample due to charging, although significant quantities were not expected from ICP measurements (Tables 5.5 and 5.6).

iv) The quantities of chlorine (fig. 5.20d) in the undoped 5N crystal are significantly larger (around 10x greater) than the level in the Se-rich Sn-doped and stoichiometric undoped crystals, with this large difference clear on the logarithmic scale. The origin of this impurity is likely to be the source material itself, as growth conditions were identical otherwise. These results therefore also

indicate that the elemental Sb (6N) and Se (5N) source used for direct synthesis contained smaller quantities of Cl. The Cl-concentration in the 5N crystal may result in a higher concentration of donor defects, leading to n-type conductivity. This Cl may also have produced SeCl interference in the Sn measurement (iii), leading to an overestimate of the Sn concentration. Conversely, for the Sn-doped crystal, low levels of Cl mean that SeCl ions are less likely to interfere in the Sn concentration measurement (fig. 5.20c), placing greater confidence in the Sn concentration measured.

v) The measured levels of iodine (fig. 5.20e) are around 10^4 x less than the levels of Sb and Se measured across all samples and at the level of noise, suggesting iodine is not present in any sample, ruling it out as a donor in these crystals.

vi) The levels of oxygen (fig. 5.20f) were consistently below 10^4 counts for the Sn doped Se-rich crystal. For the undoped stoichiometric crystal, a clear drop-off, from 10^5 to $<10^4$ counts, was observed with increased sputtering time, meaning the O may result from surface oxidisation, with levels in the bulk matching the undoped crystal grown from the same (DSE) source material. O levels are more uniform in the undoped 5N crystal, at just below 10^5 counts, even for long sputtering times, suggesting the concentration in the bulk is greater than in the other crystals, perhaps as a result of the different source material used. O impurities may occupy a Se sites, acting as isoelectronic dopants, with implications for electrical properties, but it should be noted that unlike the other impurity elements examined here, O is expected to be prevalent, and establishing a baseline free from surface O contamination is difficult. Therefore, these results may simply reflect natural variations between these samples in the amount of oxygen incorporated from the air, rather than representing differences in the chemistry of the source material.

5.8 Further Discussion

5.8.1 Crystal Growth Outcomes

The investigations into the Piper-Polich growth of Sb_2Se_3 crystals (Section 5.2) provide strong evidence that Sb_2Se_3 vapourises congruently, without segregation. This offers a great advantage for vapour-based growth techniques, such as thermal evaporation and close-space sublimation, as it ensures phase purity of the deposit.

Of the direct synthesis (from elements and compounds) and crystal-growth techniques (Piper Polich, SSVG and vertical Bridgman) discussed in this chapter, direct synthesis from the elements (Section 5.4) and vertical Bridgman (Section 5.6) had the greatest success in producing large (> 1 mm scale) pieces with properties consistent with single crystals, with the results for the vertical Bridgman technique being especially promising. If these are single crystals, this is a significant result, as it has been demonstrated for CdTe and CZTS that large single crystals may be used for investigating properties relevant to PV[9,10]. Among other factors, the improved purity, structural and compositional homogeneity and lack of grain boundaries mean that the fundamental properties of a material may be examined with minimal interference from these other factors. Besides these advantages, cleaved crystal facets often provide a flatter, cleaner surface than can easily be achieved from polishing, making single crystals especially useful when applying optical characterisation techniques. Although the presence of single crystals could not be entirely confirmed without additional characterisation (Laue diffraction or EBSD, for instance), later sections work off the assumption that these pieces are, indeed, single crystals. Single crystal Sb_2Se_3 has been characterised in previous works[11], but reference to photovoltaics[12] is rare and therefore an opportunity remains. Accordingly, Chapter 6 reports studies of these crystals using *C-V*, *J-V*, DLTS, hot-probe and Hall effect measurements.

The results of the study into the synthesis of $Sb_2Se_{3x}Se_{3(1-x)}$ solid solutions (Section 5.5) are significant, as they demonstrate that homogeneous solid solutions may indeed be formed, and suggest that the lattice parameters obey Vegard's law with some bowing. The Vegard relation for this range of compositions was not characterised to the extent originally intended (see Section 1.2) as more focus

was ultimately placed on the electrical properties of Sb_2Se_3 (see Chapter 6). However, these results suggest the possibility of making single sources for fabrication of thin film $Sb_2(S,Se)_3$ with tuneable band gaps for high efficiency solar cells[13].

5.8.2 X-ray Diffraction

The results of the single crystal x-ray diffraction measurements (Section 5.6.3) are significant as they suggest that Sb_2Se_3 surfaces of known crystal orientation can be prepared by cleavage and cutting guided by visual inspection of the cleavage steps (with an optical microscope) alone, without recourse to Laue equipment. However, the limitations of the combined XRD and visual inspection used in this work should be acknowledged: While cleaved surfaces are very likely to correspond to crystal planes, a single θ-2θ XRD scan cannot confirm if a sectioned surface is a single crystal plane, as a polycrystalline sample with a strong preferred orientation may produce the same result. Laue equipment or an imaging diffractometry method such as EBSD are therefore still necessary to fully confirm the nature of crystals, although for simplicity, these cleaved and cut surfaces are assumed to correspond to the crystal planes assigned to them in later sections of this work. Despite the limitations, it may be that this technique can also be applied to other 1D van der Waals crystals, such as Bi_2Se_3.

5.8.3 Raman Investigations

The varying Raman peak intensities that resulted from rotating the sample relative to laser polarisation (Section 5.6.5.2) indicate that sample rotation may be applied to distinguish closely-spaced peaks and provide a more detailed picture of vibrational modes in Sb_2Se_3. However, the assignment of vibrational modes was not possible with the investigation reported in this work, as the polarisation state of the laser was not known. The differences observed with rotation suggest that if the relationship between crystal axes and laser polarisation state were known, the vibrational modes could be associated with specific crystal axes, allowing the assignment of a greater number of vibrational modes for Sb_2Se_3.

Knowledge of the modes makes it feasible to identify crystal orientation based on a spectral 'fingerprint'. This has great relevance for Sb_2Se_3 photovoltaics, as the preferred orientation in films is of key importance to device efficiency [14,15]. These studies therefore greatly increase the utility of applying Raman spectroscopy to studies of thin films.

Furthermore, in terms of phase identification, the Raman spectra taken for the Sb_2Se_3 single crystals and the annealed Sb_2Se_3 thin films (fig. 5.18) add to the body of evidence that the 253 cm^{-1} peak is assigned to Sb_2O_3 and not Sb_2Se_3[8]. This is significant as many of the older papers that cover Raman spectroscopy of Sb_2Se_3 make the wrong assignment, an example being Wang, Deng and Li from 2002[16], or the highly cited paper on thermal evaporation of Sb_2Se_3 thin films from 2014[1].

5.8.4 Low-Angle Boundaries

DIC microscopy and EBSD of the cleaved (010) plane of Sb_2Se_3 single crystals (Section 5.6.4) reveals small and relatively gradual changes in misorientation organised into parallel bands. Their highly crystallographic appearance on a cleaved crystal facet makes low-angle grain boundaries arising from dislocation walls an unlikely explanation. While twin defects will introduce a rotation of the crystal lattice, the rotation observed here (3°) was too small for a twinning transformation and took place over a distance of ~ 100 nm, rather than a few crystal planes as may be expected for a twin

boundary. Similarly, stacking faults would be expected to produce distortion over a very much shorter distance, so are also thought unlikely [17]. As a result, the rippling and buckling of crystal planes, as has been observed in 2D materials, seems the most likely explanation, thus suggesting that Sb_2Se_3 emulates the mechanical properties of 2D materials, despite being 1D in the stricter sense.

While the properties of these defects were not extensively characterised in this investigation, the low-angle boundaries may be consistent with the 'kink-bands' described by Aslin *et al.*[18], which have been observed in 2D crystalline phylosillicate materials. These are mediated by 'ripplocations' a relatively new class of crystal defects that have only been reported since 2015, with the work of Kushima *et al.* [5]. Individual ripplocations are too small to appear on the scale of the images shown in figs. 5.16 and 6.16, being sub-nm in scale, but may explain the kink-band like behaviour. Further investigations employing transmission electron microscopy would be necessary to directly detect ripplocations in Sb_2Se_3, providing a valuable exploration of the strain-relief characteristics of this van der Waals material.

Furthermore, if Sb_2Se_3 crystals support strain relief through deformation of monolayers themselves, without the breaking of covalent bonds (unlike crystal dislocations[5]), as this work suggests, this is significant. Dangling covalent bonds are expected to act as non-radiative recombination centres for charge carriers, but if deformation does not result in broken covalent bonds, sites of strain may be more electrically benign than for other materials, giving Sb_2Se_3 an advantage in solar cell technology.

5.8.5 Doping of Sb_2Se_3 Single Crystals

The results of chemical analysis (Section 5.7) have provided important information on the background impurities in Sb_2Se_3 from different sources and also on the viability of adding extrinsic dopants. Generally the ICP-MS confirmed that unintentional impurities were present in levels of > 0.01 at%, or 7 x 10^{17} cm^{-3}, this being an order of magnitude lower than the 7 x 10^{18} – 1.4 x 10^{19} cm^{-3} introduced in intentional doping. Successful incorporation of Sn allows for p-type doping from Sn_{Se}

while $MgCl_2$ should allow n-type doping from Cl_{Se}. p-type doping may also be expected from Mg_{Sb}, but if this were to occur, the presence of 2x more Cl means the effects of the latter would be expected to dominate.

The theoretical work carried out by Stoliaroff *et al.*[19] supports both of these possibilities. The incorporation of these impurity elements makes it feasible to investigate whether they may contribute to extrinsic doping in Sb_2Se_3, an area of study which has had limited attention to date. This would depend on whether the elements prove to be electrically active in the material.

Finally, the SIMS results provide important information on the impurities present in different forms of Sb_2Se_3 source material, particularly the fact that a much larger quantity of Cl is present in the 5N source material compared to the material made by direct synthesis from elements. This result may be significant given that Cl is predicted to act as an n-type dopant in Sb_2Se_3, which may have relevance for all crystals and devices formed from this particular commercial source material. Once again, doping will depend on the electrical activity of Cl within Sb_2Se_3, but these results suggest that comparing the electrical characteristics of samples grown from different source material may be fruitful.

5.9 Conclusions

Several key findings resulted from the investigations into the growth, doping and physical characterisation of Sb_2Se_3 crystals and $Sb_2S_{3x}Se_{3(1-x)}$ solid solutions, which may be summarised as follows. The congruent vaporisation of Sb_2Se_3 was demonstrated through Piper-Polich and Self-selecting-vapour growth (SSVG) experiments. In the Piper-Polich case, a preferred orientation along [062] was found to align with the growth axis, although this may not apply to vapour growth of Sb_2Se_3 in general. Furthermore, the SSVG experiments were successful in producing Sb_2Se_3 crystals ≤ 1 mm in size. Similarly, the method of direct synthesis from elemental Sb and Se was able to produce ~ 1 mm scale Sb_2Se_3 crystallites, large enough for electrical characterisation without further crystal growth, and most likely forming as a result of vapour condensation.

Direct synthesis of polycrystalline $Sb_2S_{3x}Se_{3(1-x)}$ solid solutions from the pre-synthesised compounds Sb_2Se_3 and Sb_2S_3 was also carried out for compositions of x = 0.28 and 0.55 (based on EDX). These samples demonstrated upward bowing in the Vegard relation, but with only two samples synthesised, the evidence for this behaviour is limited and a greater range of compositions would be necessary to establish if this relation occurs overall.

Meanwhile, vertical Bridgman growth produced solid pieces of Sb_2Se_3 which demonstrated cleavage in a single plane to produce flat, clean surfaces, consistent with the formation of single crystals up to 1 cm in length and 4 mm in diameter. XRD measurements supported this interpretation, but full confirmation with Laue equipment or EBSD was not possible. The observed growth appeared to be encouraged by the formation of vapour-filled voids during crystal growth, most likely as a result of uneven melting of the powder and subsequent grain coalescence. XRD also provided evidence that the cleaved surface of the Sb_2Se_3 crystals was the (010) plane, while surfaces cut perpendicular to this plane, then polished, produced diffraction patterns consistent with the (100) and (001) planes. If the single crystal interpretation is correct, these results indicate that the secondary cleavage steps on the surface of the cleaved Sb_2Se_3 crystals were aligned with [001].

These cleaved surfaces also exhibited long-range defects in the form of low-angle crystallographic boundaries ~ 100 nm wide, as observed directly through EBSD, and indirectly through topographic DIC microscopy. Their exact nature is unknown, with low-angle grain boundaries a ready explanation, but the direct alignment of these boundaries with crystal axes suggests twin defects or stacking faults. However, although these options seem more likely, the width of the boundaries and the low angle of misorientation makes rippling and buckling of crystal monolayers (as is observed in 2D materials) more convincing. Such deformations are consistent with kink-bands, associated with ripplocations, but a more detailed study would be necessary to confirm if ripplocations are, in fact, present in Sb_2Se_3.

Raman spectroscopy carried out on air-annealed Sb_2Se_3 thin films exhibited a peak at 253 cm^{-1} for a high-temperature anneal, consistent with the interpretation put forward in the literature that this peak corresponds to Sb_2O_3 as opposed to Sb_2Se_3. A chemical analysis technique such as EDX would allow this interpretation to be confirmed but was not carried out in this work. Anisotropy in Raman spectra was also demonstrated by rotating the sample axially relative to the laser polarisation. This approach allowed closely-spaced Raman peaks to be distinguished due to their varying intensities, but assignment of Raman modes was not possible as the explicit relationship between the crystal axes and polarisation state of the laser was not known.

Chemical analysis through SIMS demonstrated that Cl was a key impurity present in 5N Sb_2Se_3 but not present in crystals grown from in-house source material, with the content of other impurities between the two types of source material otherwise similar (as determined from ICP-OES and ICP-MS). The incorporation of Sn and Mg impurities (the latter from $MgCl_2$) into Sb_2Se_3 single crystals at a density of 7 x 10^{18} cm^{-3} was also demonstrated from ICP-MS analysis, with the incorporation of Cl (also from $MgCl_2$) inferred at a density of 1.4 x 10^{19} cm^{-3}. This control of elemental impurities in Sb_2Se_3 single crystals suggests that extrinsic doping may be investigated if Sn and Cl are found to be electrically active dopants, as has been suggested in the literature[19]. That investigation is described in the following chapter.

5.10 References

[1] X. Liu *et al.*, "Thermal evaporation and characterization of Sb_2Se_3 thin film for substrate Sb_2Se_3/CdS solar cells," *ACS Appl. Mater. Interfaces*, vol. 6, no. 13, pp. 10687–10695, 2014.

[2] N. W. Tideswell, F. H. Kruse, and J. D. McCullough, "The crystal structure of antimony selenide, Sb_2Se_3," *Acta Cryst*, vol. 10, pp. 99–102, 1957.

[3] A. Szczerbakow and K. Durose, "Self-selecting vapour growth of bulk crystals - Principles and applicability," *Prog. Cryst. Growth Characterisation Mater.*, vol. 51, pp. 81–108, 2005.

[4] A. Kyono and M. Kimata, "Structural variations induced by difference of the inert pair effect in the stibnite-bismuthinite solid solution series $(Sb,Bi)_2S_3$," *Am. Minerol.*, vol. 89, no. February, pp. 932–940, 2004.

[5] A. Kushima, X. Qian, P. Zhao, S. Zhang, and J. Li, "Ripplocations in van der Waals layers," *Nano Lett.*, vol. 2, no. 15, pp. 1302–1308, 2015.

[6] J. Gruber, A. C. Lang, J. Griggs, M. L. Taheri, G. J. Tucker, and M. W. Barsoum, "Evidence for bulk ripplocations in layered solids," *Sci. Rep.*, vol. 6, 2016.

[7] P. Vidal-Fuentes *et al.*, "Multiwavelength excitation Raman scattering study of Sb_2Se_3 compound: fundamental vibrational properties and secondary phases detection," *2D Mater.*, vol. 6, p. 045054, 2019.

[8] A. Shongalova, M. R. Correia, B. Vermang, J. M. V Cunha, P. M. P. Salome, and P. A. Fernandes, "On the identification of Sb_2Se_3 using Raman scattering," *MRS Commun.*, vol. 8, pp. 865–870, 2018.

[9] A. Nagaoka, K. Yoshino, H. Taniguchi, and T. Taniyama, "Growth and characterization of $Cu_2ZnSn(S_xSe_{1-x})_4$ alloys grown by the melting method," *J. Cryst. Growth*, vol. 386, pp. 204–207, 2014.

[10] A. Nagaoka, D. Kuciauskas, J. Mccoy, and M. A. Scarpulla, "High p-type doping, mobility, and photocarrier lifetime in arsenic-doped CdTe single crystals," *Cit. Appl. Phys. Lett*, vol. 112, p. 192101, 2018.

[11] J. Black, E. M. Conwbll, L. Seigle, and C. W. Spencer, "Electrical and optical properties of some $M_2^{V\text{-}B}N_3^{VI\text{-}B}$ semiconductors," *J. Phys. Chem. Solids*, vol. 2, pp. 240–251, 1957.

[12] R. Bacewicz and T. F. Ciszek, "Liquid encapsulated crystal growth and electrical properties of Sb_2Se_3 and Bi_2S_3," *J. Cryst. Growth*, vol. 109, pp. 133–136, 1991.

[13] H. Deng *et al.*, "High-throughput method to deposit continuous composition spread $Sb_2(Se_xS_{1-x})_3$ thin film for photovoltaic application," *Prog. Photovoltaics Res. Appl.*, vol. 26, no. 4, pp. 281–290, 2018.

[14] O. S. Hutter, L. J. Phillips, K. Durose, and J. D. Major, "6.6% efficient antimony selenide solar cells using grain structure control and an organic contact layer," *Sol. Energy Mater. Sol. Cells*, vol. 188, no. August, pp. 177–181, 2018.

[15] Y. Zhou *et al.*, "Thin-film Sb_2Se_3 photovoltaics with oriented one-dimensional ribbons and benign grain boundaries," *Nat. Photonics*, vol. 9, no. 6, pp. 409–415, 2015.

[16] Y. L. J Wang, Z Deng, "Synthesis and characterisation of Sb_2Se_3 Nanorods," *Mater. Res. Bull.*, vol. 37, pp. 495–502, 2002.

[17] D. G. Callister, William D. Rethwisch, *Materials Science and Engineering*, 88th ed. John Wiley and Sons, 2011.

[18] J. Aslin, E. Mariani, K. Dawson, and M. W. Barsoum, "Ripplocations provide a new mechanism for the deformation of phyllosilicates in the lithosphere," *Nat. Commun.*, vol. 10, p. 686, 2019.

[19] A. Stoliaroff *et al.*, "Deciphering the role of key defects in Sb_2Se_3, a promising candidate for chalcogenide based solar cells," *ACS Appl. Energy Mater.*, vol. 3, no. 3, pp. 2496–2509, 2020.

6. Sb_2Se_3: Electrical Characterisation and Photovoltaic Devices

6.1 Introduction

This chapter reports the electrical characterisation of the vertical Bridgman-grown single crystals of Sb_2Se_3 from Chapter 5, as well as the fabrication and testing of Sb_2Se_3 photovoltaic devices. Section 6.2 describes carrier measurements using the hot probe and Hall methods. Section 6.3 reports a study of contacts and junction formation, while 6.4 gives an account of capacitive characterisation using *C-f* and Mott-Schottky plots. In Section 6.5 crystal point defects are examined with deep-level transient spectroscopy, and with photoluminescence for shallower defects. Section 6.6 covers work on the fabrication and testing of single-crystal substrate solar devices, while 6.7 concerns thin-film Sb_2Se_3 solar cells fabricated by thermal evaporation from n-type, undoped and p-type source material.

In this chapter, samples are named under the same scheme as employed for Chapter 5. The synthesis techniques employed for the single crystal samples in this chapter were: direct synthesis from elements (DSE); and vertical Bridgman growth (VB). Samples directly synthesised from the elements were assumed to be of higher purity than samples grown from the pre-synthesised 5N source material (5NAA).

For the in-house synthesised material, the stoichiometry was assumed to correspond to the precise weighed ratios of Sb and Se used in the synthesis reaction. These ratios were chosen at the weighing stage so as to produce stoichiometric (St), with a deviation from exact stoichiometry of < 0.01 at% (balance precision was 0.0013 at%) or either 0.1 at% Se-rich (SeR) or Se-poor (SeP) material. Table 6.1 summarises the sample types, with several examples of each type being fabricated for the work in this chapter. Samples had different stoichiometries, source material and dopants, but were nonetheless processed under identical conditions (ampoule volume, internal pressure, temperature, heating rates etc.) unless otherwise specified, to ensure consistency in results.

Growth Technique	Source Material	Stoichiometry	Extrinsic Dopants	Sample Code
Direct synthesis from elements (Sb_2Se_3) - **DSE**	Elemental Sb shot (6N), Elemental Se shot (5N)	Stoichiometric (< 0.01 at% variation) - **St**	Undoped – **Un**	**DSE-St-Un**
		Se – poor (> 0.1 at% variation) – **SeP**	Undoped – **Un**	**DSE-SeP-Un**
		Se – rich (> 0.1 at% variation) - **SeR**	Undoped - **Un**	**DSE-SeR-Un**
Vertical Bridgman growth - **VB**	Commercial Sb_2Se_3 (5N) – **5NAA**		Undoped - **Un**	**VB-5NAA**
			Sn-doped (~0.1 at%) – **Sn**	**VB-5NAA-Sn**
			$MgCl_2$-doped (~0.1 at%) – **MgCl2**	**VB-5NAA-MgCl2**
	Sb_2Se_3 directly synthesised from the elements (**DSE**)	Stoichiometric (< 0.01 at% variation) - **St**	Undoped - **Un**	**VB-St-Un**
		Se – poor (> 0.1 at% variation) - **SeP**	Undoped - **Un**	**VB-SeP-Un**
			Sn-doped (~0.1 at%) – **Sn**	**VB-SeP-Sn**
			$MgCl_2$-doped (~0.1 at%) – **MgCl2**	**VB-SeP-MgCl2**
		Se – rich (> 0.1 at% variation) - **SeR**	Undoped - **Un**	**VB-SeR-Un**
			Sn-doped (~0.1 at%) – **Sn**	**VB-SeR-Sn**
			$MgCl_2$-doped (~0.1 at%) – **MgCl2**	**VB-SeR-MgCl2**

Table 6.1 Sample codes for all Sb_2Se_3 single crystal sample types examined in this chapter, including details of preparation (synthesis or growth) method, type of sample, stoichiometry and extrinsic doping.

6.2 Conductivity Type of Single Crystal Sb_2Se_3

6.2.1 Hot Probe

Hot probe evaluation of carrier type was conducted as described in Section 3.5.1, on samples of material both synthesised directly from the elements and grown by vertical Bridgman.

6.2.1.1 Undoped Crystals

Sections of the Sb_2Se_3 material directly synthesised from the elements were found to be sufficiently crystalline for contacting with Au for electrical measurements. This was achievable for samples with different stoichiometries in the source material which were therefore examined with the hot probe in order to explore native conductivity type. At first, measurements of thermally-induced voltage were attempted, as this is usually the measurement of choice for resistive samples, however for unknown reasons, doing so did not produce reliable or consistent measurements. However, consistency was found when measuring current, and as a result, thermally-induced current was measured throughout this investigation.

Fig. 6.1a shows the level of thermally induced current from stoichiometric and Se-poor Sb_2Se_3 directly synthesised from the elements. The error bars refer to the level of fluctuation observed in the measured current at equilibrium. For the stoichiometric sample, a positive current was observed with increasing temperature gradient, while the current for the Se-poor sample remained at a low level for most temperature gradients, with a small negative current for large thermal gradients. These responses are compared to those from the Se-rich sample in fig. 6.1b, which exhibits positive currents of an order-of-magnitude greater than either of the other samples. Fig. 6.1c shows the thermally-induced currents for the Sb_2Se_3 single crystals grown by vertical Bridgman with stoichiometric and Se-poor composition. For both samples, the currents observed were comparable to the uncertainty due to current fluctuations. The Se-poor crystal exhibited a small negative current at high thermal gradients, while the stoichiometric crystal did not exhibit significant thermally-induced currents, even at high thermal gradients. Fig. 6.1d includes the measured current for the Se-rich crystal, which

exhibited a significantly larger thermally-induced positive current than for the Se-poor and stoichiometric crystals.

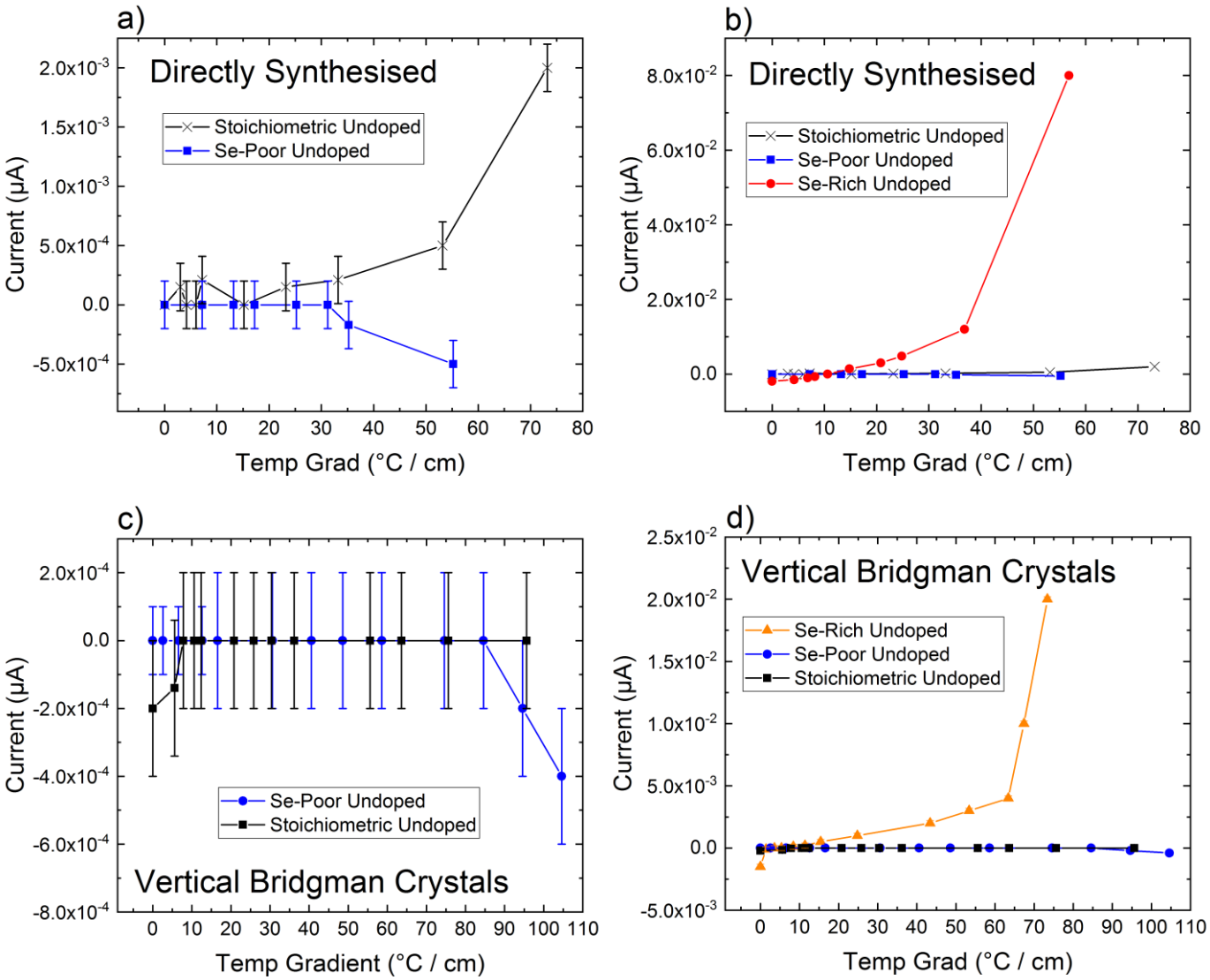

Fig. 6.1 Hot-probe results for undoped Sb_2Se_3 samples: directly synthesised from the elements with a) stoichiometric and Se-poor and b) Se-rich compositions. Results are also shown for crystals grown by vertical Bridgman with c) stoichiometric and Se-poor and d) Se-rich compositions. Se-rich compositions are p-type, stoichiometric are non-conductive, and Se-poor are non-conductive or n-type.

For the directly synthesised samples (fig. 6.1a-b), the positive current observed for the stoichiometric sample suggests p-type doping, while the negative gradient for the Se-poor sample

suggests n-type doping, based on the reference samples (Section 3.5.1). However, as these currents were not dramatically larger than the uncertainty, they suggest weak doping in each case. The positive thermally-induced current observed for the Se-rich sample (fig. 6.1b) also indicates p-type conductivity. For the vertical Bridgman-grown stoichiometric and Se-poor crystals (fig. 6.1c) the measured currents were not significantly larger than the uncertainty, meaning that the samples may be considered undoped. These results therefore indicate that p-type doping occurs within Se-rich Sb_2Se_3, with the results being consistent across samples both directly synthesised and grown by vertical Bridgman. Also, the stoichiometric, high purity Sb_2Se_3 was not self-doped to a significant level. There was some significant differences in the magnitudes of the currents observed for different samples, but there is no clear interpretation for this, as many factors may influence the current magnitudes, such as carrier mobility and deep-level carrier traps. Despite the limitations of the method, these results have important implications for the understanding of native defects within Sb_2Se_3 (Section 6.8.1).

6.2.1.2 Extrinsically Doped Crystals

The results of the hot probe measurements on the extrinsically doped Sb_2Se_3 crystals grown by vertical Bridgman are shown in fig. 6.2. Briefly, these indicate a positive thermally-induced current for the Se-poor Sn-doped and Se-rich Sn-doped crystals, with the latter exhibiting a significantly larger current magnitude (fig. 6.2a-b). Furthermore, the undoped and Sn-doped 5N crystals exhibited clear negative and positive thermally-induced currents respectively (fig. 6.2c). Finally, the Se-rich $MgCl_2$-doped crystal exhibited a negative thermally-induced current (fig. 6.2d). This current had a greater magnitude than any other sample examined, but as mentioned before, no concrete conclusions can be drawn from this observation.

The hot probe results for the Sn-doped crystals grown from: Se-poor, Se-rich and 5N Sb_2Se_3 (figs. 6.2a-b) indicate p-type doping in all cases. For the Se-poor crystal in particular, this suggests that Sn may act as an acceptor in Sb_2Se_3, as the undoped Se-poor crystal exhibited non-conductive or weakly n-type behaviour (figs. 6.1a and c). This is consistent with Sn (group-IV) acting as a substitutional acceptor as Sn_{Sb}.

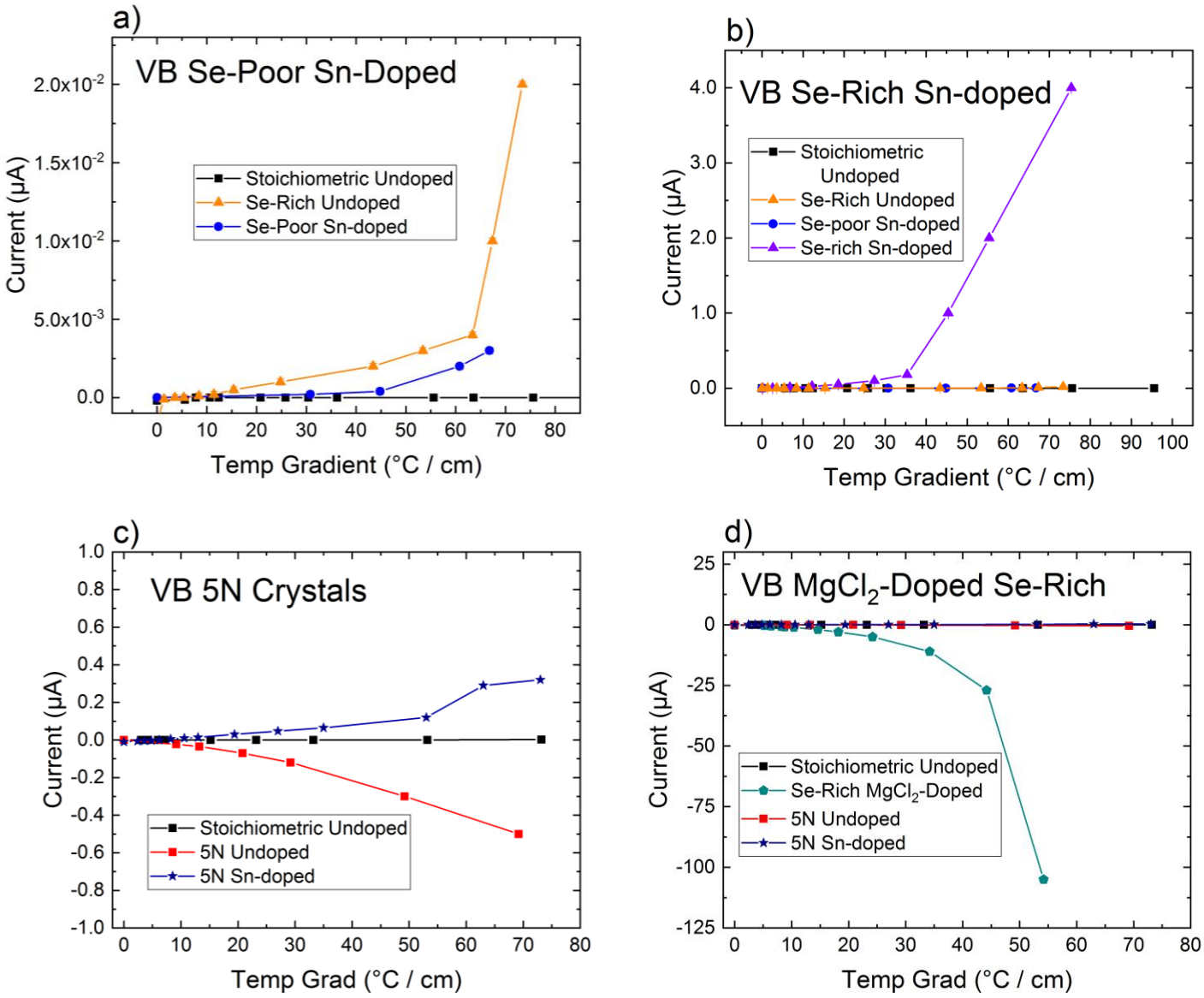

Fig. 6.2 Hot probe results for vertical Bridgman-grown Sb_2Se_3 single crystals with compositions: a) Se-poor and Sn-doped, undoped stoichiometric and undoped Se-rich b) with Se-rich Sn-doped included. c) Undoped and Sn-doped 5N crystals and stoichiometric undoped d) with Se-rich $MgCl_2$-doped included. Sn-doped crystals are p-type while undoped 5N crystals and $MgCl_2$-doped crystals are n-type.

Preparation Technique	Sample Name	Composition	Conductivity Type	Resistivity / kΩcm
Directly synthesised from elements	DSE-SeP-Un	Undoped Se-poor	Intrinsic/weakly n-type	2.0×10^3
	DSE-SeR-Un	Undoped Se-rich	Intrinsic/weakly p-type	4.9
Vertical Bridgman	VB-St-Un	Undoped Stoichiometric	Intrinsic	1.3×10^5
	VB-SeR-Un	Undoped Se-rich	p-type	2.5×10^2
	VB-SeP-Sn	Sn-doped Se-poor	p-type	4.4×10^3
	VB-SeR-Sn	Sn-doped Se-rich	p-type	6.9
	VB-5NAA-Un	Undoped 5N	n-type	1.56 - 4.92
	VB-5NAA-Sn	Sn-doped 5N	p-type	1.0×10^1
	VB-SeR-MgCl2	$MgCl_2$-doped Se-rich	n-type	$1.4 - 4.8 \times 10^{-1}$

Table 6.2 Conductivity type and resistivity values for crystalline Sb_2Se_3 samples examined with the hot probe technique. High resistivity values were observed for Se-poor and/or undoped samples, with lower values for Se-rich and/or extrinsically-doped samples.

The undoped 5N crystal (fig. 6.2c) clearly exhibited n-type conductivity, while the addition of Sn resulted in a switch to p-type, presenting further evidence for Sn as a p-type dopant. Similarly, the addition of $MgCl_2$ to the Se-rich undoped crystal resulted in a switch from p-type conductivity to n-type. The presence of Cl is the main similarity between the 5N (see SIMS in Section 5.7.3) and the $MgCl_2$-doped crystals. This suggests that Cl (group-VII) acts as a donor, which would be consistent with substitutional Cl_{Se}. The greater magnitude of thermally-induced current in the Se-rich $MgCl_2$-doped crystal compared to the undoped 5N crystal may result from a greater carrier density in the former, but this could not be determined without Hall effect or capacitance-voltage measurements.

Table 6.2 shows resistivity measurements of several of the same samples and indicates high resistivity values (> 10 MΩcm) for the directly-synthesised stoichiometric and selenium-poor samples. Meanwhile, the undoped Se-rich vertical Bridgman-grown crystal exhibited intermediate resistivity at ~ 200 kΩcm. The crystals grown by vertical Bridgman from extrinsically-doped Se-rich and 5N Sb_2Se_3 and the directly synthesised Se-rich undoped sample all exhibited relatively low resistivity values (≤ 10 kΩcm) with the lowest values measured for the Se-rich $MgCl_2$-doped crystal, at < 1 kΩcm.

The resistivities are generally consistent with the hot probe results, with high resistivity values corresponding to a low thermally-induced current and vice versa. The variations in resistivity for each of the n-type crystals (5N Sb_2Se_3 and Se-rich $MgCl_2$-doped Sb_2Se_3) indicate a non-Ohmic response. The higher conductivities may suggest greater carrier densities, but Hall effect measurements and/or capacitance – voltage profiling are necessary to determine the carrier density present, with the former carried out on 5N crystals in the following section.

6.2.2 Hall Effect Measurements

Room-temperature Hall effect measurements were made on three single crystal samples of varying thickness, grown by vertical Bridgman from undoped 5N source material, each with four In contacts place in a square, in an approximation of van der Pauw geometry (see Section 3.5.2). Fig. 6.3 shows the results, where Hall conductivity (G_{xy}) is plotted against auxillary magnetic field (H), with the plot zeroed (G_{xy} value at $H = 0$ subtracted) to symmetrise the data. The samples were measured in different ranges of magnetic field, with the relevant ranges for the t = 0.56 and 1.08 mm samples shown in fig. 6.3a, along with their linear fit lines (dashed lines) and for the t = 0.48 mm in fig. 6.3b, with its linear fit. All of the samples exhibited linear behaviour with a negative gradient of varying steepness. Of the samples studied, the 0.56 mm thick sample provided remarkably linear behaviour, meaning the data series and fit line are effectively indistinguishable in the plot of the whole range (fig. 6.3a) and allowing high precision on the linear fit.

From eq. 3.7 the Hall coefficient R_H may be determined from the gradient. In this case the negative gradient of all the series plotted means a negative R_H, indicating a negative carrier charge, i.e. n-type doping in all cases, with the electron density derived from R_H and eq. 3.8. The varying gradients of the plots arise from the variation in sample thickness (see eq. 3.7). From the carrier density and resistivity, the carrier mobility could then be derived from eq. 3.9, with all of these values shown in Table 6.3 for all 3 samples.

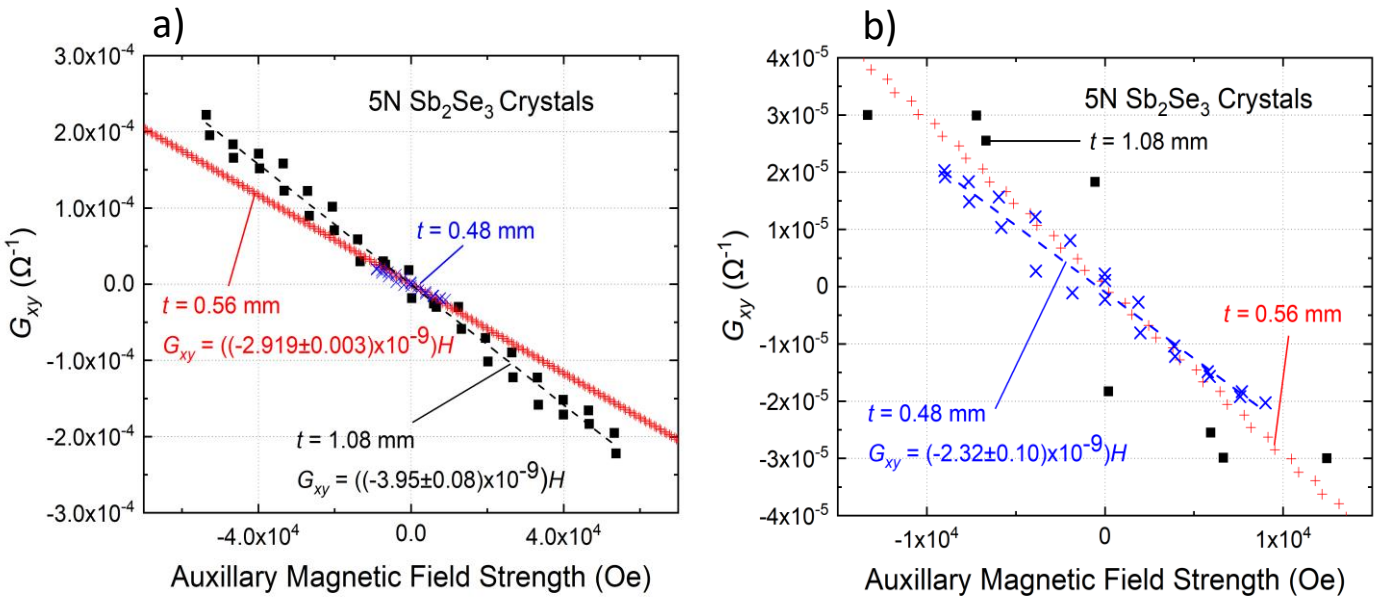

Fig. 6.3 Plot of Hall conductance (G_{xy}) against auxiliary magnetic field (H) for the three 5N Sb_2Se_3 samples synthesised by vertical Bridgman with thicknesses (t) of 0.48, 0.56 and 1.08 mm. a) full range of measurement, showing line of best fit for t = 0.56 and 0.48 mm b) same plot in a smaller range to show plot for t = 0.48 mm sample and line of best fit. The 0.56 mm thick sample (red) exhibited the most linear behaviour. All series exhibited negative gradients i.e. n-type conductivity.

Sample Code	Thickness (mm)	Electron density (cm^{-3})	Resistivity (Ωm)	Electron Mobility ($cm^2V^{-1}s^{-1}$)
VB-5NAA-Un-108	1.08	3.99×10^{16}	6.54	24.5
VB-5NAA-Un-48	0.48	3.3×10^{16}	6.04	31.3
VB-5NAA-Un-56	0.56	3.98×10^{16}	5.46	28.7

Table 6.3 Results from Hall effect measurements of In-contacted undoped 5N crystals grown by vertical Bridgman. Similar values of carrier density, resistivity and carrier density were found in all samples.

The Hall effect measurements provide further evidence for n-type doping in 5N Sb_2Se_3 single crystals, supporting the conclusions from the hot probe (Section 6.2.1). The most likely cause is Cl present in the 5N source material as an impurity (see SIMS in Section 5.7.3).

6.3 Characteristics of Metal - Semiconductor Junctions

6.3.1 Ohmic and Schottky Contacts

Given that, as demonstrated in Section 6.2, Sb_2Se_3 may be extrinsically doped either n- or p-type, which determines the Fermi level position, it is expected that the work functions of metals used for contacting will affect the Ohmic or rectifying character of the contacts. This has relevance to devices, as back-contact barriers are one factor which reduces the efficiency of photovoltaic devices[1]. The presence of contact barriers is also important for electrical characterisation, as *C-V* profiling and DLTS require contact barriers to be effective. Broadly, as explained in Section 2.2.4, metals of a high work function $\Phi_W{}^m$ are required to form an Ohmic contact on a p-type material, while low-work functions are needed to form Ohmic contacts with n-type material[2]. The opposite in each case is necessary to form a contact barrier (i.e. a Schottky contact).

Current-voltage measurements taken of both n- and p-type Sb_2Se_3 crystals with either two In or Au contacts are shown in fig. 6.4. Given that the samples had two identical contacts in each case, there was no physical distinction between forward and reverse bias, so positive and negative voltage

values simply refer to the polarity of the bias from the measurement equipment, and are arbitrary. However, for each contact, one bias polarity was expected to act as forward bias and the opposite as reverse bias, with these polarities reversed for the other contact. For the p-type Sn-doped crystal grown from 5N Sb_2Se_3 (fig. 6.4a), the use of Au contacts produced linear *I-V* behaviour, while the use of In contacts produced clearly non-linear *I-V* behaviour. For this p-type sample, the magnitude of the current was similar for both contact metals. In contrast, for the n-type $MgCl_2$-doped crystal (fig. 6.4b), In contacts produced linear *I-V* behaviour, while the use of Au contacts for the same crystal, as well as the n-type undoped and $MgCl_2$-doped 5N crystals produced non-linear behaviour. Furthermore, for the n-type samples, there was a significant difference in the magnitude of the currents measured for Au contacts compared to In contacts (around 2 orders of magnitude).

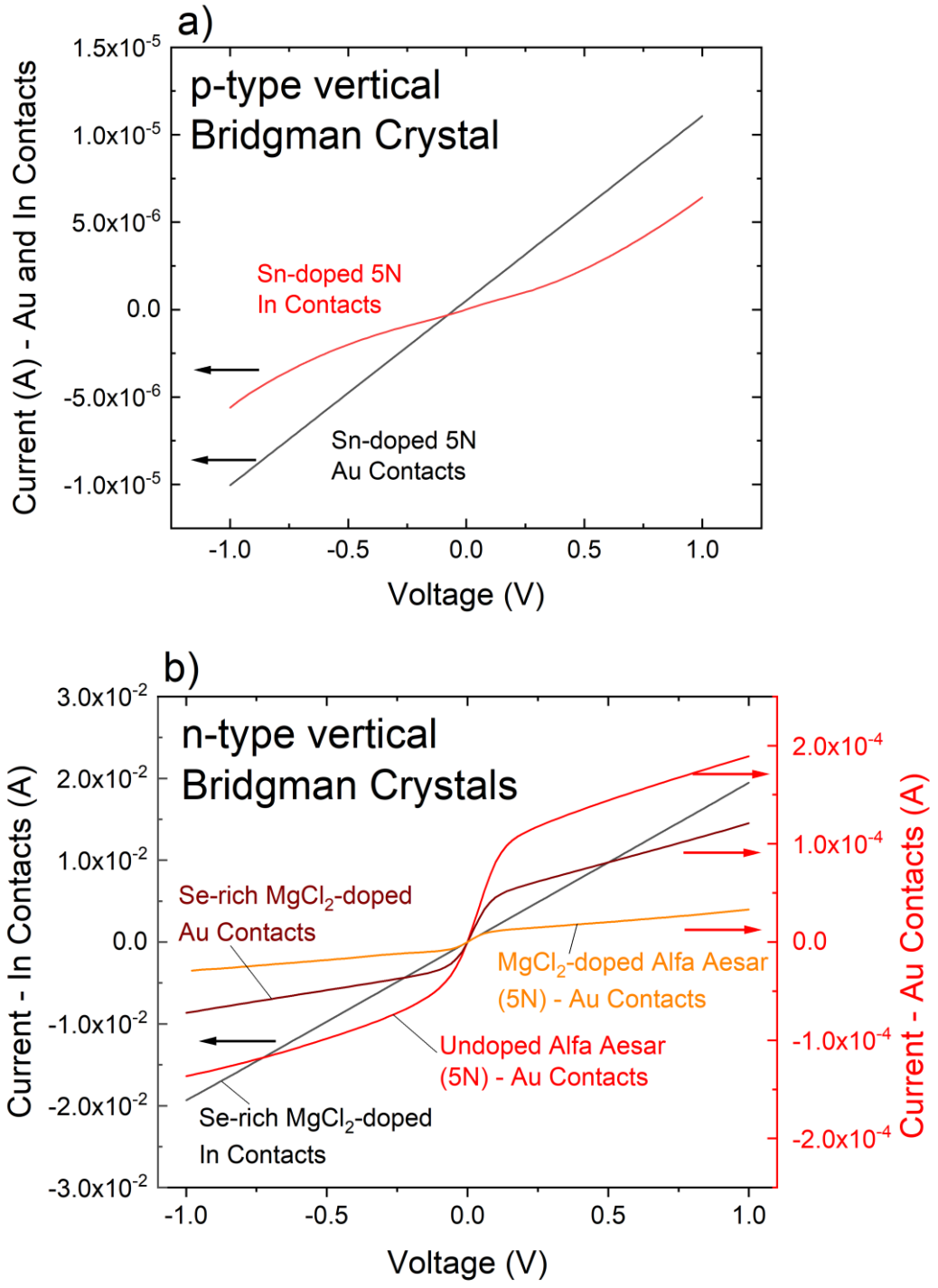

Fig. 6.4 a-b) *I-V* curves for Sb_2Se_3 single crystals grown by vertical Bridgman: a) p-type (Sn-doped 5N crystals) and b) n-type ($MgCl_2$-doped Se-rich; undoped and $MgCl_2$-doped 5N crystals), contacted with either two In or two Au evaporated contacts. Ohmic behaviour is observed for Au contacts on p-Sb_2Se_3 and for In contacts on n-Sb_2Se_3, while a contact barrier is indicated for In on p-Sb_2Se_3 and for Au on n-Sb_2Se_3.

The linear *I-V* behaviour suggests that the use of evaporated Au contacts produced an Ohmic contact on the p-type Sb_2Se_3 sample (fig. 6.4a) while the *I-V* curve for In contacts indicates a rectifying contact on the same sample type. For the n-type case (fig. 6.4b), the opposite is true – In contacts produced Ohmic behaviour on the n-type Sb_2Se_3 sample, while Au contacts formed rectifying barriers. The rectifying behaviour was also observed for the other n-type Sb_2Se_3 samples. These results are consistent with the expected behaviour of metal contacts on semiconductors (see Section 2.2.4) given the small work function of In (4.09 eV [3]) and the large work function of Au (5.3 eV [3]).

6.3.2 Barrier Height Estimation from *I-V-T* Measurements

In order to estimate the height of the Schottky barriers on Sb_2Se_3 single crystals (p-Sb_2Se_3 / In and n-Sb_2Se_3 / Au) temperature dependent *I-V* measurements were taken. The approach outlined by Bätzner was used (Section 3.5.3) in order to estimate barrier height from the temperature-dependent series resistance using eq. 3.11. The configuration used here, with two Schottky junctions lying in series with opposite biases, bears similarity to the work of Bätzner where a p-n junction and Schottky junction are in series, also with opposite biases. This means that for a non-zero bias, whether positive or negative, one junction was under reverse bias while the other was forward biased.

Fig. 6.5a shows the R_S-*V*-*T* plots for the p-type Sn-doped 5N crystal, contacted with In, from 290 K to 380 K, while fig. 6.5b shows the plot for the n-type undoped 5N crystal, contacted with Au, from 220 K to 320 K. The terms ‘forward’ and ‘reverse’ bias simply refer to the polarity of the measurement equipment, rather than being a meaningful distinction because, as previously discussed, the two contacts of these samples are identical. Having said which, *each contact* is expected to have a forward and reverse bias direction, both of which will be of opposite polarity compared to the other contact. These plots both demonstrate similar behaviour on either side of the 0 V bias point, though with some asymmetry, as well as a decrease in overall series resistance with increasing temperature.

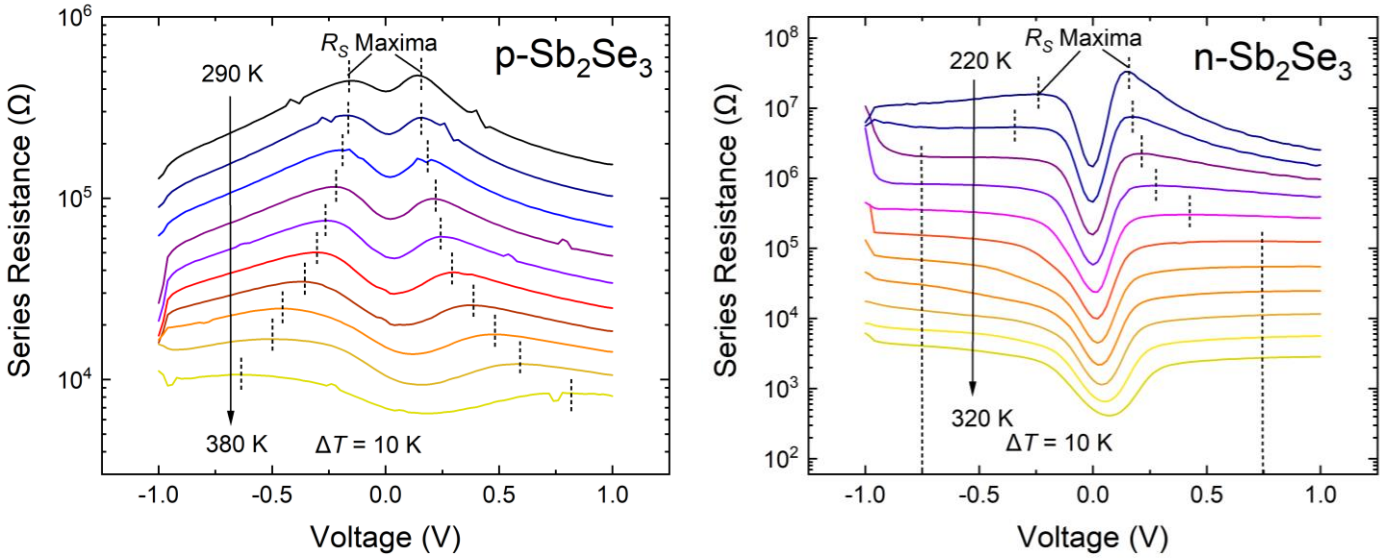

Fig. 6.5 R_S-V plots for a range of temperatures for: a) p-type Sb_2Se_3 (Sn-doped 5N) with In contacts and b) n-type Sb_2Se_3 (undoped 5N crystal) with Au contacts. Dotted lines show where R_S value was taken for each scan.

A minimum in series resistance is observed in the vicinity of the 0 V bias point, and somewhat symmetrical maxima in the values of R_S are observed at all temperatures for the p-Sb_2Se_3 sample, and at low temperatures for the n-Sb_2Se_3 sample. The series resistance is generally higher in the p-type sample than in the n-type sample for a given temperature.

The asymmetry in both samples most likely results from variations in the area, thickness and coverage of the metal contacts used in each case. Meanwhile, the higher series resistance (at a given temperature) for the p-type crystal is consistent with generally higher resistivity values observed in this set of p-Sb_2Se_3 crystals as opposed to the n-Sb_2Se_3 samples at room temperature (see Table 6.2). The series resistances were extracted separately for forward and reverse bias, as they were each expected to relate to one of the two contacts used. For the p-Sb_2Se_3 sample, and at low temperatures for the n-Sb_2Se_3 sample, the series resistance was determined at the maxima in the R_S-V curve as shown by the dotted lines in fig. 6.5, this being where the resistance from the reverse-biased junction is expected to dominate. However, at higher temperatures these maxima were no longer present for the n-Sb_2Se_3 sample, so series resistance values were taken at a fixed value of ± 0.75 V (note long

dotted lines). While this is not ideal, it was assumed that at this bias, the resistance from the reverse-biased junction would still dominate, and in most of these cases the R_S-V plot was fairly flat for a single scan, compared to the difference between scans, so errors in R_S due to the point of measurement were not expected to be significant.

From the series resistance, linearised plots based on eq. 3.11 were prepared for all samples examined with temperature-dependent *I-V*, with the results being shown in fig. 6.6 for a) the p-type Sn-doped 5N crystal, b) the n-type undoped 5N crystal, c) n-type Se-rich $MgCl_2$-doped crystal and d) n-type $MgCl_2$-doped 5N crystal. All plots demonstrate strongly linear behaviour with little scatter.

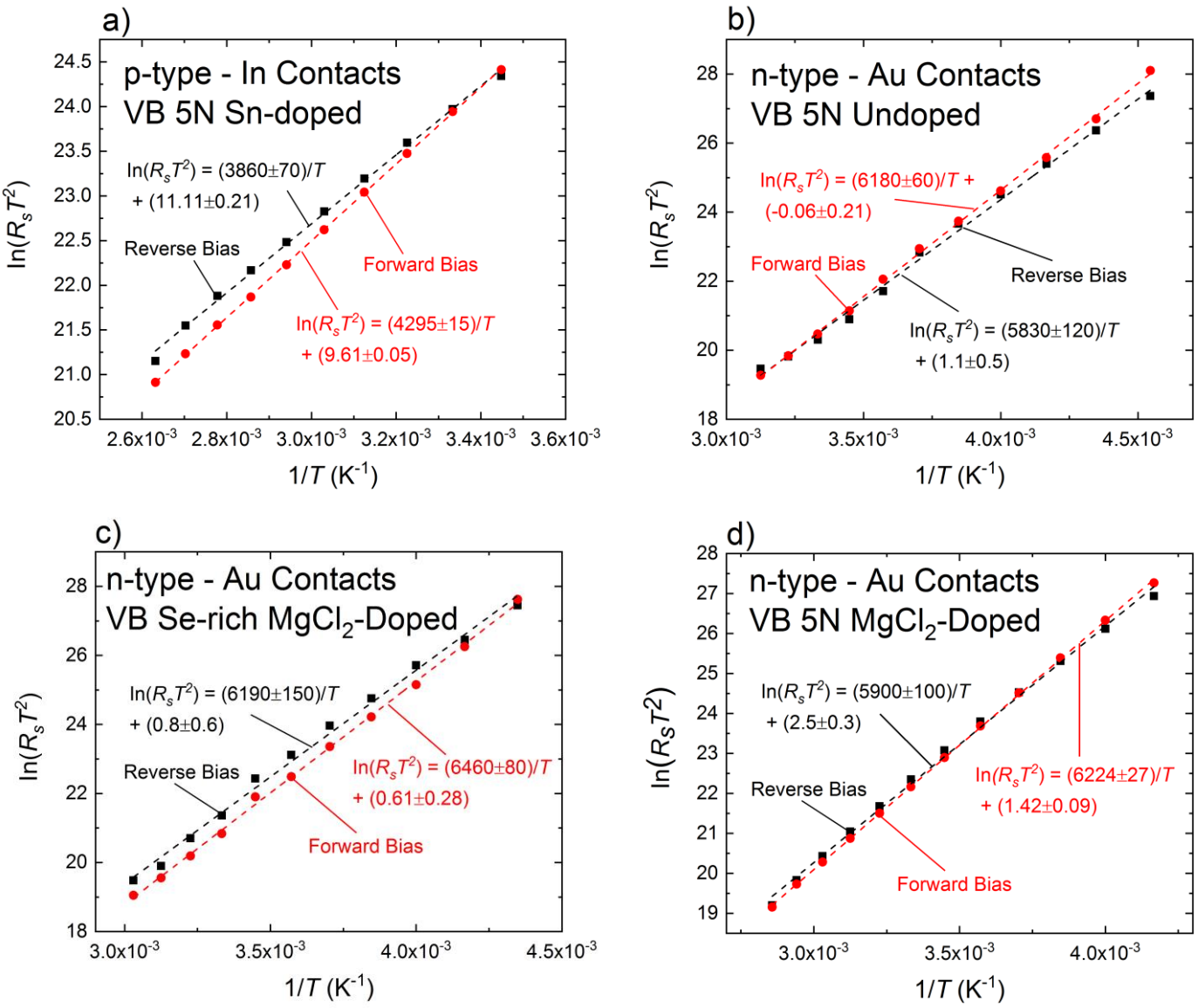

Fig. 6.6 Linearised plots of series resistance for the following Sb_2Se_3 single crystals synthesised via vertical Bridgman: a) p-type (Sn-doped 5N crystal) using In contacts, b) n-type (undoped 5N crystal), c) n-type (MgCl2-doped Se-rich crystal) d) n-type ($MgCl_2$-doped 5N crystal), these latter three all using Au contacts. Linear fits are shown with dotted lines, with equations alongside. Variation is observed between forward and reverse bias.

Fitting to the plots allowed the barrier height ($\Phi_B^{n,p}$) to be estimated from eq. 3.11, with results shown in table 6.4. The calculated barrier heights were larger for the three Au / n-type samples than the In / p-type sample. There was also some variation in the value of barrier height between forward and reverse bias for all samples. In the case of the Au / n-type samples, the difference

between forward and reverse bias was greater than the difference between samples. The largest barrier heights were observed for the $MgCl_2$-doped Se-rich crystal, although the range overlapped with the other n-type samples.

Crystal Type	Schottky Barrier Height ($\Phi_B^{n,p}$) / eV		Work Function of Sb_2Se_3 Crystal ($\Phi_W^{n,p}$) / eV	
	Forward Bias	Reverse Bias	Forward Bias	Reverse Bias
p-type Sn-doped 5N Sb_2Se_3 (VB-5NAA-Sn) – In contacts	0.3701 ± 0.0013	0.333 ± 0.006	4.46	4.42
n-type undoped 5N Sb_2Se_3 (VB-5NAA-Un) – Au contacts	0.533 ± 0.005	0.502 ± 0.010	4.77	4.80
n-type $MgCl_2$-doped Se-rich (VB-SeR-MgCl2) – Au contacts	0.557 ± 0.007	0.533 ± 0.013	4.74	4.77
n-type $MgCl_2$-doped 5N Sb_2Se_3 (VB-5NAA-MgCl2) – Au contacts	0.5363 ± 0.0023	0.508 ± 0.009	4.76	4.79

Table 6.4 Schottky barrier heights estimated from linear plots (fig. 6.6) for single crystal Sb_2Se_3 samples examined with temperature-dependent *I-V* measurements, with two values based on series resistance at forward and reverse bias respectively. Work functions for the Sb_2Se_3 crystals were estimated from the barrier heights and the work function values for Au and In[3].

The difference in values of contact barrier height observed between forward and reverse bias may suggest that in these cases, inconsistencies in contact coverage have more of an impact than the different forms of (in this case, n-type) doping. The larger barrier heights estimated for the Au / n-type samples is consistent with the room-temperature *I-V* measurements (see fig. 6.4), where a greater drop in conductance resulted from the use of Au on n-Sb_2Se_3 than the use of In did for p-Sb_2Se_3. The broadly similar estimates of barrier height for the Au / n-type samples suggest that the carrier density

(and hence the Fermi level) is comparable in all of these. Additionally, all of these barriers are significantly larger than kT at room temperature (~25 meV), suggesting that these contact metals would allow for capacitive measurements to be taken at room temperature, and indeed up to relatively high temperatures (100s of °C).

The values of Sb_2Se_3 work function in Table 6.4 ($\Phi_W{}^{n,p}$) were estimated based on the Schottky barrier heights for the Sb_2Se_3 single crystals and the work functions of Au and In[3] assuming $\Phi_W{}^n = \Phi_W{}^{Au} - \Phi_B{}^n$ and $\Phi_W{}^p = \Phi_W{}^{In} + \Phi_B{}^p$. Fig. 6.7 shows band diagrams for a) p-Sb_2Se_3 and b) n-Sb_2Se_3, both inferred from the values of Schottky barrier height and the work functions of Au and In, demonstrating the relationship between these values.

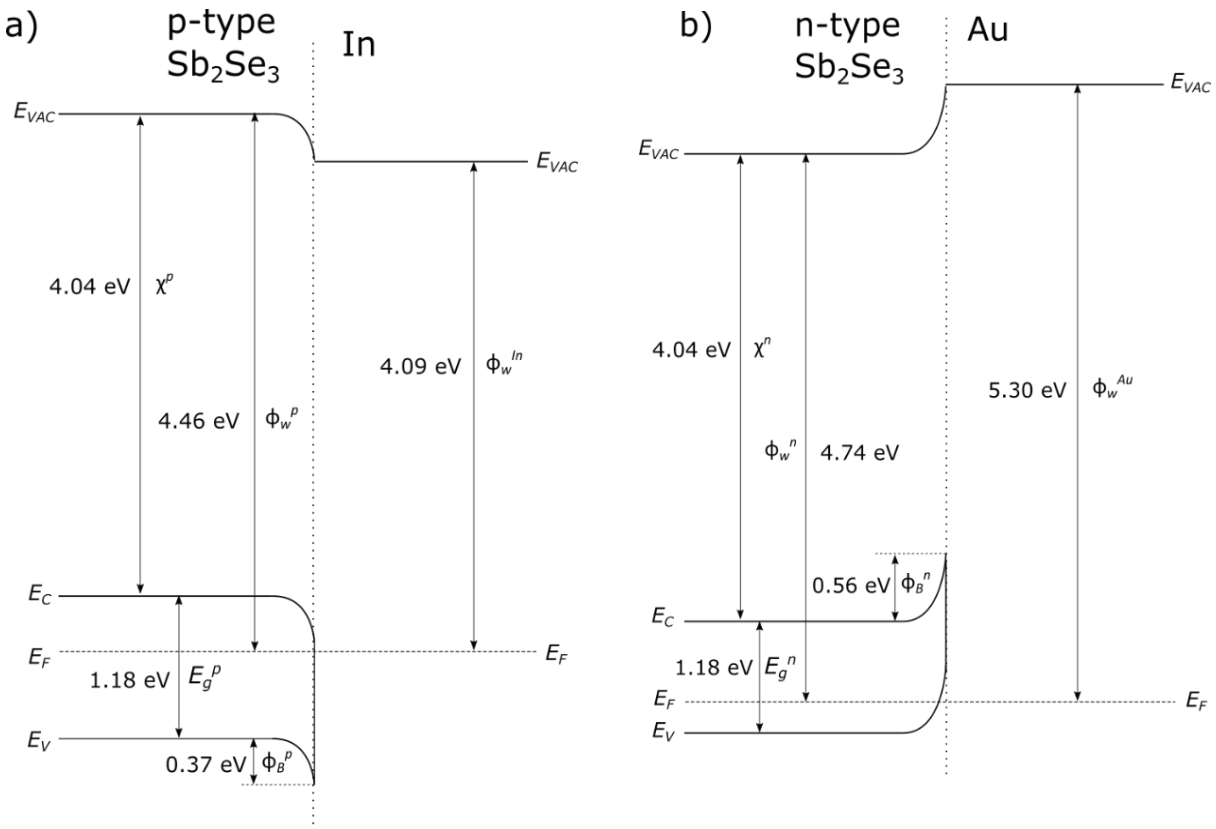

Fig. 6.7 Band diagrams (to scale) inferred from the values of Schottky barrier height (Table 6.4) for a) p-type Sb_2Se_3 with In contacts and b) n-type Sb_2Se_3 with Au contacts. The value of electron affinity for Sb_2Se_3 was taken from [4]. Both diagrams place the Fermi level in a position inconsistent with the conductivity type of the crystals.

The values of work function are consistently larger in the n-type crystals than the p-type, which is inconsistent with conductivity type, as the Fermi level is lower in p-type semiconductors than in n-type. Fig. 6.7 demonstrates how these values of Schottky barrier height result in a Fermi level position inconsistent with the conductivity type, where it is also clear that larger values of barrier height would produce more consistent Fermi level positions. Given that the conductivity types of these crystals are well known, this would suggest that the values of barrier height used to calculate the work functions of the Sb_2Se_3 crystals are underestimates. These results therefore suggest there may be interfacial layers or surface band-bending effects that are not accounted for in the simple scheme presented in fig. 6.7. However, exploring these possibilities is beyond the scope of this work.

6.4 Capacitive Measurements of Sb_2Se_3 Single Crystals

6.4.1 *C-f* Measurements and Roll-off

Capacitance-frequency (*C-f*) profiling was carried out on contacted crystals of both conductivity types, with DC biases applied, in order to determine the reliability of carrier densities measured at a given frequency, taking into account the effects of deep level traps and the high-frequency 'roll-off' effect as described in Section 3.5.4.

6.4.1.1 N-type Crystals

Three n-type Sb_2Se_3 crystals grown by vertical Bridgman, all with two lateral evaporated contacts (either one Au and one In or both Au), 0.1 cm^2 in size and 2 mm apart, were examined with *C-f* profiling: a $MgCl_2$-doped Se-rich crystal, a $MgCl_2$-doped Se-poor crystal and an undoped 5N crystal. The $MgCl_2$-doped Se-rich crystal was 2.29 mm thick and used one Au and one In contact, with a series resistance (at forward bias) of 80 Ω, while the Se-poor crystal was 2 mm thick, also using one Au and one In contact, with a series resistance (at forward bias) of 50 Ω. The undoped 5N crystal was 1 mm thick with two Au contacts, meaning the series resistance at forward bias could not be measured. The resistance was measured at the minimum (0 V bias) to be 400 Ω, similar to the values for both $MgCl_2$-doped crystals. However, one would expect the 'effective' series resistance

under bias to be smaller than this, because when one of the junctions was under reverse bias, the other junction would have been be forward-biased.

The *C-f* scans for the three samples are shown in fig. 6.8, plotted for different DC bias levels from -1 V to +1 V. All scans indicate a general decrease in capacitance with AC frequency, with the most dramatic drops occurring at low and high AC frequency. For the $MgCl_2$-doped Se-poor (fig. 6.8a) and Se-rich (fig. 6.8b) crystals, a level region is observed in the mid frequency ranges 10^4-10^5 Hz and 10^2-10^5 Hz respectively, for reverse bias only. Meanwhile, the undoped 5N crystal (fig. 6.8c) exhibited a level region in the mid-frequency range 10^3-10^5 Hz for both reverse and forward bias.

The rapid drop of capacitance with frequency in the low frequency region indicates the influence of deep-level traps, while the drop at high frequencies is consistent with the expected 'roll-off' behaviour observed for resistive samples (Section 3.5.4). The lack of a level region at forward bias for the $MgCl_2$-doped Se-poor (fig. 6.8a) and Se-rich (fig. 6.8b) crystals indicates an absence of rectifying behaviour at forward bias, due to Ohmic behaviour at the n-Sb_2Se_3 - In interface. Meanwhile the level region observed at both forward and reverse bias for the undoped 5N crystal (fig. 6.8c) results from two rectifying Au contacts being used. Based on eq. 3.12, the flat region of the scans shown in fig. 6.8 was used to estimate the 'true' capacitance values of the undoped 5N crystal, $MgCl_2$-doped Se-poor and Se-rich crystals, at 0 V bias, estimated to be 3×10^{-9} F, 3×10^{-8} F and 2×10^{-8} F respectively. The true capacitance value was used to estimate the effective series resistance under non-zero bias as being around 30 Ω for the 5N crystal, based on the observed roll-off behaviour and eq. 3.12. Meanwhile the series resistance values measured at forward bias for the $MgCl_2$-doped crystals are consistent with the roll-off behaviour and the values of true capacitance.

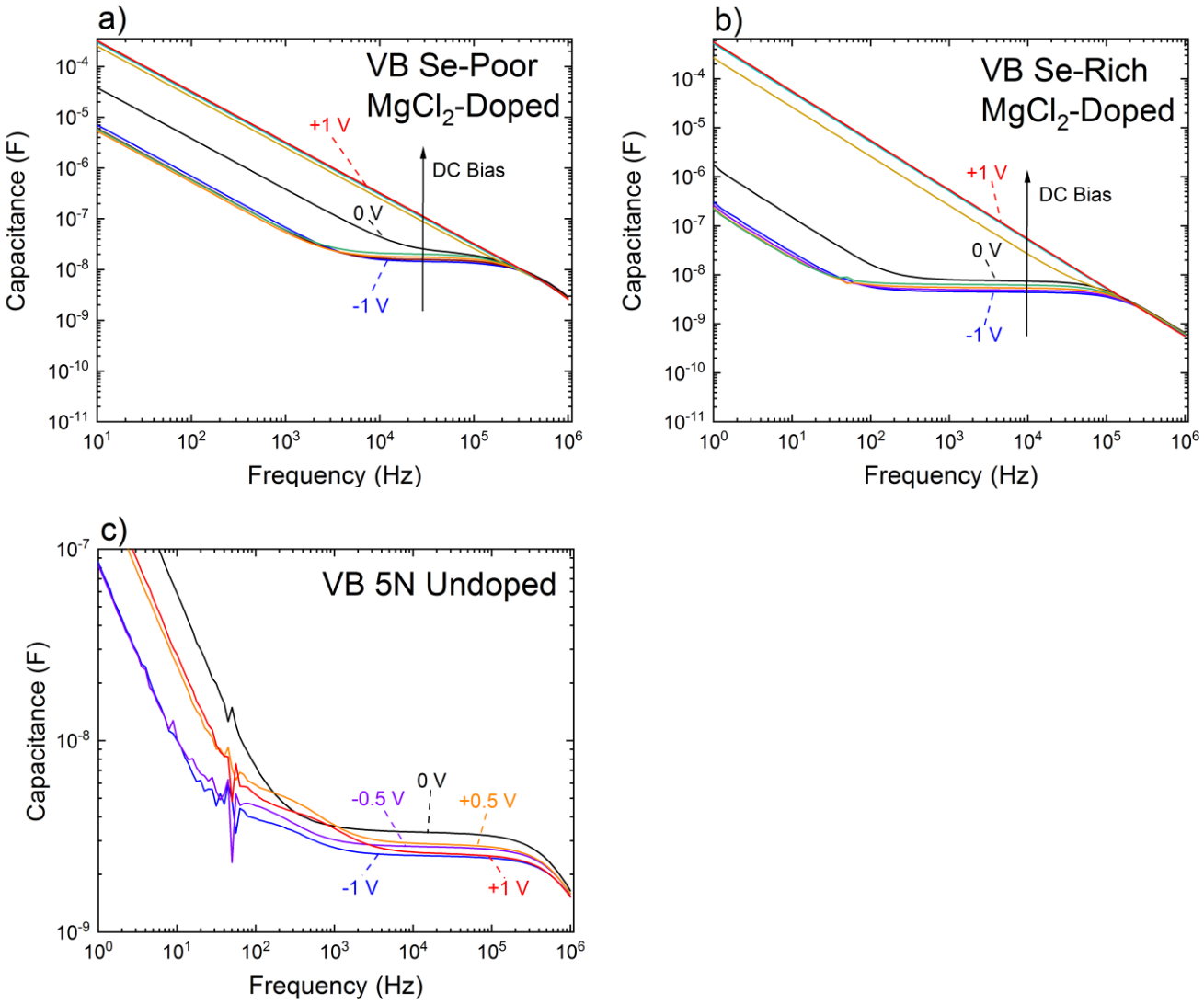

Fig. 6.8 *C-f* plots of vertical Bridgman-grown n-type Sb_2Se_3 crystals: a-b) $MgCl_2$-doped a) Se-poor with one Au and one In contact b) Se-rich with one Au and one In contact c) undoped 5N crystal with both Au contacts. Scans are shown for multiple applied DC biases from -1 V to +1 V. All scans indicate an overall decrease in capacitance with increasing frequency, with level regions in the mid-frequency range.

6.4.1.2 P-type Crystals

Both the Se-poor and Se-rich Sn-doped Sb_2Se_3 single crystals were 2 mm thick with lateral contacts 0.1 cm^2 in size and spaced 2 mm apart. The Se-rich crystal had two In contacts, while the Se-poor used one Au and one In contact. The series resistance of the Se-poor crystal was determined to be 8.6 MΩ from *I-V* measurements, while the series resistance for the Se-rich crystal could not be directly determined from *I-V* as two In contacts were used. *C-f* measurements taken for several DC bias values from 0 V to ±1 V are shown in fig. 6.9 for the Sn-doped a) Se-rich and b) Se-poor single crystals.

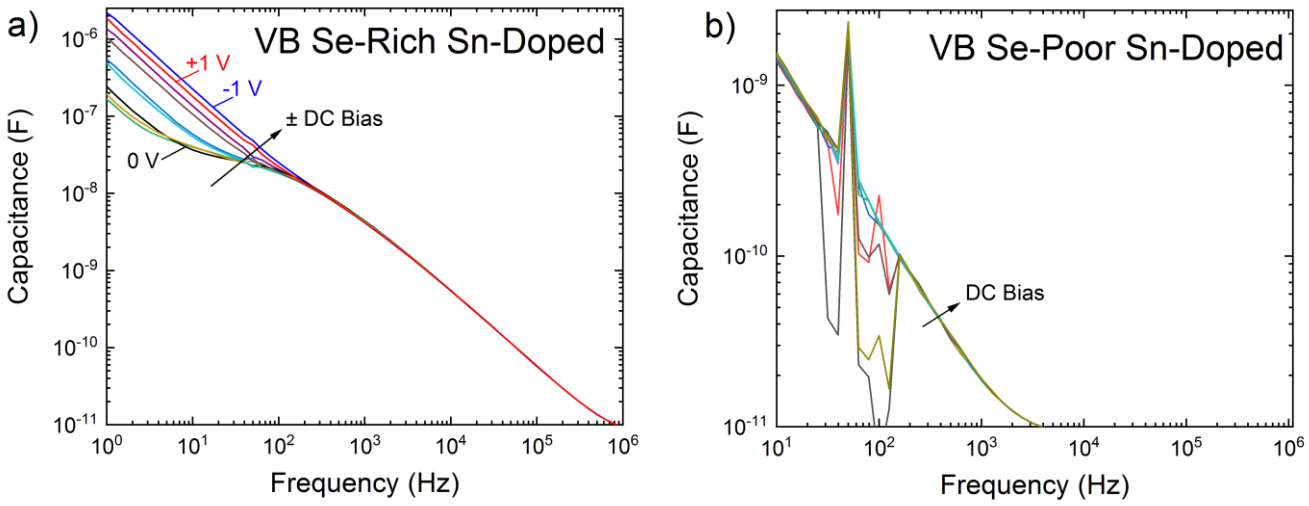

Fig. 6.9 *C-f* measurements of p-type vertical Bridgman-grown Sb_2Se_3 single crystals taken for DC bias levels from 0 V to ±1 V: a) Sn-doped Se-rich with two In contacts b) Sn-doped Se-poor with one Au contact and one In contact.

The Sn-doped Se-rich crystal demonstrated some variation with DC bias at frequencies < 100 Hz, but no significant variation at > 100 Hz, with a steep decline in overall capacitance. The Sn-doped Se-poor crystal demonstrated no variation with DC bias across the whole frequency range, and a much steeper decline in capacitance than the Se-rich. The Se-poor crystal also exhibited dramatic spikes and dips in capacitance values between 10 and 100 Hz, associated with impedance overload error. 10^{-11} F is the lower limit for the system.

The falling values of capacitance with frequency in both scans most likely result from a combination of frequency-dependent carrier capture/emission at low frequency, and the high-frequency 'roll-off' behaviour observed in resistive materials, with the rapid drop-off suggesting high series resistance values in both cases, as indicated in eq. 3.12. Given that both samples had the same dimensions, this suggests the difference in the rate of drop-off derives from varying resistivity between the samples, i.e. that the Se-poor crystal was significantly more resistive than the Se-rich, consistent with the impedance overload errors observed in the former. Furthermore, there was no flat region in either scan, meaning that the 'true' capacitance (eq 3.12) could not be determined, making measurements of carrier density difficult in both cases.

6.4.2 *C-V* Measurements and Carrier Density

Capacitance-voltage measurements were carried out on n-type Sb_2Se_3 crystals grown by vertical Bridgman: an undoped 5N crystal, $MgCl_2$-doped Se-poor and $MgCl_2$-doped Se-rich crystals, as well as a p-type Sn-doped Se-rich crystal. The data were used to produce Mott-Schottky plots to estimate carrier density (N_S), as described by eq. 3.15. A relative dielectric constant of 19.8[5] was used in all cases, based on optical measurements from thin films. However, the highly anisotropic nature of Sb_2Se_3 means that this value may be dependent on crystallography. It should suffice as a tool for comparison, however, given that for all crystals studied, the samples were contacted on the (010) crystal plane.

6.4.2.1 N-type Crystals

The highest AC frequency used in the measurement of the n-type crystals was 1 MHz, while the frequency-dependent measurements (Section 6.4.1.1) indicated the true value of the capacitance on the order of 10^{-8} F, with series resistance on the order of 10s of Ω. This places these samples on the borderline of where carrier density may be reliably measured ($\omega C_{true} R_s \sim 0.1$) based on eq. 3.16. Therefore, it was worth comparing carrier densities derived at high frequency to lower-frequency measurements.

Mott-Schottky plots for the undoped 5N crystal are shown in Fig. 6.10a, demonstrating the differences observed when measurements were taken at different AC frequencies. The scans exhibit symmetrical behaviour at relatively high frequencies, with C^{-2} increasing with DC bias, as would be expected for the one-sided junction model applied to two identical Au contacts with opposite biases. It should be noted, as a result, that the terms 'forward' and 'reverse' bias, are arbitrary, and apply only to the polarity of the measurement equipment, with no physical distinction. Overall values of C^{-2} increased at higher frequency, but the gradients of the plots did not change noticeably. The general increase in C^{-2} is consistent with the 'roll-off' in capacitance exhibited in fig. 6.8c, while the similar gradients at higher frequencies indicate that carrier densities calculated from these plots are reliable.

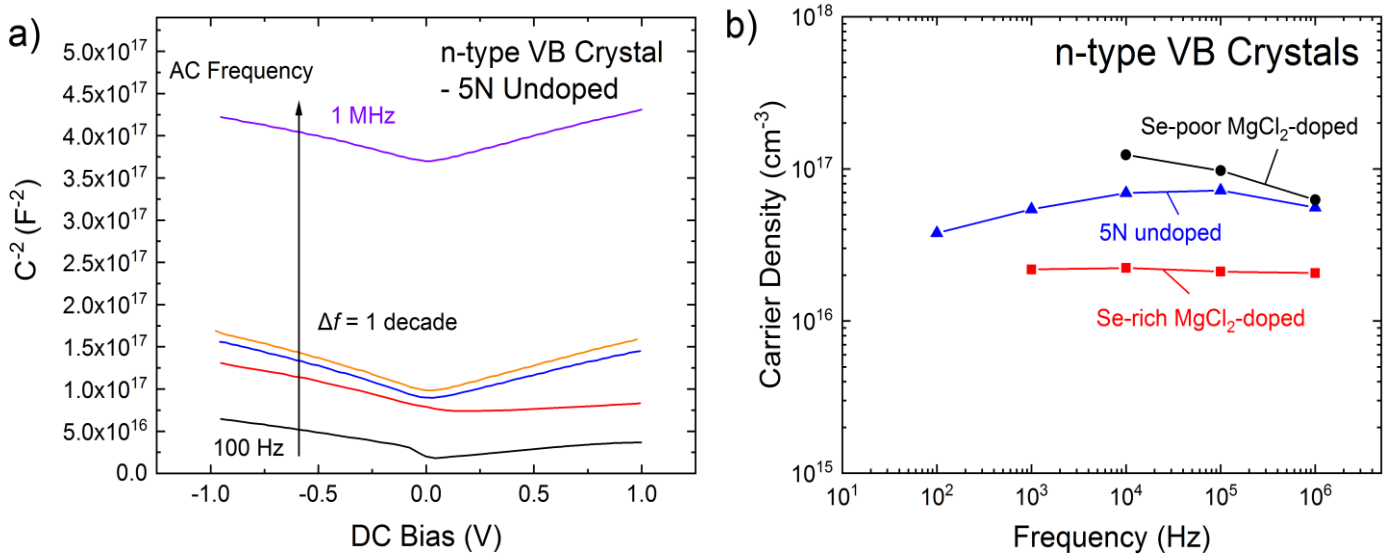

Fig. 6.10 a) Mott-Schottky plots for the n-type undoped 5N crystal taken with Au contacts at a range of frequencies from 100 Hz to 1 MHz. b) Estimated carrier densities for the n-type crystals: $MgCl_2$-doped Se-poor, undoped 5N and $MgCl_2$-doped Se-rich, plotted against AC measurement frequency. Some variation of carrier density with frequency was observed.

The gradients from Mott-Schottky plots taken at different frequencies were used to calculate the carrier densities for three n-type samples with 0.1 cm^2 contacts, shown in fig. 6.10b. The estimated carrier density for the $MgCl_2$-doped Se-rich crystal was fairly constant at ~ 2 x 10^{16} cm^{-3} while the

values for the undoped 5N crystal and the $MgCl_2$-doped Se-poor crystal were larger, and varied with frequency from 4–7 x 10^{16} cm^{-3} and 6 x 10^{16} – 1.2 x 10^{17} cm^{-3} respectively.

The reasonably constant estimates of carrier density with frequency in fig. 6.10b confirm the reliability of these values. This result is significant as the carrier density for the undoped 5N crystal, at 4–7 x 10^{16} cm^{-3}, is consistent with the value determined from Hall measurements in Section 6.2.2, at 4 x 10^{16} cm^{-3}. Furthermore, similar values of carrier density were estimated for the intentionally $MgCl_2$-doped samples to the non-intentionally doped 5N crystal, which has relevance for understanding doping mechanisms (Section 6.8.2). Overall, all methods of n-type doping studied here have yielded doping densities in the range required for photovoltaic applications. i.e. ~10^{16} cm^{-3}.

6.4.2.2 P-type Crystals

The rapid roll-off indicated by the capacitance-frequency plot of the selenium-poor Sn-doped Sb_2Se_3 single crystal, shown in fig. 6.9b, means that an accurate estimate for carrier density could not be determined. For the Se-rich Sn-doped sample, several measurements were taken at relatively low frequencies (500 Hz – 50 kHz), as the capacitance rapidly dropped off at higher frequencies (see fig. 6.9a). A representative Mott-Schottky plot is shown in fig. 6.11a for the 10 kHz measurement. This plot indicates broadly symmetrical behaviour expected for the one-sided junction approximation when two identical (In) contacts with opposite biases were used, with some variation between forward and reverse bias (once again, these biases refer only to the polarity of the measurement equipment). Fig. 6.11b shows the carrier densities estimated from Mott-Schottky plots taken at a range of frequencies, which indicate a decrease with frequency, as expected from the capacitance vs. frequency behaviour (fig. 6.9a), from 2 x 10^{17} to 1 x 10^{15} cm^{-3}.

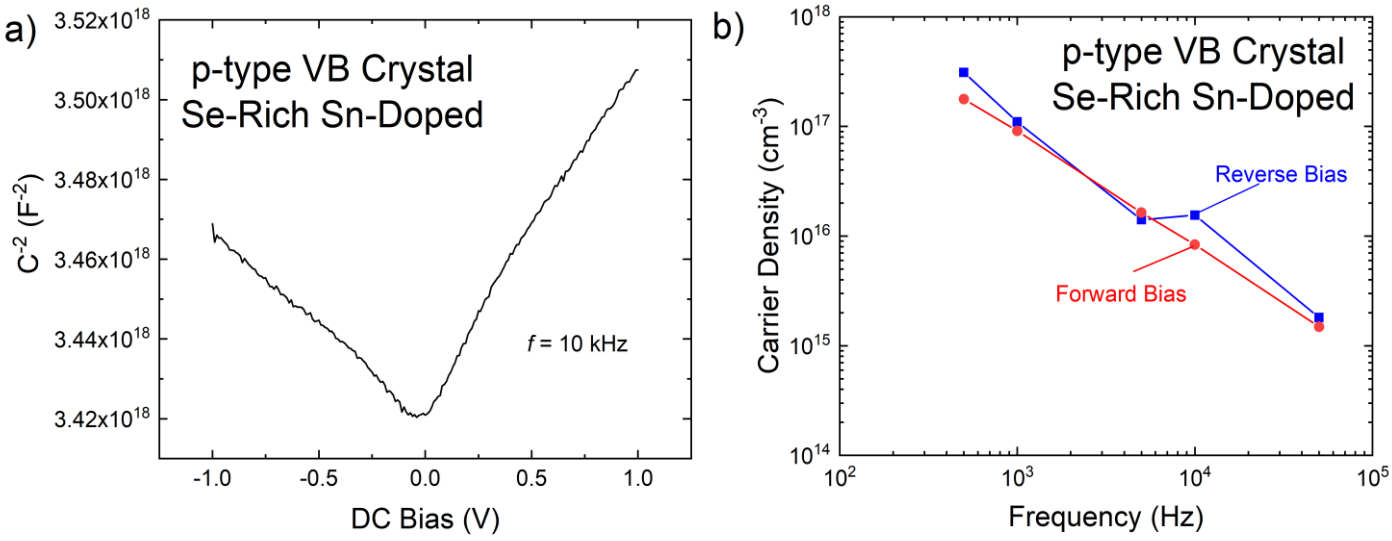

Fig. 6.11 a) Mott-Schottky plot for a Sn-doped, Se-rich Sb_2Se_3 crystal, taken at 10 kHz, indicating mostly symmetrical behaviour with some variation in gradient between forward and reverse bias. b) estimated carrier densities vs. frequency, based on gradients of Mott-Schottky plots at both forward and reverse bias. These indicate a drop of N_S with frequency where $N_s \propto \omega^{-1.1}$.

While the estimated carrier densities shown in fig. 6.11b demonstrate a drop-off with frequency, they do not indicate a situation where $(\omega C_{true} R_S)^4 >> 1$ as the carrier density does not scale as ω^{-4} (see eq. 3.16) but rather scales as $\omega^{-1.1}$. This means that measurements taken at the higher frequencies are broadly reliable and though they are still likely to give an underestimate, they may serve as a lower bound for carrier density. The low-frequency measurements are likely to be unreliable, as they may be influenced by the presence of deep-level traps. This suggests a doping density for Sn-doped, Se-rich Sb_2Se_3 ranging from 10^{15} to 10^{16} cm^{-3}.

6.5 Point Defects in Sb_2Se_3 Single Crystals

6.5.1 Deep-Level Transient Spectroscopy

Deep-level transient spectroscopy (DLTS) was carried out on an n-type undoped 5N Sb_2Se_3 crystal and a $MgCl_2$-doped Se-rich Sb_2Se_3 crystal, each with two Au contacts, with a 1 ms filling pulse duration used in both cases.

Plots of the magnitude of the capacitance change (ΔC) derived from the sinusoidal correlation function b_1 (Section 3.5.6) against temperature, are shown in figs. 6.12a-b. These both show clear peaks in ΔC at around 170, 260 and 330 K. The positions of these peaks for several correlation functions, each with a specific time constant, τ_e, were used to produce Arrhenius plots based on eq. 3.20, and shown in fig. 6.13 for a) the undoped 5N crystal (three peaks) and b) the $MgCl_2$-doped Se-rich (two peaks) Sb_2Se_3 crystal respectively. The Arrhenius plots indicated linear behaviour for all trap levels examined, with some scatter about the linear fit line. Based on the Arrhenius plots, the values of activation energy (E_A) were derived from the gradient of the linear fit (dashed lines in fig. 6.13) and eq. 3.20 while the capture cross-section (σ_n) values were derived from the fitted linear intercept and eq. 3.20. These values were estimated for each level and reported in Table 6.5. In order to estimate the magnitude of capacitance change, ΔC, the nominal values of E_A and σ_n (from the linear fit of the Arrhenius plots) were then used to provide peak positions for the calculated peaks in the ΔC plots shown in figs. 6.12a-b. With the peak positions fixed, the values of ΔC and width were varied manually so as to provide the best visual match to the peaks in each case (where the calculated peaks differ from the position or width of the experimental peaks this is because the calculated peak positions were derived from the linear fits to the Arrhenius plots, rather than resulting from direct fitting of the experimental peaks). The highest temperature peak for the $MgCl_2$-doped crystal could not be used to produce an Arrhenius plot with reasonable values for E_A (results were larger than the Sb_2Se_3 band gap). In calculating the value of N_T, eq. 3.18 was employed, making use of the values of ΔC from the calculated peaks, with the values of N_S (and associated uncertainty) being based on the carrier concentration determined from *C-V* measurements of these same samples (Section 6.4.2.1). High precision in the value of ΔC was not crucial for these estimates because when estimating the trap

concentration N_T from eq. 3.18, the dominant source of uncertainty was expected to be the doping density N_S.

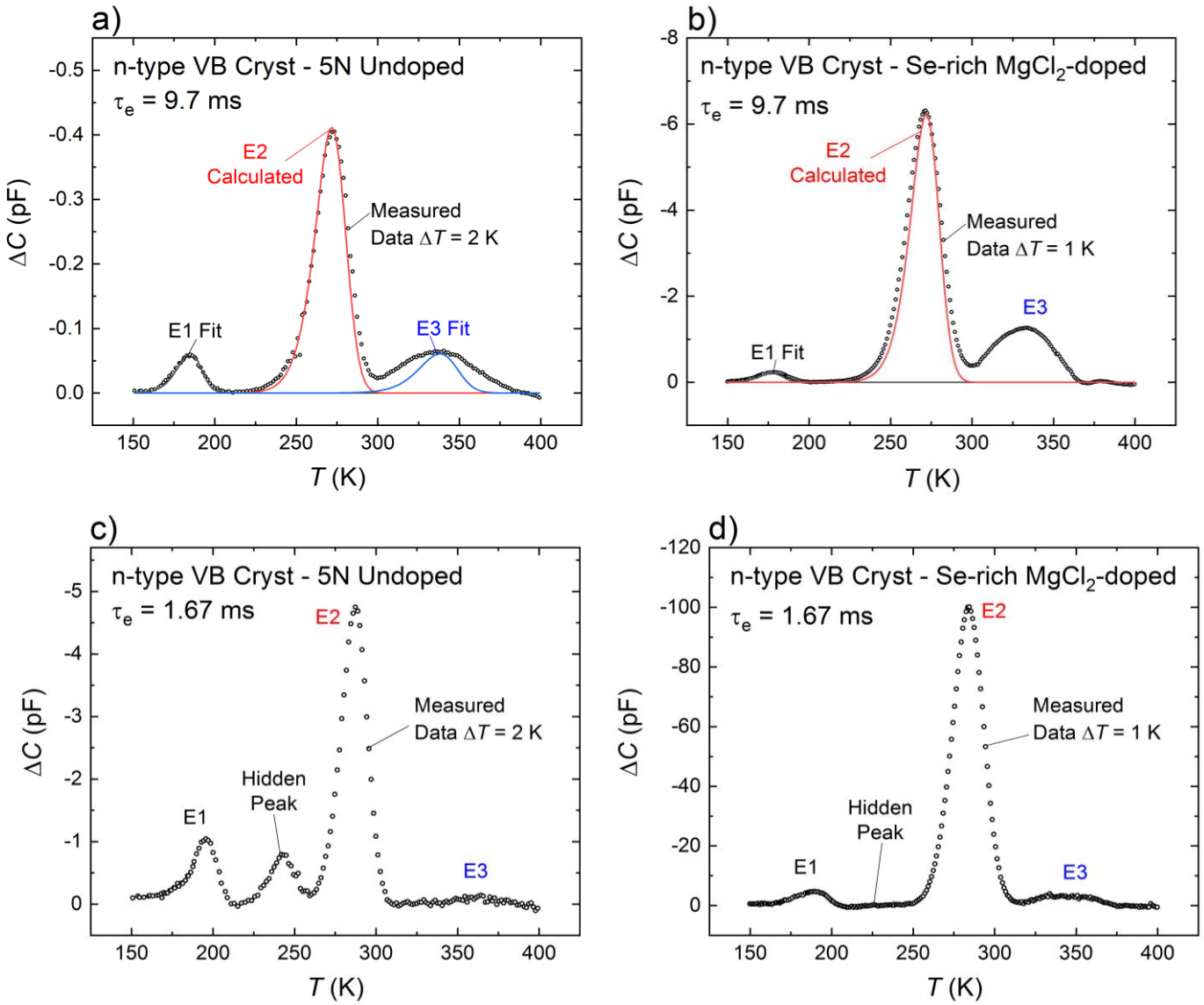

Fig. 6.12 DLTS data for n-type vertical Bridgman-grown Sb_2Se_3 single crystals for 1 ms pulse width: a-b) Plots of ΔC against temperature, for τ_e = 9.7 ms, for the crystals: a) undoped 5N crystal and b) $MgCl_2$-doped Se-rich crystal. c-d) ΔC vs. temperature scans for τ_e = 1.67 ms, for c) the undoped 5N crystal and d) the Se-rich $MgCl_2$-doped crystal. Peaks in the vicinity of 170, 260 and 340K appear in all scans, as well as a hidden peak in c), with calculated peaks (red) based on values of E_A and σ_n from the linear fits to Arrhenius plots, matched visually to the experimental peaks where possible through manual adjustment of ΔC.

The similar form of the temperature scans for the two crystals (figs. 6.12a-b) suggests that deep-level defects of similar activation energies are present in both Sb_2Se_3 samples. This implies either that the peaks represent defects native to Sb_2Se_3 (e.g. V_{Sb} and V_{Se}), or that similar defects result from the unintentional impurities in the undoped 5N crystal as in the intentionally $MgCl_2$-doped crystal. The form of the experimental peaks, especially the peaks at 330 K, suggest the presence of multiple overlapping peaks, meaning that more than three primary deep-level defect levels are represented. The analysis was carried out assuming single defect levels for each peak, so this may be the reason for the very large values of capture cross-section observed for E2 in the $MgCl_2$-doped crystal (see Table 6.5), as multiple overlapping levels are, in fact, represented.

The temperature scans for shorter time constants (figs. 6.12c-d) offered clear indication of a hidden peak at ~ 240 K for the undoped 5N crystal, with only the suggestion of a peak for the $MgCl_2$-doped crystal. In the former case, the range of time constants where the peak was visible was not great enough to produce an Arrhenius plot. The estimated values of E_A from the Arrhenius plots (Table 6.5) support the suggestion that defects of similar energy are present in both crystals.

However, the scatter of points about the linear fit in the Arrhenius plots (fig. 6.13) leads to significant uncertainties on these values. This is especially true for the cross-section values, since small uncertainties on the linear intercept $\ln(\chi_n\sigma_n)$ (eq. 3.20) produce large uncertainties on σ_n.

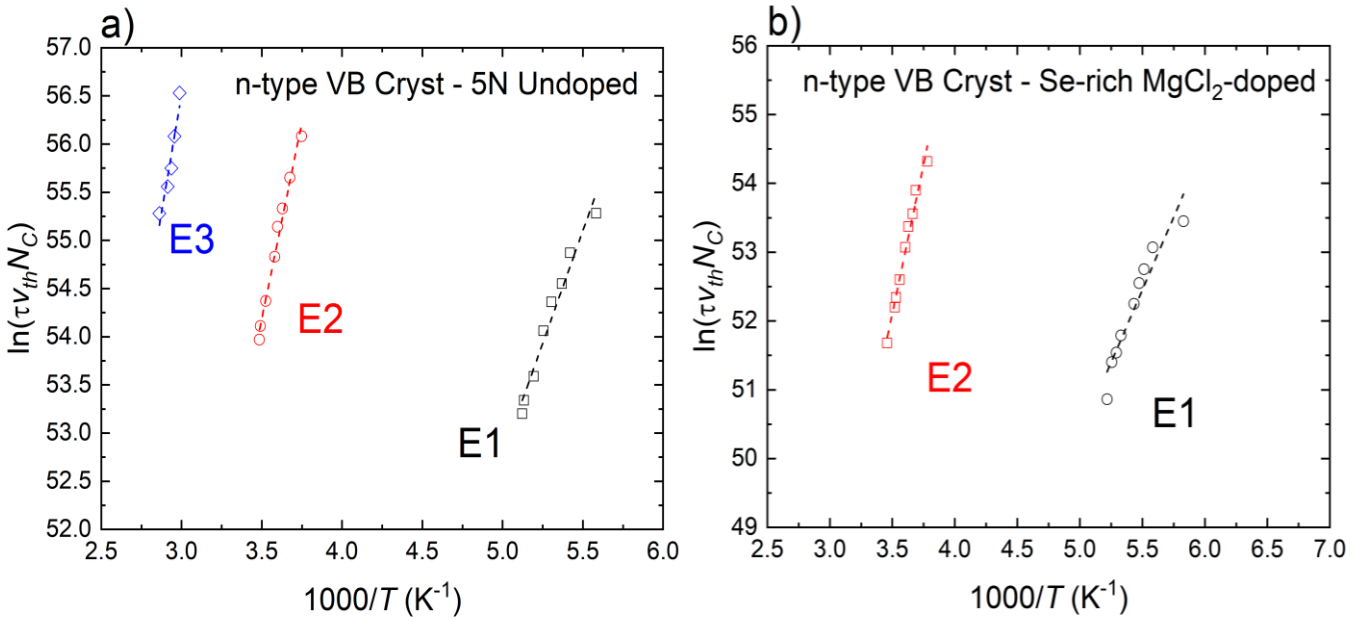

Fig. 6.13 Arrhenius plots for a) the three principal peaks for the undoped 5N crystal and b) two of the principal peaks for the $MgCl_2$-doped crystal. Linear fits are shown with dashed lines.

Sample	Defect	E_A - Trap activation energy (E_C - E_T) (meV)	σ_n - Capture cross-section (cm^2)	N_T - Trap density (cm^{-3})
VB-5NAA-Un	E1	400 ± 30	$2 \times 10^{-14} – 1 \times 10^{-12}$	$(2.2 \pm 0.6) \times 10^{14}$
	E2	700 ± 40	$2 \times 10^{-12} – 3 \times 10^{-11}$	$(1.4 \pm 0.4) \times 10^{15}$
	E3	850 ± 130	$1 \times 10^{-14} – 3 \times 10^{-10}$	$(1.1 \pm 0.3) \times 10^{14}$
VB-SeR-MgCl2	E1	360 ± 40	$1 \times 10^{-14} – 5 \times 10^{-12}$	$(1.06 \pm 0.03) \times 10^{14}$
	E2	750 ± 40	$6 \times 10^{-11} – 2 \times 10^{-9}$	$(3.19 \pm 0.08) \times 10^{14}$

Table 6.5 Electron trap parameters extracted from Arrhenius plots (fig. 6.13) for the n-type undoped 5N crystal (VB-5NAA-Un) and the n-type $MgCl_2$-doped Se-rich crystal (VB-SeR-MgCl2). Similar values of activation energy were found for both samples for the electron traps E1 and E2.

6.5.2 Photoluminescence

Photoluminescence measurements were carried out (Section 3.5.7) on the following Sb_2Se_3 single crystal samples: stoichiometric undoped, Se-rich Sn-doped, Se-rich $MgCl_2$-doped and an undoped 5N crystal. The results of the PL measurements are shown in fig. 6.14a for all samples, taken at 10 K with 37 mW laser power.

These results indicate clear differences in the PL spectra for samples with different dopants. No major peaks were observed in the spectrum for the undoped Sb_2Se_3 crystal, while a prominent peak at 1.10 eV, with small shoulders at 0.91 eV and 1.22 eV, was observed for the $MgCl_2$-doped crystal. The Sn-doped crystal exhibited a major peak at 0.87 eV, while the undoped 5N crystal exhibited peaks at 0.86 eV, 1.09 eV and 1.22 eV. These peaks all lie in a similar energy range to those reported in the literature[6] for polycrystalline Sb_2Se_3 (see Table 6.6).

Power-dependent measurements were taken in the range 0.26 – 37 mW for all three doped crystals and PL intensity (read-off from the peak maximum in each case, with no fitting) was plotted against laser power on a log-log (Schmidt) plot with the results shown in figs. 6.14b, c and d respectively. This was done in order to determine the coefficient *m* in the relation, $PL \propto P^m$ (eq. 3.21), where *PL* is photoluminescence intensity and *P* is laser power [7].

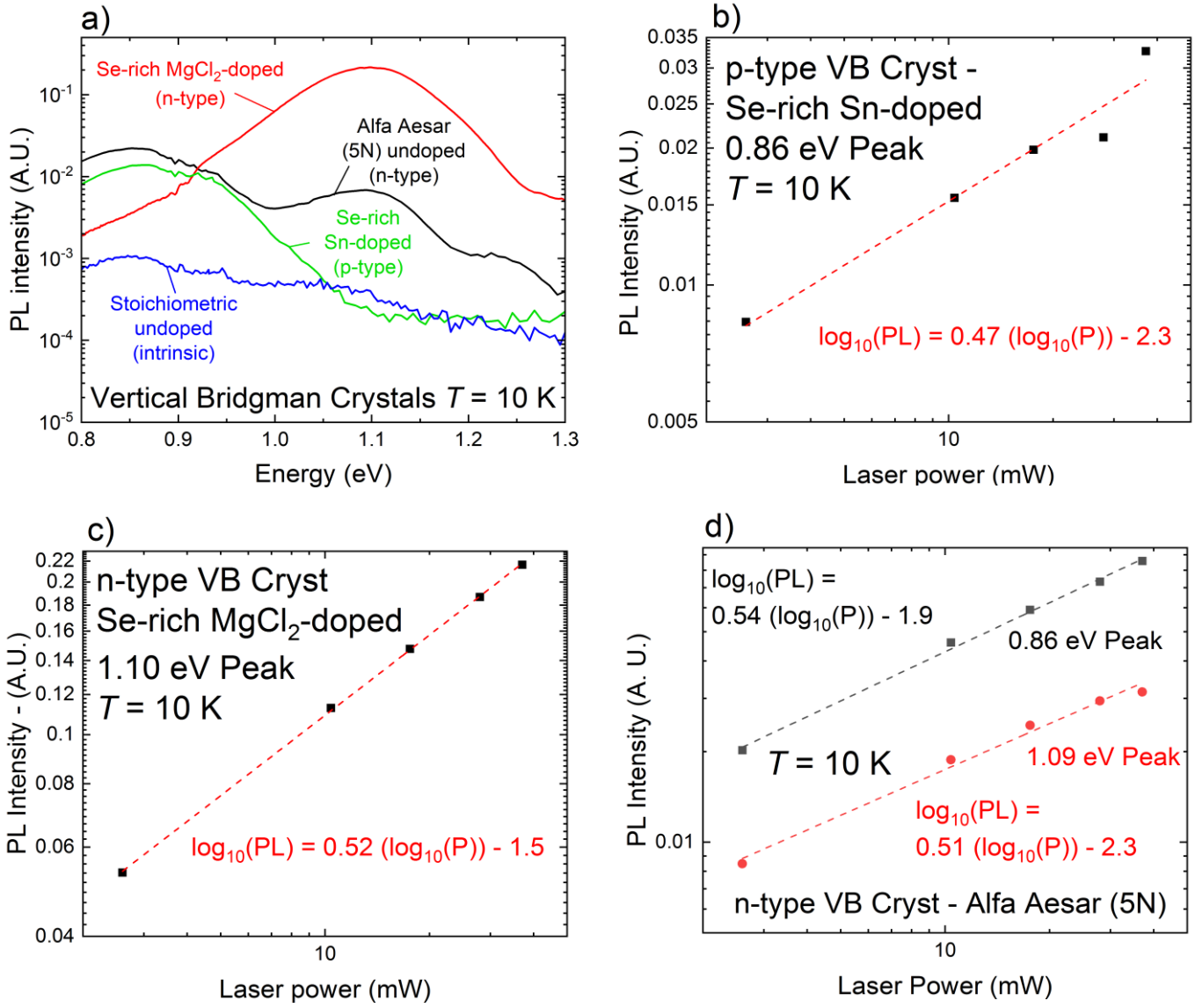

Fig. 6.14 a) Plots of PL spectra taken at 10 K and 37 mW laser power for the Sb_2Se_3 single crystals: stoichiometric undoped, Se-rich $MgCl_2$-doped, Se-rich Sn-doped, undoped 5N. Broad peaks appear for all doped crystals, but not the stoichiometric undoped. b-d) Log-log (Schmidt) plots of photoluminescence intensity against laser power for all major peaks.

The value of *m* was found in this work to be around 0.5 for all major peaks examined, comparable to the 0.6 value observed by Grossberg *et al.*[6] for similar peaks from polycrystalline Sb_2Se_3 and providing evidence that the peaks represent transitions within the band-gap of Sb_2Se_3. As outlined by Schmidt *et al.*[7], transitions where ($m < 1$) may include donor-acceptor-pair

recombination (DAP), or hole-donor/electron-acceptor recombination, while Grossberg *et al.*[6] assigned DAP transitions to their spectra for Sb_2Se_3, which is also likely to be the case here.

Both the $MgCl_2$-doped and the Sn-doped crystals exhibited peaks in the region of 0.9 eV, and although these do not necessarily result from the same transition in each case, the peaks are broad, and have a similar power-dependences (0.47 vs. 0.52), so are not noticeably different in behaviour. While this caveat holds for the other peaks, there is also a strong similarity in both the energy position and power-dependent behaviour for the 1.10 eV peak in the $MgCl_2$-doped sample and the 1.09 eV peak in the 5N crystal. Furthermore the 0.87 eV peak in the Sn-doped crystal and the 0.86 eV peak in the 5N crystal are very close in energy and exhibit similar power dependences (0.47 vs. 0.54). It is interesting to note that both Sn and Cl have been detected in an undoped 5N crystal using SIMS (Section 5.7.3). This may play a role in both the 0.86 eV and 1.09 peaks appearing in the spectra for the crystal, although the amount of Sn detected may have been an overestimate due to interference effects. Given that the band gap of Sb_2Se_3 has been measured (via photoreflectance) to be 1.3 eV at 100 K[8], all of the peaks indicate transition energies smaller than the bandgap, as expected for DAP transitions.

Temperature dependent PL measurements are shown in fig. 6.15 for the following Sb_2Se_3 single crystals: a) the Se-rich Sn-doped crystal taken with 5 K temperature increments, b) the Se-rich $MgCl_2$-doped crystal, taken with 10 K temperature increments and c) the undoped 5N crystal, taken with 5 K temperature increments. These results show a decrease in the PL intensity of all peaks with increasing temperature, although at different rates. The intensity of the 1.22 eV peak for the $MgCl_2$-doped crystal (fig. 6.15b) clearly drops more rapidly with temperature than the 1.10 eV peak. Meanwhile, for the 5N crystal (fig. 6.15c), the intensity of the 1.22 eV peak drops more rapidly than the 1.09 eV peak, which in turn occurs more rapidly than for the 0.86 eV peak.

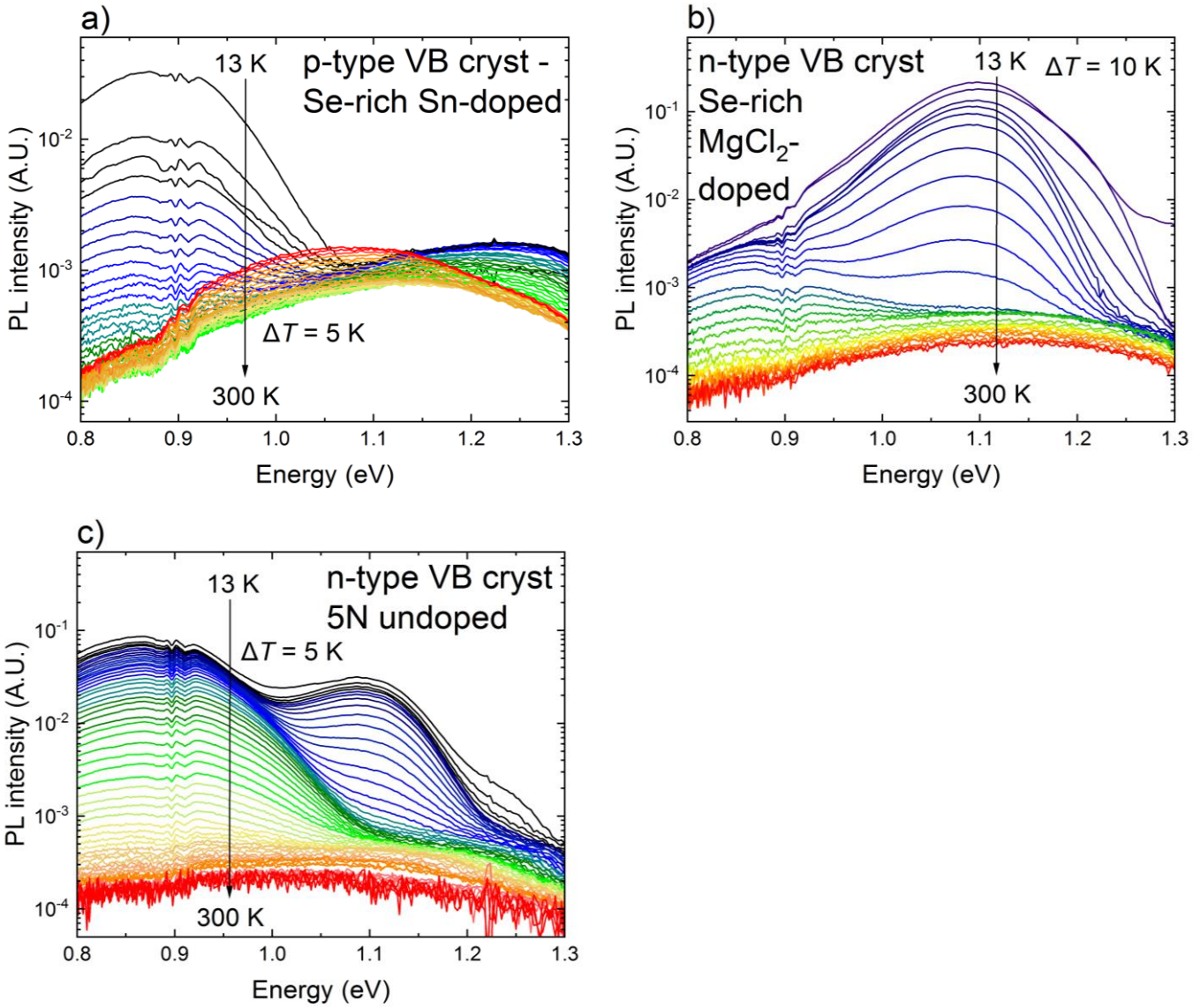

Fig. 6.15 Photoluminescence spectra for Sb_2Se_3 crystals grown by vertical Bridgman: a) Sn-doped, b) $MgCl_2$-doped and c) undoped 5N crystal, with measurements taken at a range of temperatures and 37 mW laser power. All peak intensities decrease with increasing temperature, though at different rates.

Sample Type	Sample Name	Peak energy (eV)	Thermal activation energy E_T (meV)
Grossberg *et al.* [6]			
Annealed polycrystalline bulk Sb_2Se_3 from Alfa Aesar (5N) source		0.94	93 ± 3
		1.10	65 ± 6
		1.24	33 ± 5
This work			
Se-rich $MgCl_2$-doped crystal	VB-SeR-MgCl2	0.91	-
		1.10	-
		1.20	-
Se-rich Sn-doped crystal	VB-SeR-Sn	0.87	-
Undoped 5N crystal	VB-5NAA-Un	0.86	-
		1.09	-
		1.22	-

Table 6.6 Peak energies observed in PL spectra of doped Sb_2Se_3 single crystals in comparison with literature values determined from polycrystalline Sb_2Se_3[6].

Changes in the PL peak intensity with temperature may be described by eq. 3.22, a theoretical expression for discrete energy levels. Fitting to this function is possible, as demonstrated by Grossberg *et al.*[6] but requires fitting for the parameters I_0, α_1, α_2 in addition to E_T, which, in turn, requires reasonable initialisation of these parameters. Such fitting has not yet been carried out for the spectra in this work due to these complications. Despite this, it is clear from eq. 3.22 that a more rapid quench with temperature strongly suggests a shallower defect level. If these peaks correspond to the same defect levels in all samples (not necessarily true) then the thermal activation energy seems to be greatest for the defect peak at ~0.9 eV, then the ~1.10 eV peak, then the ~1.2 eV peak. This is consistent with the trends in ref. 6 (Table 6.6).

6.6 Solar Cells Fabricated from Single Crystal Sb_2Se_3

Single crystal solar cell devices were fabricated on cleaved (010) faces of vertical Bridgman-grown Sb_2Se_3 single crystals through the evaporation of Au back contacts and sputtering of CdS as a PV partner layer (Section 3.2.8). In some cases, tin-doped indium oxide (ITO) was also sputtered onto the CdS, with Ag paste applied to act as a top contact (fig. 6.16b). In other cases, no ITO was used, and Ag paste was applied directly onto the CdS (fig. 6.16a). The labelling of the samples is based on the type of single crystal used as the substrate and the type of front contact used, with the full details shown in Table 6.7.

Crystal Substrate	Stoichiometry	Extrinsic Dopants	Contact Type	Sample Code
Cleaved (010) plane of 5N Sb_2Se_3 single crystal (**VB-5NAA**)		Undoped - **Un**	ITO layer contacted with Ag paste – **ITO**	**SCSD-5NAA-Un-ITO**
Cleaved (010) plane of single crystal grown from source material directly synthesised from the elements (**VB-SeP/St/SeR**)	Se – rich (> 0.1 at% variation) - **SeR**	Sn-doped (~0.1 at%) – **Sn**	Ag paste only - **Ag**	**SCSD-SeR-Sn-Ag**
			ITO layer contacted with Ag paste – **ITO**	**SCSD-SeR-Sn-ITO**

Table 6.7 Details for the solar devices fabricated from single-crystal Sb_2Se_3 substrates.

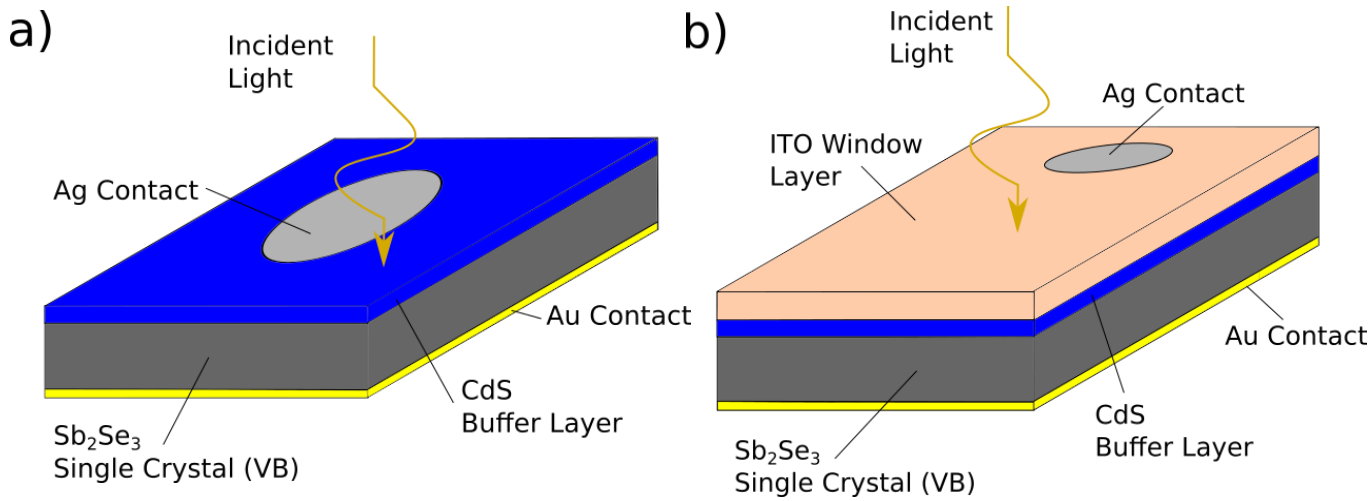

Fig. 6.16 Illustration of the Sb_2Se_3 single crystal devices fabricated with a CdS partner layer as well as a) an Ag front contact only or b) an ITO window layer and Ag contact, with both utilising a single Au back contact.

6.6.1 *J-V* Measurements

6.6.1.1 N-type Sb_2Se_3 Devices

Light and dark current density - voltage plots for the n-type single crystal devices (SCSD-5NAA-Un-ITO-1 and 2) are shown in figs. 6.17a-b. In both cases, the *J-V* scans show strongly rectifying behaviour but there is no photocurrent. Despite this, these samples offer clear evidence for n – n+ isotype junctions (Section 6.8.3). Additionally, 'rollover' behaviour is observed at around +0.75 V for device 1 (fig. 6.17a) and a small kink is found at around +0.6 V for device 2 (fig. 6.17b). The magnitude of the current density increases overall under AM1.5 illumination compared to dark, which may be a result of heating from the lamp increasing the conductivity of the device, but there is no significant current density at 0 V bias for either device.

The *J-V* plots indicate, in all cases, rectifying behaviour at the n-Sb_2Se_3-CdS interface, with the 'rollover' and small kink in the scans suggesting the presence of a back-contact barrier. This is likely to exist at the Au / n-Sb_2Se_3 interface, which was shown in Section 6.3.1 to be rectifying.

6.6.1.2 P-type Sb_2Se_3 Devices

The *J-V* scans for two p-Sb_2Se_3 devices with no window layer, (SCSD-SeR-Sn-Ag-1 and 2) are shown in figs. 6.17c-d. These indicate the same rectifying but not photoactive behaviour as was observed for the n-type devices, with no evidence of a back-contact barrier. The diode-like behaviour indicates the formation of a p-n junction between the p-Sb_2Se_3 and the CdS, with rising forward bias curves indicating the absence of a contact barrier and suggesting an Ohmic interface between the p-Sb_2Se_3 and the Au contact, consistent with what was observed for Au-contacted p-Sb_2Se_3 single crystals (Section 6.3.1). The Au / p-Sb_2Se_3-CdS-Ag structure therefore failed to give photovoltaic devices.

Figs. 6.17e-f show *J-V* curves for two further p-type devices fabricated from the same single crystal substrates, but with an ITO window layer atop the CdS layer, with an Ag paste contact for current extraction (SCSD-SeR-Sn-ITO-1 (a) and 2 (b)). These indicate rectifying behaviour, very similar to the devices with Ag-only contacts, also with no sign of kinks or rollover. Device 1 exhibits a photocurrent (fig. 6.17e) of ~10^{-3} $mAcm^{-2}$, but it is very small compared to the values expected for solar cells generally (> 1 $mAcm^{-2}$). This suggests that the addition of the ITO window layer results in some improvement in light collection over the Ag contact alone, but it is minimal. Meanwhile device 2 (fig. 6.17f) was rectifying but not photoactive.

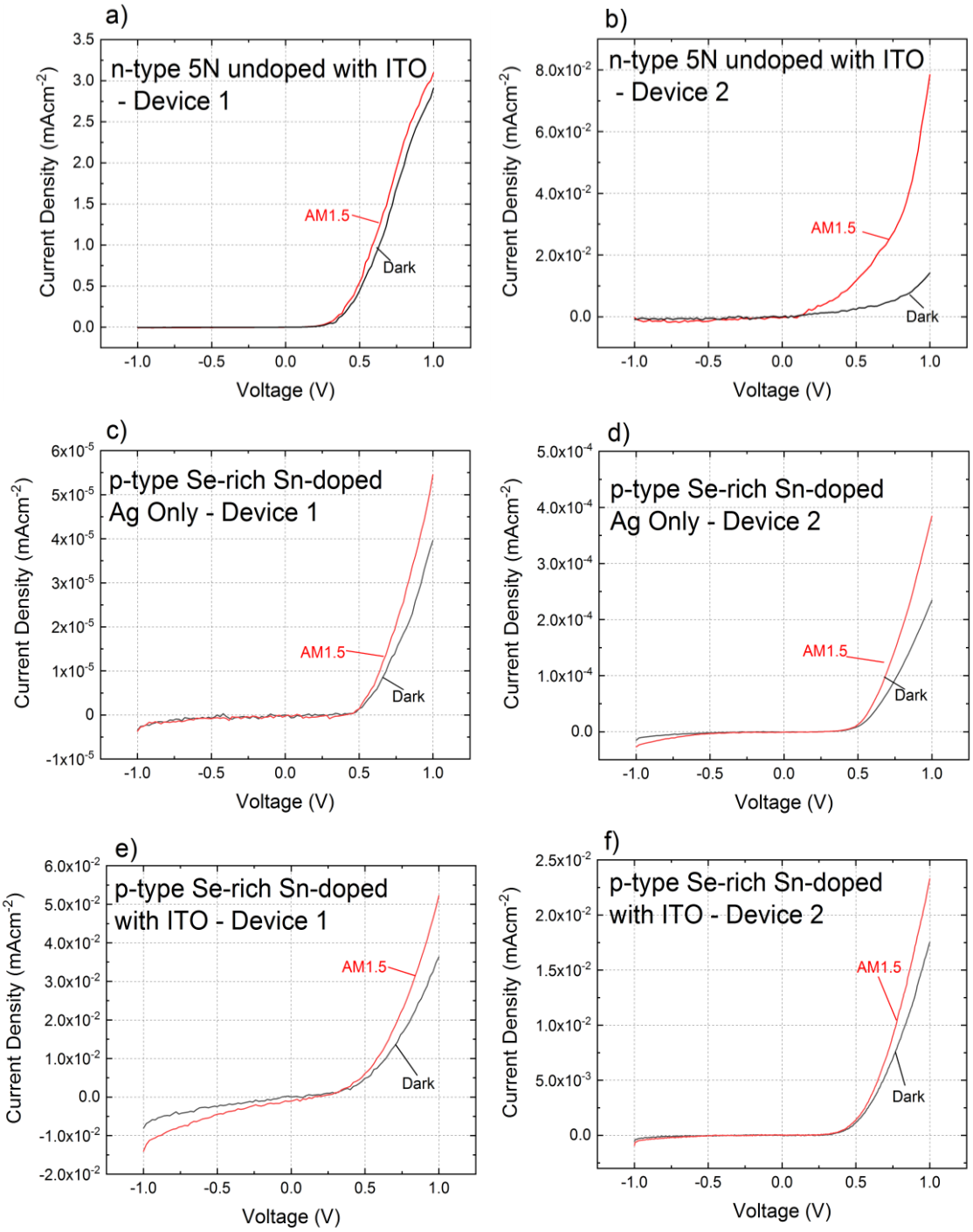

Fig. 6.17 *J-V* plots for Sb_2Se_3 single crystal devices with CdS buffer layer and Au back contact taken in the dark and under AM1.5 illumination. a-b) n-type Sb_2Se_3 cells, with ITO top contact. Both samples exhibit rectifying behaviour, with some evidence for a back-contact barrier. c-d) p-Sb_2Se_3 cells with no window layer and Ag as a top contact directly on CdS. Both exhibit rectifying behaviour but no significant photocurrent under solar illumination. e-f) p-Sb_2Se_3 cells with ITO window layer, with a very small photocurrent density (10^{-3} mAcm^{-2}) observed in device 1 (e), but none observed for device 2 (f).

6.7 Thin Film Thermally Evaporated Sb_2Se_3 Devices from Doped Source Material

Thermally evaporated (TE) Sb_2Se_3 devices were fabricated in superstrate configuration from n-type undoped 5N source material, intrinsic stoichiometric undoped Sb_2Se_3 source material synthesised directly from the elements and p-type Sn-doped Se-rich Sb_2Se_3 source material synthesised directly from the elements.

Source Material	Anneal Time (mins)	Ageing in Air (days)	Sample Code
Undoped 5N - 5NAA (n-type)	10	7	TE-5NAA-Un-10m-7d
		21	TE-5NAA-Un-10m-21d
	20	7	TE-5NAA-Un-20m-7d
		21	TE-5NAA-Un-20m-21d
	25	0	TE-5NAA-Un-25m-0d
		14	TE-5NAA-Un-25m-14d
		21	TE-5NAA-Un-25m-21d
	30	7	TE-5NAA-Un-30m-7d
		21	TE-5NAA-Un-30m-21d
	40	7	TE-5NAA-Un-40m-7d
		21	TE-5NAA-Un-40m-21d
Directly Synthesised from the Elements Undoped Stoichiometric - DSE-St-Un (intrinsic)	10	7	TE-St-Un-10m-7d
		21	TE-St-Un-10m-21d
	20	7	TE-St -Un-20m-7d
		21	TE-St -Un-20m-21d
	25	0	TE-St -Un-25m-0d
		14	TE-St -Un-25m-14d
		21	TE-St -Un-25m-21d
	30	7	TE-St -Un-30m-7d
		21	TE-St -Un-30m-21d
	40	7	TE-St -Un-40m-7d
		21	TE-St -Un-40m-21d

(continued)

Directly Synthesised from the Elements Sn-doped (0.1 at%) Se-rich (0.1 at%) - DSE-SeR-Sn (p-type)	10	7	TE-SeR-Sn-10m-7d
		21	TE-SeR-Sn-10m-21d
	20	7	TE-SeR-Sn-20m-7d
		21	TE-SeR-Sn-20m-21d
	25	0	TE-SeR-Sn-25m-0d
		14	TE-SeR-Sn-25m-14d
		21	TE-SeR-Sn-25m-21d
	30	7	TE-SeR-Sn-30m-7d
		21	TE-SeR-Sn-30m-21d
	40	7	TE-SeR-Sn-40m-7d
		21	TE-SeR-Sn-40m-21d

Table 6.8 Details for thermally evaporated (TE) Sb_2Se_3 devices discussed in this section. The source materials were n-type, p-type and intrinsic. See text for further details.

The fabrication parameters for the thermally evaporated Sb_2Se_3 devices are shown in Table 6.8 and an illustration of the device structure is shown in fig. 6.18. Superstrate plates with deposited Sb_2Se_3 (see Section 3.2.8) were split into smaller plates, each separately annealed to form a device. The sample name of the devices denotes the type of source material used in the deposition, as well as the length of time for the post-growth annealing applied at 300°C under nitrogen atmosphere. After annealing, device plates were immediately spin coated with P3HT to act as a hole transport layer, 28 Au contacts deposited, then left in air for a period of days before *J-V* measurements were taken, with this indicated in the sample name.

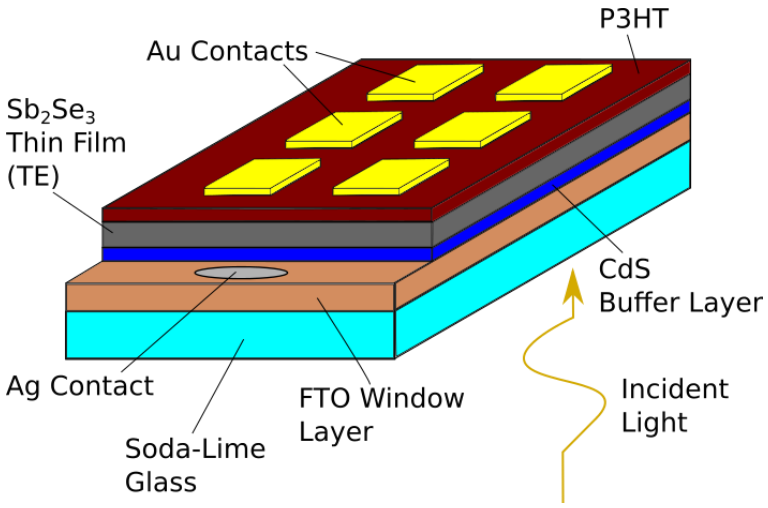

Fig. 6.18 Illustration of the superstrate solar cell structure used for the thermally evaporated Sb_2Se_3 thin film solar cells fabricated from doped source material. Electrodes were attached to the Ag contact and one Au contact for each cell measurement.

6.7.1 SEM images of thin film grain structure

Fig. 6.19 shows scanning electron microscopy (SEM) images of the grain structure of Sb_2Se_3 thin films deposited from n- and p-type source material and annealed under N_2 for varying lengths of time (details are included in the figure caption). Earlier work from the University of Liverpool laboratory, with the same equipment as for this investigation[9], has demonstrated thermally evaporated films which are amorphous in their as-grown state, if deposited at below 450°C. When imaged with SEM, a sample deposited at 350°C appeared smooth and featureless, with the image reported in that work reproduced in fig. 6.20a. Meanwhile, a sample deposited at 500°C looked much more crystalline, with an image reproduced in fig. 6.20b.

In this work, the thermally evaporated films were not imaged immediately after deposition, but since they were deposited at room temperature in the same equipment as used in ref 9, they were assumed to take the same amorphous form as shown in fig. 6.20a.

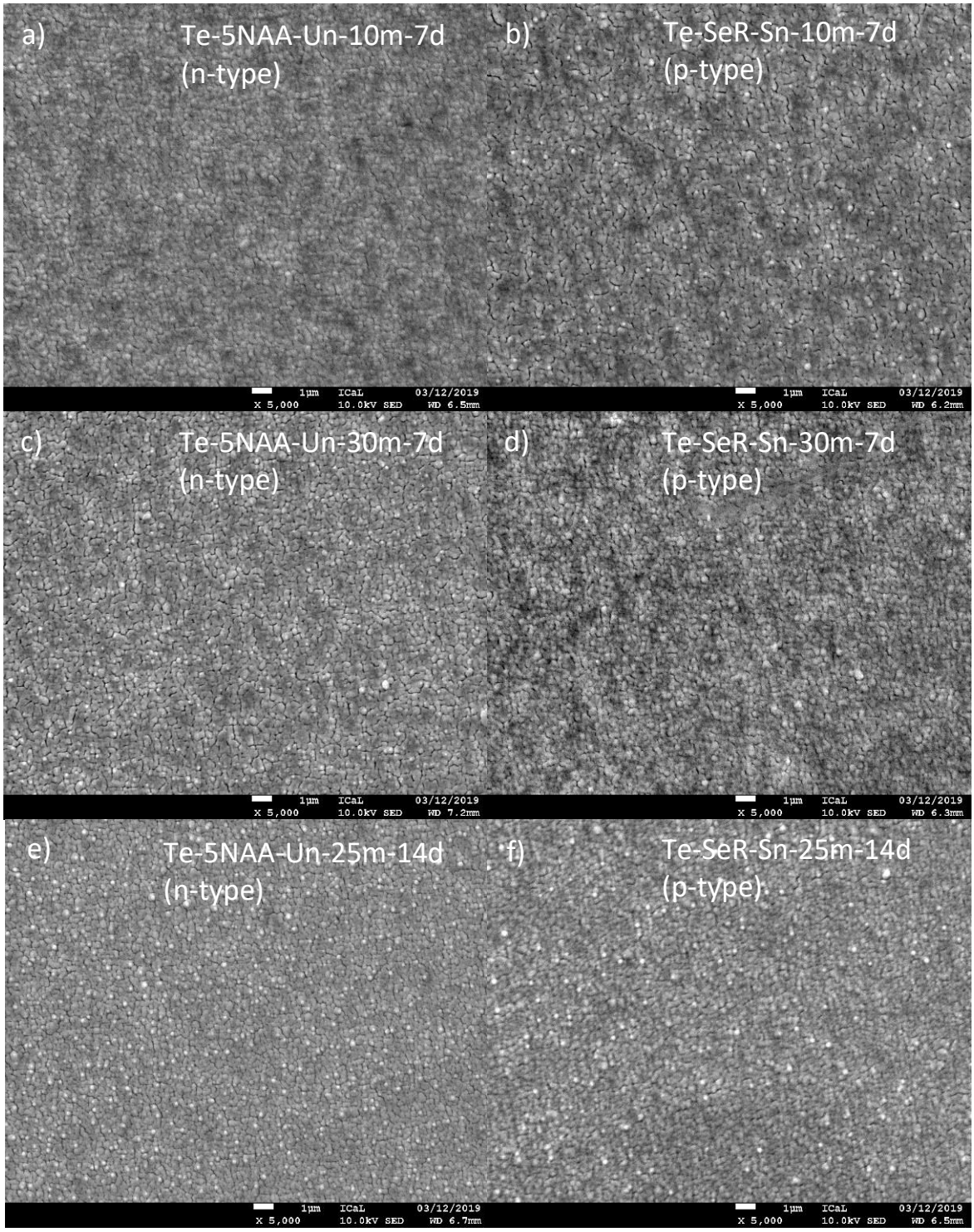

Fig. 6.19 SEM images of: a) n-type film annealed for 10 mins, b) p-type film annealed for 10 mins c) n-type film annealed for 30 mins d) p-type film annealed for 30 mins, e) n-type film annealed for 25 mins f) p-type film annealed for 25 mins. Grain sizes of around 200-500 nm are consistently achieved across all samples, with variations in film density and roughness with impurity content and anneal time.

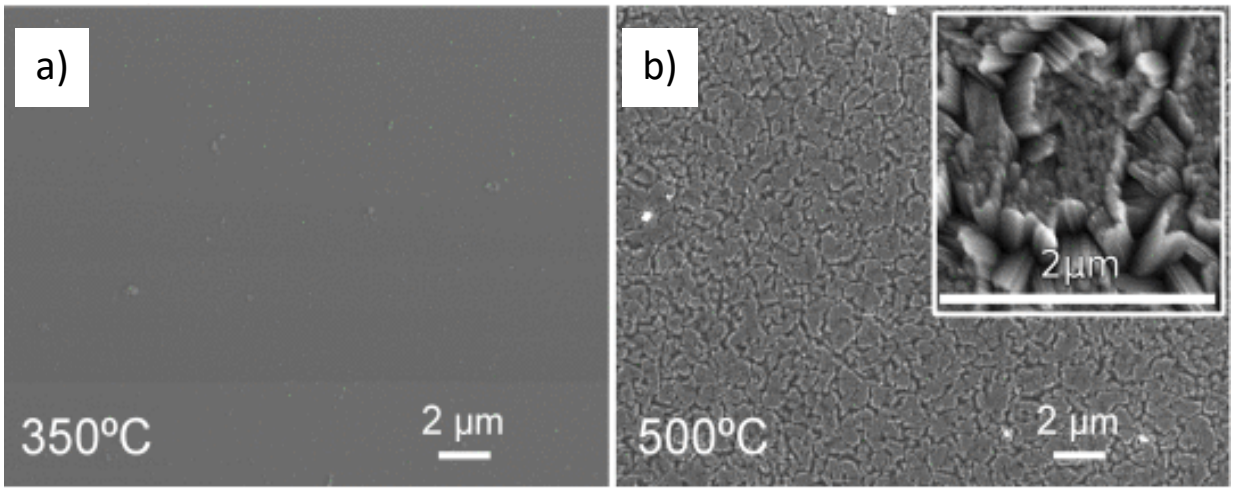

Fig. 6.20 SEM images of thermally evaporated Sb_2Se_3 thin films deposited at a) 350°C, showing amorphous film and b) 500°C, showing crystallised film. Images reproduced from ref 9.

All images of the annealed samples from this work (fig. 6.19) show a small-grained polycrystalline structure to the films, rather than an amorphous form, with grain sizes of ~200-500 nm in all cases, although precise estimates could not be determined at this level of magnification. There was some variation in appearance with impurity content (i.e. Cl or Sn impurities), even for films annealed for the same length of time. For example, a slightly denser grain structure can be seen for the n-type (Cl-doped) 10 min annealed film (a) as opposed to the p-type (Sn-doped) (b) and the other samples. The p-type film annealed for 30 mins (d) also appeared somewhat rougher than its n-type equivalent (c) but was otherwise similar. Finally, the two films annealed for 25 mins, (e and f) appear very similar. The n-type film appeared marginally more densely packed than the p-type, but what differences could be discerned based on these images were small.

These results would suggest that all anneal times employed at 300°C are sufficient to crystallise the deposited Sb_2Se_3 layer, as none of the films resembled the amorphous film shown in fig. 6.20a. X-ray diffraction or Raman spectroscopy would provide further, less ambiguous evidence for crystallinity, but these were not carried out for the thin film samples studied in this work. This result is interesting given that ref 9 only reported crystallisation of evaporated films when deposited at temperatures greater than 450°C. The reason for the difference is not clear, although in that work, the samples were heated to these higher temperatures during deposition, which was carried out under

vacuum, while in this case, the films were deposited at room temperature under vacuum, then separately annealed under an N_2 atmosphere (1 atm pressure), so the two processes were not identical. The variation in grain density between films annealed for the same amount of time suggests that variations in temperature over the period of the anneal have a significant impact on surface morphology. However, the similar grain sizes suggest that the anneal time does not affect crystallite size. The 10-min annealed n-type device exhibited the densest grain structure (fig. 6.19a) and it remains to be tested in the following sections whether this had an impact on device performance.

6.7.2 AM1.5 *J-V* Measurements of Thermally Evaporated Devices After 7 Day Ageing

AM1.5 *J-V* measurements were taken for several thin film thermally evaporated Sb_2Se_3 device plates one week after fabrication. All contacts in the devices were measured except where shorts were detected (defined as an impedance below 1 kΩ at 10 μA probe current). *J-V* plots for the best-performing (champion) cells for each device are shown in fig. 6.21, for anneal times of 10-40 mins. The negative bias regions of these plots indicate diode leakage, giving small values of short circuit current and open circuit voltage compared to state of the art Sb_2Se_3 devices[10]. For the *J-V* scan of the p-type device annealed for 40 mins, the s-shaped curve suggests a significant contact barrier in addition to the main junction.

The working parameters of these devices, extracted from the *J-V* curves, are presented in figs. 6.22a-f. These demonstrate, with some exceptions, in order: efficiency (η) values in the vicinity of 1%, open-circuit voltage (V_{OC}) values of 0.20-0.30 V, short circuit current (J_{SC}) values of 8-10 $mAcm^{-2}$, fill factor (*FF*) values of 35-40%, series resistance (R_S) values of 10-20 Ω and shunt resistances (R_{Sh}) of around 150 Ω. The overall efficiencies of these devices (fig. 6.21a) fell well short of high-performing Sb_2Se_3 devices (> 6%) such as those synthesised from close-space sublimation[10].

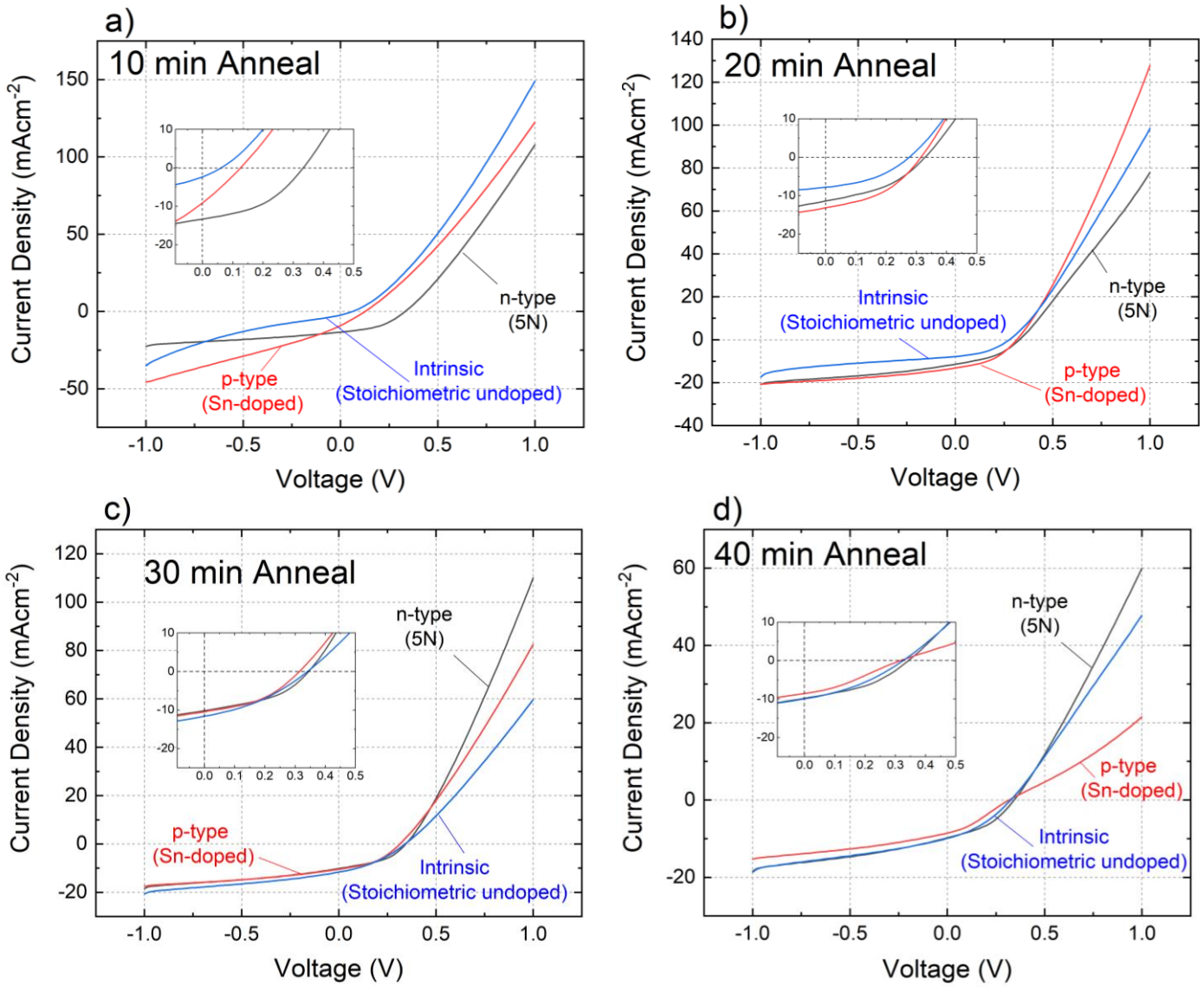

Fig. 6.21 *J-V* plots for champion devices for all conductivity types after 7 day ageing, after anneal times of: a) 10 mins, b) 20 mins, c) 30 mins, d) 40 mins. Significant differences are observed in the form of the curves where devices were fabricated from source material with different dopants.

The low R_{sh} observed for all devices is consistent with the diode leakage observed for the champion cells (fig. 6.21), which may be a key reason for the low efficiencies overall. There was a significant variation in the working parameters depending on conductivity type, but also a large spread in working parameters within a single device plate, i.e. from one contact to another, with overlapping error bars in most cases. The exception to this is the samples annealed for 10 mins, where there was a clearer separation of error bars, with the n-type device exhibiting an average η of 1.65%,

while the p-type was 0.27% efficient and the intrinsic was 0.02%. The smallest spread in values between conductivity types was found for a 30 min anneal time, where average η ranged from 1.0% to 1.3%.

For all anneal times, the average performance of the n-type cells was superior to that of p-type and intrinsic devices, but given the large spread in values for a single sample plate, meaningful comparisons could not be made. The significant differences in performance for the 10 min anneal may be related to film density, given that the most dense-looking grain morphologies were also observed for n-type annealed sample (as described in Section 6.7.1), but the difference is subtle, and the spread in working parameters along with the general similarity in the appearance of the thin films means that no clear trends relating the film surface morphologies to device performance could be established. It may be that performance differences may result from the conductivity type of the Sb_2Se_3 films, but it may be more informative to compare the same device plate with respect to a separate variable, such as device ageing time, to learn about how conductivity type impacts performance.

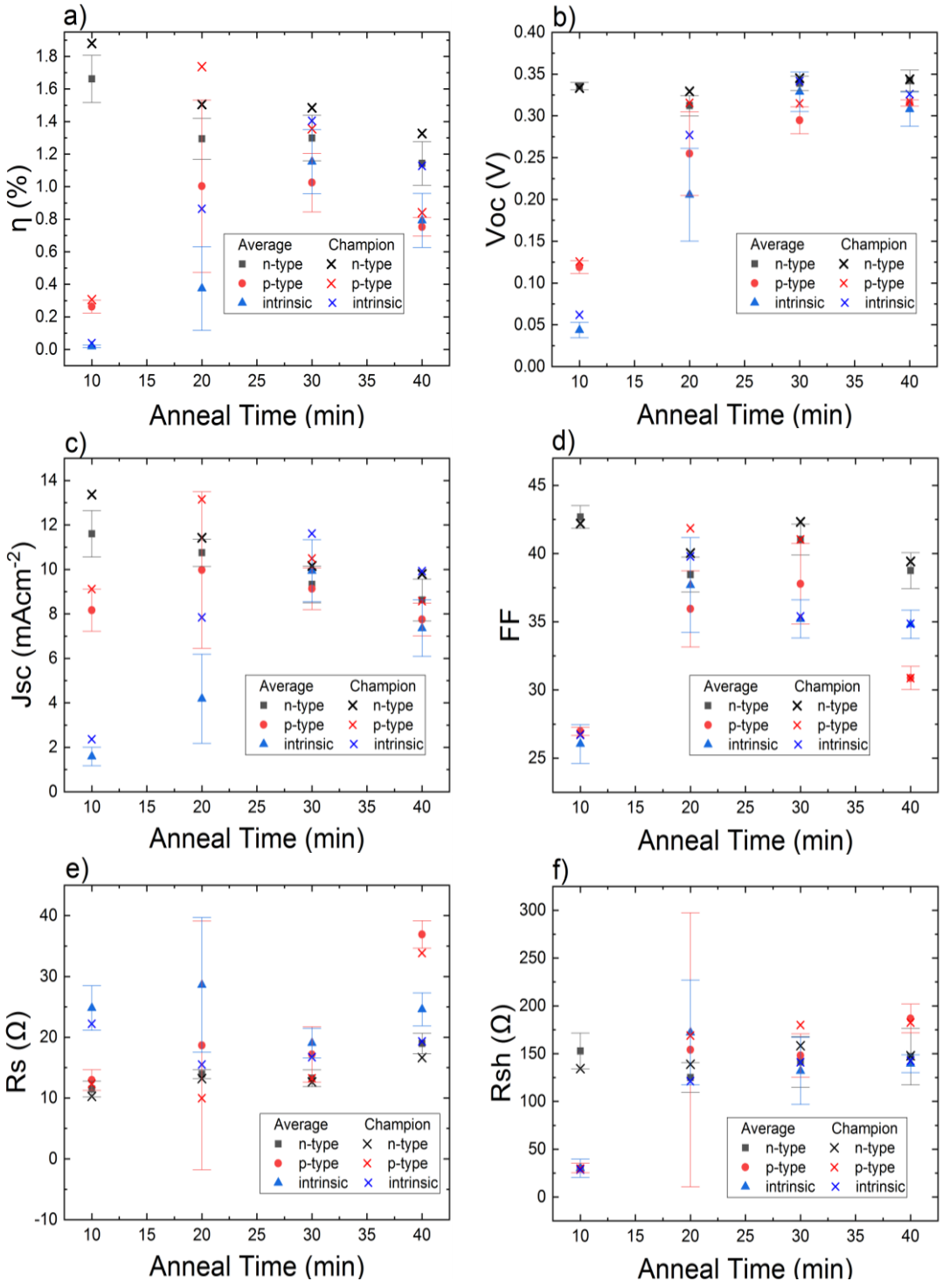

Fig. 6.22 Plots indicating the values of the PV working parameters a) η, b), V_{OC}, c) J_{SC}, d), *FF*, e) R_S and f) R_{Sh} for devices formed from thermally evaporated n-, i- and p-Sb_2Se_3 source material. Average values are shown with solid markers, standard deviation with error bars and values for the champion (highest efficiency) cell in each case with a cross. All samples shown were aged in air at room temperature for 7 days following annealing before measurements were taken.

6.7.3 AM1.5 *J-V* Measurements of Sb_2Se_3 Devices Before and After Ageing

The effects upon thermally evaporated Sb_2Se_3 thin film devices of ageing in the dark, in air, at room temperature, were investigated for devices of all doping types, fabricated with a 25 min anneal. *J-V* measurements were taken on n-type, intrinsic and p-type devices on the same day as annealing (0d) and then again on the same devices two weeks later (14d).

The *J-V* curves for the champion cells are shown in fig. 6.23. These indicate clear changes with ageing, with the n-type and intrinsic curves becoming steeper at forward bias after ageing. Meanwhile, the curve for the p-type cell became much less steep at forward bias. This indicates reduced series resistance in the n-type and intrinsic cells, but increased series resistance in the p-type cell.

The working parameters for these thin film devices are shown in fig. 6.24 and reveal trends in the efficiency after ageing. The average efficiencies for the n-type and intrinsic devices did not change significantly, remaining at 0.65% and going from 0.9% to 0.85% respectively, but there was a dramatic drop for the p-type device, from 1.02% to 0.67%. Furthermore, the efficiency values for the champion n-type and intrinsic cells exhibited a slight increase after aging, going from 0.95% to 1.02% and from 1.13% to 1.18% respectively. The working parameters which exhibited the greatest change through the aging process were the J_{SC} and *FF*, with the latter resulting predominantly from changes in R_S. The ageing behaviour depended upon conductivity type, since the samples were otherwise the same. The increased efficiency for the champion n-type cell is surprising, since for other technologies (e.g. perovskite cells[11]), ageing degrades, rather than improves, the device performance.

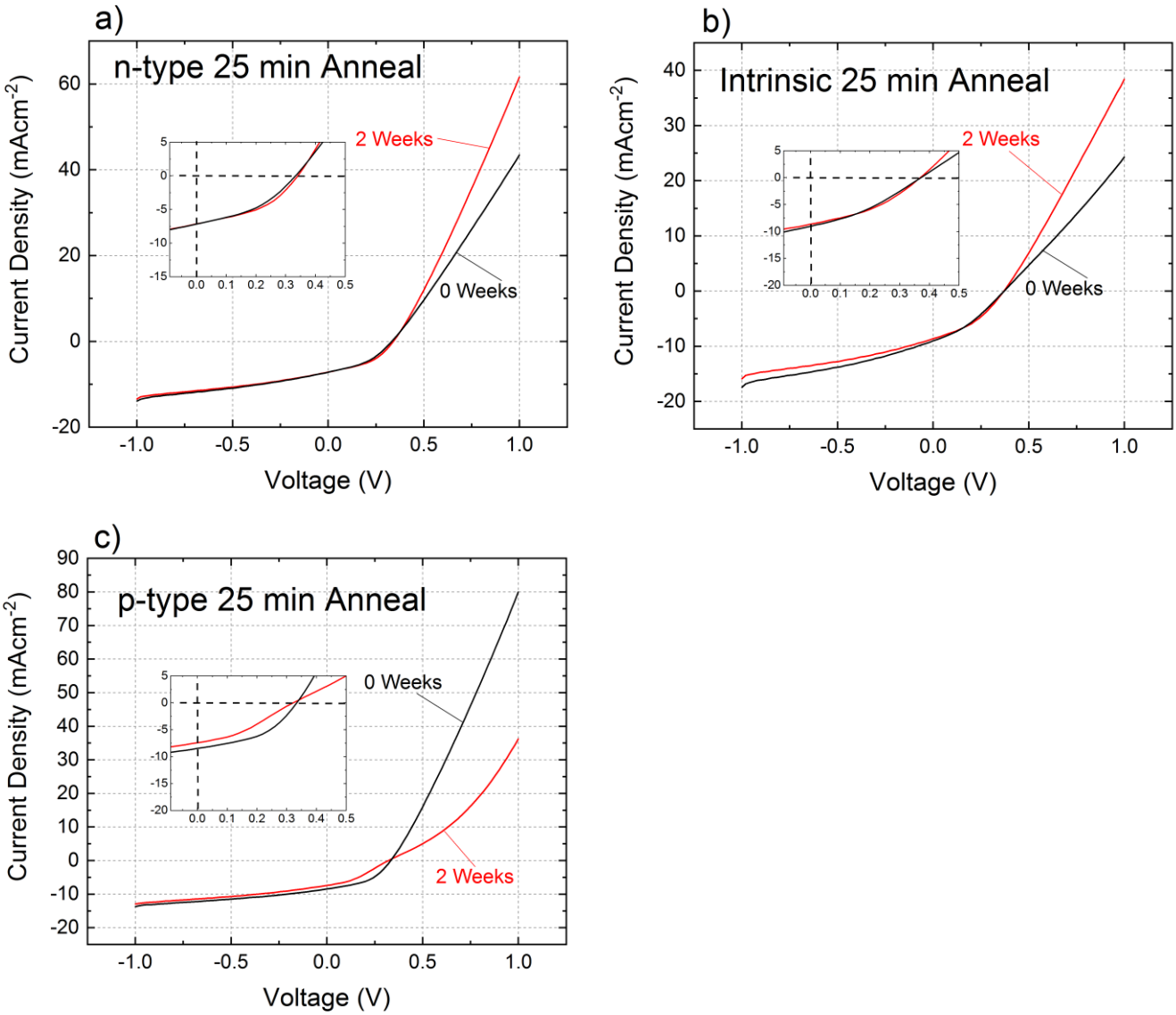

Fig. 6.23 *J-V* curves for devices Sb_2Se_3 thin film devices fabricated with a 25 min anneal at 300°C, for: a) n-type, b) intrinsic and c) p-type samples. Curves are plotted before and after ageing for 2 weeks.

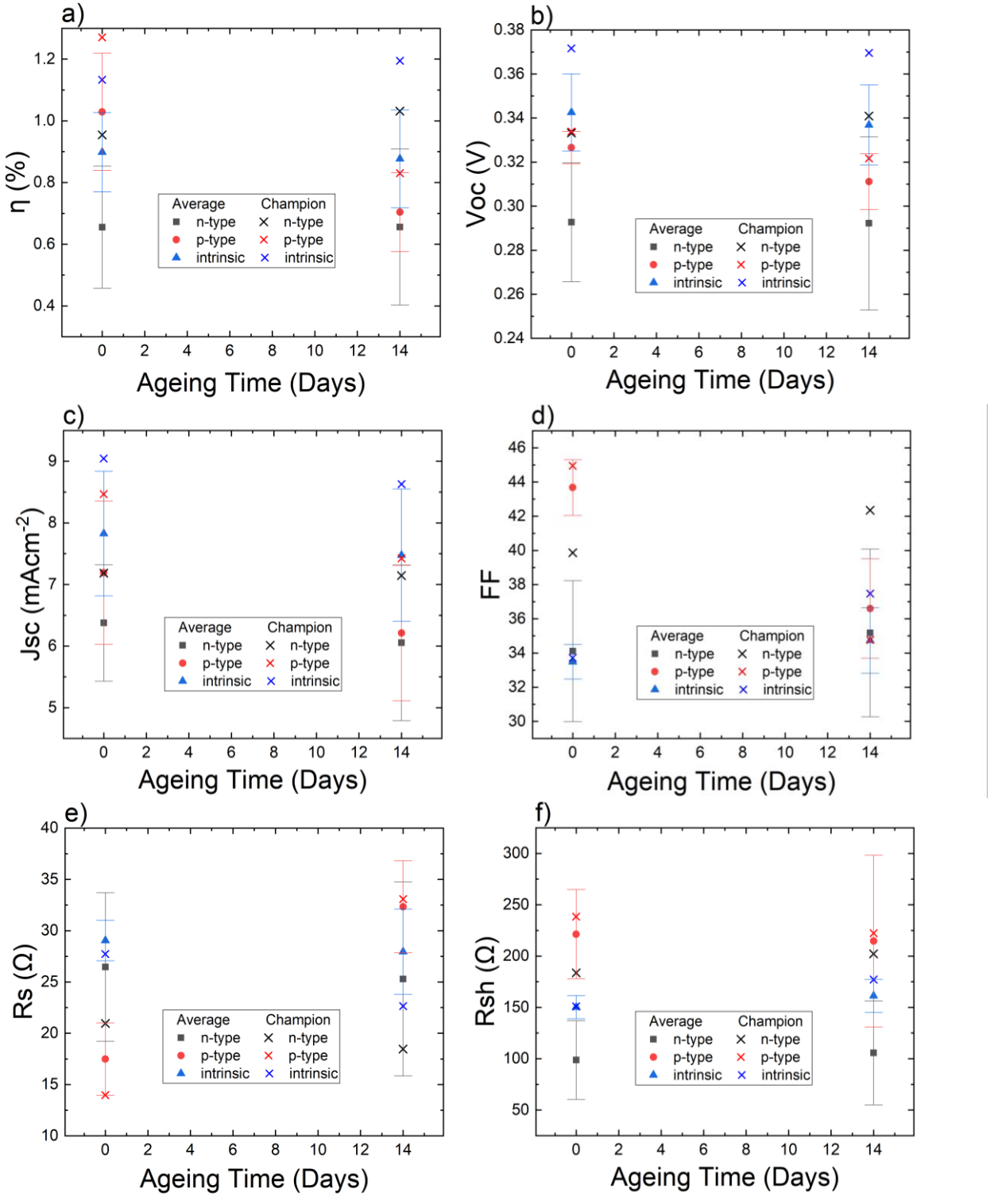

Fig. 6.24 Working parameters: a) η, b), V_{OC}, c) J_{SC}, d), *FF*, e) R_S and f) R_{Sh} for the n-type, intrinsic and p-type Sb_2Se_3 thin film devices as-grown (0d), and 2 weeks later (14d). Average values, standard deviations and values for the highest efficiency cells are shown with a cross.

The dramatic increases in series resistance observed for the p-type device suggest the formation of an increased back-contact barrier, while the reduced series resistance values with ageing for the n-type cells imply a reduced back-contact barrier. Fig. 6.25 illustrates a model to speculate the reason for these changes, supposing (without any specific numerical parameters used to construct the diagram) an intrinsic material of similar bandgap to Sb_2Se_3 were introduced at the back surface of the Sb_2Se_3 absorber layer. This is inferred from the observed electrical behaviour, and proposes that the contact barrier height (Φ_B^n) for the n-type cell (fig. 6.25a) would separate into two smaller barriers Φ_{B1}^n and Φ_{B2}^n (fig. 6.25b), where $\Phi_{B1}^n + \Phi_{B2}^n = \Phi_B^n$. Meanwhile a hole-blocking barrier (Φ_B^p) would emerge at the back-contact for the p-type cell (fig. 6.25d). This behaviour is likely to be the result of oxidisation of Sb_2Se_3, to form Sb_2O_3 + Se, or less highly-doped Sb_2Se_3, for example, but fig. 6.25 does not attempt to model these specific cases, as it is recognised that the actual band diagrams for the aged sample may be significantly more complicated, especially if interface states are taken into account.

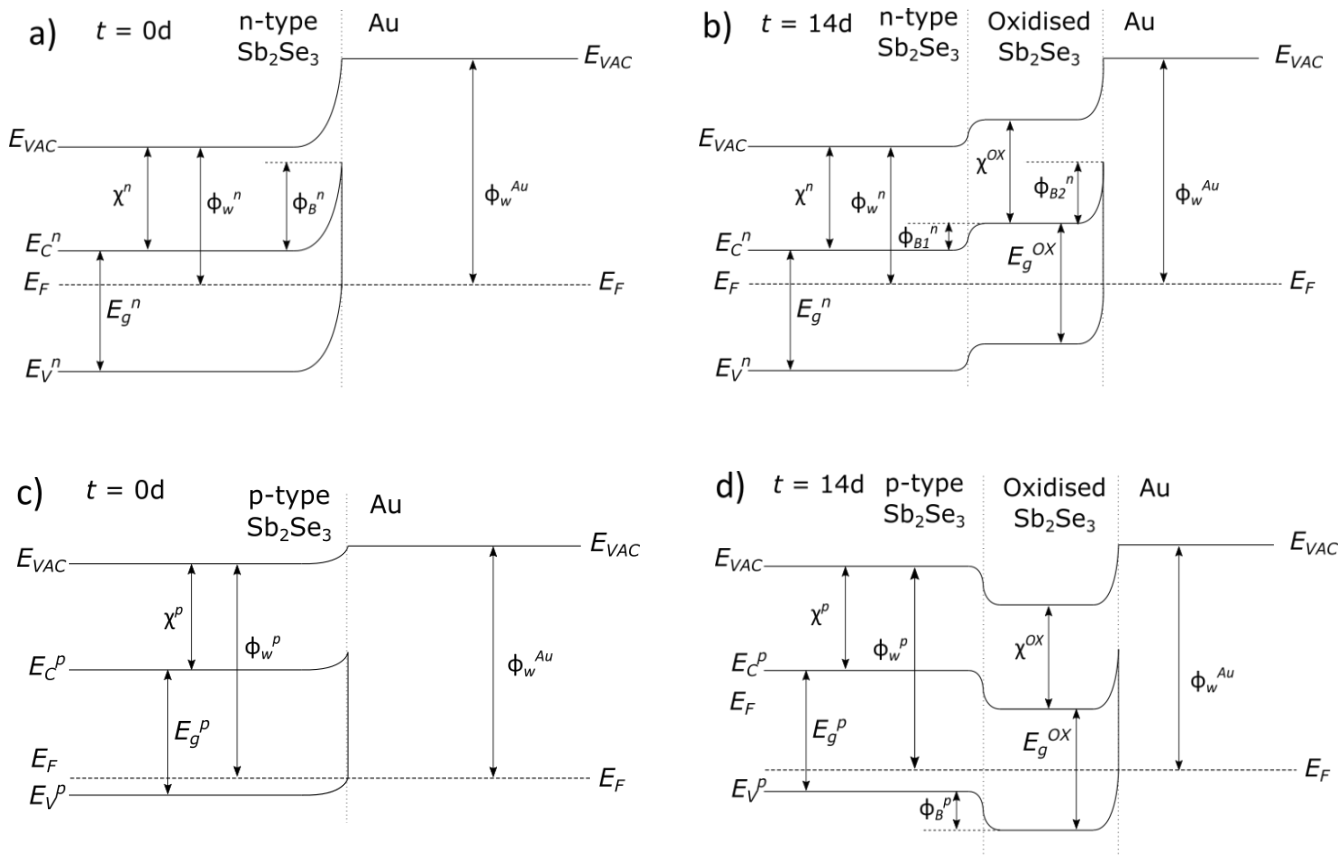

Fig. 6.25 Model for the effect on band positions from ageing of a-b) n-type and c-d) p-type Sb_2Se_3 thin film devices, where an intrinsic material of comparable bandgap to Sb_2Se_3 is assumed to be introduced at the interface due to oxidisation. Contact barrier heights for the n-type device: Φ_{B1}^{n} + $\Phi_{B2}^{n} = \Phi_{B}^{n}$. A contact barrier ($\Phi_{B}^{p}$) is introduced (d) for the p-type device.

6.7.4 *C-V* Measurements of Champion Thermally Evaporated Sb_2Se_3 Cells

The small values of series resistance determined in the champion cells from the *J-V* plots (see figs. 6.22e and 6.24e), at around 10-30 Ω, indicate that the junctions may be characterised with *C-V* profiling at 1 MHz AC frequency without risk of signal roll-off (Section 3.5.4). These measurements were taken 21 days after annealing, under the assumption that any ageing process had already run its course. *C-V* scans are shown for the champion cells of the 30 min annealed n-type, intrinsic and p-type devices, in fig. 6.26a, with Mott-Schottky plots shown in fig. 6.26b.

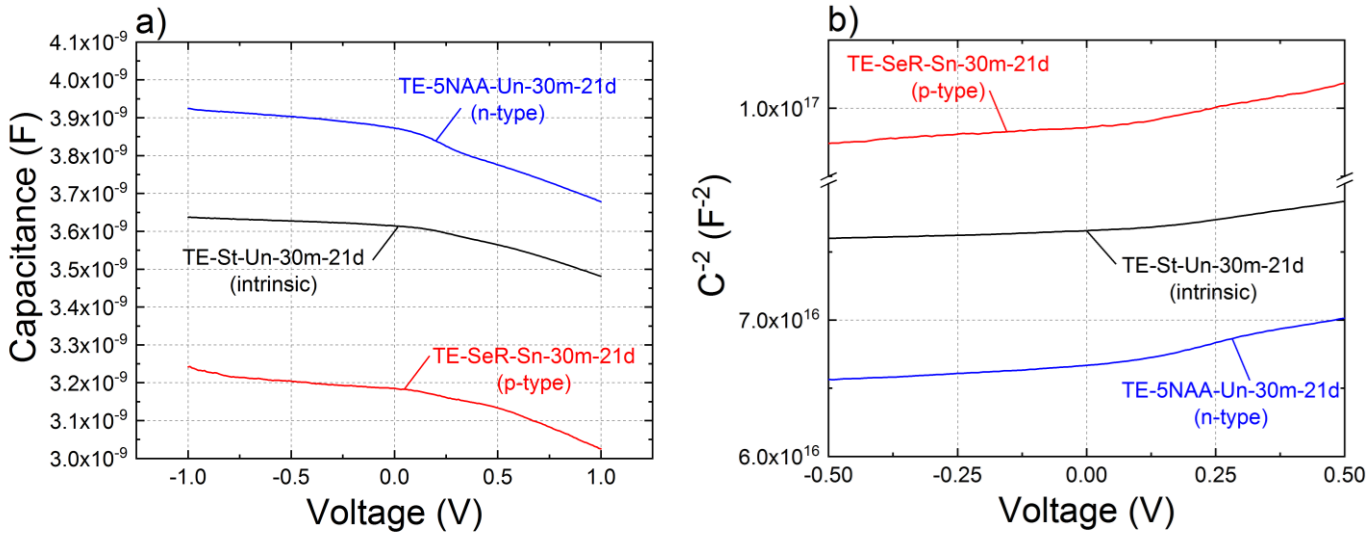

Fig. 6.26 a) Capacitance-voltage scans taken for the n-type, intrinsic and p-type champion cells annealed for 30 mins, after 21 days of aging. Scans exhibit decreasing capacitance with forward bias, contrary to expectations. b) Mott-Schottky plots for the same sample set, also exhibiting a reversed gradient compared to expectations.

The overall magnitude of capacitance in all cases was 3-4 x 10^{-9} F, while the scans indicate, in all cases, an increase in capacitance at reverse bias and decrease at forward bias. This is the opposite of the behaviour that would be expected based on the 'one-sided-junction' approximation [12]. The change in capacitance with bias was larger for the n-type and intrinsic cells, than for the p-type cell. The behaviour described is present across doping type, and the reversed *C-V* profile relative to expectations suggests that a space-charge region at the back contact dominated the measurement,

rather than the photoactive junction (as a back-contact barrier will be biased in reverse to the photoactive junction). This same behaviour was found for other anneal times (not shown). Back contact barriers may be expected to emerge for all doping types as n-type Sb_2Se_3 forms a Schottky barrier with Au (Section 6.3.1), and a back-contact barrier is expected to form for p-type Sb_2Se_3 as a result of ageing (Section 6.7.3). Either explanation may hold for the intrinsic Sb_2Se_3 device, depending on the position of its Fermi level. If the back-contact barrier did dominate the measurement, it does not mean that the capacitance of the photoactive junction may be neglected, complicating the interpretation of these scans.

From the Mott-Schottky plots derived from these scans (fig. 6.26b), values of carrier density (N_S), were estimated from eq. 3.15 for the same three samples. These results are presented in Table 6.9, indicating carrier densities in the region of 1×10^{15} cm^{-3} for all devices measured, with slightly larger values observed at reverse bias than at forward bias. The values of N_S are generally consistent between device doping type, while the overall carrier densities are smaller than those estimated for the single crystals (Section 6.2.2 and 6.4.2). The values of N_S for the intrinsic cell, which are slightly higher than for the n-type and p-type cells, are not expected, as the undoped stoichiometric Sb_2Se_3 source material for this crystal was assumed not to contain significant dopant impurities. It may be that native defect doping is more dominant in thin films as opposed to single crystal material, for which no significant native doping was inferred in stoichiometric Sb_2Se_3 (Section 6.2.1.1).

Sample	N_S (cm^{-3})	
	Reverse Bias	Forward Bias
TE-5NAA-Un-30m-21d (n-type)	$(3.46 \pm 0.04) \times 10^{15}$	$(9.43 \pm 0.11) \times 10^{14}$
TE-St-Un-30m-21d (intrinsic)	$(6.56 \pm 0.12) \times 10^{15}$	$(1.55 \pm 0.03) \times 10^{15}$
TE-SeR-Sn-30m-21d (p-type)	$(3.10 \pm 0.05) \times 10^{15}$	$(1.064 \pm 0.011) \times 10^{15}$

Table 6.9 Values of carrier concentrations (N_S) for thermally-evaporated Sb_2Se_3 champion cells, calculated from the gradients of the Mott-Schottky plots (fig. 6.25b) and eq. 3.15 for both forward and reverse bias. Cells of all doping types exhibit carrier densities in the region of 1×10^{15} cm^{-3}.

Interdiffusion from the CdS buffer layer may also play a role in doping, which would be relevant to the extrinsically-doped devices too, as processing conditions were the same. Carrier densities similar to those reported in this work were seen in Sb_2Se_3 / CdS devices by Zhou *et al.* [13], where diffusion of Cd into the Sb_2Se_3 layer, causing n-type doping, provided the explanation. However, the inverted *C-V* profile seen here was not reported in that work, where a buried homojunction was also reported. It is therefore uncertain whether these results provide accurate carrier density values, as two junctions (or three, if a buried homojunction is also present) may have been probed.

6.7.5 EQE Measurements of Champion Thermally Evaporated Sb_2Se_3 Cells

The CdS buffer layer may also be expected to affect the external quantum efficiency (EQE) of these devices. Fig. 6.27 shows EQE plots for the champion n-type, intrinsic and p-type thermally evaporated Sb_2Se_3 cells, for a range of anneal times. For all cells measured, the response peaked at around 550 nm, with a steady drop-off towards the Sb_2Se_3 band gap at 1053 nm thereafter.

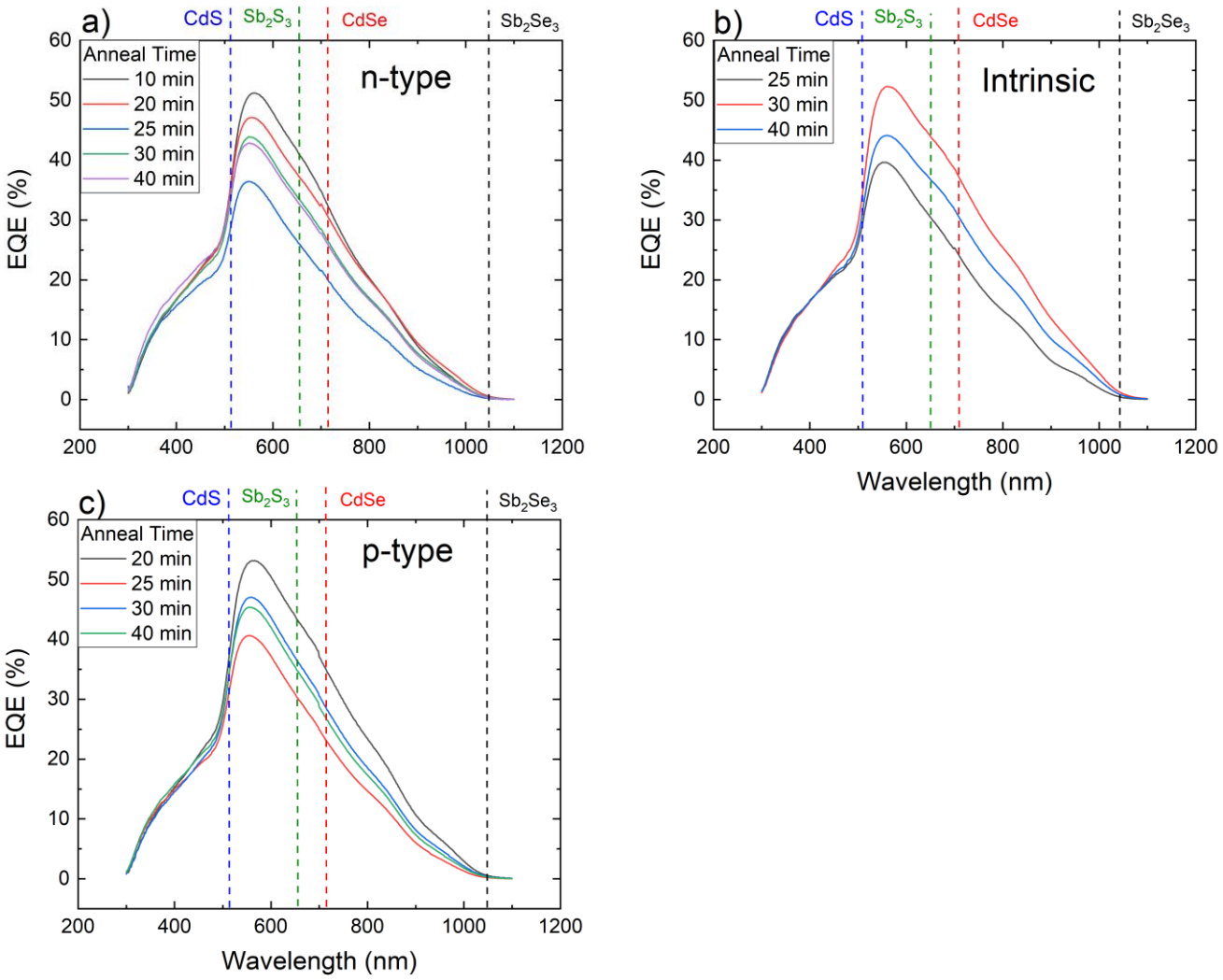

Fig. 6.27 EQE spectra for thermally evaporated Sb_2Se_3 champion cells for a range of anneal times: a) n-type, b) intrinsic and c) p-type. The absorption onsets for CdS and Sb_2Se_3 as well as the possible reaction products CdSe and Sb_2S_3 are shown on all plots.

All samples also saw a drop to a shoulder in EQE at shorter wavelengths, coinciding with the absorption onset of CdS at 513 nm. The EQE at short wavelengths suggests either a loss of carriers near the front of the device (where shorter wavelengths are absorbed), or the parasitic absorption of photons, most likely due to the CdS layer, given the position of the CdS band gap. Further parasitic absorption due to the reaction of CdS and Sb_2Se_3 at the interface to form CdSe and Sb_2S_3, may be expected, as the band gaps of CdSe and Sb_2S_3 are 1.74 eV and 1.88 respectively. However, if such parasitic absorption was present, it had a minimal impact on the EQE spectra, as no significant drops

were observed at the absorption edges of these compounds. In fact, there were no clear differences in the form of the spectra overall, except that there was a tendency for peak EQE to decrease with anneal time, but this does not hold in all cases. For instance, the EQE for the n-type samples followed the series 10 > 20 > 30 > 40 > 25 min.

The losses at longer wavelengths observed in all spectra suggest short carrier lifetimes, as longer wavelengths tend to generate carriers deeper in the Sb_2Se_3 layer, which must then diffuse to the junction near the front of the cell to be separated and avoid recombination. One explanation for the short carrier lifetimes is the large prevalence of grain boundaries within the thin films, due to the small (200-500 nm) grain sizes observed with SEM (Section 6.7.1). However, there are no clear trends in film morphology with anneal time that correlate to EQE. Furthermore, the similar results for cells of different conductivity types suggest that varying band-offsets are not a key factor in the different EQE values observed either.

6.8 Further Discussion

6.8.1 Conductivity Type of Sb_2Se_3

A significant early result of the experiments detailed in this chapter is a deeper understanding of the mechanisms behind the conductivity type of Sb_2Se_3 (Section 6.2). The undoped single crystals synthesised directly from the elements exhibited clear differences in the hot probe investigation based on stoichiometry alone, with the stoichiometric and Se-poor crystals generally non-conductive, and the Se-rich crystals p-type. This would suggest that pure, stoichiometric Sb_2Se_3 is not doped by native defects. Going further, it would suggest that donor defects associated with the Se-poor condition tend to be more deep-level than acceptors associated with the Se-rich condition. Density functional theory (DFT) calculations reported in Stoliaroff *et al.*[14] suggest that the antisite defects Sb_{Se} under Se-poor condition, and Se_{Sb} under Se-rich condition, are the native defects with the lowest formation energy in Sb_2Se_3, with the paper arguing that the former is a deep-level defect, while the Se_{Sb3} antisite is a shallow acceptor, which is consistent with our results.

A high-density of antisite Sb_{Se} and Se_{Sb} defects are also predicted by DFT calculations in Hobson *et al.*[15](see List of Publications, article 3) which draws upon the work presented in this

chapter. Furthermore, DFT calculations from Savory *et al.*[16] predict Se-poor Sb_2Se_3 to be non-conductive, with the Fermi level pinned at 0.632 eV. However, that work also predicts Se-rich Sb_2Se_3 to be non-conductive, with the Fermi level pinned at 0.641 eV, in contrast to the results presented in this work, and to Stoliaroff *et al.*[14] The DFT calculations assumed fully equilibrium conditions, which may explain the difference to the results in this work, where some non-equilibrium properties were guaranteed in the crystals.

Another significant result of the hot probe experiments was that the conductivity of Sb_2Se_3 crystals was shown to be very sensitive to the type of source material used, with undoped Sb_2Se_3 synthesised from the elements (6N Sb and 5N Se) non-conductive or weakly p-type. Meanwhile, hot probe and Hall effect measurements indicated that the undoped 5N crystals were strongly n-type. Indeed, The n-type conductivity of these single crystals is further supported by photoemission measurements, also reported in [15] and summarised briefly below.

Ultraviolet (UPS), soft x-ray (XPS) and hard x-ray (HAXPES) radiation were used on undoped 5N crystals, the last at an x-ray synchrotron facility[15]. The crystals were mechanically cleaved under vacuum in order to remove the influence of surface oxidisation, and the same individual crystal was not used in all cases. The published results are reproduced in Table 6.10, which reports the valence band offset (relative to Fermi-level) observed for different excitation radiation energies.

Excitation Energy (eV)	Avg. Penetration Depth (nm)	E_F - E_V (eV)
21.2 (UPS)	0.2	0.72 ± 0.13
1487 (XPS)	2	0.8 ± 0.4
5921 (HAXPES)	6	0.98 ± 0.28

Table 6.10 Results of photoemission spectroscopy measurements on undoped 5N crystals grown by vertical Bridgman. Measurements were carried out with UPS XPS and HAXPES[15].

The photoemission results (Table 6.10) indicate a valence band offset (E_F-E_V) ranging from 0.7 eV to 1 eV with a trend to increase with the energy of radiation used (and by implication, penetration depth). The largest error on the measurement was 0.4 eV for the XPS measurement, with the smallest error of 0.13 eV for UPS.

Given the band gap of Sb_2Se_3 is around 1.18 eV at room temperature[8], these results indicate that at all penetration depths, the nominal Fermi level was higher than the mid-gap point (0.59 eV). For UPS and XPS, the uncertainties extended to, or below, the mid-gap point (minima of 0.59 and 0.4 eV respectively), but for the HAXPES measurements, the whole uncertainty range lay above the mid-gap point. This offers strong evidence that at the deepest penetration depth, the 5N Sb_2Se_3 crystals exhibit n-type doping. The trend towards decreasing valence band offset with lower penetration depth indicates upward band-bending near the surface of the samples as shown in fig. 6.28.

This supports both the Hall effect (Section 6.2.2) and hot probe (Section 6.2.1) measurements, suggesting the presence of an extrinsic n-type dopant in the 5N source material. Given that chemical analysis (Section 5.7) indicated that Cl is the only impurity present in significantly larger proportions in this Sb_2Se_3 compared to the Sb_2Se_3 directly synthesised from the elements, there is strong evidence that Cl is responsible for this n-type conductivity, through formation of the donor Cl_{Se}. This provides additional evidence that Sb_2Se_3 is very sensitive to impurities, and that native defects may not be the dominant conductivity mechanism in published reports where conductivity type was not directly investigated.

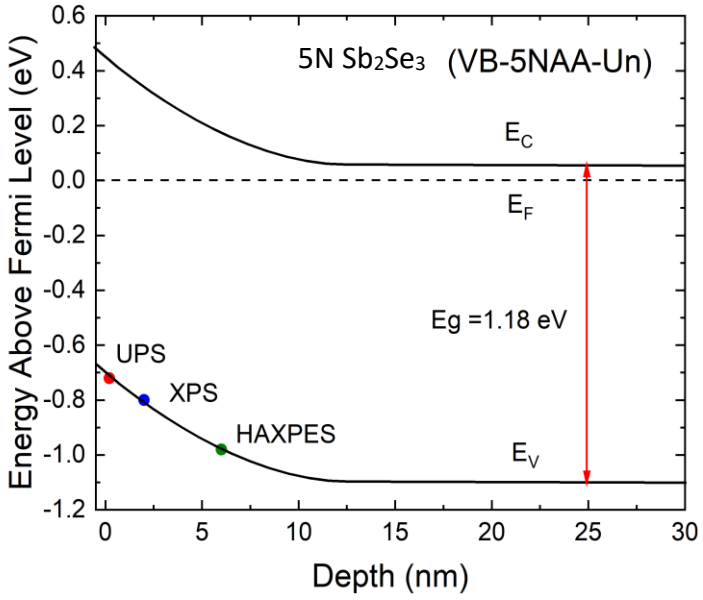

Fig. 6.28 Proposed band bending close to the surface of (010) crystal plane of undoped 5N Sb_2Se_3 single crystal cleaved under vacuum, with band-bending based on the valence band offsets in Table 6.10.

These results are in line with those reported by Bacewicz *et al.* [17], where Sb_2Se_3 synthesised directly from the elements was non-conductive, while commercial Sb_2Se_3 source material was found to be conductive. In that case, the conductivity present in the pre-synthesised Sb_2Se_3 was p-type, so it is likely that a different impurity was present to that observed in this work.

6.8.2 Routes for Extrinsic Doping of Sb_2Se_3

Hall effect (Section 6.2.2) and *C-V* (Section 6.4.2.1) measurements indicated large carrier densities in the $MgCl_2$-doped crystals and undoped 5N crystals, all with Cl as a major impurity, demonstrating that Cl is an n-type dopant for Sb_2Se_3. Indeed, DFT calculations[15] suggest that the formation energy (fig. 6.29, reproduced from [15]) of the donor defect Cl_{Se} is low in Sb_2Se_3 even for high Fermi levels, making it an efficient dopant, although the presence of Cl_i interstitial defects prevents Cl from being ideal.

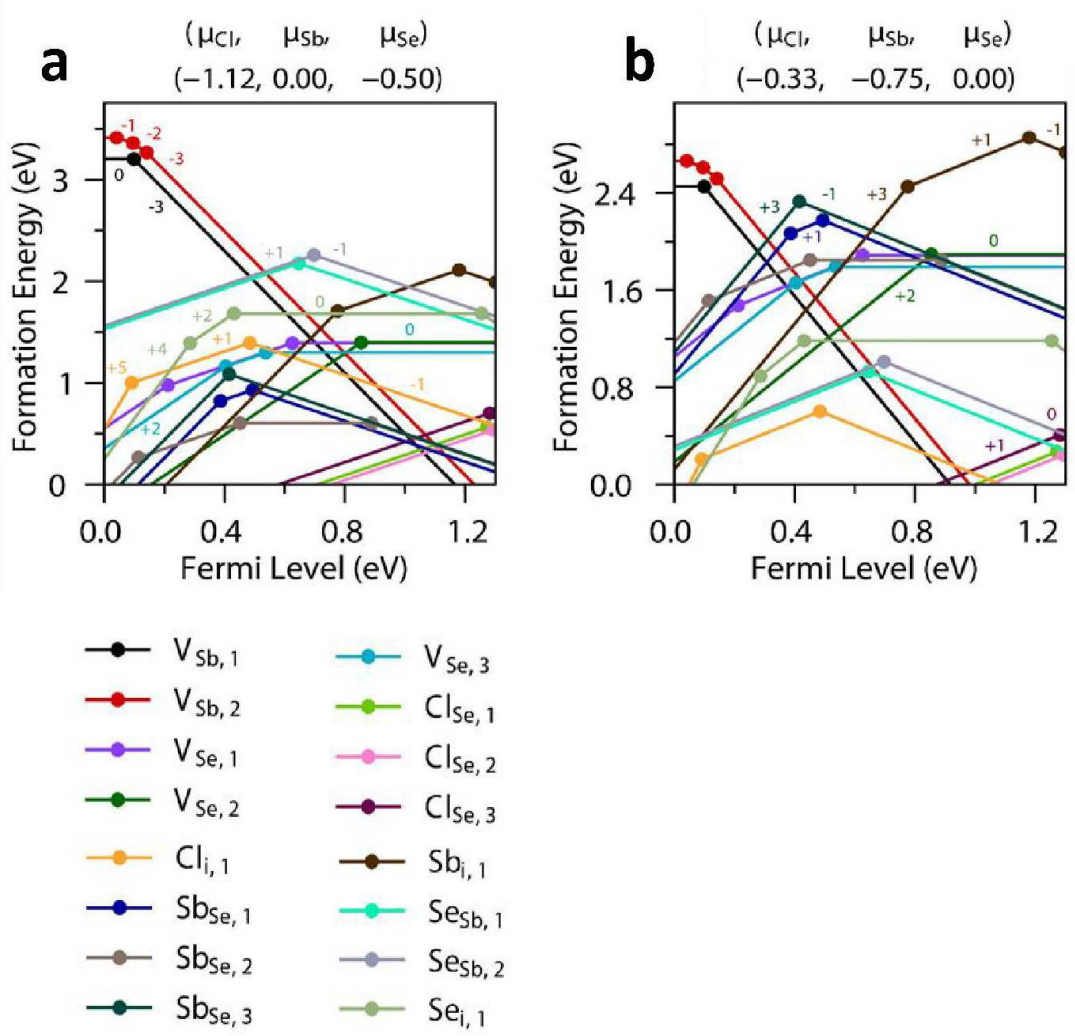

Fig. 6.29 Calculated formation energies for point defects in Cl-doped Sb_2Se_3, under a) Se-poor and b) Se-rich conditions. Reproduced from[15].

For Se-rich material (fig. 6.29b), the calculated formation energies for Cl_{Se} donors are lower than for Se-poor, but a crossing point with V_{Sb} defects at 0.9 eV predicts Fermi-level pinning at this energy. Meanwhile, for Se-poor material (fig. 6.29a), this crossing point does not occur until around 1.0 eV. This may explain the higher carrier density estimated from *C-V* data for the Se-poor $MgCl_2$-doped crystal, compared to the Se-rich (fig. 6.11b). This has implications for device design if n-type doping with Cl is desired. Additionally, it should be noted that the carrier density of the undoped 5N crystal measured by Hall effect (Section 6.2.2) and *C-V* (Section 6.4.2.1) was comparable to the Se-poor $MgCl_2$-doped crystal, even though it was expected to contain much less Cl than the 0.1 at% (7 x

10^{19} cm^{-3}) added to the doped crystals. Furthermore, HAXPES measurements (Section 6.8.1) indicated a valence-band offset of 0.98 eV for an undoped 5N crystal, around the point where Fermi level pinning is predicted to limit Cl-doping (see fig. 6.29).

The similar values of contact barrier heights derived from *I-V-T* measurements of the n-type crystals (Table 6.4) suggest that Cl levels above those present in the 5N crystals do not result in significant upward shifts in the Fermi level position. As a result, the 5N crystals appear to already contain sufficient Cl for doping at a level of 7 x 10^{16} cm^{-3}, almost to the highest doping that appears to be achievable, at 1 x 10^{17} cm^{-3}.

The greater conductivity in Se-rich Sn-doped Sb_2Se_3 crystals as opposed to Se-poor (fig. 6.3) suggests that Sn-related donor defects generally have a lower formation energy in the Se-rich composition, or that the formation of defects which restrict carrier mobility (and/or compensate doping) are more favourable under the Se-poor composition. Either way, this suggests that Se-rich compositions are necessary to achieve significant p-type doping, while the addition of Sn provides a significantly greater carrier density than native doping alone. This is consistent with experimental reports where the addition of Sn enhanced the conductivity of Sb_2Se_3 crystals[18], as well as theoretical work that predicts the same[14]. The generally lower conductivities observed for p-type crystals relative to the n-type (Table 6.2) are consistent with the lower mobilities of holes compared to electrons (due to larger effective mass). Additionally, however, the *C-V* measurements (Section 6.4.2.2) suggest a lower carrier density in the p-type (Se-rich) crystal than for the n-type samples. This result suggests that Sn may not be an ideal p-type dopant, something which is predicted by Stoliaroff *et al.*[14] (due to the formation of additional deep-level defects) and observed experimentally by Bacewicz *et al.*[17], although it should be noted that the latter paper reported Se-poor material. Other p-type dopants merit study as a result (Section 7.6).

6.8.3 Isotype Junctions for Sb_2Se_3

The work detailed in this chapter indicates that it is possible to extrinsically dope Sb_2Se_3 n-type with Cl, with the Hall effect (Section 6.2.2) and *C-V* measurements (Section 6.4.2.1) indicating that carrier densities practical for photovoltaics (10^{15}-10^{16} cm^{-3}) may be achieved. Furthermore, the most commonly used commercial Sb_2Se_3 source material, Alfa Aesar (5N) has been demonstrated to be n-type due to Cl impurities. Nevertheless, for the majority of reports of solar cell fabrication using Sb_2Se_3 the conductivity type of the material is not investigated. Rather it is assumed to be p-type which would be compatible with the n-type CdS or TiO_2 partner layers most often used.

The results of the study into single-crystal Sb_2Se_3 solar cells (Section 6.6) indicate that an isotype n-n+ heterojunction[19] may be formed through the deposition of highly n-type doped CdS onto n-type single crystals of Sb_2Se_3. This is supported by the paper Hobson *et al.*[15] which demonstrates solar cells based on isotype n-n+ heterojunctions and having efficiencies of 7.3%. This second result comes as some surprise, as few other reports of solar cells utilising an isotype heterojunction could be found in the literature, with none reporting a device at this level of efficiency. Ref 20 reports a cell formed from monolayer $CuInSe_2$/InSe, but such reports are rare, and significant efficiencies were not achieved in this case. Additionally, in ref 19, a large array of heterojunction devices, both isotype and anisotype (junction consisting of p and n-type semiconductors) are discussed, but no photovoltaic cells with significant efficiencies are mentioned. In support of this, theoretical modelling described in ref 21 determined very few material combinations that could produce isotype solar cells with viable efficiencies, with anisotype combinations far more favourable. In spite of conflicting with expectations, the conductivity measurements of the Sb_2Se_3 used in this case leaves an isotype hetereojunction as the simplest explanation based on current evidence.

The study into thermally evaporated thin film Sb_2Se_3 devices (Section 6.7) also demonstrates isotype junction-based solar cells, as cells fabricated from n-type source material achieved similar efficiencies to the p-type ones, further supporting the conclusion that p-type source material is not necessary to achieve functional Sb_2Se_3 solar cells. The p-type cells performed best immediately after fabrication, as would be expected for anisotype junctions, but surprisingly, soon dropped below the

performance levels of the n-type and intrinsic cells. This indicates that assumptions about conductivity type based on device performance are not always valid.

This is important moving forward, as isotype devices would require different cell architectures to p-n devices if they are to be optimised. Isotype thin film devices are a rarity within the field, but with the high efficiencies already demonstrated for Sb_2Se_3[15], the study of different isotype material combinations may become more attractive. It may be that the simplest conception of an isotype junction (and its associated disadvantages for PV) does not apply in the case of Sb_2Se_3, either as a result of surface band-bending or another phenomenon, which could also be true of other materials.

6.8.4 Ageing Effects in Sb_2Se_3 Thin Film Devices

The results of the ageing study (Section 6.7.3), may be hypothesised as being due to the emergence of an insulating interfacial layer at the back contact. The formation of Sb_2O_3 seems a likely culprit, as it is an insulating material, and the etching of Sb_2O_3 from the back-contact of Sb_2Se_3 devices has been shown to reduce series resistance[22]. However, this did not result in improved efficiency overall, so the effect of Sb_2O_3 formation is difficult to predict. Alternatively, the displacement of Se and/or Cl atoms in the Sb_2Se_3 absorber layer by Sb_2O_3 formation near the surface may be expected to reduce the carrier density, shifting the Fermi level upwards for p-type and downwards for n-type, but the question remains of what effect the displaced Se/Cl atoms may have.

This observation has important implications, as it could partly explain why good efficiency values have been achieved for n-type isotype Sb_2Se_3 devices, despite this not being ideal from a first-principles standpoint. Indeed, p-Sb_2Se_3 devices may still be expected to have the potential for higher efficiency values, but the ageing process may be a limiting factor for devices of this kind. Therefore, it is very important to understand in greater detail the nature of the material that forms at the back contact due to ageing. It may be, for instance, that to achieve the best efficiencies in p-type Sb_2Se_3 devices, this material must be etched, or encapsulation may be required to prevent oxidisation. On the other hand, if n-type Sb_2Se_3 could be paired with a suitable p-type partner (as an alternative to CdS or TiO_2), higher efficiencies may be expected than for an isotype junction, and the material that forms as a result of ageing may be intentionally added at the back contact in order to boost efficiencies further.

In short, if the mechanism behind the ageing were identified, there is scope for it to be exploited in the case of n-Sb_2Se_3 devices or mitigated in the case of p-Sb_2Se_3 devices, to achieve higher efficiencies overall (Section 7.6).

6.8.5 Point Defects in Sb_2Se_3

The measurements taken using DLTS (Section 6.5.1) and photoluminescence (Section 6.5.2) provide information on the different point defects that may be present in Sb_2Se_3. However, assignment of these defects is not straightforward. Firstly, it is important to note that usable results could only be obtained for doped crystals. The undoped crystals' high resistivity (Table 6.2) meant they could not be measured with *C-V* profiling, while undoped crystals did not produce detectable PL, even at the lowest temperature used (fig. 6.14a). Hence the defect levels reported here may be more likely to result from dopants than native defects, but the latter may nevertheless play a part.

For the DLTS measurements, the electron traps observed at similar energy levels in the undoped 5N crystals to the $MgCl_2$-doped crystals (figs. 6.12-13, Table 6.5) may result from common Cl-related defects. The exception is the 240 K peak that appears for the 5N crystal for short time constants but not the $MgCl_2$-doped crystal (fig. 6.13c-d) and may result from an impurity present in the former crystal and not the latter, a possible example being Sn (Section 5.7). Interpretation of both scans is complicated by the likelihood that each large peak in the temperature scans consists of several smaller peaks, with the unrealistically high values of capture cross-section for E2 in the $MgCl_2$-doped crystal (Table 6.5) perhaps the greatest indication of this. Scans of ΔC against time constant for a single temperature (isothermal DLTS) would be required to separate these closely spaced peaks (Section 7.6). A higher density of Cl-related traps may be expected in the 0.1 at% $MgCl_2$-doped crystal compared to the 5N, but this is not observed for these electron traps, offering some support to the defects being native.

The estimated defect levels for the prominent peaks in this work are compared to those reported in the literature in Table 6.11, as well as to some levels calculated via DFT[26], where they matched most closely with the estimates from this work, and from which the assignments for the defect levels in this work are made, if these defects can be assumed to be native. The activation

energies for defects calculated via DFT are defined as E_C-E_T to allow easy comparison. Where assignments are made in the literature, they are also reported.

Measurement Type	Type	Activation Energy E_C-E_T, E_T-E_V (meV)	Assignment
Conductivity[23]	Hole trap	111	Se_{Sb}
		578	
Admittance Spectroscopy[24]	Hole Trap	300-400	Bulk defect
		200-600	Bulk defect
		500-600	Interface defect
DLTS[25]	Hole Trap	480-490	
		710-740	
	Electron Trap	600-610	
DLTS (This work)	Electron Trap	400	V_{Se2}
		700	Se_{Sb1} or V_{Sb1}
		850	V_{Sb2}
DFT[26]	Donor	500	V_{Se2}
	Acceptor	750	Se_{Sb1}
		750	V_{Sb1}
		850	V_{Sb2}

Table 6.11 Estimated types, activation energy and assignments for deep-level defects in Sb_2Se_3. Experimental and calculated values from the literature are compared to the values estimated in this work. Activation energies are defined as E_C-E_T for electron traps and E_T-E_V for hole traps, while the activation energies of defect levels calculated from DFT are defined as E_C-E_T.

If only the prominent peaks are considered, and they are assumed to be for native defects, then the electron trap level at ~400 meV may be the V_{Se2} defect, and the trap level at ~ 700 meV may be the Se_{Sb1} or V_{Sb1} defect. Given that both of these appear in the $MgCl_2$-doped Se-rich crystal, this interpretation is more plausible for the 700 meV trap level than the 400 meV, given that the formation

energy of V_{Se2} is expected to be large for n-type Se-rich Sb_2Se_3 (fig. 6.28). Of the two possible levels for the 700 meV peak, the V_{Sb1} may be more likely as its formation energy is expected to be lower for high Fermi levels. The trap level observed at ~850 eV could be the V_{Sb2} defect[26], but this energy level could only be quantified for the 5N crystal, where the stoichiometry of the source was unknown, leaving this assignment ambiguous. All of these assignments neglect the likely influence of impurities.

The lack of photoluminescence peaks in the undoped Sb_2Se_3 suggests that band-to-band recombination in the spectra is not significant. This is consistent with reports of Sb_2Se_3 having an indirect conduction-band minimum at lower energy than its direct minimum[27], and suggests that where peaks are observed, they are not band-to-band transitions. This is consistent with the energies of the peaks in fig. 6.15a, which lie within the low-temperature bandgap of Sb_2Se_3[8]. The strong correlation between the energies and intensities of the peaks present in the PL spectra (assigned to DAP transitions) and the impurity content of the crystals suggests the transitions are indeed mediated by impurities.

The rapid quenching of the peak at 1.2 eV with increasing temperature suggests a shallow defect level, especially if this is the same defect level reported in Grossberg *et al.*[6]. The fact that this peak appears in the spectra for the n-type 5N crystal and the n-type $MgCl_2$-doped crystal, but not the p-type Sn-doped or intrinsic undoped crystal, suggests it may be associated with the n-type doping. The 1.1 eV peak that also appears in these spectra and quenches less rapidly, may result from a deeper level defect associated with Cl-impurities. Alternatively, this peak may result from a native defect which forms at higher Fermi levels, such as V_{Sb} (fig. 6.29). The 0.9 eV peak may result from Sn-related defects, as Sn is present in the Sn-doped crystal and the undoped 5N crystal (Section 5.7), but the low transition energy and the slow quenching with temperature suggest a relatively deep-level defect, so not likely to be responsible for the p-type doping. This suggests that Sn introduces a deep-level defect as well as a shallow acceptor in Sb_2Se_3, as was argued by Stoliaroff *et al.*[14], reducing its utility as a dopant element.

This interpretation, of linking the observed peaks directly to impurity content, differs from that of Grossberg *et al.*[6]. Despite the same peaks appearing in their spectra, the peak at 0.9 eV is

assigned to a Se_{Sb} antisite defect, which is plausible as the Sn-doped crystal was p-type and Se-rich, a condition where the formation energy of Se_{Sb} is low (fig. 6.29). Meanwhile the 1.1 eV peak was associated with grain boundaries, something that seems unlikely in single crystals, unless it occurs at the van der Waals boundaries in a process that is suppressed in the Sn-doped p-type crystal. In the work of Grossberg *et al.*, the impurity content of the thin films studied was not known, but these differing conclusions illustrate how complicated the interpretation of PL spectra may be. Studies involving known, relative concentrations of an impurity element are necessary to more clearly understand the effects of impurities upon PL spectra (Section 7.6).

6.9 Conclusions

This chapter reports key findings made into the properties of Sb_2Se_3 relevant to solar cells. The findings are summarised in Table 6.12, with the values derived from the measurements included. Table 6.12 also contains a brief summary of the implications of these results for device design, discussed in more detail below.

From these results, one surprise is that the pure, stoichiometric Sb_2Se_3 crystals in this investigation did not seem to be natively conductive, nor did the Se-poor condition induce n-type conductivity. Conversely, however, the Se-rich condition did lead to p-type conductivity, while added extrinsic Sn was observed to induce p-type conductivity, even in Se-poor material, with higher conductivity found for Se-rich material, and so suggesting that a Se-excess produced more effective doping. Meanwhile, n-type conductivity was found in samples with Cl impurities, whether Se-poor or Se-rich, although slightly higher carrier densities were found in the former.

Sample Type Single Crystals	Conductivity Type	Carrier Density / cm^{-3}	Barrier Height / eV	Deep-Level Carrier Trap Activation Energies / meV	Major Photoluminescence Peak Positions (T=10K) / eV	Implications for Future Device Design
Undoped Stoichiometric	Intrinsic	-	-	-	None	Pure stoichiometric Sb_2Se_3 may not be self-doping
Undoped Se-poor	Intrinsic	-	-	-	-	V_{Se} may not contribute to electron density
Undoped Se-rich	P-type	-	-	-	-	V_{Sb} may contribute to hole density
Sn-doped Se-poor	P-type	-	-	-	-	Sn may act as a p-type dopant
Sn-doped Se-rich	P-type	1 x 10^{15}	0.37 (In)	-	0.9	Doping to high levels with Sn may not be possible
Cl-doped (impurity in source)	N-type	7 x 10^{16}	0.56 (Au)	400, 700, 850	0.9, 1.1, 1.2	Cl may act as an n-type dopant, PL peaks associated with impurities
$MgCl_2$-doped Se-poor	N-type	1 x 10^{17}	-	-	-	Doping to high levels may be achieved with $MgCl_2$ and Se-poor stoichiometry
$MgCl_2$-doped Se-rich	N-type	1 x 10^{16}	-	360, 750	1.1, 1.2	Cl donor impurities may compensate V_{Sb} acceptors. Deep-level traps may be native

Thermally Evaporated Solar Cells	Conductivity Type	Carrier Density / cm^{-3}	Max. Efficiency (Avg. for Device) / %	Efficiency Change with Ageing (Champion Cell)	Implications for Future Device Design
Cl-doped (impurity in source)	N-type	3 x 10^{15}*	1.65	Slight improvement	Ageing may improve back-contact for n-Sb_2Se_3 cells
Undoped stoichiometric	Intrinsic	7 x 10^{15}*	1.12	Unchanged	Ageing effect varies with conductivity type
Sn-doped Se-rich	P-type	3 x 10^{15}*	1.01	Significant reduction	Ageing may degrade back-contact for p-Sb_2Se_3 cells

Table 6.12 Compiled parameters for Sb_2Se_3 single crystals and thermally evaporated solar cells based on the investigations in this work, and possible implications for device design in future. *Values are uncertain as depletion approximation may not apply to *C-V* measurements.

Doped p-type crystals were subsequently found to form Schottky barriers with In, while n-type crystals formed Schottky barriers with Au, and barrier heights were estimated. An isotype n-n+ heterojunction was also demonstrated through the deposition of CdS onto n-Sb_2Se_3 crystals. The contact barrier with Au allowed DLTS to be carried out on n-type crystals and deep level carrier traps to be identified, which may be associated with vacancy defects V_{Sb} and V_{Se}, or perhaps impurities. Photoluminescence measurements produced broad peaks, thought to represent DAP transitions and considered more likely to result from Cl and Sn impurity defects than native point defects, since they did not appear for undoped crystals.

Sb_2Se_3 source material with known impurity content was also utilised to produce thin film solar cells via thermal evaporation with different conductivity types, all demonstrating ~ 1 % efficiency. N-type solar cells became slightly more efficient with ageing, while p-type solar cells dropped significantly in efficiency. An insulating interfacial layer at the back contact was thought to be responsible for this behaviour, which may be Sb_2O_3, but this requires further analysis.

These results are all expected to inform the production of Sb_2Se_3 thin film devices and other future studies, as outlined in Section 7.6.

6.10 References

[1] S. Uličná, P. J. M. Isherwood, P. M. Kaminski, J. M. Walls, J. Li, and C. A. Wolden, "Development of ZnTe as a back contact material for thin film cadmium telluride solar cells," *Vacuum*, vol. 139, pp. 159–163, 2017.

[2] J. Nelson, *The Physics of Solar Cells*, 1st ed. London: Imperial College Press, 2003.

[3] W. M. Haynes, *CRC Handbook of Chemistry and Physics*, 95th ed. London, New York: CRC Press, Taylor & Francis Group, 2014.

[4] Y. Cao *et al.*, "Towards high efficiency inverted Sb_2Se_3 thin film solar cells," *Sol. Energy Mater. Sol. Cells*, vol. 200, p. 109945, 2019.

[5] C. Chen *et al.*, "Optical properties of amorphous and polycrystalline Sb_2Se_3 thin films prepared by thermal evaporation," *Appl. Phys. Lett*, vol. 107, p. 43905, 2015.

[6] M. Grossberg, O. Volobujeva, A. Penežko, R. Kaupmees, T. Raadik, and J. Krustok, "Origin of photoluminescence from antimony selenide," *J. Alloys Compd.*, vol. 817, p. 152716, Oct. 2019.

[7] T. Schmidt, K. Lischka, and W. Zulehner, "Excitation-power dependence of the near-band-edge photoluminescence of semiconductors," *Phys. Rev. B*, vol. 45, no. 16, pp. 8989–8994, 1992.

[8] M. Birkett *et al.*, "Band gap temperature-dependence of close-space sublimation grown Sb_2Se_3 by photo-reflectance," *APL Mater.*, vol. 6, p. 84901, 2018.

[9] L. J. Phillips *et al.*, "Current enhancement via a TiO_2 window layer for CSS Sb_2Se_3 solar cells: performance limits and high Voc," *IEEE J. Photovoltaics*, vol. 9, no. 2, pp. 544–551, 2019.

[10] O. S. Hutter, L. J. Phillips, K. Durose, and J. D. Major, "6.6% efficient antimony selenide solar cells using grain structure control and an organic contact layer," *Sol. Energy Mater. Sol. Cells*, vol. 188, no. August, pp. 177–181, 2018.

[11] S. Mariotti, O. S. Hutter, L. J. Phillips, P. J. Yates, B. Kundu, and K. Durose, "Stability and performance of $CsPbI_2Br$ thin films and solar cell devices," *Appl. Mater. Interfaces*, vol. 10, pp. 3750–3760, 2018.

[12] P. Blood and J. W. Orton, *The Electrical Characterization of Semiconductors: Majority Carriers and Electron States*, 1st ed. London: Academic Press Limited, 1992.

[13] Y. Zhou *et al.*, "Buried homojunction in CdS/Sb_2Se_3 thin film photovoltaics generated by interfacial diffusion," *Appl. Phys. Lett*, vol. 111, no. 10, p. 13901, 2017.

[14] A. Stoliaroff *et al.*, "Deciphering the role of key defects in Sb_2Se_3, a promising candidate for chalcogenide based solar cells," *ACS Appl. Energy Mater.*, vol. 3, no. 3, pp. 2496–2509, 2020.

[15] T. D. C. Hobson *et al.*, "Isotype heterojunction solar cells using n-type Sb2Se3 thin films," *Chem. Mater.*, vol. 32, no. 6, pp. 2621–2630, 2020.

[16] C. N. Savory and D. O. Scanlon, "The complex defect chemistry of antimony selenide," *J. Mater. Chem. A*, vol. 7, no. 17, pp. 10739–10744, 2019.

[17] R. Bacewicz and T. F. Ciszek, "Liquid encapsulated crystal growth and electrical properties of Sb_2Se_3 and Bi_2S_3," *J. Cryst. Growth*, vol. 109, pp. 133–136, 1991.

[18] S. Chen *et al.*, "Enhanced electrical conductivity and photoconductive properties of Sn-doped Sb_2Se_3 crystals," *J. Mater. Chem. C*, vol. 6, no. 24, pp. 6465–6470, 2018.

[19] B. L. Sharma and R. K. Purohit, *Semiconductor Heterojunctions*, 1st ed. Oxford: Pergamon Press, 1974.

[20] H. Ji *et al.*, "Self-assembly of a lateral quasi-Ohmic $CuInSe_2$/InSe isotype heterojunction for flexible devices by pulsed laser deposition," *Appl. Phys. Lett.*, vol. 115, no. 16, pp. 1–6, 2019.

[21] H. J. Pauwels, "Analysis and Evaluation of Isotype Heterojunction Solar Cells," *Solid State Electron.*, vol. 22, pp. 988–990, 1979.

[22] H. Shiel *et al.*, "Chemical etching of Sb_2Se_3 solar cells: surface chemistry and back contact behaviour," *J. Phys. Energy*, vol. 1, p. 045001, 2019.

[23] C. Chen *et al.*, "Characterization of basic physical properties of Sb_2Se_3," *Front. Optoelectron.*, vol. 10, no. 1, pp. 18–30, 2017.

[24] X. Hu *et al.*, "Investigation of electrically-active defects in Sb_2Se_3 thin-film solar cells with up to 5.91% efficiency via admittance spectroscopy," *Sol. Energy Mater. Sol. Cells*, vol. 186, no. July, pp. 324–329, 2018.

[25] X. Wen *et al.*, "Vapor transport deposition of antimony selenide thin film solar cells with 7.6% efficiency," *Nat. Commun.*, vol. 9, p. 2179, 2018.

[26] M. Huang, P. Xu, D. Han, J. Tang, and S. Chen, "Complicated and unconventional defect properties of the quasi-one-dimensional photovoltaic semiconductor Sb_2Se_3," *ACS Appl. Mater. Interfaces*, vol. 11, no. 17, pp. 15564–15572, 2019.

[27] J. J. Carey, J. P. Allen, D. O. Scanlon, and G. W. Watson, "The electronic structure of the

antimony chalcogenide series: Prospects for optoelectronic applications," *J. Solid State Chem.*, vol. 213, pp. 116–125, 2014.

7. Conclusions

This chapter summarises the conclusions and further work for each of the three results chapters. Sections 7.1 and 7.2 separately cover the conclusions and further work respectively for the CZTSSe results (Chapter 4); while Section 7.3 and 7.4 similarly cover the crystal growth and physical properties of Sb_2Se_3 and $Sb_2(S,Se)_3$ (Chapter 5); and Section 7.5 and 7.6 cover the electrical properties of Sb_2Se_3 single crystals and thin-film solar cells (Chapter 6). Section 7.7 compares the results for the two materials and assesses whether the initial aims of this project were achieved. A list of publications resulting from the work is given after the end of this chapter.

7.1 Conclusions for Chapter 4, CZTSSe

The major conclusions for Chapter 4 may be summarised as follows. Solution growth from a NaCl/KCl mixture was employed to produce $Cu_2ZnSnS_{4x}Se_{4(1-x)}$ monograins at ~ 100 μm scale, 10x larger than in previous works using the same solvent[1], for $0 \leq x \leq 1$. Raman spectroscopy of the series end members CZTS and CZTSe produced peaks at 196 and 338 cm^{-1}, indicating greater ordering in these monograins than in feedstock synthesised directly from the elements (peaks observed at 194 and 334 cm^{-1}), suggesting the crystallisation of ordered kesterite from the solution. The mechanism for this was ordering not directly known, but it may be that during cooling, these samples remained at temperatures in the vicinity of the kesterite order-disorder transition (~200°C) long enough for significant re-ordering of the crystal lattice to occur. The additional mass of the NaCl/KCl mix may have allowed the CZTSSe to remain at these temperatures for longer than the CZTSSe feedstock during its cooling phase, resulting in greater ordering in the former. The CZTS peak in the Raman spectrum was more sensitive to ordering than the CZTSe peak. The whole series was also measured with XRD, which allowed the CZTSe-CZTS Vegard relation to be determined with twice the number of the data points as in previous works, as: a (Å) = -0.268(3)x + 5.6949(17) and c (Å) = -0.516(6)x + 11.345(3). The composition dependence of Raman A modes was measured

as: ω_{CZTSe} (cm^{-1}) = (44.6 ± 1.6)x + (194.6 ± 0.8) and ω_{CZTS} (cm^{-1}) = (7.1 ± 1.3)x + (329.0 ± 0.8), potentially allowing for back-correlation of compositions from both linear trends.

The comparison of lattice parameters with series reported in the literature was as follows: *a*-values were systematically lower by 0.02 Å and *c*-values by 0.01 Å across the whole series compared to the Cu-poor series (Cu/(Zn+Sn) = 0.91 to 0.96) reported by Nagaoka *et. al.*[2]. *a*-values were greater by 0.01 Å at x = 0 and 0.03 Å at x = 1, while *c*-values were lower by 0.04 Å at x = 0 and equal at x = 1 compared to the series in He *et al.*[3] where metals stoichiometry varied from Cu/(Zn+Sn) = 0.8 to 1.2. The evolution of the CZTSe-like Raman *A* mode matched well with the series reported by Adachi in [4] of ω_{CZTSe} (cm^{-1}) = 46.8x + 194.9 averaged from the series in He *et al.* and the series in Grossberg *et al.*[5] where Cu/(Zn+Sn) ranged from 0.88 to 0.97. The evolution of the CZTS-like Raman *A* mode was less consistent with the series reported by Adachi in [4], which exhibited a slope of 12.2x cm^{-1} compared to 7.1x cm^{-1} in this work. Based on these results, the CZTSe-like Raman mode was identified as favourable for back-correlation, as a good linear fit was achieved and these results suggest it is less sensitive to ordering and metals stoichiometry than lattice parameters or the CZTS-like mode.

7.2 Further Work on CZTSSe

Building upon this work, there are several clear routes for productive further studies, which may consist of the following. A series of CZTSSe thin films across the $0 \leq x \leq 1$ range would allow the Vegard relation for bandgap to be established. The bandgap could be estimated via Tauc plots from transmission/reflection measurements, with composition (x) back-correlated from the bulk sample series using lattice parameters and/or Raman peaks. Bandgap values could also be measured for the bulk samples directly via x-ray photoemission spectroscopy (XPS) to determine the valence band position and inverse photoemission spectroscopy (IPES) for the conduction band position.

Additionally, the thick, flat, densely-packed CZTSSe plates produced from the square seed plates (grain size 100 μm) may have utility in several further experiments. Plates could be combined with PV partner layers form test devices with a low-prevalence of grain boundaries, in a scheme similar to the monograin devices already demonstrated by Mellikov in [4]. The same flat sections could also be

mapped with cathodoluminescence (CL) to compare the non-radiative carrier recombination rates at the grain boundaries to the bulk, while the inclusion of EBSD may allow the orientation of grain boundaries with the highest and lowest recombination rates to be determined. The results could then be compared to theoretical calculations of recombination rates at grain boundaries, such as has already been carried out for CdTe[7]

7.3 Conclusions for Chapter 5, Growth of Sb_2Se_3 and $Sb_2(S,Se)_3$ Crystals

The major conclusions for Chapter 5 may be summarised as follows. Growth by the vertical Bridgman method resulted in Sb_2Se_3 pieces exhibiting cleavage behaviour which suggested the formation of single crystals 4 mm in diameter and 1 cm in length - large enough for characterisation with XRD. Assuming monocrystalline nature, oriented {100} crystal planes of these samples were prepared using visual inspection alone, taking advantage of the (010) cleavage planes and cleavage steps parallel to [001].

Extended defects ~ 100 nm wide, representing a small-angle rotation of the crystal planes, were detected in the Sb_2Se_3 crystals, and are consistent with the 'kink-bands' discussed in relation to 'ripplocations' observed in other van der Waals materials[8].

Raman spectra of air-annealed Sb_2Se_3 thin films exhibited a 253 cm^{-1} peak for high-temperature anneals, consistent with reports that this peak results from native oxide Sb_2O_3 rather than Sb_2Se_3. Furthermore, anisotropy in Raman spectra from single crystals was demonstrated when the laser polarisation was rotated, allowing the closely spaced overlapping A_g Raman mode peaks at 187 and 191 cm^{-1} to be resolved, and suggesting a route for further assignment of Raman modes.

Chemical analysis detected a larger Cl concentration in 5N Sb_2Se_3 compared to Sb_2Se_3 synthesised directly from the elements (The electrical effects of this were explored in Chapter 6), while crystals doped with Sn and $MgCl_2$ were shown to have incorporated Sn and Mg impurities at

0.1 at%, matching weighed quantities, with Cl concentration inferred as being double that of Mg (Again, the electrical effects are reported in Chapter 6).

7.4 Further Work on Sb_2Se_3 Single Crystals

The availability of what were presumed to be oriented single crystals of Sb_2Se_3 from the growth described in this work, along with the initial polarisation-dependent Raman study presented in Chapter 5, paved the way for a fully comprehensive study of anisotropy in Raman spectra from Sb_2Se_3 (See List of Publications, article 2). The study combined density functional simulations of vibrational symmetries with anisotropic Raman spectra from experiments (not included in this thesis). Additionally, much of the intended follow-on work from the crystal growth and materials preparation was included in Chapter 6, as described in the next section.

However further additional studies based on the conclusions in Chapter 5 were also identified. For instance, variations in band positions with plane orientation could be measured using XPS (for the valence band) and/or IPES (for the conduction band) aiding device design. Additionally, given the anisotropy of the Sb_2Se_3 crystal structure, ellipsometry could be employed on the crystalline surfaces described in this work to probe anisotropies in the dielectric constant, allowing quantities such as carrier density to be determined more accurately.

Another productive area of investigation would be to establish whether the low-angle boundary defects observed in Sb_2Se_3 single crystals are electrically benign by: employing EBSD to detect sub-grain boundaries and quantify misorientation; and combining this investigation with CL mapping to allow non-radiative recombination rates to be correlated with misorientation.

7.5 Conclusions for Chapter 6, Electrical Characterisation of Sb_2Se_3 Single Crystals and Devices

The investigations described in Chapter 6 involved the measurement of conductivity type, carrier density, carrier mobility, metal-semiconductor barrier heights, deep-level defect activation energies

and photoluminescence transition energies for Sb_2Se_3 single crystals of varying stoichiometry and impurity content. The fabrication of thin film solar cells from doped source material also allowed the effects of doping upon efficiency, PV working parameters, carrier density and EQE to be investigated. All of the measured parameters are summarised in Table 6.12 and the key conclusions are below.

Based on hot-probe measurements, pure, stoichiometric Sb_2Se_3 single crystals were found to be non-conductive, suggesting no native conductivity. Pure, Se-poor crystals were similarly non-conductive, suggesting that Se-vacancies did not contribute significantly to conductivity. However, Se-rich crystals exhibited p-type conductivity, while the addition of Sn reduced resistivity in p-type Se-rich crystals and induced p-type conductivity in Se-poor crystals, suggesting that Sn may introduce acceptors into Sb_2Se_3. A maximum carrier density of ~ 10^{15} was achieved for Sn-doped Se-rich crystals.

Meanwhile, hot-probe results indicated Cl to be an n-type dopant for Sb_2Se_3. When added to a Se-rich crystal, Cl was found to compensate the p-type conductivity and induce n-type. The largest electron density observed from Cl-doping was ~ 1 x 10^{17} cm^{-3}, observed under Se-poor conditions. With the conductivity type of different crystal samples established, Schottky barriers were formed for a p-Sb_2Se_3 / In interface and a n-Sb_2Se_3 / Au interface, with barrier heights measured at 0.36 eV and 0.56 eV respectively.

The formation of Schottky barriers allowed the associated space charge region to be probed with DLTS, and deep-level carrier traps at 400, 700 and 850 meV were detected in 5N single crystals, (i.e. n-type with chlorine) with the 400 and 700 meV traps also seen in Se-rich $MgCl_2$-doped Sb_2Se_3. Traps were tentatively assigned to the native defects V_{Sb} and V_{Se}. Shallow defects were also detected through photoluminescence peaks at 0.9, 1.1 and 1.2 eV. These were associated with donor-acceptor pair recombination, in agreement with previous studies[10], but with Sn and Cl impurities suggested as the cause, which has not been reported previously.

J-V investigations demonstrated n-n+ isotype junctions for both n-type single crystals and thermally evaporated Cl-doped Sb_2Se_3, both partnered with deposited n-type CdS. Furthermore,

thermally evaporated thin film Sb_2Se_3 / CdS solar cells with n-type, intrinsic and p-type Sb_2Se_3 layers were all fabricated, all reaching ~ 1 % efficiency. Ageing of the thin film devices in air appeared to raise the back-contact barrier height for p-type devices, reducing efficiency, but lower it for n-type and intrinsic devices, slightly increasing efficiency. This may be due to a resistive interfacial layer of Sb_2O_3 forming from oxidisation. It should be noted that the fabrication process for these cells was not optimised, so it is not known whether these oxidisation effects also apply to solar cells with more refined synthesis processes.

7.6 Further Work on the Electrical Properties of Sb_2Se_3

The observation of n-type conductivity in Cl-doped Sb_2Se_3 was the key result enabling a journal article which demonstrated that high-efficiency Sb_2Se_3 solar cells could be produced based on isotype n-n+ heterojunctions (See List of Publications, article 3). Once again, since the author's work in this paper was part of a large collaborative team effort, a description of the solar cell results has not been included in this thesis. Besides that work, suggested further work based on the results in Chapter 6 is outlined below.

As a starting point, isotype solar cells could be examined for other PV materials such as CZTSSe, CIGS and CdTe. Something else to consider is that applying p-type partner layers to n-type Sb_2Se_3 may improve upon the ~6% efficiencies reported for isotype n-n+ cells (through better charge separation) so this is worth investigating. Investigating n-type material further, alternative halogens to Cl, such as Br and/or I should be examined as n-type dopants, as suggested by Stoliaroff *et al.*[11]. For one thing, the room temperature liquid and solid phases of these elements may simplify their incorporation. Similarly, alternative p-type dopants to Sn are worthy of further study, such as Zn, Ge and Pb. The position of the valence band maxima for these dopants could be measured with photoemission (as has been done for n-type crystals[12]) and compared.

Another way to aid the production of thin film solar cells may be to further investigate the ageing effects observed for thermally-evaporated Sb_2Se_3 solar cells of different conductivity types. There are several clear next steps. Firstly, it is worth investigating whether solar cells fabricated by other methods with more optimised processes, such as CSS, exhibit the same changes in working parameters with ageing, or if this is simply a result of the early development stage of the cells in this work. Secondly, etching studies of the type reported in Shiel *et al.*[13] could be carried out to see how cells of different conductivity type are affected by the removal of interfacial layers. Changes in band positions with ageing and after etching could be measured with photoemission, while Raman may track compositional changes. Thirdly, if the reaction products responsible for the ageing behaviour could be identified, the engineered deposition of these materials at the back surface, e.g. Sb_2O_3 and Se, may be carried out to test their effect on PV working parameters.

Returning to the fundamentals, point defects could be characterised further by fabricating new sample sets with controlled stoichiometry and varying impurity concentration. This could be engineered through weighing in stages – for instance two Sb_2Se_3 samples with known Sb or Se excesses (determined by weighing) could be mixed and secondary reaction carried out, with their ratios providing finer control over the stoichiometry. Similarly, a Sb_2Se_3 sample with a relatively high, known concentration of a dopant impurity could be combined with varying quantities of undoped material to provide a range of concentrations. This would allow extrinsic defects to be assigned more easily as their density would be expected to correlate with the impurity concentration. For deep-level point defects, refinement of the measurement protocols used in DLTS may allow closely spaced, overlapping peaks that represent different defects to be resolved. In particular, scans of ΔC against emission time constant (isothermal DLTS) could be productive. Finally, positron annihilation lifetime spectroscopy may provide a complimentary means to determine the concentration and type of vacancies within Sb_2Se_3 single crystals. At the time of writing, single crystals of stoichiometric, Se-rich and Se-poor samples have been provided to Prof D. Keeble of Dundee University to undertake this work.

7.7 Final Conclusions

There were two major strands of investigation covered in this thesis, the study of CZTSSe and of Sb_2Se_3. The similarities between these two materials allowed them to be studied in parallel: Both are crystalline metal chalcogenide semiconductors, with similar bandgaps making them suitable as PV absorber layers. Both are also chemically stable in air and in sunlight at ambient temperatures, but both require their processing to occur under inert atmospheres to prevent oxidisation. In practical terms, this meant that similar methods of synthesis and structural analysis could be applied to either material, making it economical to study both. This approach has value since as outlined in Chapter 1, there is no single perfect solar cell material, with all emerging technologies presenting some flaw or another. Furthermore, there is no way of knowing for certain at the research stage if these flaws can ultimately be overcome, or if they will eventually make a technology unviable for commercial

application. This makes a pluralistic approach to emerging materials prudent, motivating the study of two related, but still quite different materials in this work.

Despite this, it does remain important to continually assess the relative merits of different technologies as they develop. The structure of this project, studying two different metal chalcogenide thin film materials, made it well-placed to compare CZTSSe and Sb_2Se_3 this way.

At the outset, the ambitions for both materials were similar. An initial aim was to demonstrate processing routes that could produce single crystals of each material. Such crystals were hoped to act as test-beds to examine the presence of point defects (through, for instance, PL and DLTS measurements), with the concentration of such defects adjusted through fine control of stoichiometry and impurity content in a series of single crystal samples. An additional aim for Sb_2Se_3 was to understand the origin of conductivity better, as this was somewhat ambiguous in the literature prior to this work. Investigations of the lattice parameter and bandgap Vegard relations for varying S-Se ratios were also originally intended for both materials, to assess the viability of bandgap tuning, with single crystals once again intended for use as reference samples.

In terms of single crystal production, the differing chemical complexity of the materials was a key factor: there was strong evidence for success with Sb_2Se_3, most likely due to its congruent melting. However, single crystal growth with CZTSSe was never achieved as its peritectic transition complicated its solidification from solution. The binary nature of Sb_2Se_3 was therefore a significant advantage in this regard. Essentially, this meant that the aim to examine point defects in CZTSSe single crystals was not practical, while there was an opportunity to do this for Sb_2Se_3. The focus for CZTSSe therefore shifted towards greater understanding of the lattice parameter Vegard relation, and the polycrystalline samples produced from the NaCl/KCl mix, while not single crystals, were well-suited to this type of investigation.

In contrast, the production of Sb_2Se_3 single crystals did lead to success in the observation of point defects, as reported in the sections on PL and DLTS, in line with the original aims of the project. Meanwhile, there was less focus on measurement of the $Sb_2(S,Se)_3$ Vegard relation, despite its clear

utility. This was in large part because more time was devoted to establishing the origin of conductivity in Sb_2Se_3, which became far more pressing with the observation of n-type conductivity, and leaving less time in the project to focus on the Vegard relation. All of these factors ultimately led to the project taking the form reported in this work.

In the experimental work of this thesis, the binary nature of Sb_2Se_3 continued to be an advantage, as it allowed the stoichiometry and impurity content to be controlled with a relatively small number of samples, whereas the phase space of CZTSSe is so flexible that attempting to control stoichiometry and impurity content in the manner carried out for Sb_2Se_3 may not have been practical, even if single crystals had been produced. Indeed, while in Chapter 4, the lattice parameter Vegard relation from CZTSe to CZTS was characterised with greater precision than previous works, this remains only a single line on the multi-dimensional phase space of CZTSSe, and questions remained as to how the differing metals stoichiometry may have affected this series as compared to similar work in the literature.

The difficulties encountered with CZTSSe in this work mirror the difficulties encountered by makers of solar cells, since as described in Chapter 2 (Section 2.3.3), the variability of chemical and structural phases in CZTSSe, and the presence of secondary phases is thought to be a key reason for the efficiency gap.

However, despite clear apparent disadvantages, we should be mindful that to date, the efficiencies of the champion CZTSSe-based devices are still superior to those based on Sb_2Se_3, as outlined in Chapter 2. But we should also note that this does most likely come as a result of a significantly larger body of literature for CZTSSe than Sb_2Se_3 (see Section 2.4.1), and the fact that tuning of the S-Se ratio has allowed optimisation of the bandgap. This is something that is likely to be achievable with $Sb_2(S,Se)_3$ also, although there was ultimately limited focus upon it in this work. The champion efficiencies for CZTSSe have also not increased significantly in the last few years, with the current record of 12.6% set in 2014[14], while they are still increasing rapidly for Sb_2Se_3 (9.2% in 2019[15], up from 7.6% in 2018[16]), despite the relatively small body of literature dedicated to its study. The work presented in this thesis is expected to contribute more significantly to the literature

on Sb_2Se_3 than CZTSSe, as it is adding to this smaller body of literature, but also, the conclusions of the work into Sb_2Se_3 point to several routes to understand the material better, with clear applications in improving device performance. While some early steps have been made in identifying the nature of point defects in Sb_2Se_3, with clear routes to better understanding (as related in Section 7.6), accurate determination of the key point defects in CZTSSe remained elusive. The next steps are less clear for CZTSSe and arguably, due to its complexity, larger studies with more comprehensive sample sets (often with more difficulty involved in sample preparation), are necessary, making progress intrinsically more difficult. On the other hand, the indirect minimum in the conduction band of Sb_2Se_3 (see Section 2.4.1) may be a barrier for higher efficiency levels in future, which is not a problem for CZTSSe. It may be that the advantages of Sb_2Se_3 (e.g. benign grain boundaries) outweigh this fundamental disadvantage, but it should be kept in mind.

Ultimately, judged on the work in thesis, Sb_2Se_3 currently looks more promising than CZTSSe as a candidate for commercial scale-up. Generalising the material to $Sb_2(S,Se)_3$ and tuning the S-Se ratio in order to optimise the bandgap is one route that has not yet been significantly exploited, but efficiency increases may be expected as a result, and it is not unfeasible that $Sb_2(S,Se)_3$ may eventually overtake CZTSSe in terms of efficiency. The cheaper, more plentiful source elements and lower toxicity (see Section 2.3.1) still make CZTSSe superior in principle, but for now, Sb_2Se_3 appears to offer great promise as a material that balances low costs and low toxicity with the potential for high efficiencies.

7.8 References

[1] A. S. Ionkin, B. M. Fish, W. J. Marshall, and R. H. Senigo, "Use of inorganic fluxes to control morphology and purity of crystalline késterite and related quaternary chalcogenides," *Sol. Energy Mater. Sol. Cells*, vol. 104, pp. 23–31, 2012.

[2] A. Nagaoka, K. Yoshino, H. Taniguchi, and T. Taniyama, "Growth and characterization of $Cu_2ZnSn(S_xSe_{1-x})_4$ alloys grown by the melting method," *J. Cryst. Growth*, vol. 386, pp. 204–207, 2014.

[3] J. He, L. Sun, S. Chen, Y. Chen, P. Yang, and J. Chu, "Composition dependence of structure and optical properties of $Cu_2ZnSn(S,Se)_4$ solid solutions: An experimental study," *J. Alloys Compd.*, vol. 511, pp. 129–132, 2011.

[4] K. Ito, *Copper Zinc Tin Sulfide-Based Thin-Film Solar Cells*, 1st ed. Nagano: John Wiley and Sons, 2015.

[5] X. Zeng *et al.*, "$Cu_2ZnSn(S,Se)_4$ kesterite solar cell with 5.1% efficiency using spray pyrolysis of aqueous precursor solution followed by selenization," *Sol. Energy Mater. Sol. Cells*, vol. 124, pp. 55–60, 2014.

[6] T. D. C. Hobson *et al.*, "Vegard relation and Raman band reference data generated from bulk crystals of kesterite phase composition series $Cu_2ZnSnS_{4x}Se_{4-4x}$ (CZTSSe $0 \leq x \leq 1$)," *Cryst. Growth Des.*, vol. 20, no. 4, pp. 2164–2173, 2020.

[7] C. J. Tong and K. P. McKenna, "Passivating grain boundaries in polycrystalline CdTe," *J. Phys. Chem. C*, vol. 123, no. 39, pp. 23882–23889, 2019.

[8] A. Kushima, X. Qian, P. Zhao, S. Zhang, and J. Li, "Ripplocations in van der Waals layers," *Nano Lett.*, vol. 2, no. 15, pp. 1302–1308, 2015.

[9] N. Fleck *et al.*, "Identifying Raman modes of Sb_2Se_3 and their symmetries using angle-resolved polarised Raman spectra," *J. Mater. Chem. A*, vol. 8 no. 17, p. 8337, 2020.

[10] M. Grossberg, O. Volobujeva, A. Penežko, R. Kaupmees, T. Raadik, and J. Krustok, "Origin of photoluminescence from antimony selenide," *J. Alloys Compd.*, vol. 817, p. 152716, Oct. 2019.

[11] A. Stoliaroff *et al.*, "Deciphering the role of key defects in Sb_2Se_3, a promising candidate for chalcogenide based solar cells," *ACS Appl. Energy Mater.*, vol. 3, no. 3, pp. 2496–2509, 2020.

[12] T. D. C. Hobson *et al.*, "Isotype heterojunction solar cells using n-type Sb_2Se_3 thin films," *Chem. Mater.*, vol. 32, no. 6, pp. 2621–2630, 2020.

[13] H. Shiel *et al.*, "Chemical etching of Sb_2Se_3 solar cells: surface chemistry and back contact behaviour," *J. Phys. Energy*, vol. 1, p. 045001, 2019.

[14] W. Wang *et al.*, "Device characteristics of CZTSSe thin-film solar cells with 12.6% efficiency," *Adv. Energy Mater.*, vol. 4, no. 7, 2014.

[15] Z. Li *et al.*, "9.2%-efficient core-shell structured antimony selenide nanorod array solar cells," *Nat. Commun.*, vol. 10, no. 1, pp. 1–10, 2019.

[16] X. Wen *et al.*, "Vapor transport deposition of antimony selenide thin film solar cells with 7.6% efficiency," *Nat. Commun.*, vol. 9, p. 2179, 2018.

List of Publications

Article 1 was written based on the results reported in Chapter 4, article 2 based on the results in Chapter 5, and article 3 based on the results in Chapter 6.

1. Theodore D. C. Hobson, Oliver S. Hutter, Nicole Fleck, Luke M. Daniels, Jonathan D. Major, Tat Ming Ng, and Ken Durose "Vegard relation and Raman band reference data generated from bulk crystals of kesterite phase composition series $Cu_2ZnSnS_{4x}Se_{4-4x}$ (CZTSSe $0 \leq x \leq 1$)," *Cryst. Growth Des.*, vol. 20, no. 4, pp. 2164–2173, 2020.

2. Nicole Fleck, Theodore D. C. Hobson, Christopher N. Savory, John Buckeridge, Tim D. Veal, Maria R. Correia, David O. Scanlon, Ken Durose, Frank Jäckel "Identifying Raman modes of Sb_2Se_3 and their symmetries using angle-resolved polarised Raman spectra," *J. Mater. Chem. A*, vol. 8, no. 17, p. 8337, 2020.

3. Theodore D. C. Hobson, Laurie J. Phillips, Oliver S. Hutter, Huw Shiel, Jack E. N. Swallow, Christopher N. Savory, Pabitra K Nayak, Silvia Mariotti, Bhaskar Das, Leon Bowen, Leanne A. H. Jones, Thomas J. Featherstone, Matthew J. Smiles, M. A. Farnworth, G. Zoppi, Pardeep K. Thakur, Tien-Lin Lee, Henry J. Snaith, Chris Leighton, David O. Scanlon, Vin Dhanak, Ken Durose, Tim D. Veal, Jonathan D. Major "Isotype heterojunction solar cells using n-type Sb_2Se_3 thin films," *Chem. Mater.*, vol. 32, no. 6, pp. 2621–2630, 2020